INVESTIGATION OF LOWER LIMB BIOMECHANICS DURING CYCLING FOR INJURY PREVENTION

BING FANGBO

PhD

The Hong Kong Polytechnic University

2025

The Hong Kong Polytechnic University

Department of Biomedical Engineering

Investigation of Lower Limb Biomechanics during Cycling for Injury Prevention

Bing Fangbo

A thesis submitted in partial fulfillment of the requirements for the degree of Doctor of Philosophy

March 2025

CERTIFICATE OF ORIGINALITY

I hereby declare that this thesis is my own work and that, to the best of my knowledge and belief, it reproduces no material previously published or written, nor material that has been accepted for the award of any other degree or diploma, except where due acknowledgment has been made in the text.

Signature: ________________________________

(Bing Fangbo)

ABSTRACT

Cycling is a popular sport that requires precise biomechanical adjustments to optimize performance and minimize injury risks. Among the factors, workload level and saddle height are important in practical riding and training, which could influence the loads on the lower limbs and cycling efficiency. Although the two factors have been explored in previous studies, the conclusions remain controversial. This research investigates the biomechanical effects of saddle height and workload using experimental measurements, dynamic calculations of musculoskeletal (MSK) model, finite element (FE) analysis, and machine learning techniques. The study aims to provide evidence-based recommendations to prevent overuse injuries and enhance performance while offering tools for personalized adjustments.

The first study measured electromyography (EMG) of four major lower-limb muscles under different cycling conditions including five saddle heights (95%, 97%, 100%, 103%, and 105% of the greater trochanteric height, GTH) and three workload levels (25%, 50%, and 75% of functional threshold power, FTP). Twenty-seven amateur cyclist performed 15 × 2 mins riding tests. Results revealed that muscle activations of rectus femoris (RF) and biceps femoris (BF) were predominantly influenced by workload, while the medial gastrocnemius (MG) was significantly influenced by saddle height. Balanced activation among muscles was observed at the saddle height of 100% GTH which might be the optimal choice.

The second study developed a MSK multibody model incorporating detailed lower-limb muscles to calculate the muscle forces and joint contact forces under various cycling situations. The model was driven by the markers' trajectories and pedal reaction forces (PRFs) and torques.

A good agreement between the predicted and measured muscle activations was observed. Generalized estimating equations were used to assess the impacts of saddle height and workload, as well as their interactions, on the interested outcomes adjusted for gender, BMI, and cadence. The results indicated that lower saddle heights and higher workloads were associated with increased joint forces on the hip, knee, and ankle joints, as well as their surrounding muscles. Therefore, selecting a higher saddle height within the comfortable physiological range and maintaining a moderate workload can help mitigate the risks of overuse injuries. On the other hand, cycling symmetry was analyzed according to PRFs, joint angles, and muscle activations. The optimal symmetry in PRFs occurred at the saddle heights of 100% and 103% of GTH. The asymmetry index of knee joint angles increased with the increase of saddle height.

The third study established a FE model of knee joint to assess the influence of saddle heights on stress and strain of menisci and cartilages during cycling. The model was constructed based on MRI of right knee joint of a male subject. Bones were simplified to rigid bodies. Major muscles and ligaments were simulated by connectors with defined mechanical properties. The input force loads were PRFs and muscle forces during the crank angle from 90° to 180°. The displacement constraints were the knee flexion angle. The results revealed that stress and strain on the menisci and cartilages decreased with higher saddle heights. This reduction in joint loading highlights the protective role of increasing saddle height within a physiological range.

The last study developed a k-nearest neighbors machine learning model to classify saddle height into high, moderate, and low levels based on the features of hip, knee, and ankle joint angles in cycling. This model demonstrated a high classification accuracy of 99.79%, offering a data-driven method to identify appropriate saddle height tailored to dynamic riding characteristics of individuals.

This research concludes that moderate workload and optimal saddle height are crucial for achieving balance in muscle activation, reducing joint stress, and maintaining pedaling symmetry. The workload should be set according to the personal FTP. Saddle height around 100%-103% of GTH is recommended to optimize performance and minimize injury risks. Cyclists and coaches can adopt evidence-based adjustments to prevent overuse injuries and enhance riding efficiency. Clinicians can use the data to develop personalized rehabilitation training protocols. Future research should validate these findings across diverse populations and outdoor riding conditions, incorporating advanced biomechanical modelling and machine learning to further refine cycling optimization strategies.

PUBLICATIONS

Bing, F., Zhang, G., Wei, L., & Zhang, M. (2025). A machine learning approach for saddle height classification in cycling. Frontiers in Sports and Active Living (*accepted*).

Bing, F., Zhang, G., Wang, Y., & Zhang, M. (2024). Effects of workload and saddle height on muscle activation of the lower limb during cycling. BioMedical Engineering OnLine, 23(1), 6.

Bing, F., Wang, Y., Chen, S. F., Zhang, G., & Zhang, M. (2023). Effects of cycling rehabilitation training on patients with knee osteoarthritis: A systematic review and meta-analysis. Rheumatology: Current Research, 13(4), 18.

Zhang, G., Fu, Y., Wei, L., **Bing, F.**, Cai, H., Chen, T. L. W., & Zhang, M. (2025). Continuously monitoring runners' adaptive strategies to prolonged running on an outdoor track with straight and curved paths: Insights from the varying intersegment coordination variability and shock absorption during a full marathon. Journal of Science and Medicine in Sport, 9.

Zhang, G., Chen, T. L. W., Wei, L., **Bing, F.**, Cai, H., Liu, Y., ... & Zhang, M. (2025). Investigating rearfoot asymmetry in male marathon runners: dual IMUs reveals biomechanical trade-offs related to performance maintenance. Journal of Biomechanics, 191, 8.

Chen, S. F., Wang, Y., **Bing, F.,** & Zhang, M. (2023). The effects of alteration in muscle activation on the iliotibial band during an exhaustive run. BMC Sports Science, Medicine and Rehabilitation, 15(1), 99.

Chen, S., Wang, Y., **Bing, F.,** & Zhang, M. (2023). Effects of Running Speeds and Exhaustion on Iliotibial Band Strain during Running. Bioengineering, 10(4), 417.

ACKNOWLEDGMENTS

Completing this doctoral journey has been both a profoundly challenging and rewarding endeavor. As I reflect on the past years, I am deeply touched by the unwavering support, selfless guidance, and emotional encouragement I have received from countless individuals.

First, I am eternally indebted to my supervisor, Prof. Ming Zhang, whose wisdom and mentorship have shaped every facet of this work. Prof. Zhang exemplified academic rigor and creativity, challenging me to refine my hypotheses while granting me the freedom to explore unconventional ideas. He also takes care of my physical and mental health in life. He is both a good teacher and a good friend, and I am grateful to have such an excellent supervisor.

I extend my sincere appreciation to my colleagues, Dr. Guoxin Zhang, Dr. Shane Fei Chen, Dr. Tony Lin-Wei Chen, Dr. Yan Wang, Dr. Qitao Tan, Dr. Tommy Tung-Ho Hong, Dr. Yinghu Peng, Dr. Duo Wai-Chi Wong, Dr. Meizi Wang, Ms. Linjuan Wei, Ms. Hejin Cai, and Dr. Jason Tak-Man Cheung. Thanks for their willingness to share research experience, help solve problems, and give important advice for my research.

No words can adequately capture my gratitude to my family. I am grateful to my parents whose sacrifices enabled my pursuit of academic without scruple. They are my warmest harbor and eternal spiritual support. Thanks to Dr. Xia, his unwavering companionship transformed this arduous adventure into a shared warm journey.

In closing, to all mentors, peers, and loved ones, your company and help have been my greatest blessing on this academic journey. It is my privilege to express my heartfelt gratitude here.

TABLE OF CONTENTS

LIST OF FIGURES

LIST OF TABLES

LIST OF ABBREVIATIONS

ACL	Anterior Cruciate Ligament
AMS	AnyBody Modeling System
ANOVA	Two-way Analysis of Variance
ASI	Asymmetry Index
A-P	Anterior-Posterior
BDC	Bottom Dead Center
BF	Biceps femoris
BMI	Body Mass Index
CV	Coefficient of Variability
CI	Confidence Interval
DOF	Degree of Freedom
DT	Decision Tree
EMG	Electromyography
FE	Finite Element
FTP	Functional Threshold Power
GAS	Gastrocnemius
GEE	Generalized Estimating Equation
GluMax	Gluteus Maximus
GTH	Greater Trochanter Height
IMU	Inertial Measurement Unit
ITBS	Iliotibial Band Syndrome

KNN	K-nearest Neighbors
LCL	Lateral Collateral Ligament
LE	Logarithmic Strain
LOOCV	Leave-One-Out Cross Validation
MCL	Medial Collateral Ligament
MG	Medial Gastrocnemius
ML	Machine Learning
MRI	Magnetic Resonance Imaging
MSK	Musculoskeletal
MVC	Maximal Voluntary Contraction
M-L	Medial-Lateral
NB	Naïve Bayes
OPL	Oblique Popliteal Ligament
PCL	Posterior Cruciate Ligament
PFPS	Patellofemoral Pain Syndrome
PFL	Popliteofibular Ligament
PRF	Pedal Reaction Force
P-D	Proximal-Distal
QIC	Quasilikelihood under Independence Model Criterion
RF	Rectus Femoris
RMS	Root Mean Square
ROM	Range of Motion
RPM	Revolutions Per Minute
SD	Standard Deviation
SMOTE	Synthetic Minority Over-sampling Technique

SOL	Soleus
SVM	Support Vector Machine
TA	Tibialis Anterior
TDC	Top Dead Center
VI	Vastus Intermedius
VL	Vastus Lateralis
VM	Vastus Medialis

CHAPTER 1 INTRODUCTION

1.1 Background

The bicycle was first born as a means of transportation and later cycling evolved into a competitive and recreational sport. In the early years, England and the United States dominated track cycling, and then track cycling became increasingly popular in other areas, especially in Europe. Nowadays, it has become a global sport, attracting the attention of many fans all over the world. The number of people taking up cycling has increased dramatically in the past decade (Barbarossa, 2020; Pucher & Buehler, 2017). Interestingly, the COVID-19 pandemic also increased the number of people riding bicycles on the streets around the world (Budi, 2021).

Cycling is the most sustainable mode of urban transportation. It causes little damage to the environment and exercises our bodies at the same time. Therefore, it has been advocated by urban planners, the government, and researchers, which has promoted the further development of cycling. Besides this, various factors contribute to the popular trend of cycling, such as increased public health awareness, environmentally friendly awareness, media publicity effect, and the latest fashion lifestyle. The most fundamental reason is the health benefits of cycling, which can improve cardiovascular fitness, help in weight loss, and strengthen lower-limb muscles (Oja et al., 2011). The heart rate during cycling is usually 2-3 times higher than usual (Horton et al., 2017). This can exercise myocardial contractility, enhance vascular wall elasticity, improve microcirculation, and then make cardiopulmonary function gain. People who frequently cycle have a much lower chance of acquiring cardiovascular disorders, such as heart attacks and strokes (Green, 2021). Furthermore, the main lower limb muscular groups, including the quadriceps, hamstrings, glutes, and calves, are worked out by cycling, while it is a low-impact activity that minimizes stress on the joints. This makes it a better exercise for individuals with physical disabilities and joint pain compared to running and even walking. The gentle nature combined with the easily adjusted intensity of cycling makes it appropriate for a wide range of age groups, from children to seniors. Stationary cycling has been proven to be an effective postoperative rehabilitation exercise and intervention method in clinics for people with physical disabilities (Johnston, 2007). Previous experiments showed that older women with knee osteoarthritis improved their lower limb muscle power significantly after an eight-week cycling training program (Macaluso et al., 2003). A similar investigation found that individuals with arthritis who engaged in a 12-week community cycling program experienced decreased knee pain and had better performance in walking tests relative to the comparison group (Salacinski et al., 2012). It will become increasingly common in rehabilitation protocols by raising cardiovascular fitness, strengthening muscles, increasing joint mobility, and offering psychological support, while minimizing injury risks.

Although there is little doubt about the health advantages of cycling, some studies illustrate that cycling can cause pain to joints and kinds of diseases (Abdullatif K Althunyan et al., 2017; Van der walt, 2014). As more and more people take up cycling, the number of related injuries has grown and become a concern (Silberman, 2013). Cycling-related injuries are typically categorized into two main types: traumatic injuries, which result from sudden incidents such as falls or collisions, and non-traumatic injuries, often caused by repetitive stress or improper cycling mechanics over time. The prevalence of overuse injuries, which are the cumulative result of improper cycling over a long period, among cyclists is over 85% (Van der walt, 2014). The most common areas of pain are the knee, lower back, shoulder, wrist, and perineum.

Professional cyclists are more likely to have anterior knee pain and lower back pain than amateur cyclists (Silberman, 2013). The knee joint pain may be caused by too long riding time, and the body's incoordination during cycling.

Different riding methods and bicycle settings can have opposite effects on health. The factors, including saddle height, crank length, cadence, riding posture, and foot position, are important to cycling efficiency, injury risks, and therapeutic outcomes. Bike fitting aims to choose the appropriate components and settings for the requirements, goals, and physical conditions of riders. A small adjustment, especially in the contact part of the bicycle and cyclist, can affect the kinetic chain, thereby changing cycling efficiency, power, and comfort. In addition to the bicycle factor, physical factors are also related to injuries. Cyclists must have professional skills and good neuromuscular coordination to control the bicycle. The cycling biomechanics involves the roles played by muscles, joints, and tendons which are crucial for cycling performance and injury prevention.

Studies have shown that lower-limb muscles modify their recruitment patterns in reaction to mechanical demands (Lanferdini et al., 2014). For instance, as the riding velocity increased, the activation times of rectus femoris (RF), biceps femoris (BF), and gastrocnemius (GAS) muscles were advanced relative to knee joint angles, and the electromyography (EMG) signals of BF presented a double burst pattern (Suzuki, 1982). The EMG of vastus lateralis (VL) was significantly influenced by resistive load, with heavier loads mitigating performance decline and muscle recruitment reduction (Matsuura et al., 2011). Through continuous feedback loops involving sensory input from muscles and joints, the central nervous system is managed to produce optimal patterns of muscular activation, which is a major factor in these alterations. However, there is a relatively consistent view of the major muscle groups' activation patterns during the cycling sports among the previous studies (R. C. H. So et al., 2005). The gluteus maximus (GluMax) acts mainly in hip extension. soleus (SOL), gastrocnemius (GAS), and tibialis anterior (TA) are the ankle stabilizers. The knee extensors are the VL, VM, and RF, while the knee flexors are the GAS, hamstrings, and BF (Ryan, 1992). As mentioned earlier, some muscles do more than one job. This is because multi-joint muscles connect at least two joints and serve different demands at different cycling stages. Since the single-joint muscles have more straightforward roles in movement while the multi-joint muscles require more intricate coordination to orchestrate complex movements across multiple joints, they have distinct muscle activation profiles. Besides, the roles of synergistic muscles, and agonist and antagonist muscles may change with the varying riding conditions and the muscle fatigue (Raasch, 1999). Therefore, changes in muscle activation patterns are complex, yet crucial for the development of an appropriate cycling training program.

The majority of studies concentrated on the lower limb joints because cycling mostly involves periodic motion of the lower limbs. Hip, knee, and ankle joints pulled by the surrounding muscles to extend and flex. Mean range of motion (ROM) of knee is between 45° and 115°, and that of ankle is from 2° plantarflexion to 22° dorsiflexion (Ericson M O, 1988). The ROM of the hip is ranging from 30° to 70° (Ericson M O, 1988). However, the ROMs of joints are affected by the bike sitting like saddle height. Half of the joint injuries due to improper riding have occurred in the lower extremities. Among them, injuries in the knee joints account for 62% of all overuse injuries (Silberman, 2013). Studies indicated that improper bike setup might result in varying degrees of knee joint pain in different areas (Barrios, 1997). The possible causes of this disease are excessive riding intensity or increasing mileage, and too low or forward saddle settings. As a rule of thumb, raising the saddle height, reducing the crank length, and everting foot can relieve pain in the anterior knee. For the lateral knee joint pain, increasing toe out and distance between feet could relieve it and prevent further deterioration such as Iliotibial band syndrome (ITBS). Although many studies have contributed to exploring the biomechanics of lower limb joints, the current research is not systematic, and there are some controversial conclusions. The interpretation of cycling biomechanics and the internal relationship between various riding conditions and injuries is insufficient.

The two handlebars, the left and right pedals, and the saddle make up the five contact points between cyclist and bicycle. The bicycle configuration, such as saddle height, affects the position of these points which further affects the biomechanics of lower limbs. If the saddle height is too low, the knee has a large flexion angle when generating the peak driving force, which will lead to a large force on the knee joint. The maximum muscle force can only be produced by muscles of a specific length which is affected by the joint angle. The saddle usually is adjusted from vertical and horizontal directions. Its inclination angle is adjusted to prevent damage to the perineum. Some studies have suggested that the horizontal position of the saddle should be placed where the knee projection intersects the pedal shaft. Triathletes set their saddles more forward than road cyclists, which could increase the likelihood of knee injuries (Ricard, 2006). The saddle height can be adjusted relative to the bicycle frame or the length of segments, such as the greater trochanter or pubic to the floor. The knee joint angle when the pedal is located at the crank angle of 6 o'clock, the bottom dead center (BDC), or top dead center (TDC) is another reference for saddle adjustment. Although several adjustment approaches have been proposed, it is not clear which one is more advantageous. The adjustment strategies and biomechanical mechanism of each method are also not clear.

Workload level directly affects loading on the lower limbs. Athletes and patients can precisely regulate their workload by cycling training platforms to exercise specific muscles or restore joint function. A study indicates that a greater workload led to prolonged activation periods for TA and BF muscles (Kamyar Momeni, 2014). Another study indicated that the contribution of the knee joint to the total mechanical work of lower limb joints increased with the increase in workload (Rodrigo R. Bini, 2010). This indicates that the workload may affect the coordination pattern of the lower-limb muscles. Pedal reaction forces (PRFs) could suggest these changes to some extent. In a riding test of recreational cyclists, the peak PRF increased at a greater workload (Kamyar Momeni, 2014). The cadence also has an influence on the pedal forces and muscle forces, but it was different in previous studies, which reduces the comparability between the conclusions. In addition, gender, age, and riding experience are also influencing factors and should be considered. While some research has examined the workload impacts or saddle height influences, few studies have investigated the possible coupling between the two factors. If there is a coupling effect between them, studying the influence of one factor alone may lead to incorrect conclusions.

Exploring the relationship between cycling conditions and lower limb biomechanics is of great significance for optimizing cycling performance and preventing injuries. The functions of muscles and joints could be changed according to the mechanical demands imposed by external conditions. Overuse injuries often result from improper bike setting. Understanding the biomechanics of lower limbs during cycling is useful for identifying the risk factors and achieving greater cycling efficiency.

1.2 Objectives of the Study

Cycling has become popular not only as a recreational activity and competitive sport but also as a mode of transportation. However, this growing involvement has also resulted in a rise in the incidence of musculoskeletal (MSK) injuries among cyclists. Despite recognized risks associated with improper cycling conditions, studies that systematically examine their essential connection are still lacking. Therefore, this study aims to enhance the understanding of lower limb biomechanics during cycling, with a specific focus on how saddle height and workload impact performance and injury risks. To achieve this overarching goal, the study is structured with four key objectives:

1) Performing dynamic simulation of lower limb MSK model to assess the muscle forces and joint loads during cycling. Key components of this objective include:
    a. Accurately modeling the lower limb anatomy and simulating the riding process under various conditions.
    b. Verifying the accuracy of the model by contrasting it with the measured EMG signals.
    c. Analyzing the impacts of saddle height and workload on the muscle forces and joint contact forces.
2) Performing finite element (FE) analysis of knee joint to calculate the stress and strain of menisci and cartilages during cycling with different saddle heights. Key components of this objective include:
    a. Establishing a knee joint model based on the magnetic resonance imaging (MRI) data and meshing the model.
    b. Defining parameters such as material properties and loads for FE calculation.
    c. Analyzing stress and strain distributions under different saddle heights.
3) Exploring the impacts of saddle height and workload on lower-extremity muscles and joints. Specific aspects of this objective include:
    a. Assessing the impacts of workload and saddle height on the activations of muscles, muscle forces, as well as the joint contact forces.

    b. Evaluating how changes in saddle height influence lower limb biomechanics and cycling symmetry in terms of joint angles, PRFs, and muscle activations.

    c. Analyzing the potential injury risks related to the saddle height and workload.

4) Establishing a machine learning (ML) model to identify the appropriateness of saddle height. Key components of this objective include:

    a. Calculating the features of hip, knee, and ankle joint angles under conditions of different saddle heights.

    b. Extracting and selecting the critical feature set from the data that correlate with saddle heights.

    c. Comparing ML algorithms to construct a high-accuracy model that can precisely classify the saddle height into high, moderate, and low levels.

1.3 Outline of the Dissertation

Chapter 1 provides the research background on cycling, including its popularity, health benefits, related injuries, and possible causes of injuries. Based on this information, our research question was formulated. This chapter established the goals and structure of the dissertation.

Chapter 2 reviews previous research on lower limb biomechanics during cycling, including kinematics and kinetics. The various factors related to cycling performance and injury risks are discussed. Especially, the roles of saddle height and workload in lower limb biomechanics are examined. The findings from previous studies are reviewed. Furthermore, an overview of current MSK models, FE models, and ML models pertaining to cycling was provided.

Chapter 3 details the study design and research methodology adopted to achieve the study objectives. The recruitment criteria and physical information about the participants are listed. The specific protocols for conducting cycling tests under different riding conditions are described, including the experiment procedure, data collection, and data analysis. The modeling, verification, and outcomes of multibody MSK dynamic simulation are stated. The process of FE modeling and calculation is presented. The statistical analysis used to evaluate the impacts of saddle height and workload level on the lower-limb biomechanics is described. The developing process of the ML model to identify the saddle height level is explained, including the preprocessing of joint angles, feature extraction, dataset construction, and comparison of the ML models.

Chapter 4 presents the results and main findings from the cycling experiments. It is organized into seven sections. The first are the EMG results from experiments. The second are the kinematics and kinetics results from dynamic simulation, including muscle forces and joint contact forces. The third part is the results about cycling symmetry according to the PRFs, lower limb joint angles, and muscle activations from the experiments. The fourth are the FE analysis results of stress and strain of the knee joint. The fifth is the developed ML model, reporting the identification performance using different features and optimal model parameters.

Chapter 5 discusses the results combined with existing literature. Corresponding to the results, the first part is the discussion of EMG results and the implications for injury prevention. The second part illustrates the validity and limitations of the developed MSK model and interprets the results of the dynamics affected by saddle height and workload. The third part discusses the cycling symmetry under different cycling conditions. The fourth part discusses the impacts of saddle height on the stress and strain of menisci and cartilages of knee joint. Last part demonstrates the effectiveness of using joint angles for saddle height identification by ML model and states how this model can enhance bike fitting practices. Based on the above information, we provide recommendations for optimal saddle height and appropriate workload level to minimize injury risk and enhance performance. In the last section, the limitation of this study is addressed.

Chapter 6 summarizes the key findings from the research, along with their significance in promoting optimal bike setting and cycling conditions for injury prevention and performance enhancement. The practical implications for cyclists, coaches, and bike fitters based on study findings are emphasized. Furthermore, recommendations are put forward for potential areas of cycling study.

CHAPTER 2 LITERATURE REVIEW

2.1 Biomechanics of Cycling

With the development of the global cycling boom, problems accompanying riding have become hot spots among the cycling community. Especially, the balance between cycling performance and related injuries. Some biomechanical aspects must be considered. It is well known that cycling reduces the load on the knee joint and can effectively exercise the lower limbs. As a result, it is applied in rehabilitation treatments. The therapist should also provide the appropriate cycling prescription based on the biomechanical mechanism, including saddle height, riding resistance, and pedal position.

2.1.1 Lower-limb muscles and joints

The hip joint is a ball-and-socket joint that connects the femur to the pelvis. The hip joint is surrounded by several muscles, including the GluMax, gluteus medius, and hip flexors, which are essential for cycling (Byrne et al., 2010). Different from spine and pelvis, the hip joint is responsible for generating power during cycling. GluMax, the largest muscle in the body, is the primary hip extensor and generates power during the downstroke phase of pedaling. The hip flexors, including the iliopsoas, RF, and sartorius, allow for hip flexion (Byrne et al., 2010). Besides, the hip joint plays a role in blood circulation by increasing blood flow to the lower body during cycling. Increased blood flow delivers oxygen and nutrients to the muscles which benefits the improvement of cycling performance (R. C. So et al., 2005).

During cycling, the knee joint undergoes a cyclic motion of flexion and extension. The quadriceps, hamstrings, and calf muscles work together to generate pedaling force and stabilize the knee joints. The ligaments of the knee joint, including the anterior cruciate ligament (ACL) and the medial collateral ligament (MCL), provide stability and support to the joint during cycling. The ACL is susceptible to injury in cyclists due to the twisting and pivoting motion that occurs during cycling. The meniscus and cartilage act as a shock absorber for the knee joint motion, which are subjected to friction during each knee flexion and extension. Prolonged inappropriate cycling can lead to cartilage and meniscus wear, and it is irreversible. Injuries of menisci are common in cyclists, especially during high-intensity cycling (Zhang & Ma, 2023). Compared with non-cyclists, the degree of chondromalacia and cartilage pathology are more common and severe in cyclists (Stone et al., 2016). Thus, investigating the biomechanical characteristics of meniscus and cartilage of the knee joint during cycling is crucial.

The ankle joint performs the dorsiflexion and plantarflexion during cycling. This motion is controlled by the GAS, SOL, and TA. The GAS and SOL muscles, collectively known as the calf muscles, generate force during the downstroke of the pedal stroke, while the TA helps to pull the foot back up on the upstroke. The deltoid ligament helps to prevent inward rotation and eversion of the ankle, while the lateral ligaments help to prevent outward rotation and inversion. The Achilles tendon is particularly important for generating force during the pedal stroke. The peroneal tendons help to stabilize the ankle joint. The relationship between the movement of lower limb joints and muscles is shown in Figure 2.1.

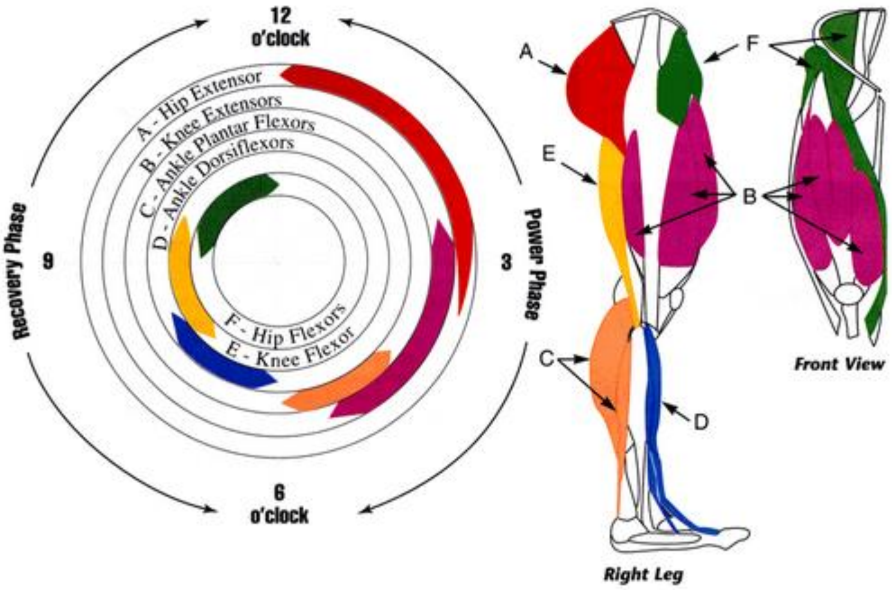

Figure 2.1 Correspondence between lower limb muscle activations and joint movements (Michelle Lee, 2016).

2.1.2 Kinematics

The kinematic parameters of cycling include speed, cadence, power, and joint angles. Kinematic analysis involves recording the positions of joints and coordinates of segments to analyze the translations and rotations of the limbs. The most common method is using the motion capture system with multiple cameras to track the reflective markers attached to the subjects. A complete pedaling cycle includes power and recovery phases. The power phase begins with the downward movement of the pedal from the TDC. The hip and knee joints extend, and the ankle joint plantarflex. As the pedal reaches the BDC, the hip joint continues to extend, while the knee joint begins to flex and the ankle joint dorsiflex. The recovery phase begins as the cyclist pulls the pedal up, causing the hip joint to flex, the knee joint to flex, and the ankle joint to plantarflex.

The research on the kinematics of the lower body is far more than that of the upper body. The periodicity of the cycling allowed the researchers to select a few cycles as representative of the overall movement. The action of cycling is symmetrical, with significantly more activity in the sagittal plane than in the frontal and transverse planes. Although there are some differences between the motions of the left and right limbs (Edeline et al., 2004), these differences can be overlooked in healthy individuals in order to reduce the amount of data. The motion angles of the main power joints of the lower limbs are shown in Figure 2.2. The maximum ROMs of the hip, knee, and ankle joints are 42-44°, 73-78°, and 21-25°, respectively (Bini & Hume, 2016). ROMs were influenced by the saddle height and the position of the foot relative to the pedal. Increasing the saddle height is an effective way to enlarge the ROM (Ericson, 1988). In comparison to top cyclists, rookie riders have a smaller absolute range of ankle motion in the sagittal plane. Elite cyclists also had greater coordination between lower limb joints in the sagittal plane which may be related to more excellent muscle recruitment patterns (Chapman et al., 2009).

The findings of Bini et al. revealed that knee joint mechanics exhibited greater susceptibility to fatigue compared to ankle and hip joints during cycling tests (R. R. Bini, F. Diefenthaeler, et al., 2010). A decrease in the mean value of the ankle joint angle and an increase in the ROM indicated a decrease in its dorsiflexion activity. The knee joint experienced an increase in the average angles due to heightened muscle engagement as well as the hip, whereas the hip's range of motion diminished. This indicates a tendency for more extensions at the hip and knee. Changes in joint angles are directly correlated with muscle length (Sanderson et al., 2006). Changing muscle length might mean a more efficient way of exerting force when fatigue sets in. But in other studies (Amoroso, 1993; Sanderson & Black, 2003), this total change was not statistically different. Bini et al. defined fatigue from 90% of the total riding time and observed a significant reduction in cadence (R. R. Bini, F. Diefenthaeler, et al., 2010). Similarly, when the cadence was reduced by 20%, the ankle angle increased but its ROM decreased (Rodrigo Rico Bini et al., 2010). Therefore, the lower limb kinematic performance is also influenced by cadence. The joint angle, however, is unaffected by the workload (Bini et al., 2012). The muscle excitation state provides an explanation. The length of the SOL and GAS shortened as the cadence rose, although the shortening velocity increased (Sanderson et al., 2006). As seen in the integrated EMG, this might result in higher levels of excitement. Each muscle operates within a unique range of force-velocity curves (Sanderson et al., 2006), and further research into the coordination of muscles is needed, which may help athletes develop strategies to adjust joint angles and delay the onset of fatigue.

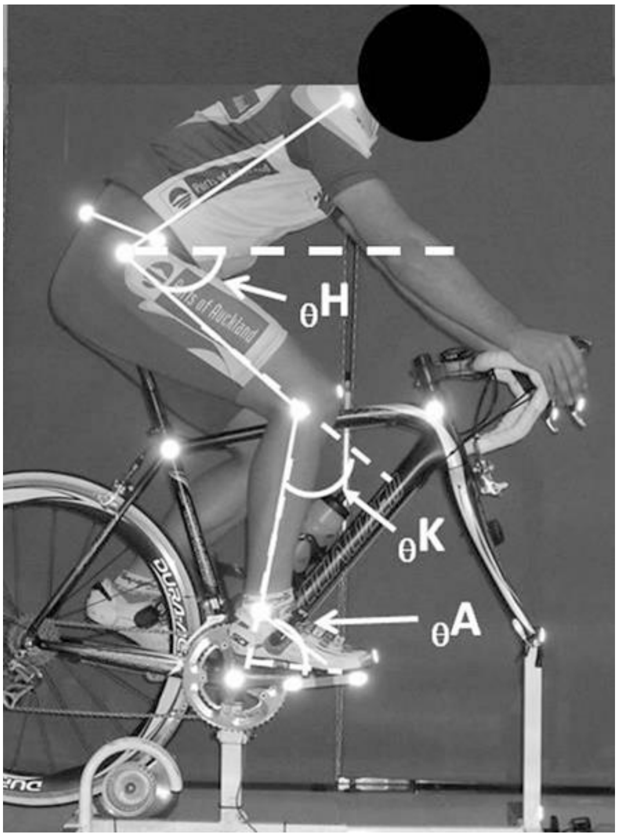

Figure 2.2 Motion angles of hip, knee, and ankle joints during cycling (Rodrigo Rico Bini et al., 2014).

2.1.3 Kinetics

Optimizing the relationship between cyclists and bicycles is the key to improving performance. There are five contact points - two handles, two pedals, and a seat. The contact forces suggest the rationality of the bicycle setting and the comfort of the cyclists. PRFs can be used to calculate the cycling efficiency and dynamic simulation (Rodrigo R Bini, 2013). The calculated joint contact forces and moments reflect the coordination between the joints, and also provide the information of injury risks (Callaghan, 2005).

The hip, knee, and ankle joints are involved in a series of coordinated movements that allow for efficient power transfer from the cyclist's legs to the pedals. During the downstroke of the pedal, the hip flexors generate a force that pulls the thigh upward, while the gluteal muscles generate a force that pulls the thigh downward during the upstroke. The hip abductors and adductors contribute to the lateral stability of the hip joint during cycling. For the knee joint, the extension and flexion forces are the main forces. During the downstroke, the quadriceps muscles generate a force that extends the knee, while the hamstrings and GAS muscles generate a force that flexes the knee during the upstroke. The patellofemoral joint also experiences forces from the quadriceps tendon, which acts as a pulley to transmit forces from the quadriceps to the tibia. The moments generated by these forces result in a net extension moment at the knee during the downstroke and a net flexion moment during the upstroke. The main ankle joint forces are the plantarflexion and dorsiflexion forces. During the downstroke of the pedal, the GAS and SOL muscles generate the plantarflexion force on the ankle, while the TA generates the dorsiflexion force during the upstroke (Bini & Carpes, 2014).

The changes in the kinematic and kinetic variables are not always synchronized. Cadence modifications can change the joint angles and their respective ROMs but do not significantly impact the overall mechanical power and the proportion of the output power of each joint relative to the total power requirement. On the contrary, when the workload increased from 0 N to 10 N, the mechanical work of three lower limb joints increased significantly (R. R. Bini, A. C. Tamborindeguy, et al., 2010). High workload led to an increase in knee joint extension and abduction moments, which increased joint vertical force and raised the risk of injuries (Fang et al., 2016). The knee joint increased its power output and work proportion among the three joints to compensate for the declined mechanical work from the hip. Yunqi et al. noted that joint moments and joint mechanical work were impacted by both posture (e.g. standing posture vs. sitting posture) and the slope of the riding road (Tang et al., 2020).

Fatigue affects the kinetics of the joint in addition to the kinematic variables. In the third period of the fatigue test with maximal power output, the knee joint moment increased as well as its contribution to the total net joint moments. However, no significant change in PRFs was observed (Bini & Diefenthaeler, 2010). Sayers et al. analyzed the kinematic changes of the three lower limb joints during the 60-minute cycling experiment (Sayers et al., 2012). During the drive phase at the end of the experimental time, subjects tended to increase hip extension and ankle flexion range. The authors indicated that tibia rotation might be an important fatigue indicator because its variability increases. Peveler et al. reported significant reductions in ankle plantarflexion and knee flexion at higher intensities and speculated that the increase in ankle dorsiflexion at higher intensities was a compensation for the changes in saddle height which was not the result of autonomous selection (Peveler, 2012). Mornieux et al. noted that the hip moment rose by 4% with the increase in power from 150 W to 350 W, and the hip moment reduced by 4% as cadence rose from 60 rpm to 80 rpm (Mornieux et al., 2007). The change in the knee moment in this experiment is exactly the reverse of the hip joint. The ankle moment did not change significantly (Mornieux et al., 2007). The main cycling energy comes from the muscles around the hip and knee, while the muscles around the ankle transfer the power and keep the crank rotating continuously (Zajac et al., 2002).

Extrinsic factors, such as saddle height, have been investigated for biomechanical effects on the knee joint. Bini et al. pointed out that the proportion of overall mechanical work performed by the knee was negatively correlated with the saddle height which was decreased at higher saddle heights (R. R. Bini, A. C. Tamborindeguy, et al., 2010). The further back the horizontal position of the saddle, the greater the tibial shear force, but the impact on the pressure of the tibia and patella is minimal (Bini et al., 2013). As the net cycling power increased, the extension power of the knee joint decreased while the flexion power increased (Barratt, 2016). This suggests that cyclists tend to rely more on the flexion strength of the knee joint as the power increases. The increase in crank length induced an increase in torques and larger ROM of the knee and hip joint angles (Ferrer-Roca et al., 2016). However, they only analyzed the torque through crank power, without exploring changes in joint torques.

2.1.4 Cycling symmetry

Symmetry in cycling plays a critical role in performance optimization, energy efficiency, and injury prevention, as cycling involves repetitive pedaling motions. Disruptions in symmetry can lead to biomechanical inefficiencies, reduced power output, and increased risks of overuse injuries.

Research shows that 25% - 45% of people prefer to use their right leg during lower extremity movements (Čuk, 2001). Cycling symmetry has a significant impact on muscle activation, force application, and kinematics. Research shows that the difference in cycling power between limbs is from 5% to 20% (Carpes, 2007). In a 40 km cycling time trial, competitive cyclists showed an asymmetry in crank torque output and the asymmetry index decreased at a higher exercise intensity (Carpes, 2007). Cadence might be an influential factor of bilateral symmetry, as there was a linear relationship between the symmetry index of average negative power and cadence, but it was highly variable among subjects (Smak W, 1999). The EMG of BF, medial gastrocnemius (MG), and VL were asymmetry for both cyclists and non-cyclists which were strongly affected by cycling intensity (Carpes et al., 2011). The asymmetries of kinematics and kinetics were also found and more pronounced in the non-cyclist subjects, who therefore rode less efficiently (Carpes et al., 2010; Edeline et al., 2004). However, the kinetic asymmetries may not be related to bilateral differences in muscle activations, even symmetrical muscle forces might cause kinematics differences and lead to bilateral differences in joint torques (Edeline et al., 2004).

In addition to the effect of cadence and external workload on cycling symmetry as described before, fatigue may also have an impact (Carpes, 2007). The increased effort might contribute to more pedaling symmetry, either because of the increased power level or accumulated fatigue (Sanderson, 1991). But another study came to the opposite conclusion that the asymmetries of lower-limb torque increased with the increase of power output (Rodrigo R Bini & Patria A Hume, 2014). The asymmetry in saddle pressure increased after a 30-minute constant-workload cycling, suggesting that the fatigue might exacerbate specific bilateral asymmetries which was reflected in the variations of muscle activation (Lepasalu et al., 2024). However, the asymmetry index in another study changed only about 5% before and after fatigue which was nonsignificant (Farrell & Neira, 2023), although the asymmetry of cycling power was reproducible. The prevailing view is that fatigue changes the mechanical patterns, recruitment of muscles, and muscle activation patterns during cycling, but does not change the effectiveness of pedal force (Amoroso et al., 1993; Diefenthaeler et al., 2007). This may contribute to the controversial findings of the influence of workload on cycling asymmetry. Additionally, the response of individual symmetry to different riding speeds was extremely different, but there was a large cycling asymmetry of lower limbs when the cadence was below 60 rpm and above 90 rpm (Liu & Jensen, 2012).

Previous studies have shown a connection between asymmetry and cycling performance, even though the specific influences are uncertain. A 4-km cycling experiment unexpectedly showed that the asymmetry of effective pedal force had a positive relationship with riding performance which was evaluated by the finishing time (Bini, 2015). However, in later cycling experiments with a longer distance, larger and more symmetry pedal forces were not associated with better riding performance (Bini, 2016). Another study reported that there was no significant difference in the asymmetry represented by elite and sub-elite cyclists in terms of kinetics and kinematics, questioning whether cycling symmetry and performance are related (García-López, 2015). An opposite finding was demonstrated by a previous study that the relationship between asymmetry and cycling performance was negative (Rannama et al., 2015). But the asymmetries of the hip and ankle kinematics were not significantly changed. The current limited literature does not clarify the link between asymmetry and cycling parameters as well as performance. More research is required to figure out the relationship between muscle activations, kinematics, kinetics, and pedaling asymmetries.

2.1.5 Pedal reaction forces

Pedal reaction forces (PRFs) are important in the calculation of cycling efficiency and power output, and the dynamic simulation. PRF is a vector quantity with both magnitude and direction and can be decomposed into its radial and tangential components, which respectively contribute to the forward propulsion of the bicycle and the lateral stabilization of the cyclist (Fonda & Sarabon, 2010). The magnitude and direction of the PRF are influenced by the rider's body position, pedaling technique, and bicycle setting. The ratio of the force parallel to the crank to the overall force applied to the pedal is known as the pedal force effectiveness. Figure 2.3 shows the pedal forces and effective force in cycling. The direction of the measured PRF is opposite to that of the pedal force, as they are mutual reaction forces.

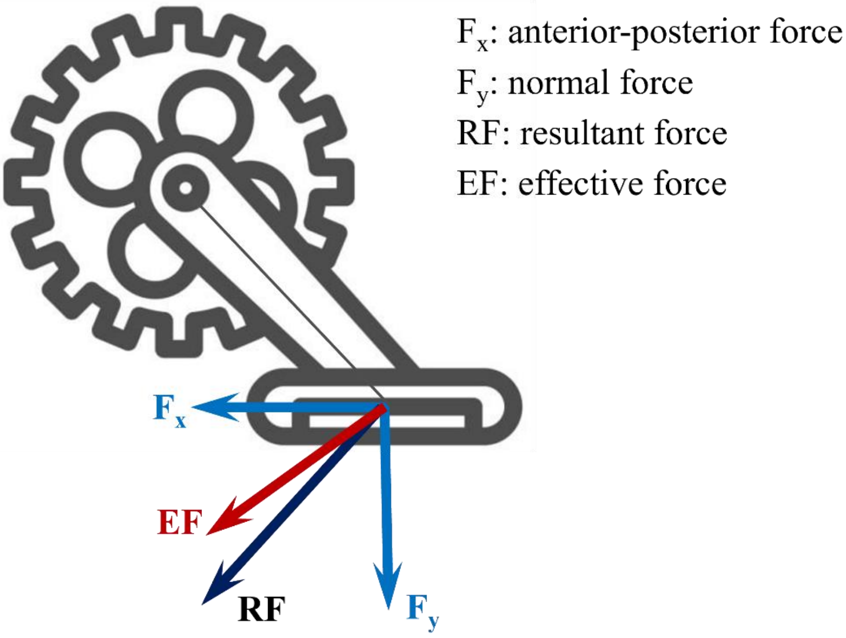

Figure 2.3 Diagram of pedal forces.

The sensor types for measuring PRFs include pressure, strain gauge, piezoelectric, load cell, and small force plate (Rodrigo Rico Bini, 2014). All of them can measure the vertical force (F_z), and some can measure the anterior-posterior force (F_x) and mediolateral force (F_y). The pedals equipped with six-axis sensors are still limited, which enable to measure the 3D forces and torques. It should be noted that the majority of current experimental measurements for PRFs were used in the laboratory which is different from outdoor cycling. Additionally, including real measured pedal forces into the input parameters in the dynamic simulation can improve the realism and accuracy of results. Bini et al. set the saddle height according to the static knee angle within ±10° and found that saddle height changed joint kinematic performance but had no effect on pedal force effectiveness (R. R. Bini et al., 2014). However, the dynamometric 2D right pedal with strain gauge in the studies only measured F_z and F_x, and a lower pedal force effectiveness may be obtained if F_y is considered. The research considering 3D forces and torques in dynamic calculation is still limited.

2.2 Cycling Injuries

If there is high stress on the hip, knee, and ankle joints during cycling, cyclists would get chronic pain and disability. Since cycling is a periodically repeated movement of pedal stroke, the largest proportion of injuries is non-traumatic/overuse injuries, which is somewhat related to the biomechanical mechanisms. Improper body position can lead to serious overuse injuries with long-time riding. Bike-fitting is an important and effective approach to adjust the cyclist-bike interface and prevent overuse injuries.

2.2.1 Upper body injuries

Neck and lower back pain are common complications for some professional cyclists with more than 58% (Clarsen et al., 2010). Because they often ride in a special position during competition and training, that is, their back is greatly bent down and held as level as possible to reduce riding resistance. This more aerodynamic posture can strain the cervical extensor muscles' endurance and cause neck pain. Different degrees of lumbar kyphosis are inevitable. Long-term training may improve the flexion ability of the cervical spine muscles, which in turn can relieve pain (Deakon, 2012). Most cyclists were not willing to stop training or drop out of a race just because of lower back pain. Strategically adjusting the positions of handlebars and seats can quickly reduce the pain and help the cyclist continue riding during an episode of pain (Muyor, 2015). More than one in five riders felt that lower back pain affected their performance. In contrast, neck pain and hand numbness have been reported but are generally mild. It is usually because the cyclist holds the handlebars for a long time and compresses the ulnar nerve at Guyon's canal in the wrist. The prevalence of hand pain varies widely among the different studies (Dettori, 2006). More reasonable distribution of weights, timely adjustment of hand position, and wearing gloves can release pressure and reduce discomfort to a certain extent.

Besides, cycling has also been reported to cause shoulder and forearm injuries, but the percentages are relatively low.

2.2.2 Lower body injuries

The probability of serious complications is much higher in the lower body than in the upper body, since the lower limbs are the source of power and the motion range is greater.

In the hip joint, common injuries in cycling include hip impingement, labral tears, and gluteal tendinopathy. The symptoms of internal hip pain are intermittent groin pain, which is reported in more than 80% of patients (Clohisy et al., 2009). These injuries are often caused by repetitive hip flexion and extension movements, as well as excessive or improper use of the hip muscles. Achieving peak hip flexion during the TDC of pedal stroke may result in a considerable angle that could trigger pain in individuals with symptomatic hip joint pathology (Wadsworth & Weinrauch, 2019). Additionally, cyclists may experience bursitis or snapping hip syndrome, which can cause pain and limited mobility.

As for the knee joint, cyclists commonly complain of anterior knee pain. These injuries are often caused by repetitive knee flexion and extension movements and can result in chronic pain and inflammation in the knee joint. The knee joint is an important force part in cycling with a high incidence of pain. The number of studies on knee joint biomechanics is relatively large. Bicycle type, cycling goal, body mass index, and other physical activities were all associated with the occurrence of knee pain (A. K. Althunyan et al., 2017). A previous study investigated post-race physical injuries in 169 professional cyclists and insufficient saddle-pedal distance was significantly associated with the incidence of knee pain (Sabeti-Aschraf, 2010). Another study investigated the effect of knee and trunk flexion angles on cycling experience and found that larger knee flexion not only led to higher levels of fatigue and pain perception in the thighs and knees, but also caused trunk discomfort (Priego Quesada et al., 2016). They recommended setting the saddle height with a knee angle of about 40° as a bike-fitting way to reduce joint overuse.

Pain in the ankle is associated with an abnormal recruitment pattern of the gluteus medius and is accompanied by weakness of the hip abductor muscles (Kotler et al., 2016). Excessive ankle dorsiflexion angle and improper foot-pedal relative position may lead to Achilles tendon pain. Additionally, proper cycling shoes are very important (Gregor, 1994). Hard-soled shoes can be used as rigid bodies to better transfer power to the pedals, but too stiff or tight cycling shoes can cause metatarsalgia and interdigital neuralgia. Discomfort in the foot can lead to abnormal ankle movement patterns and wear the ankle joint in the long term. However, the number of studies on ankle kinetics is still scarce.

2.2.3 Other injuries

Head injuries occurred only in traumatic injuries, such as bicycle crashes, possibly accompanied by soft tissue injuries, fractures, and concussions. Buttock and perineal pain are caused by saddle sores and pudendal nerve compression. When the body leans forward, the center of gravity shifts to the front side, resulting in compression of the cavernous artery and obstruction of flow (Kotler et al., 2016). Adjusting the height and width of the saddle is an effective measure. The characteristics of the saddle should be customized specifically for male and female riders.

2.3 Factors Associated with Injuries

Cycling injuries can arise from a variety of factors, each impacting biomechanics and contributing to injury mechanisms. Understanding these factors is essential for cyclists to minimize the risk of injury.

2.3.1 Saddle height and bicycle setup

Although bike fitting is not very popular in China, it should be a necessary process before riding begins. Proper bike fitting is essential for optimizing performance and preventing injuries, as misalignments can lead to repetitive strain on various body parts. Bicycle settings including saddle position, crank length, Q factor, handlebar height, and reach should be adapted to the individual's anatomy.

The saddle can be adjusted from the vertical position, horizontal position, and tilt angle position. The saddle tilt angle usually remains horizontal. While some cyclists tilt the saddle slightly forward to reduce the pressure of the saddle on the perineal nerve, especially male cyclists. The horizontal position of the saddle is advised that the vertical projection of the knee should intersect the pedal axis to reduce the knee joint force (Wanich et al., 2007). The forward saddle position is more likely to cause knee injuries. Although the ideal saddle height remains controversial, it is a consensus from previous studies that saddle height is closely related to knee pain (Asplund & St Pierre, 2004; Callaghan, 2005). An excessively high saddle can cause hyperextension of the knee during pedaling, leading to conditions such as patellofemoral pain syndrome. Conversely, too low a saddle can increase strain on the hip flexors and lower back due to altered pedaling mechanics.

There are many methods to set the optimal saddle height, mainly based on the anthropometrical and the motion range of the knee joint angle. Table 2.1 summarizes some common methods. Mestdagh et al. suggested that the optimal saddle height should be 107% of the greater trochanter height (de Vey Mestdagh, 1998). Gregor et al. suggested a wider range of lengths, namely 106%-109% of the greater trochanter height (GREGOR et al., 1991). Hamley et al. indicated that a saddle height of 109% of the inseam length resulted in the minimum time to exhaustion during constant workload cycling (Hamley & Thomas, 1967). This saddle height adjustment has a higher probability of the knee angle being between 25° and 35° than LeMond's method which is widely accepted and used (LeMond, 1988). When the crank is at 6 o'clock, a knee joint angle of 25° to 35° is thought to minimize harm from weak joint force (Peveler et al., 2005). Peveler et al. believed that a knee flexion angle of 25° for saddle height setting was better than 35° in terms of cycling performance and injury prevention because it resulted in a lower O_2 consumption. The variation relationship between joint angles and energy expenditure is still unknown. Ventura et al. showed that oxygen consumption increased and total efficiency decreased when the saddle was raised (Ferrer-Roca, 2014). This result is contrary to Peveler et al.'s study, which may be due to the distinction between the determining method of the saddle height. Price and Donne noted that the efficiency reduced and the production of VO_2 rose as the saddle height varied from 96% to 104% of the trochanteric height. They recommend that the ideal saddle height range should be between 96% and 100% (Price & Donne, 1997). The distance from the saddle to the pedal is linearly correlated to the inseam leg length (Baino, 2011). Static knee angle measurement method underestimated the dynamic knee flexion angle by about 17% (Peveler, 2012). Bini et al. measured lower limb joint angles statically and dynamically and found that only when the joint angle was measured statically by the crank at 3 o 'clock the results were consistent with dynamic measurements (Bini & Hume, 2016). Static measurement of the joint angle at the BDC between 25° and 35° and dynamic measurement of the angle between 30° and 40° resulted in the same saddle height (Millour et al., 2019). The common methods for measuring the length of the inseam present very similar mean bias, and no single measurement is widely agreed upon (Millour & Bertucci, 2017). Gatti et al. proposed a formula to predict the optimal saddle height based on the length of the inseam, the minimum/maximum knee flexion angle, and the seat tube angle, but it cannot be used in clip-free cycling (Gatti et al., 2022). A more in-depth analysis of the relationship between the anthropometric parameters and the optimal saddle height is highly desirable. We expect a method to accurately establish the link between them.

Table 2.1 Common methods for determining saddle height

	Name	Method	Pros and Cons
Anthropometrical of lower limb	Hami Thomas method	109% of the inseam length	Pros: according to the characteristics of human anatomy; more convenient measurement.
	Raymond method	88.3% of the distance between the top of the saddle and the bottom center of the frame is the inseam length	
	Greater trochanter method	Vertical distance of the greater trochanter to the ground when standing	Cons: individual differences in thigh and calf length; range of motion of lower limb joints in actual motion are not considered.
	Ischial tuberosity method	The vertical distance from ischial tuberosity to the ground when standing	
	Heel method	When the crank is in line with the riser and the heel is on the pedal, the knee can be fully extended	
Angle of the knee joint	Hamley method	The angle of knee flexion varies from patient to patient when the pedal is positioned at the bottom dead center	Pros: in line with the kinematic characteristics of the knee joint in the actual riding.
	Howard method	The knee angle was 30° when the pedal was located at the bottom dead center	Cons: complicated measurement.

Previous study shows that the handlebar height used for racing resulted in three times greater flexing load moment on the vertebrae from C7 to T1 compared to the vertical sitting position (Kolehmainen, 1989). The force produced from the upper body considering the contact with handlebars accounts for 3%-5% of the total crank power output (Costes, 2016). The wind tunnel tests on track cyclists showed that handlebar height has a greater impact on the area of riding resistance than the distance between hands (Underwood & Jermy, 2013). Thus, changes in the position of the hand-to-handlebar contact point also have an influence on the riding performance.

Beyond the positions of the saddle and handlebar, several other components of the bike also influence cyclist biomechanics, such as crank length, pedal alignment, and frame size. Crank length directly impacts the ROMs of the hip, knee, and ankle joints. Longer cranks generally require greater angular excursions at these joints, which may increase joint stress, while a shorted crank causes a higher peak knee extension moment (Park et al., 2022). The pedal misalignment, including cleat position, can cause overuse injuries such as iliotibial band syndrome or Achilles tendonitis (Paton, 2009). Frame size must accommodate the cyclist's body dimensions. The inappropriate setting of these structures can increase the risk of injuries. Therefore, bike fitting is a long-term beneficial action that can safeguard cyclists' health and improve cycling efficiency.

The optimal saddle height has been the current hotspot since saddle height is most influential for cycling biomechanics and the easiest part to adjust. The bike-sharing industry has boomed in recent years in China. The only thing a shared bike can adjust is the saddle height. However, the definition of the optimal saddle height remains controversial. Therefore, we chose saddle height as an independent variable to quantify this definition in terms of human biomechanics.

2.3.2 Cycling workload and intensity

Workload refers to the overall physical demand placed on the cyclist, while intensity describes the effort exerted during pedaling. Power output, cadence, crank torque, and heart rate are common parameters used for defining the cycling workload and intensity (Gilman, 1993). The relevant measurement tools are power meters, heart rate monitors, and subjective rating scales such as the Rate of Perceived Exertion (Zinoubi et al., 2018). A greater workload requires more mechanical power from the musculoskeletal system and changes the joint mechanics. During submaximal cycling at increased power outputs, cyclists adopted different intermuscular coordination strategies to optimize performance while minimizing metabolic costs in different cycling stages (Barratt, 2016). Studies have shown that prolonged exposure to high workloads without adequate recovery can result in cumulative trauma to the muscles and joints involved in cycling, which might be related to patellar tendinopathy and iliotibial band syndrome (Priego Quesada et al., 2019). What's more, workload can affect seat pressure which is related to the erectile dysfunction of male cyclists (Bressel & Cronin, 2005). The mean pressure of the seat increased as the workload increased (Carpes et al., 2009). Fang et al. studied the changes in knee biomechanical parameters under different cycling conditions of five workloads and a constant cadence (Fang et al., 2016). They found that greater workloads caused increased peak torques at the knee joint when it extended, as well as the pedal component forces. Further research is needed on what level of workload does not cause knee problems, as well as for rehabilitation training for such as knee osteoarthritis. There is an interaction between the cadence and the workload. The most economical cadence increases as the workload increases. For example, the best cadences were 60 rpm at 0 W and 80 rpm at 350 W, but there was no difference in maximal oxygen uptake (Foss & Hallen, 2004). On the contrary, Rossato et al. reported that increasing the workload resulted in a decrease in the freely chosen cadence because a lower pedaling cadence is more effective during the recovery period, and cyclists tend to improve pedaling efficiency (Rossato et al., 2008). Gerda et al. pointed out that the effect size was affected by the cadence but not by the workload (Strutzenberger et al., 2014). The cycling conditions for generating power maximization are different from efficiency maximization. However, they focused on the difference of effects between the circular and non-circular chainring, and the latter type is not usual.

The relationship between cycling workload and injuries is complex and multifaceted. Increasing the workload will undoubtedly increase the stress on the muscles and joints, but neuromodulation of the muscle movement pattern allows the cyclist to adapt to the increased workload. The upper limit of training workload is to prevent injury, and the lower limit is to have the effect of building muscles. Therefore, it is very important to explore the relationship between riding workload and muscle state, and joint kinetics.

2.3.3 Other factors

Other factors associated with cycling injuries are footwear, riding posture, physical conditions, and riding environment. For instance, riders tend to choose hard soles, which are more effective in transferring power from lower limbs to pedals. Cyclists who maintained a more aggressive aerodynamic position experienced higher levels of discomfort in the neck and lower back compared to those with a more upright posture. There is a trade-off between reducing air resistance and joint stress. Road conditions (e.g., potholes, gravel), weather (e.g., rain, wind), and traffic levels can change the riding resistance, and impact control ability of cyclists. It is not possible to study the impact of all factors on cycling biomechanics. Therefore, the above conditions should be strictly controlled as constant conditions in the experiment.

2.4 Cycling-Related Computational Models

Computational modeling and simulation play an important role in the research of cycling biomechanics, which helps researchers save time and cost on experiments and enables them to investigate thoroughly muscle forces, joint forces, and even bone stress. These tools have been extensively used to investigate performance optimization, injury mechanisms, and rehabilitation strategies in cycling research recently.

2.4.1 Musculoskeletal models for cycling

Multibody musculoskeletal (MSK) models have become indispensable tools for simulating and analyzing the biomechanics of cycling. The models represent the human body as a system of interconnected rigid segments, with joints modeled as constraints that allow specific degrees of freedom (DOFs).

Early on, the MSK-ergometer model was established as a two planar four-bar linkage coupled by the crank (Schutte, 1993). The lower limb joints were thought to be pin joints, apart from the knee which was a three-degrees-of-freedom joint with two constrained degrees. Only three muscle groups were modeled by musculotendon actuators. A study comparing knee loading during forward and backward pedaling employed a planar two-leg bicycle-rider MSK model (R.R. Neptune, 2000). The motion and the activation of muscles were represented through a series of mathematical equations with assumptions. However, the planar model is unable to explore motion beyond the sagittal plane and the calculation accuracy of the formulas needs to be improved.

At present, the commonly used software for 3D MSK modeling is OpenSim (National Centre for Simulation in Rehabilitation Research, Stanford University, U.S.) and Anybody System (AnyBody Technology, Denmark). The muscle forces calculated by the BIKE3D model in Anybody have been validated in EMG experiments with good correlations (Yoon- Ho Shin, 2015). Therefore, the MSK dynamic model provides an effective and economical tool for exploring the influence of various factors on bike fitting. A higher version of BikeModel3D in Anybody was modified in a previous study for the inverse-inverse dynamics technique (Farahani et al., 2015). They proposed parameterization functions to describe the motions and muscle excitations. The upper body was fixed as same as the most models. The crank torque was assumed to be a sinusoidal function. These simplifications are reasonable only in steady pedaling with constant crank angular velocity. In a study investigating the control strategies for functional electrical stimulation cycling, a simplified model from OpenSim database was used (de Sousa, 2016). The hips and knees moved freely, while the lumbar, pelvis, and ankle were locked. Therefore, the muscle and joint forces in results are limited. Their conclusions may only be applicable to rehabilitation patients because of the significant difference between the healthy riders and patients. A 16-DOFs lower limb MSK model containing more muscles was developed for cycling with typical cadence and power, although it is participant-specific (Clancy et al., 2023). They also found that adding a term of minimizing tibiofemoral forces to the optimization objective function improved the realism of the simulation and better matched the experimental data while preserving the riding kinetics. A full-body model including 86 muscles and 13 segments was used to study the influence of saddle setbacks on knee joints (Menard et al., 2020). This model is derived from the MSK model originally applied for gait and running.

In fact, there are currently far more MSK models for studying gait and running than for cycling research. However, the physiological requirements of cycling, such as muscle forces and joint coordination patterns, are obviously different from gait and running. Therefore, it is necessary to develop a cycling-specific MSK model.

2.4.2 Finite element analysis in cycling

Finite element (FE) analysis was originally used to solve engineering problems in civil and aviation and was extended to the biomechanics field in the late 1970s (Erdemir et al., 2012). Until now, it has become an indispensable tool for investigating the biomechanics and engineering aspects of sports (Erdemir et al., 2012). Its ability to simulate complex interactions between components of the human body, cycling equipment, and environmental forces makes it ideal for understanding cycling dynamics. In contrast to the MSK dynamics simulation, FE analysis can provide comprehensive details on the stress-strain distribution of musculoskeletal structures, which is useful in identifying risk factors and locations of overuse injuries. Besides, it aids in the design and improvement of bicycle and riding equipment, such as frames, pedals, and helmets, for improving performance and preventing injuries.

FE models are limited to studying the mechanical response and stress distribution of bone in cycling. Most of the related research focuses on the optimization of bicycle structure (Cahyono et al., 2017), the evaluation of safety devices such as helmets (Abdullah, 2015), and the simulation of car accidents (Wang et al., 2021). The problem of perineum injuries during cycling has aroused concern. A previous study created a 3D voxel-based FE model according to computer tomography data of a male cyclist (Spears et al., 2003). However, the pelvis model in the upright position was completely different from the real riding state. The saddle was modeled as an incompressible rigid body, which is also inconsistent with the fact. A study built a 3D geometric model of the knee joint based on publicly available MRI data (Bratianu et al., 2004). They simulated the knee joint motion in walking and jumping situations based on the kinematics data from subjects. However, there may be a mismatch between the kinematics and MRI data because they are from different sources. Aerodynamics is a critical factor in competitive cycling and equipment design. Obispo established a FE model of the knee joint containing the tibia, femur, fibula, two major cartilages, and menisci based on the MRI of the subject (Yazdkhasti, 2023). He compared the tibial contact pressure of amputee patients and normal subjects in three motion states, including cycling, elliptical, and walking, and found that cycling had the lowest compressive stress. However, the static analysis used in this study could not simulate the true viscoelastic material properties of cartilage and meniscus. Additionally, performing calculations at a specific moment is insufficient because riding and walking are motion processes with time dimensions. FE analysis was used to investigate the impact of cycling on the wear and longevity of total hip arthroplasty prosthesis in a previous study (Toh et al., 2023), revealing a significant but acceptable increase in prosthesis wear with cycling. But this FE model only contained prosthesis which simulated cycling by setting the initial position and dynamic loads.

The MSK multibody model is efficient for motion simulation but not complex enough to precisely assess tissue behavior. FE analysis can calculate stress and deformation at the tissue level but require significant modeling and computational costs. The combination of the two methods can compensate for each other's shortcomings (Tawhai et al., 2009). For instance, the FE analysis of the knee joint in motion can be driven by the results of MSK dynamics calculation, and the FE model of microstructural tissue can calculate the response at a more microscopic level as shown in Figure 2.4 (Erdemir et al., 2012). The mechanical analysis of microscopic and tissue levels can help to understand the biomechanics of motion at the human body level. Therefore, FE analysis plays an important role in multiscale analysis problems. In cycling research, Wang et al. created a FE head model coupled to a pedestrian multibody model of the whole body from neck to feet (Wang et al., 2021). It was repositioned according to the riding posture and used to explore the effectiveness of helmets in two types of cycling accidents. In a study predicting the effect of gait patterns on foot tissue loading, the authors coupled MSK dynamics and the FE model of the foot, allowing simulation of locomotion guided by tissue stresses (Halloran et al., 2010). Another study explored the effect of body weight on knee joint biomechanics by coupling the MSK model and FE model of knee joint (Adouni et al., 2024). The estimated muscle forces were applied as input loads in FE analysis, and the joint reaction moments were inputted back to the dynamic simulation if it was larger than 1 N·m. But they did not consider the biphasic behaviors of cartilage and meniscus in the model. Mo et al. also developed the MSK-FE coupled model for the synchronous calculation of the dynamics and tissue stress of the lower limb in the normal gait (Mo et al., 2019). They proposed a new feedback control strategy that couples the Proportion-Integration-Differentiation controller and muscle activation signals which improves the accuracy of simulation. However, most of the previous MSK-FE models are designed for gait research, and there are few models related to cycling.

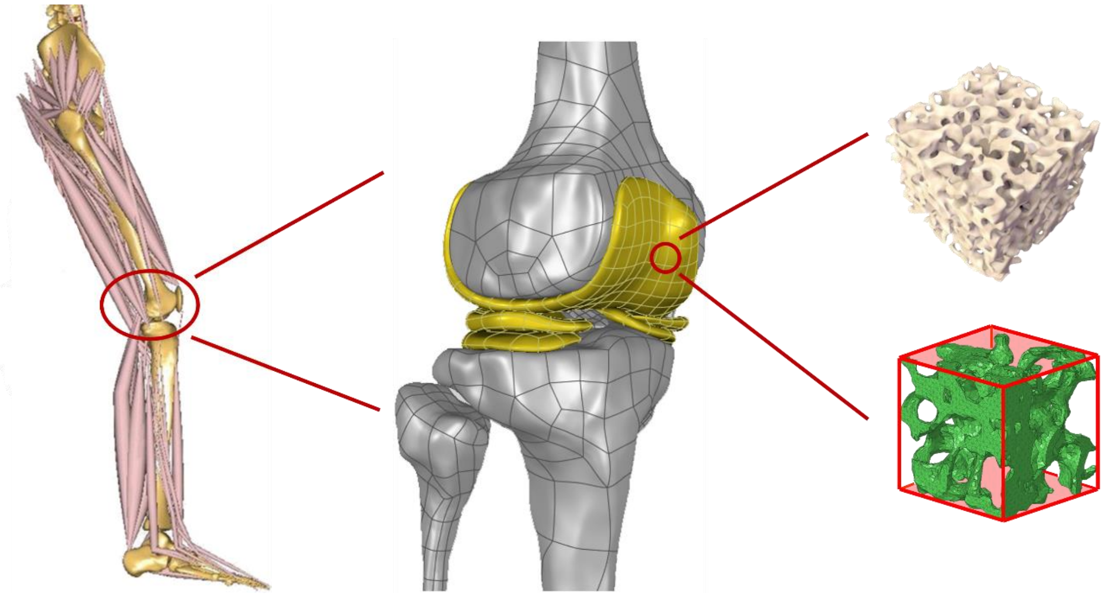

Figure 2.4 Finite element (FE) modeling of knee joint in the musculoskeletal multibody model, and FE analysis in microtissue levels.

2.4.3 Machine learning applications in cycling

Motion capture systems and sensor technologies are widely used in the evaluation of cycling performance and cyclists' competition levels. However, these methods cannot be performed regularly because of the high costs and time consumption. The integration of ML in cycling has gained more attention in recent years, which are being applied to enhance performance analysis, injury prevention, training optimization, and equipment design (Stessens et al., 2024). Specifically, lactate, heart rate, oxygen uptake, power output, cycling effectiveness, and functional threshold power (FTP) are the common target predictors that are related to the physical condition of cyclists. Additionally, predicting the race rank and optimizing cycling routes can be used in various competitions (Kholkine, 2020; Ofoghi et al., 2013). Optimizing bicycle structure by ML is to personally balance individual comfort and riding performance

(Regenwetter, 2022). Table 2.2 shows the author, publication year, research topic, target variables, input variables, and prediction/classification accuracy of research that adopted the ML method in cycling sports.

Table 2.2 Machine learning models and applications in cycling

Reference	Topic	Model type	Target	Input	Accuracy
Hilmkil (2018)	Predict the cyclist's heart rate at a time point	LSTM neural network model	Heart rate	Time, speed, distance, power, cadence, power/weight, altitude, 30s heart rate	RMSE: 5.62
Lemaitre (2018)	Estimate cycling power without measurement	Gradient boosting algorithm	Power	Acceleration, slope, derivative of heart rate	R^2: 0.83
Kataoka and Gray (2019)	Predict power performance in real-time of professional cyclists at the *Tour de France*	Tree-based model with random forest	Power	Friction, wind resistance, position energy, kinematic energy	MAE: 66.81
van der Zwaard et al. (2019)	Classifying cyclists into three anthropometric clusters and predicting their sprint and endurance performance	K-means clustering algorithm	Three anthropometric clusters	Body shape, size, composition	-
Wu et al. (2020)	Predict personalized exercise intensity	Multiple regression model	slope S	Waist-to-hip ratio, grip strength, left lower limb muscle, bone strength index	Adjusted R^2: 0.8336
Zignoli et al. (2020)	Estimating an individual's oxygen uptake during cycling exercise	Neural network composed with long-short term	Oxygen uptake	Mechanical power output, cadence, heart rate, respiratory	R^2: 0.89 ± 0.04 (trial 1), 0.8 ± 0.15 (trial 2)

		memory neurons		frequency, pasted inputs	
Hollaus et al. (2022)	Cadence detection used the data from IMU mounted on the saddle tube	Convolutional neural network with LSTM	Cadence	Acceleration in X, Y, and Z axis	95.06%
Stockwell (2023)	Create a predictor of FTP with greater accuracy	Weighted linear regression	FTP	Average power, maximum critical power, average time spent	MAE: 10.38
Hedge et al. (2023)	Predict oxygen uptake kinetics during heavy-intensity cycling	Temporal convolutional networks	Oxygen uptake $\dot{V}_{O_2}$	heart rate, percent heart rate reserve, estimated minute ventilation, breathing frequency, work rate	Correlation between the predicted and measured $\dot{V}_{O_2}$: r = 0.974
Torres (2024)	Predict the index of effectiveness with the minimum number of predictors	Artificial neural networks with recursive feature elimination	Cycling effectiveness index	Lower limb joint kinematics, power output, individual's mass, cadence, knee over pedal spindle	Adjusted R^2: 0.95
Ahmadi et al. (2024)	Predict real-time pedaling forces with low computational time	Neural network model	Radial and mediolateral forces	Body height and weight, power, cadence, crank angle	RMSE: 0.15-0.20 for radial force, 0.22-0.26 for mediolateral force
Li et al. (2024)	Predict pulmonary oxygen uptake across different exercise intensities	Neural network model	V_{O_2}	Heart rate, muscle oxygen of left and right legs	RMSE: 2.95; Correlation

					coefficient: 0.94
Smiley and Finkelstein (2024)	Predict physical exertion using physiological signals collected from wearable device	LSTM network model	F1 score	Pulse oximeter heart rate	91.7%
Parsaei (2024)	Predict the marker's location on the lower limb without markers for analyzing cycling kinematics	Neural network and regression model	Marker's location	Subject's height and weight, the cycling ergometer dimensions	R^2: 0.99 ± 0.12; RMSE: 2.12 ± 0.71

LSTM: long-short term memory; RMSE: mean root squared error; MAE: mean absolute error; IMU: inertial measurement unit; FTP: functional threshold power.

Accurately predicting heart rate and oxygen uptake is essential for optimizing training regimens and monitoring exertion levels. Hilmkil et al. used a long short-term memory (LSTM) neural network to predict a cyclist's heart rate at specific time points, achieving a mean root squared error of 5.62 (Hilmkil, 2018). LSTM-based neural network was also used to estimate oxygen uptake during cycling incorporating mechanical power output, cadence, and heart rate (Zignoli et al., 2020). But the sample size of seven riders is too small. Similarly, Li et al. also applied a neural network to predict pulmonary oxygen uptake across different exercise intensities, using heart rate and muscle oxygen saturation from both legs, with a correlation coefficient of 0.94 between predicted and measured values (Li et al., 2024). In addition to the neural network, a temporal convolutional network was used to predict oxygen uptake kinetics during heavy-intensity cycling, achieving a strong correlation (r = 0.974) between predicted and measured values (Hedge et al., 2023). The model obtained from laboratory riding tests on a cycle ergometer may be unable to be applied in outdoor and competition riding.

Power estimation is a crucial aspect of cycling performance assessment. Lemaitre used a gradient boosting algorithm to estimate cycling power without direct measurement, using input variables such as acceleration, slope, and heart rate derivative (Lemaitre, 2018). However, the data set came from only five riders, which may reduce the universality of the model. Predicting power in real-time is more important in competition. A tree-based random forest model was applied to predict the real-time power of cyclists in the Tour de France (Kataoka & Gray, 2019). Their model incorporated friction, wind resistance, and kinematic energy, reducing prediction error by 56.79% compared to the conventional model. However, the difference between professional and amateur riders may limit the application of the model to other cycling levels.

Cadence and pedaling efficiency are critical factors in cycling biomechanics. A convolutional neural network combined with LSTM was used to detect cadence from data collected via an inertial measurement unit (IMU) mounted on the saddle tube (Hollaus et al., 2022). This data collection method reduces the measurement impact on cyclists by replacing the sensors mounted on the pedals and cranks. Torres et al. applied an artificial neural network with a recursive feature elimination approach to predict the cycling effectiveness index with minimal predictors, achieving an adjusted R^2 of 0.95 (Torres, 2024). Besides, the neural network model was used to predict radial and mediolateral forces (Ahmadi et al., 2024). However, the input parameters required include power, cadence, and crank angle which increases the complexity of the measurement. The vertical force cannot be predicted, and the accuracy of the mediolateral force also needs to be improved.

To reduce the complexity of marker-based motion capture experiments, a neural network regression model was developed to predict marker locations on the lower limb during cycling, using subject height, weight, and ergometer dimensions (Parsaei, 2024). The model achieved a high analysis accuracy with an R^2 value of 0.99 ± 0.12. This markerless approach has great application potential in clinical, exercise rehabilitation, and competitive sports.

Despite the promising applications of ML in cycling, several limitations exist in current research. Many studies focus on specific physiological parameters such as heart rate and oxygen uptake, neglecting biomechanical factors like joint kinematics and saddle height adjustments. Additionally, most models rely on datasets from professional or well-trained cyclists, limiting their applicability to amateur cyclists or those with diverse anthropometric characteristics. Several investigations involved fewer than 10 participants, restricting the model's broader applicability. Another limitation is the lack of real-time feedback integration in current models, which restricts their practical applications in dynamic cycling environments.

Future research should incorporate a broader range of biomechanical data and recruit more participants, allowing for personalized and adaptive recommendations. One promising direction is the development of ML models that classify saddle height based on simple measurements of kinematics during cycling. Proper saddle height is crucial for injury prevention and pedaling efficiency, yet current ML applications in cycling have not adequately explored this aspect. Automatically distinguishing the appropriate saddle height will help cyclists optimize their riding posture and reduce strain on joints.

2.5 Summary and Research Gap

The literature on cycling biomechanics and injuries reveals a complex interplay between various factors that influence cycling performance and injury risk. Section 2.1 discussed the biomechanics of cycling, highlighting how joint angles, muscle activations, and pedal mechanics contribute to pedaling. In Section 2.2, the focus shifted to cycling injuries, which are categorized into traumatic and non-traumatic injuries. Non-traumatic injuries have attracted the attention of many scholars due to their pervasiveness. Most of them occur in the lower limb joints. Section 2.3 examined factors associated with injuries, notably the saddle height and cycling workload. The literature emphasizes that incorrect saddle height can lead to overuse injuries, and workload greatly affects the activation and coordination patterns of muscles. A large workload could exacerbate biomechanical inefficiencies and lead to joint injuries. Section 2.4 reviewed the ML models and applications in cycling. Models such as LSTMs, neural networks, and regression techniques have been successfully applied to predict heart rate, oxygen uptake, cycling power, cadence, and pedaling forces.

Despite the extensive body of research on saddle height and cycling workload, significant gaps remain in the understanding of the interaction between the factors and their implications for cycling biomechanics and injury risk. Notably, the definition and determination methods for optimal saddle height are still controversial, with varying recommendations across studies. Determining by knee joint angle is the most recognized method, but it is too complex to perform in daily life, such as in using shared bicycles. These highlight the need for a convenient and standardized approach for adjusting saddle height to enhance performance and minimize injury risk.

On the other hand, the relationship between cycling workload and biomechanics remains unclear. While existing literature acknowledges that changing workload can influence joint mechanics and muscle activation patterns, the specific mechanisms linking workload to injury susceptibility have not been thoroughly elucidated.

ML has been proven to be a valuable tool for advancing cycling performance analysis, injury prevention, and biomechanics optimization. However, many studies focus on specific physiological parameters such as heart rate and oxygen uptake, without considering joint kinematics and bike setting. There are still a few ML models that relate to kinematics and saddle height which are important in injury protection and performance improvement.

This study aims to address these gaps by employing experimental measurements, dynamics calculations, and FE analysis. Through the multifaceted approaches, the study seeks to provide clearer insights into the influence of saddle height and workload on lower limb biomechanics. This aspires to contribute valuable knowledge of injury protection and performance improvement that can inform the best practices for cyclists and coaches. Furthermore, another objective is to bridge the gap in ML applications in cycling by focusing on saddle height classification based on lower limb joint angles, which could be incorporated into dynamic bike-fitting to improve pedaling efficiency and reduce injury risks.

CHAPTER 3 METHODOLOGY

3.1 Overview of the Study

Figure 3.1 shows the workflow of this study which was divided into four main parts. The first part is the cycling experiment, including recruitment of subjects, installation of experimental equipment, riding tests, and data collection. The second part is the inverse dynamics calculations for the musculoskeletal (MSK) multibody model, including the model establishment, verification, and calculation. The inputs are the marker trajectories, pedal forces, and pedal torques which are recorded from the experiment. The outputs include joint contact forces, muscle forces, and muscle activation. The third section consists of geometric modeling based on magnetic resonance imaging (MRI), meshing, and parameter setting for finite element (FE) analysis. The stress, strain, and relevant parameters of soft tissues of the knee joint can be obtained. The last part is to establish a ML classification model with high accuracy of saddle height based on kinematic data which is the lower limb joint angles measured in experiments.

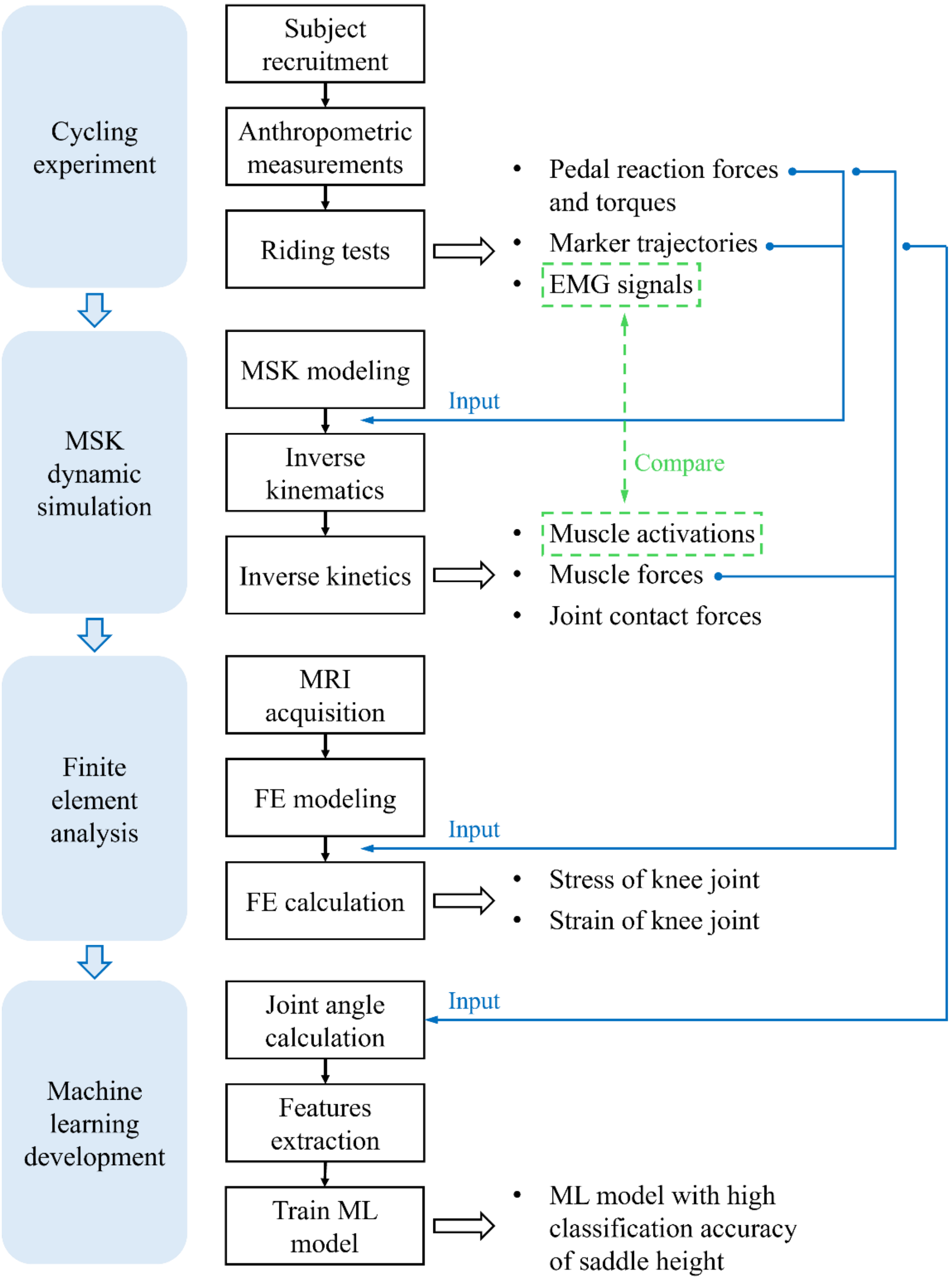

Figure 3.1 The workflow of the study. MSK: musculoskeletal; EMG: electromyography; FE: finite element; ML: machine learning.

3.2 Cycling Experiment

3.2.1 Participants

Subject recruitment was mainly conducted on university campuses, but the target population was not limited to students and teachers. The inclusion criteria of participants were that: 1) they should age between 20 and 30 years, 2) they should have a normal body mass index (BMI) between 18.5 and 24.0 kg/m^2, 3) the males should be 165-180 cm tall, and females should be 155-175 cm tall, 4) they should have amateur riding experience at least, and 5) they can ride a bike independently for two hours without any assistance. The exclusion criteria were: 1) the frequency of cycling less than once per week, 2) the average cycling time of less than 10 minutes every time, 3) having any pain or discomfort in the lower extremities, 4) having been diagnosed with any musculoskeletal disease in the past six months.

The study utilized an effect size of 0.25, considered small, along with a β level of 0.8 to ensure adequate statistical power and an α level of 0.05 to maintain a standard threshold for significance, which were selected to balance the detection of meaningful effects while minimizing the risk of Type I and Type II errors in the analysis. G*power 3.1.9.7 was used for statistical power calculation. A total of at least 24 samples was determined through power analysis to ensure sufficient statistical power for the statistical approach - repeated ANOVA design.

In the end, twenty-seven amateur cyclists completed the experiment with valid data. Table 3.1 provides an overview of the participants' demographic details. Everyone provided written consent after thoroughly reviewing the necessary documentation, which outlined the experiment's purpose, procedures, potential risks, and benefits. This process ensured that all individuals were fully aware of their involvement and rights before participating. Experiment was approved by the University Human Subjects Ethics Sub-Committee (Number: HSEARS20220615001).

Table 3.1 The participant demographics

Characteristics	Value (n = 27, mean ± SD)
Gender	15 male, 12 female
Age (years)	24.64 ± 3.19
Height (cm)	170.54 ± 6.86
Weight (kg)	62.42 ± 9.51
BMI (kg/m^2)	21.34 ± 2.00
Greater trochanter height (cm)	87.64 ± 4.91

BMI, body mass index

3.2.2 Experimental equipment

Trajectories of reflective markers were recorded at 250 Hz by an eight-camera motion analysis system (Vicon Motion Analysis Inc., UK) in the experiment. The same type and tight tracksuits were worn by the subjects. They were asked to wear sneakers with sole thickness of no more than 3.5 cm. To identify joint centers and body segments, 33 reflective markers were placed on the subject's skin as shown in Figure 3.2. The anatomical locations and nomenclature of the markers in Anybody and Nexus are detailed in Table 3.2.

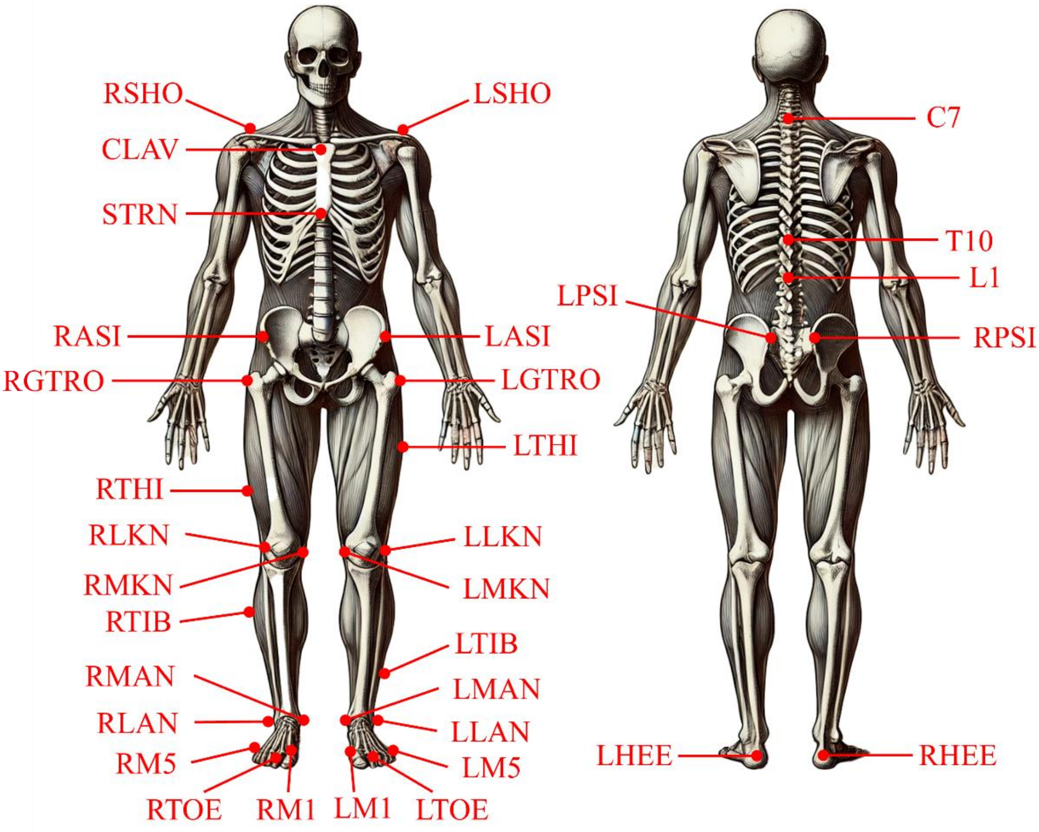

Figure 3.2 The position of reflective markers on the participants.

Table 3.2 Marker labels and positions

Segments	**Marker names**	**Landmark locations**
Shoulder	LSHO	Left shoulder
	RSHO	Right shoulder
	CLAV	Jugular notch
Sternum	C7	7th cervical vertebrae
	STRN	Sternum
Lumbar vertebrae	T10	10th thoracic vertebra
	L1	1st lumbar vertebra
	LASI	Left anterior superior iliac crest
Pelvis	RASI	Right anterior superior iliac crest
	LPSI	Left posterior superior iliac crest
	RPSI	Right posterior superior iliac crest
Left thigh	LGTRO	Left greater trochanter
	LTHI	Over the upper lateral 1/3 surface of the left thigh

Segments	**Marker names**	**Landmark locations**
	LLKN	On the lateral flexion-extension axis of the left knee
	LMKN	On the medial flexion-extension axis of the left knee
Right thigh	RGTRO	Right greater trochanter
	RTHI	Over the lower lateral 1/3 surface of the left thigh
	RLKN	On the lateral flexion-extension axis of the left knee
	RMKN	On the medial flexion-extension axis of the left knee
Left shank	LTIB	Over the lower lateral 1/3 surface of the left shank
	LLAN	Left lateral malleolus
	LMAN	Left medial malleolus
Right shank	RTIB	Over the upper lateral 1/3 surface of the left shank
	RLAN	Right lateral malleolus
	RMAN	Right medial malleolus
Left foot	LHEE	Left calcaneus
	LM5	Left head of the 5th metatarsal
	LM1	Left head of the first metatarsal
	LTOE	Left head of the second metatarsal
Right foot	RHEE	Right calcaneus
	RM5	Right head of the 5th metatarsal
	RM1	Right head of the first metatarsal
	RTOE	Right head of the second metatarsal

A mountain bike (Marlin 7 Gen 2, Trek, Intrepid Corporation, USA) and a cycling smart trainer platform (Tacx NEO 2T, Garmin, USA) for accurate workload regulations were assembled for the riding tests. The gear ratio was fixed throughout the tests. The pedals (Sensix, Poiters, France) instrumented with six-component force-torque sensors were used in place of the original bike pedals. I-Crankset software for force-torque pedals and Nexus software for the motion capture system were synchronized. Figure 3.3 displays the main experimental equipment and the photo of a subject during the riding test.

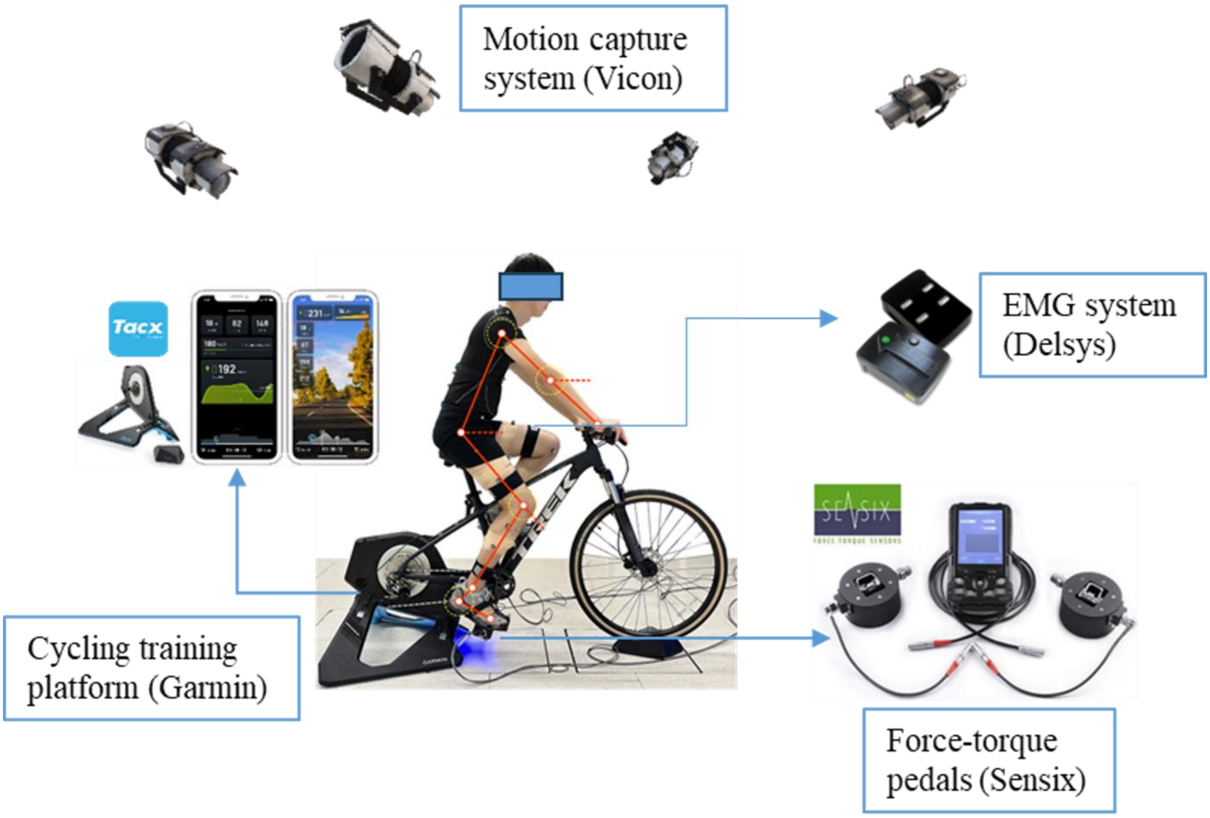

Figure 3.3 The main experimental equipment.

The surface EMG of the rectus femoris (RF), tibialis anterior (TA), biceps femoris (BF), and medial gastrocnemius (MG) muscles of subjects were recorded using Delsys Trigno wireless EMG System (Delsys, Boston, MA) at a sample rate of 2000 Hz. EMG signals were collected from a total of eight muscles, evenly distributed between the bilateral legs, allowing for the assessment of potential asymmetries. Trigno wireless sensors were affixed to the abdomen of the target muscles. The direction of the electrode position was parrel to the muscle fiber as referred by Surface ElectroMyoGraphy for the Non-Invasive Assessment of Muscles (SENIAM) (Hermens et al., 1999). The specific attaching position, muscle name, and function are summarized in Table 3.3.

Table 3.3 The muscle function and attaching position of the surface EMG electrodes

Muscle	**Location**	**Orientation**	**Muscle function**
Rectus Femoris (RF)	The electrodes need to be placed at 50% on the line from the anterior spina iliaca superior to the superior part of the patella.	From the front of the spina iliaca superior to the top of the patella.	Help the hip joint flex and the knee extend.
Biceps Femoris (BF)	The electrodes need to be placed at 50% on the line between the ischial tuberosity and the lateral epicondyle of the tibia.	Along the axis connecting the ischial tuberosity to the tibia's lateral epicondyle.	Flexion and lateral rotation of the knee joint. The long head also extends and assists in lateral rotation of the hip joint.
Tibialis Anterior (TA)	The sensors should be positioned one-third of the distance on the line connecting the fibular head to the medial malleolus.	Along the line that runs from the medial malleolus tip to the fibula tip.	Dorsiflexion of the ankle joint and assistance in inversion of the foot.
Medial Gastrocnemius (MG)	Positioning sensor on the muscle's most prominent protrusion and aligned parallel to the limb's longitudinal axis.	In the direction of the leg.	Flexion of the ankle joint and assist in flexion of the knee joint.

3.2.3 Experimental protocol

The participants filled out a questionnaire on their cycling experience and their physical condition before carrying out the trial. The weight, height, widths, and lengths of lower-limb segments, and the great trochanteric height (GTH) of subjects were measured and recorded.

The initial height of the saddle was adjusted to a self-selected height when the subject thought it was comfortable. Before the formal experiment, the subject's fitness level was assessed by a four-minute functional threshold power (FTP) test (Gavin et al., 2012). Since the standard FTP measurement is typically derived from a one-hour cycling session, a conversion formula was applied to estimate their one-hour FTP based on the shorter-time test, which allowed for a practical and time-efficient evaluation while maintaining comparability to traditional FTP benchmarks (MacInnis et al., 2018):

$$P_{4\,min} \times 0.75 = P_{60\,min} \tag{3.1}$$

Subjects rested for at least 10 minutes after completing the FTP test. EMG electrodes from No.1 to No.8 were in order affixed to the RF, TA, BF, MG of the left lower limb, and RF, TA, BF, MG of the right lower limb. Since the amplitude of the EMG signal is greatly affected by the detecting conditions, the data was normalized by maximal voluntary contraction (MVC) to reduce the errors. Each muscle underwent the MVC test employing the designated posture in opposition to static resistance, including supine and prone, according to the literature (Rachelle Bordlee, 2015). The subjects were given enough time to perform warm-ups, stretching, and rest before the MVC test. Upon completion of the MVC test, reflective markers were attached to the subjects with kinesiology tape. The subject stands in an anatomical position to check the marker number and record the static data.

Saddle heights were set to 95%, 97%, 100%, 103%, and 105% of the height of the subject's GTH. The subjects rode in three workload levels (50%, 75%, and 100% of FTP which was expressed as watts) under each condition of saddle height. Under each test, the participant rode for two minutes at the needed steady cadence (85 - 95 rpm). The order of the testing conditions was randomized. A minimum rest interval of two minutes was provided between each experimental condition, allowing participants adequate recovery time, to prevent weariness.

PRFs and torques were recorded synchronously with the motion capture system, as well as the EMG signals of bilateral legs.

3.2.4 Data processing

A complete pedaling cycle consists of two periods and two key time points as shown in Figure 3.4. The propulsive and recovery periods are divided by the top dead center (TDC) and bottom dead center (BDC). All data analyses were performed during the propulsive and recovery periods, respectively. For each riding test, the first 30 seconds and the last 30 seconds were excluded from the two-minute data. The data of five complete pedaling cycles were taken for subsequent computation and analysis.

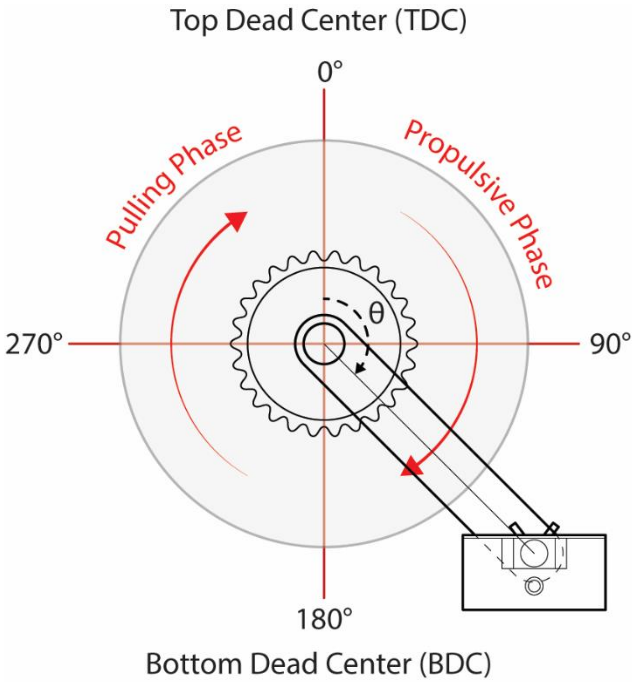

Figure 3.4 The period division of a complete pedaling cycle.

EMG data

The generation of EMG signal is a complex process involving neural activation, propagation of action potentials along muscle fibers, and collective electrical activity from multiple motor units (Farina, 2016). The EMG signal in the muscle resting state is close to a straight line, which is the baseline. Signals burst when the muscle is activated. This process can directly determine the muscles involved in cycling motion. The procedure of EMG signal processing is filtration, rectification, smoothing, and average, as shown in Figure 3.5.

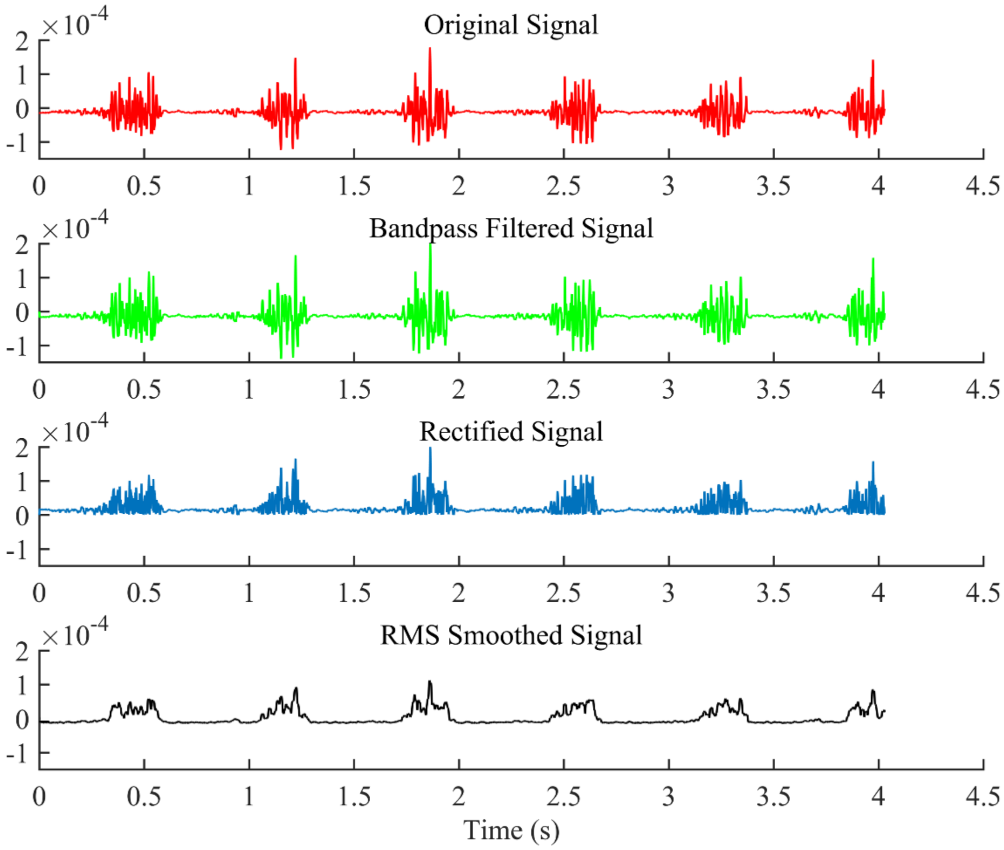

Figure 3.5 The processing method of EMG signal by taking rectus femoris for example.The raw EMG signals contain unwanted noise and artifacts caused by electrical interference, motion artifacts, and physiological noise from adjacent muscles and body movements. Therefore, the first step is filtering. A fourth-order band-pass Butterworth filter with cutoff frequencies set between 10 Hz and 500 Hz was designed in MATLAB R2024a (MathWorks Inc., Natick, Massachusetts, USA). The cutoff frequency was adjusted according to previous studies to fit our experimental data (Rouffet & Hautier, 2008). This filtering process removed low-frequency noise (such as motion artifacts) and high-frequency interference (such as

electrical noise) while preserving the relevant frequency components associated with muscle activation during riding.

Following filtering, the processed EMG data underwent full-wave rectification to convert all values to positive. Because muscle contractions generate both positive and negative electrical potentials, we focus on the magnitude of muscle activity rather than its direction. Signal rectification was carried out to convert all signal values into integrals and then obtain the total activation signal.

A moving root mean square (RMS) approach with a 70 ms moving window was employed to smooth the rectified EMG data. Similar to filtering, smoothing also can remove noise. The difference is that it also builds an envelope. The signal over a specified time window was effectively averaged. The choice of a 70 ms window is long enough to capture changes in muscle activation while filtering out noise (Bini et al., 2008; Dingwell et al., 2008). This smoothing technique provides a clearer representation of muscle activation patterns by reducing high-frequency fluctuations that can obscure true muscle activity. Then, the EMG signals were normalized, which was performed by dividing the RMS values by the MVC values. This approach allowed standardized measurements across participants, enabling meaningful comparisons of muscle activation levels during cycling. The processed EMG was divided into multiple complete pedaling cycles. The mean of five pedaling cycles was calculated to obtain the final EMG envelope under each cycling condition for specific muscles as shown in Figure 3.6.

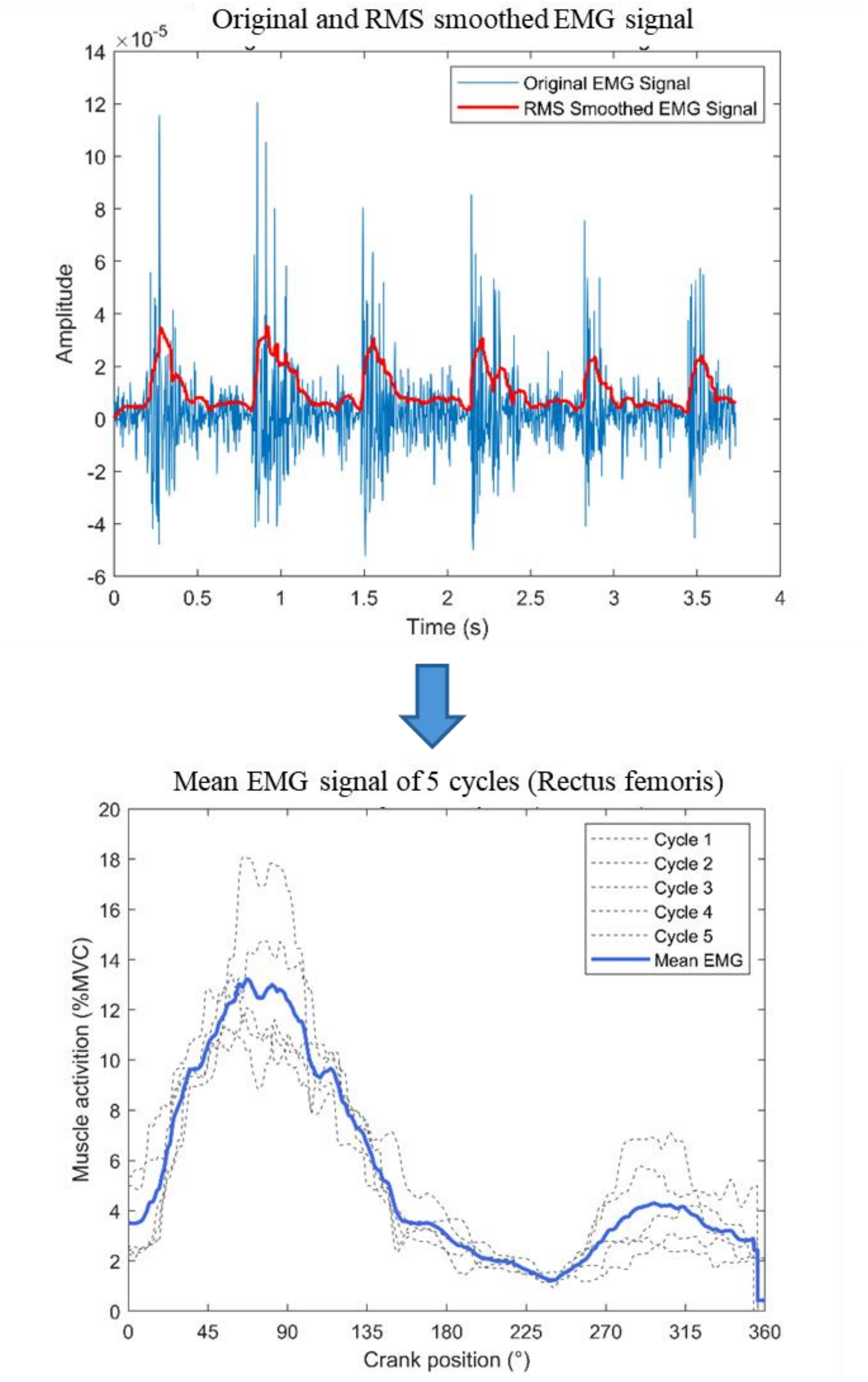

Figure 3.6 EMG envelope and the final EMG results from the mean envelope of five pedaling cycles.

The onset and offset timings and duration of muscle activation are key metrics in motion analysis to further reveal muscle activation and coordination patterns. The mean EMG amplitude of less than the half standard deviation was used to determine the threshold for muscle activation. The activation duration is defined as the interval from onset to offset points.

Symmetry

Cycling symmetry between the left and right legs, in terms of kinematics and kinetics, is crucial for optimizing cycling performance and preventing injuries. The assessment of lower limb symmetry was typically done through biomechanical analysis and performance testing in previous research (Rodrigo R Bini & Patria A Hume, 2014; Rannama et al., 2015).

In this study, cycling symmetry was examined based on the PRFs, muscle activations, and joint angles of the hip, knee, and ankle. The first 1500 and last 1500 data of each riding test were removed, which was the data of the first 6 seconds and last 6 seconds, to avoid an unstable riding state at the beginning and end. The resultant PRF ($F_{resultant}$) was calculated from the square mean root of the force components in the three directions.

$$F_{resultant} = \sqrt{F_x^2 + F_y^2 + F_z^2} \tag{3.2}$$

F_x is the anterior-posterior PRF, F_y is the medial-lateral PRF, F_z is the vertical PRF. The integrated area of the PRF curve with the crank angle as the X-axis variable from 0° to 360° was calculated by the following formula:

$$F_{AUC\_left} = \int_0^{360} F_L(x) d_x \tag{3.3}$$

$$F_{AUC\_right} = \int_0^{360} F_R(x) d_x \tag{3.4}$$

F_L is the X-axis, Y-axis, Z-axis, or resultant PRF of left pedal, and F_R is the corresponding force of right pedal. F_{AUC_left} is the integrated area under the left PRF curve, F_{AUC_right} is corresponding variable of left PRF.

The asymmetry indexes (ASIs) were calculated by:

$$ASI\ (\%) = \frac{|X_R - X_L|}{0.5 \times (|X_R| + |X_L|)} \times 100 \tag{3.5}$$

X_R is the data of the right leg, X_L is the data of left leg. A greater ASI indicates a more asymmetric riding state on the left and right sides.

The F_{AUC_left} and F_{AUC_right} were put into the equation (3.5) as X_L and X_R to obtain the ASI of PRFs. Similarly, the integral area of the muscle activation curve with the crank angle as the X-axis variable was calculated. For instance, if $F_L(x)$ is the muscle activation of left BF muscle, the F_{AUC_left} is the integral area under the curve of BF activation. The ASI of BF activation during cycling can be calculated by entering the F_{AUC_left} and the matching F_{AUC_right} of the right BF into the equation (3.5). The ASIs of RF, TA, BF, and MG were calculated under various riding conditions.

The final ASI of joint angle was the mean of ASI values of each pedaling cycle from 0° to 360° which was defined based on the right crank. The right crank is 0° at TDC and 360° at TDC again after passing BDC. Because the same interception time was used for each pedaling cycle on the left and right sides, and the left and right sides differ by 180°. The curve of the left joint angles shifted 180° to the right to eliminate the phase difference. The X_R and X_L in ASI formula for joint angle are defined as:

$$X_L = JA\_left_{0°,1°,\ldots,360°} \tag{3.6}$$

$$X_R = JA\_right_{0°,1°,\ldots,360°} \quad (3.7)$$

JA_left and JA_right are the flexion angles of left and right joints, respectively. So, there are 361 ASIs, and the final ASI is:

$$ASI = (ASI_{0°} + ASI_{1°} + \cdots + ASI_{360°})/361 \quad (3.8)$$

The ASI is presented by the mean value of ASI at every crank angle.

3.2.5 Statistical analysis

First, the residual analysis and Shapiro-Wilk test were conducted. The data of processed EMG met the assumption of two-way analysis of variance (ANOVA). Therefore, the impact of saddle height and workload on muscle activation was evaluated via the ANOVA. When significant main effects or interactions were found, post hoc comparisons were performed via paired-sample t-tests with Bonferroni corrections. The 95% confidence interval (CI) was adopted. Effect sizes were calculated as partial eta squared (η^2), classified as large ($\eta^2 \geq 0.15$), medium ($0.06 \leq \eta^2 < 0.15$), and small ($\eta^2 < 0.06$). IBM SPSS statistics 26.0 (IBM Corporation, Armonk, NY, USA) was used for the above analyses.

3.3 Musculoskeletal Modelling and Simulation

MSK modeling and simulation have been a powerful tool in understanding sport biomechanics. Despite the growing body of research in this area, current models have primarily been established for walking and running. But cycling has a different demand for lower limb dynamics. This study aims to calculate the lower-limb muscle forces and joint contact forces with different saddle heights and workloads by MSK multibody dynamic simulation. By quantifying the effects of riding settings, we can identify optimal configurations that improve performance and reduce injury risk. Figure 3.7 shows the workflow of MSK multibody dynamic simulation.

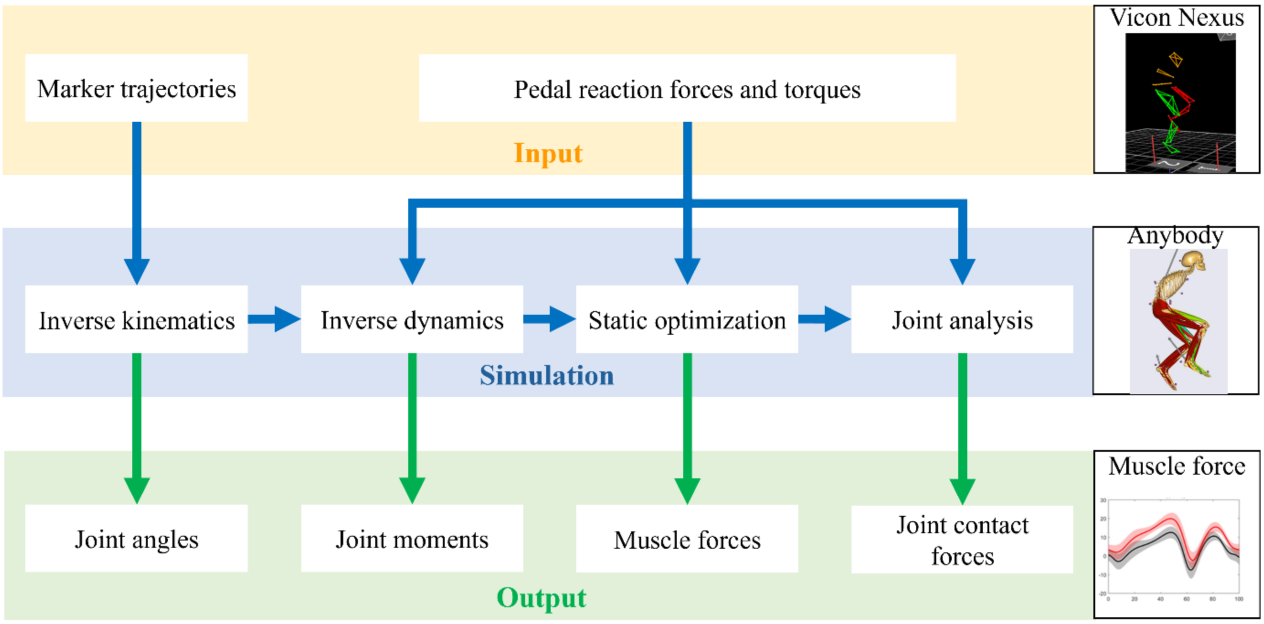

Figure 3.7 The workflow of musculoskeletal multibody dynamic simulation.

3.3.1 Establishment of musculoskeletal model

The AnyBody Modeling System (AMS) is a sophisticated software platform designed for MSK multibody modeling and simulation. The software provides a comprehensive environment for creating the detailed MSK model, allowing users to simulate various activities, such as cycling, walking, and lifting. AMS utilizes advanced algorithms to calculate biomechanical parameters of the human body in motion. Managed model repository (AMMR) in AMS includes detailed full-body MSK models, body part models, and examples from various research studies. A recent study suggested that AMS seemed to be more accurate in predicting muscle forces since it included more comprehensive muscles than other methods and software (Gautam et al., 2024). Therefore, we establish the MSK multibody model for cycling simulation in AMS v.7.4 (AnyBody Technology, Aalborg, Denmark).

Twente Lower Extremity Model v.2.1 (TLEM2) was used as the generic MSK model in this study. This model has been proved by many previous studies, and the calculation results are robust. The model was modified to match the requirements of the riding motion. The model consisted of a simplified upper body (head, cervical spine, thorax, and lumbar) and 11 segments representing the lower limbs (pelvis, right and left thigh, patella, shank, foot, talus) (De Pieri et al., 2018). There were 169 Hill-type muscles and 6 DOFs of one-leg joints. The DOFs of lower-limb joints were three rotations in the hip, flexion/extension in the knee, plantar/dorsal flexion in the ankle, and eversion/inversion in the subtalar joint. No additional DOF was introduced for the patella because its position was defined as a function of the knee flexion angle (De Pieri et al., 2018). Two virtual muscles were added symmetrically to the left and right foot to simulate the support of pedals. The addition of virtual muscles enhances the fidelity of the simulation without establishing pedals and the complex connection between pedals and feet.

3.3.2 Inverse dynamic simulation

Before the calculation, the anthropometric data of each participant were utilized to scale and adjust segment dimensions, the principal axes, and the moments of inertia to personalize the generic model, according to the Length–mass–fat scaling law. The input parameters for dynamic calculation were the measured PRFs and torques by sensors and trajectories of markers obtained from the experiment. The weighted least squares method was used to optimize and update the markers' trajectories, which corresponded to the fixed marker position in the original MSK model to the experimental marker position in the C3D file. The updated marker position by iterative calculation should meet the equation:

$$\min_{q} \sum_{i \in \mathrm{marker}} w_i \left\|(x_i^{exp} - x_i(q)\right\|^2 \tag{3.9}$$

Where q represents vectors to be solved; w_i represented the weight of every maker; x_i^{exp} represents the three-dimensional coordinates of reflective markers collected by experiment; $x_i(q)$ represents virtual reflective ball coordinates.

The calculation for motion consisted of inverse kinematics to determine the necessary joint angles and inverse dynamics analysis to get the forces and torques acting on the body. The updated kinematic parameters from the first step were used in the inverse dynamics calculation to obtain the joint moments. Then the static optimization was performed to get muscle forces. Ultimately, the joint contact forces were obtained by the last dynamic step. In the calculation of muscle forces, the polynomial muscle recruitment criteria were minimized to simulate the physiological minimum fatigue criterion, which was defined as:

$$\min_{f} G(f^M) = \sum_{i=1}^{n^{(M)}} (\frac{f_i^{(M)}}{N_i^{(M)}})^3 \tag{3.10}$$

$$0 \le f_i^{(M)}, i = 1, \dots, n^{(M)} \tag{3.11}$$

Where $f_i^{(M)}$ represents the i^th muscle force, $n^{(M)}$ defines the number of muscles, $N_i^{(M)}$ shows the strength of the muscle. *C* is the coefficient matrix for the dynamic equilibrium equations, *f* is a vector of unknown muscle, and joint reaction forces, and *d* contains all external loads and inertia forces.

3.3.3 Validity of the model

The verification process is essential for ensuring that the computational model accurately reflects physiological realities and predicts muscle behavior under various cycling conditions. The developed MSK model was verified by comparing the predicted muscle activations of the RF, TA, BF, and GAS with the recorded EMG data in the experiment.

Pearson correlation coefficient (*r*) was used to examine the agreement between the measured and calculated muscle activations. The peak value, peak timing, cycling phase of maximum activation, and duration of muscle activation were compared. The definitions of these four indexes are:

1) Peak value: the maximum muscle activation during a pedaling cycle.
2) Peak timing: the crank angle when the maximum activation was reached.
3) Cycling phase of maximum activation: expressed as number 1,2,3, or 4; the cycling phases are the first phase (0° - 90°), the second phase (90° - 180°), the third phase (180° - 270°), and the fourth phase (270° - 360°).
4) Duration of muscle activation: the interval time from onset to offset, expressed as a percentage of a complete cycle.

3.3.4 Outcomes

Muscle forces are important in motion analysis as they influence the joint contact forces and the stress distribution on the articular surfaces (Moissenet et al., 2017). Quadriceps such as RF, VL, and VM drive knee extension and hip flexion in cycling. The roles of hamstrings such as BF aid hip/knee involve controlling the range of motion and maintaining joint steadiness. GluMax powers hip extension and stabilizes the pelvis. GAS and SOL enable ankle plantarflexion, maintaining pedal smoothness, while TA dorsiflexes the ankle during the recovery phase. Therefore, the calculated muscle forces of RF, TA, BF, GAS, SOL, VL, VM, and GluMax were selected for analysis.

During cycling, the contact forces at the hip, knee, and ankle joints reflect the mechanical stress on the lower limbs. Improper riding posture and condition setting can lead to compensatory injuries with peak joint forces being the key injury-causing factors. Additionally, joint contact forces are related to muscle activation and synergy. Analyzing the interaction between muscle forces and joint contact forces is crucial for preventing injuries and designing rehabilitation programs. Therefore, the component contact forces of hip, knee, and ankle joints in the medial and lateral (M-L), proximal-distal (P-D), and anterior-posterior (A-P) directions were outputted for analysis.

3.3.5 Statistical analysis

The Pearson correlation coefficient was classified as strong ($|r| \geq 0.7$), moderate ($0.4 \leq |r| < 0.7$), low ($0.1 \leq |r| < 0.4$), and negligible correlations ($|r| < 0.1$) (Mukaka, 2012). The Shapiro-Wilk normality test indicated that the distribution of the data deviated from normalcy, as confirmed by the p-value < 0.05. A generalized estimating equation (GEE) model with a log link and a Gamma distribution was used to explore the associations between the experimental variables (saddle height and workload) and outcomes which were the maximum and mean of muscle forces and joint forces. The degrees of associations were estimated by the Wald statistic for a workload × height interaction term, with separate estimations if $\alpha < 0.05$ for the interaction term. An exchangeable covariance structure was employed. Each model was adjusted by gender, BMI, and cadence, regarding their known influence on the muscle and joint forces (Graham, 2018; Rossi et al., 2019). The null models for the analysis were set at 25% FTP for workload and 95% GTH for saddle height which served as reference conditions to evaluate the effects of independent variables on cycling biomechanics. The GEE model performance was assessed by Quasilikelihood under the independence model criterion (QIC). Risk ratios with 95% CI were calculated. The significance was set at $p < 0.05$. The data was analyzed in SPSS 26.0.

3.4 Finite Element Analysis

Figure 3.8 shows the process of FE analysis, including MRI data acquisition, inverse construction of the 3D knee joint model, model preprocessing, mesh generation, explicit FE calculation, and data post-processing.

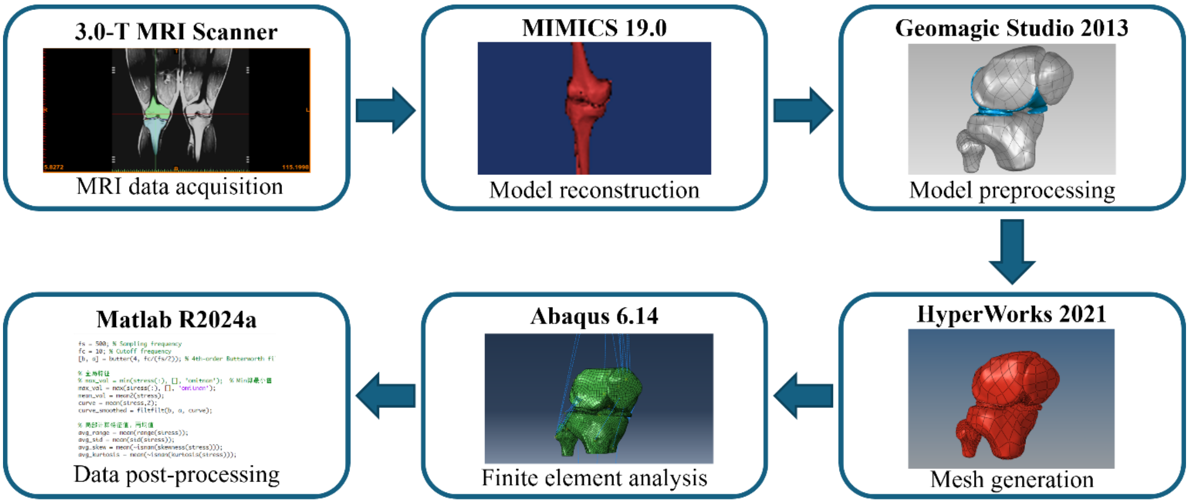

```
fs = 500; % Sampling frequency
fc = 10; % Cutoff frequency
[b, a] = butter(4, fc/(fs/2)); % 4th-order Butterworth fi

% 全局特征
% max_val = min(stress(:), [], 'omitnan');  % Min即最小值
max_val = max(stress(:), [], 'omitnan');
mean_val = mean2(stress);
curve = mean(stress,2);
curve_smoothed = filtfilt(b, a, curve);

% 局部计算特征值，再均值
avg_range = mean(range(stress));
avg_std = mean(std(stress));
avg_skew = mean(~isnan(skewness(stress)));
avg_kurtosis = mean(~isnan(kurtosis(stress)));
```

Figure 3.8 Workflow of finite element analysis.

3.4.1 Establishment of model

One willing subject was recruited from those who had previously completed the cycling experiment. This healthy male was 173 cm tall and weighed 72 kg. His right lower limb in a neutral and non-weight-bearing condition was fixed by a customized ankle-foot-orthosis to obtain the MRI. The 3.0-T MRI scanner (Siemens, Erlangen, Germany) was configured at Proton Density sequence, 0.6 mm slice interval, and a resolution of 0.5104 mm pixel size.

Inverse 3D modeling from MRI was done in MIMICS 19.0 (Materialise, Leuven, Belgium). The suitable grayscale thresholds were applied to create masks for bones and soft tissues. Figure 3.9 shows the segmented masks and initial model of the tibia and femur. The images were manually edited layer-by-layer to obtain accurate tissue boundaries.

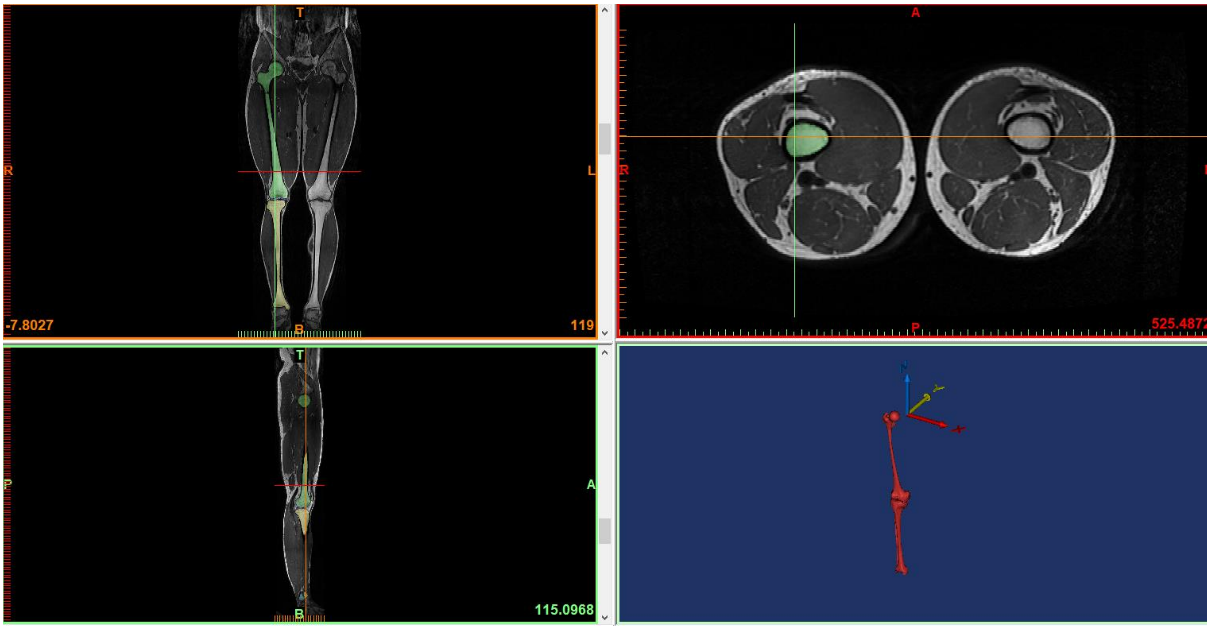

Figure 3.9 Masks and initial model of tibia and femur in Mimics.

The 3D geometries were constructed inversely from the 2D MRI. The 3D geometries after processing, including wrapping and smoothing, were exported in STL format. The constructed tibia, femur, fibula, patella, tibia cartilage, femur cartilage, and menisci were inputted into Geomagic Studio 2013 (Geomagic, Morrisville, USA). Boolean operation was performed to subtract the overlapping sections between two parts. Because this study focused on the joint contact state, the lower end of the femur, the upper end of the tibia and the fibula were selected for interception with the x-y plane. Then each part was geometrically edited and smoothed, and surface patches were created. The entities of the meniscus and cartilage of the tibia and femur were established. The processed surfaces and entities were saved as .igs files. The meshing of each part was done in HyperMesh 2021 (Altair Engineering, U.S.). The 2D and 3D types of elements were triangle and tetrahedron with first order, respectively. The target element size of bones was 4 mm and that of meniscus and cartilage was 2.5 mm. The minimum size was 0.8 mm for the parts requiring a finer mesh where the curvature of the surface changes significantly, such as the cartilage edges. The total element number of the model was 25,981. The meshed parts were saved as .inp files, respectively.

The mesh convergence analysis of menisci and cartilages was performed by testing the model with mesh sizes of 2.7 mm, 2.6 mm, 2.5 mm, and 2.4 mm. The results of stress and strain were gradually converged. The difference between the results of 2.5 mm and 2.4 mm was less than 3%. Therefore, the larger size was adopted in the calculation.

3.4.2 Finite element calculation

The above models were imported into Abaqus 6.14 (Simulia, Dassault Systemes, France) as individual parts. The bones, including the femur, tibia, fibula, and patella, were modeled as 3D discrete rigid bodies, while the menisci and cartilages were represented as 3D deformable bodies. All parts were assembled according to their original coordinates to ensure anatomical accuracy. The material properties of cartilage and menisci were defined based the previous studies (Halonen et al., 2014; Oloyede et al., 1992; Trad et al., 2017) as summarized in Table 3.4. The cartilage was modeled as isotropic and uniform, while the meniscus material behaviors incorporated anisotropic linear elastic properties which were expressed as engineering constants.

Table 3.4 Material properties of menisci and cartilages

Parts	Behavioral laws	Density	Elastic
Cartilage	Linear elastic isotropic	1.8×10^{-9} t/mm^2	E = 18.45MPa, ν = 0.42
Menisci	Engineering constants	1.3×10^{-9} t/mm^2	E1= 49.59, E2=119.94, E3=49.59, Nu12 = 0.12, Nu13 = 0.12, Nu23 = 0.12, G12 = G13 = G23 = 18.98

The anterior cruciate ligament (ACL), posterior cruciate ligament (PCL), medial collateral ligament (MCL), lateral collateral ligament (LCL), popliteofibular ligament (PFL), and oblique popliteal ligament (OPL) were implemented as connectors. The ligament behaviors were defined using a nonlinear and uncoupled force (F) – displacement (R) relationship, as detailed in Table 3.5, based on the previous research (Chen et al., 2003; Kiapour et al., 2014). In addition to the ligaments, key muscles involved in cycling mechanics were also modeled as axial connectors, including RF, VM, VL, vastus intermedius (VI), BF, and medial and lateral GAS were also established as axial connectors. The coordinates for the connector endpoints were derived from the corresponding anatomical landmarks obtained from Mimics.

Table 3.5 Elastic parameters of ligaments

Ligament	Definition	F data (N)	U data (mm)
ACL	Nonlinear	0.01, 0.001, 850, 12500	-0.01, -0.001, 0, 9.32
PCL	Nonlinear	0.01, 0.001, 1215, 22500	-0.01, -0.001, 0, 9.46
MCL	Nonlinear	0.01, 0.001, 843, 9160	-0.01, -0.001, 0, 9.08
LCL	Nonlinear	0.01, 0.001, 600, 6660	-0.01, -0.001, 0, 9.1
PFL	Nonlinear	0.01, 0.001, 466, 6660	-0.01, -0.001, 0, 9.3
OPL	Nonlinear	0.01, 0.001, 310, 3300	-0.01, -0.001, 0, 10

ACL: anterior cruciate ligament; PCL: posterior cruciate ligament; MCL: medial collateral ligament; LCL: lateral collateral ligament; PFL: popliteofibular ligament; OPL: oblique popliteal ligament.

The interactions between each pair of tibial cartilage, menisci, and femoral cartilage were modeled as frictionless and hard contact. The cartilages were tied to the outside layer of their corresponding bones. Rigid body constraints were applied between the bones (tibia, femur, patella, and fibula) and their associated reference points. A reference point was established below the tibia at the pedal-foot contact location, representing the position of the PRFs. Structural distributing constraints were used to couple the lowest nodes of the tibia and fibula to this reference point.

The simulation modeled the knee extension movement as the crank rotated from 90° to 180°, with the following three steps: 1) initial positioning, the femur was rotated to achieve the knee joint angle corresponding to the crank's initial position at 90°; 2) initial loading, muscle forces and PRFs corresponding to the 90° crank angle were applied to the appropriate connectors of muscles and reference points of PRFs; 3) dynamic simulation, the knee joint extension was simulated as the crank moved from 90° to 180°. The reference points of tibia and fibula were fixed in the initial step (U1=U2=U3=UR1=UR2=UR3=0), and the ends of two menisci were fixed for displacement (U1=U2=U3=0) but not for rotation. In step one, the fixed displacement (U1=U2=U3=0) was applied to the nodes on the surface of the tibial plateau. In step two, the displacement of reference point of femur was fixed (U1=U2=U3=0). Its' rotation around y and z axis were 0°, and the rotation around x-axis was applied according to the knee joint angle obtained from the cycling experiment as shown in Table 3.6.

Three different cycling conditions were evaluated, corresponding to saddle heights of 95%, 100%, and 105% of GTH with the same workload of 25% FTP. PRFs were measured by pedal force sensors, while knee joint angles and muscle forces were obtained from the inverse dynamic calculation of the MSK multibody model. The force loadings are illustrated in Figures 3.10 and 3.11.

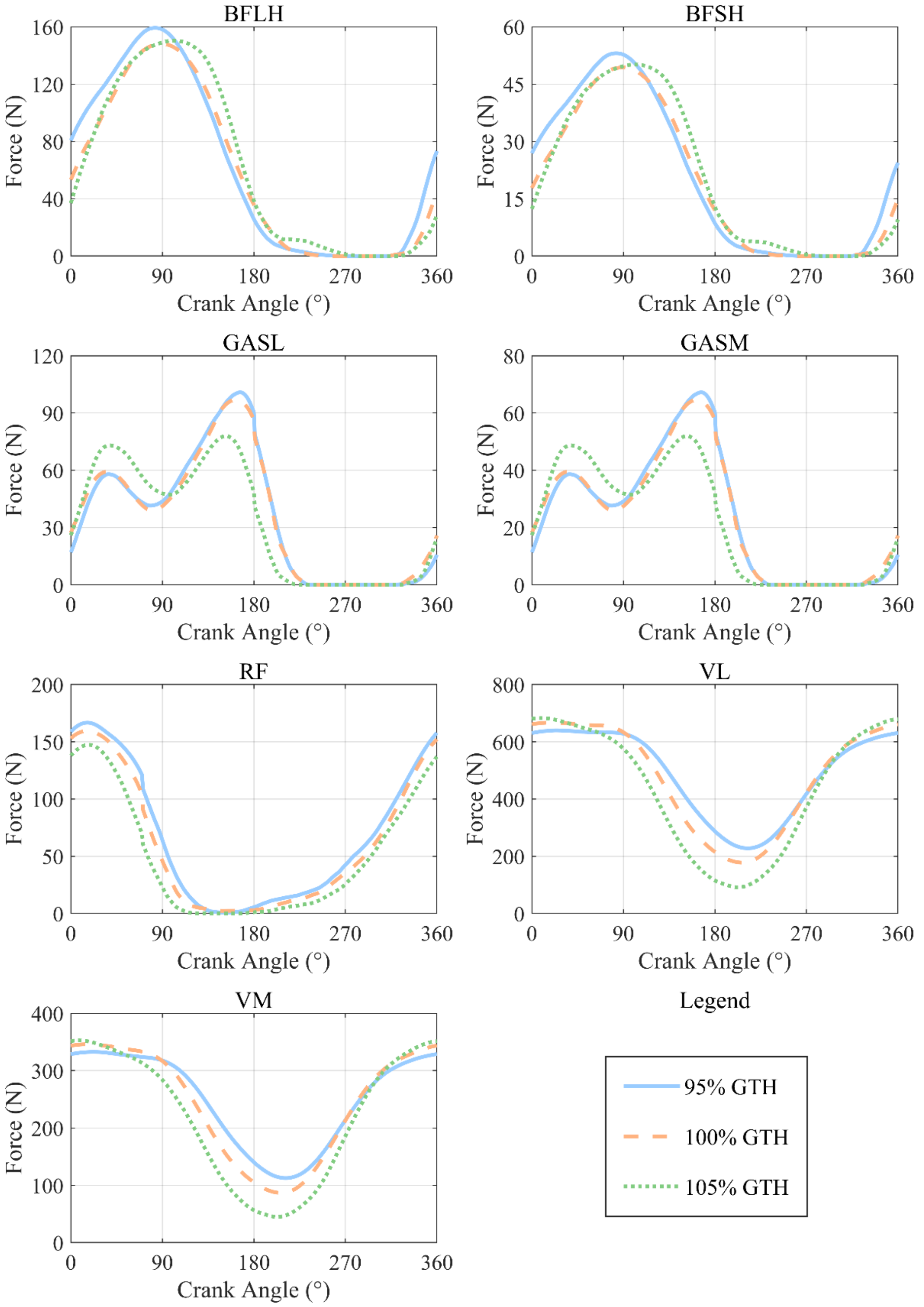

Figure 3.10 Muscle forces used as force loading in finite element analysis. BFLH: biceps femoris long head; BFSH: biceps femoris short head; GASL: gastrocnemius lateral; GASM: gastrocnemius medial; RF, rectus femoris; VL: vastus lateralis; VM: vastus medialis; GTH: greater trochanter height.

Table 3.6 The rotation boundaries under three riding conditions

Saddle height	Initial joint angle (rad)	Finial joint angle (rad)
95% GTH	1.67	1.21
100% GTH	1.54	1.01
105% GTH	1.36	0.77

GTH: greater trochanter height.

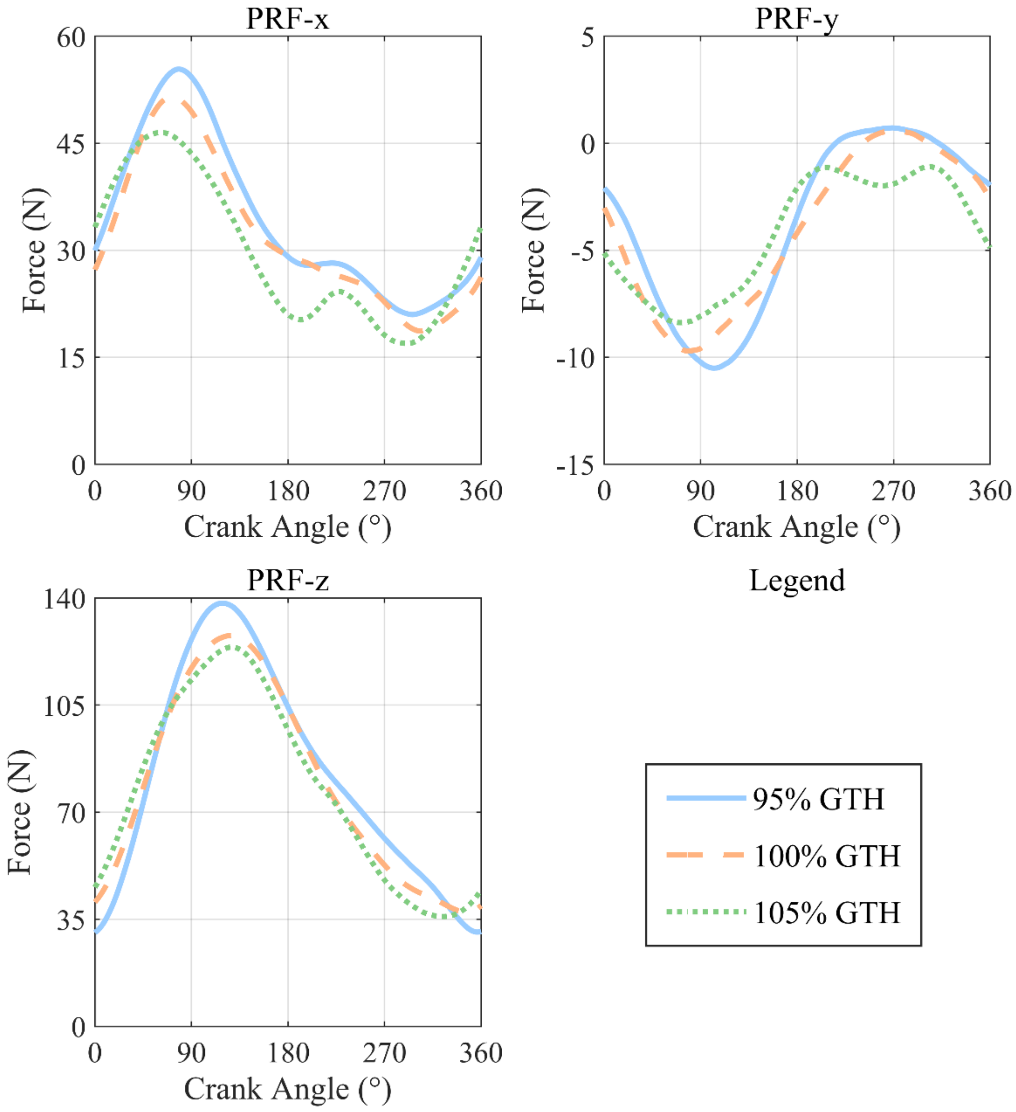

Figure 3.11 Pedal reaction forces used as force loading in finite element analysis. PRF: pedal reaction force; GTH: greater trochanter height.

The simulation was performed using the dynamic explicit solver in Abaqus. Step times were set to 0.1 s, 0.02 s, and 0.18 s for the three steps, reflecting the actual duration of the movement. A mass scaling factor of 10 was applied to reduce computational time while maintaining stability.

Field outputs were stress components and invariants (S), logarithmic strain components (LE), total strain components, translations and rotations (U), contact area (CAREA), contact pressure (CPRESS), and all energy magnitudes. History outputs were internal energy (ALLIE), kinetic energy (ALLKE), total energy (ETOTAL), total forces and moments of connector (CTF), and relative displacements and rotations of connector (CU).

3.4.3 Postprocess

When the ratio of ALLKE to total energy was below 5%, the model was deemed quasi-static, and the simulation was considered to be stable. Stress and displacement contour maps were generated using the Abaqus visualization module. Key results, including Mises stress, maximum and minimum principal stress, and maximum principal LE of menisci and cartilages, and the CPRESS and CAREA between the menisci and cartilages, were exported to Excel for further post-processing and analysis in MATLAB R2024a (The MathWorks Inc., Massachusetts, USA).

3.5 Machine Learning Model for Saddle Height Classification

The purpose of this sub-study is to construct an accurate ML model to classify saddle heights based on easily measured kinematic data. The kinematic data was the joint angles of hip, knee, and ankle which were derived from the riding experiment described in section 3.1. Saddle heights were classified as too low (95% of GTH), moderate (from 97% to 103% of GTH), and too high (105% of GTH). The process of constructing the model is the pre-processing of joint angles, feature extraction and selection, setting the model parameters, and comparing the performance of four ML models.

3.5.1 Data processing and feature extraction

As mentioned in section 3.1, the movement trajectories of the subjects' lower limbs during the cycling experiment were recorded by the Vicon motion capture system. After inspection and screening, data from 16 subjects were selected. Utilizing the Plug-in Gait lower body model within the Nexus 2.16.0 framework, the comprehensive kinematic analysis was performed to evaluate joint angles during riding movement. The corresponding marker set as shown in Figure 3.12 was selected from the 33 markers used earlier in the experiment according to the tutorial.

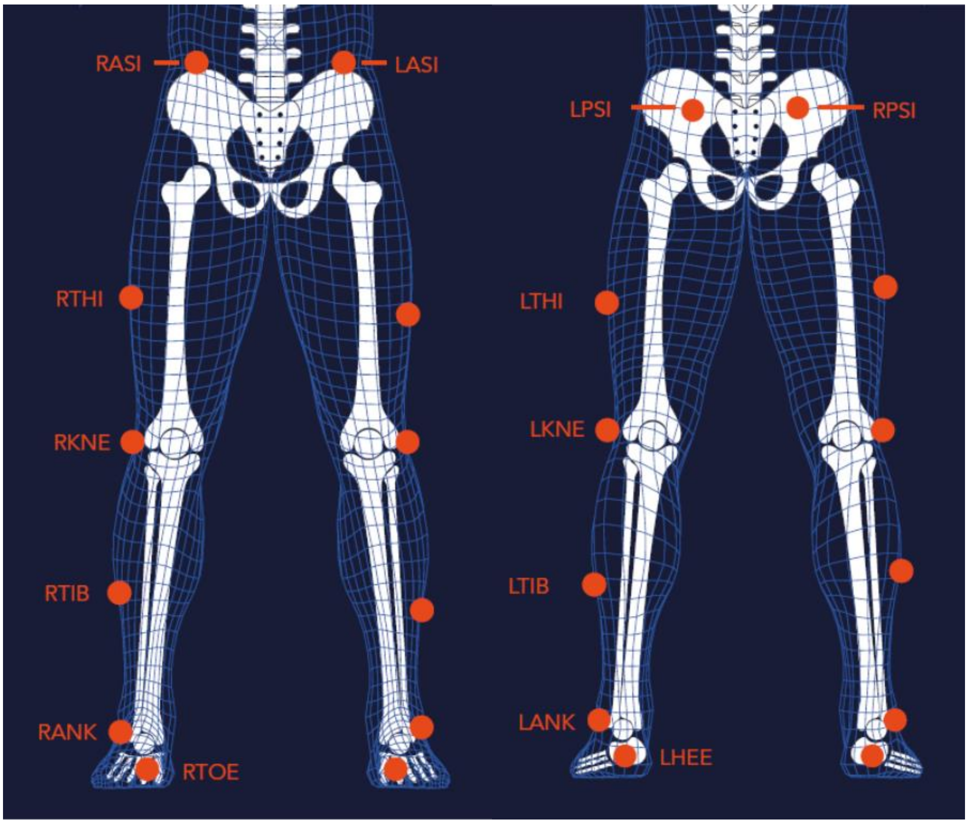

Figure 3.12 Marker set used in Plug-in Gait lower body model. (Nexus 2.16.0 documentation).

The static data was processed first to define the coordinate system and establish baseline joint positions. Then the dynamic Plug-in Gait model was performed to get the kinematic results. The trajectories of the right ankle (RANK marker) and joint angles of the hip, knee, and ankle of the right leg were output for further analysis. For hip and knee joints, the X, Y, and Z angles represent the flexion/extension, the abduction/adduction, and the internal/external rotation, respectively. For the ankle joint, the X, Y, and Z angles represent the dorsiflexion/plantarflexion, the inversion/eversion, and the internal/external rotation.

The marker trajectories were first processed using a fifth-order low-pass filter to eliminate high-frequency noise. The cutoff frequency for this filter was 6 kHz, equivalent to half of the sampling frequency, following the Nyquist theorem. Then the maximum Z-coordinate values of the RANK marker, corresponding to the TDC position, were identified. A pedaling cycle was defined as the interval between two adjacent maximum Z-coordinate values (Figure 3.13). Outlier data was excluded to ensure the accuracy and reliability of the results. After the preprocessing step, data from 16 participants were analyzed, encompassing a total of 40,428 pedaling cycles across different cycling conditions of five saddle heights.

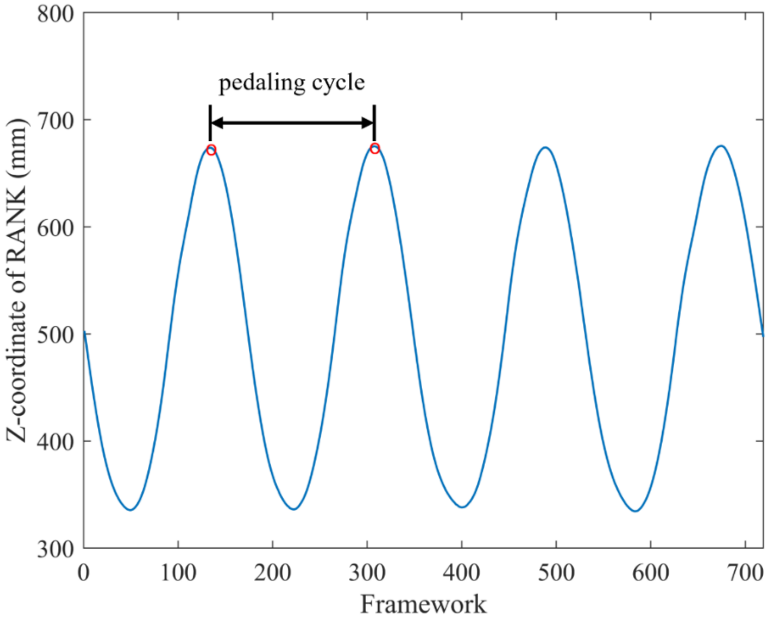

Figure 3.13 Definition of one pedaling cycle by Z-coordinate of RANK's trajectory.

The joint angle data were segmented into individual cycles based on the defined framework of pedaling cycles. Each joint was characterized by its angular movements in three directions (X, Y, and Z), yielding a total of nine distinct joint angles per cycle. For each pedaling cycle, a comprehensive set of features was extracted to describe the joint angle characteristics. These features included the maximum value, minimum value, the corresponding crank angle of maximum and minimum joint angles (ranging from 0° to 360°), the root mean square (RMS) value, mean, standard deviation (SD), coefficient of variability (CV), and the ROM value for each joint angle. Thus, a total of 81 features were calculated from each pedaling cycle. The final constructed feature array was 40,428 × 81.

The features were normalized by their maximums, meaning that each feature value was divided by the maximum in the column of the feature array in which this value resided. Because the amount of experimental data for the appropriate saddle heights was much more than the data for the too-high and too-low saddle heights, the synthetic minority over-sampling technique (SMOTE) was performed in Python 3.10 (Python Software Foundation, United States). This is important because imbalanced datasets can lead to a biased model that favors the majority class. SMOTE aims to improve the performance of classifiers by generating synthetic examples of the minority class, thereby balancing the class distribution. The process of SMOTE was 1) identifying minority class samples; 2) for each minority class sample, identifying the k nearest neighbors; 3) for each randomly selected neighbor, creating a synthetic sample by interpolating between the minority class sample and the neighbor; 4) repeating the process until achieving the desired balance between the classes. The other two classes were resampled according to the data number of appropriate saddle height so that the data number of the three classes was the same 24,118. The resampled feature array was 72,354 × 81. The label vector was 72,354 × 1 containing the class numbers 1 (low saddle heights), 2 (appropriate saddle heights), and 3 (high saddle heights). The vector of the subject number was 72,354 × 1 containing numbers from 1 to 16 that were used to label the subject to which the feature values of each row belong.

3.5.2 Optimal feature set

Forward sequential feature selection was used to identify the optimal feature set from the whole feature set (containing 81 features) in each ML model. This approach starts with no features in the model and incrementally adds features based on their contribution to improving the accuracy of the classification model. The accuracy of the model was expressed as the misclassification rate, which was the number of misclassified samples as a percentage of the total number of samples (Zhang et al., 2024).

The feature selection process shown in Figure 3.14 was 1) initialization: starting with an empty set of selected features; 2) evaluation metric: establishing the misclassification rate to evaluate the model; 3) iterative feature addition: for each feature not currently in the selected set, evaluate the model's performance by adding the feature to the currently selected set, then train the model using the updated feature set and calculate the misclassification rate; 4) select the best feature: identify the feature that results in the lowest misclassification rate and add this feature to the selected set; 5) repeat: repeat the evaluation and selection process until iterating over all the features and obtain the lowest misclassification rate. In the fourth step, k-fold cross-validation was used to assess the performance and generalizability of the model. We adopted five-fold cross-validation, which means dividing the dataset into five equally sized folds. Each fold was used as the test set and the remaining four folds as the training set. The model was trained on the training set and was evaluated on the test set. By using multiple train-test splits, k-fold cross-validation provides a more reliable estimate of model performance compared to a single train-test split and is suitable for small datasets (Wong & Yeh, 2020).

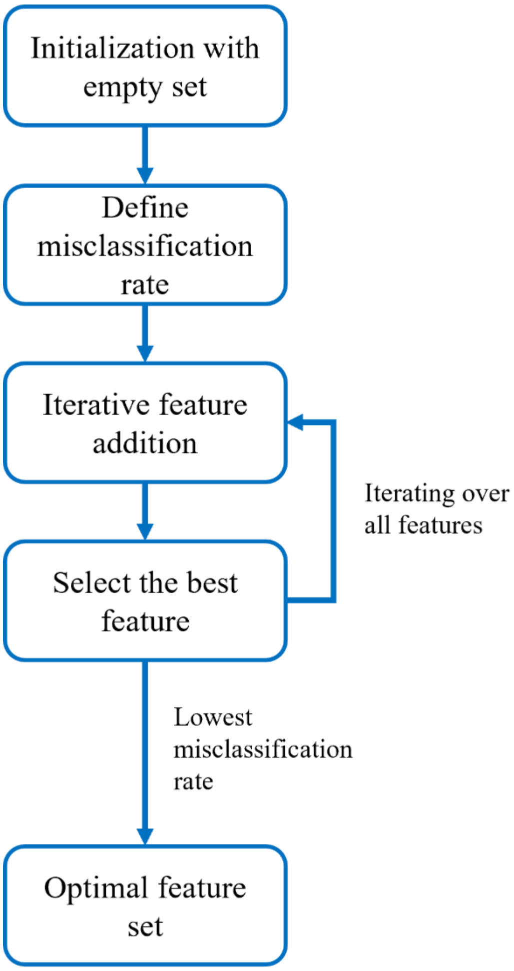

Figure 3.14 The process of deciding the optimal feature set.

3.5.3 Comparison of machine learning models

Support Vector Machine (SVM) is a powerful ML algorithm known for its ability to handle high-dimensional data and perform well in classification tasks. K-Nearest Neighbors (KNN) is a simple yet effective model that relies on proximity to classify data points, making it highly adaptable to various datasets. Naïve Bayes (NB) is a probabilistic model often used for its computational efficiency and strong performance in text classification and spam filtering. Decision Trees (DT) are intuitive models that use a tree-like structure to make decisions, valued for their interpretability and effectiveness in both classification and regression problems. These four models are the commonly used ML models (Bansal et al., 2022). SVM works by finding the hyperplane that best separates different classes in the feature space and is computationally intensive and sensitive to parameter choices. KNN is a non-parametric, instance-based learning algorithm used for classification and regression but is slow for large datasets. NB is a family of probabilistic algorithms based on Bayes' theorem, which assumes independence among predictors. DT is a non-linear model that makes decisions based on a series of questions about the features. Each internal node represents a feature, each branch represents a decision rule, and each leaf node represents an outcome.

The classification performance of the four models was compared based on the obtained optimal feature set. The accuracy of the classification was examined by leave-one-out cross-validation (LOOCV). LOOCV is a special case of k-fold cross-validation that maximizes the training data used and minimizes bias (Vehtari et al., 2016). The data were divided into 16 groups according to the subject number, and each group of data was used as the test set in turn, and the remaining 15 groups of data were used as the training set. In total, the classification accuracy was measured 16 times, and the average of the results was used to represent the performance of the model. The loss function was the lowest misclassification cost. The optimizer was the Bayesian optimization.

CHAPTER 4 RESULTS

4.1 Electromyography

The statistical analysis indicated that EMG data met the normal distribution and homogeneity of variance ($p > 0.05$). One-way ANOVA with Greenhouse-Geisser correction was performed on the maximum and mean of EMG envelopes. The results showed that saddle height mainly affected the mean value of MG ($F(4,205) = 5.685$, $p < 0.0005$, $\eta^2 = 0.1$), the maximum EMG of RF ($F(2,207) = 8.108$, $p = 0.001$, $\eta^2 = 0.073$) and BF ($F(2,207) = 3.281$, $p = 0.04$, $\eta^2 = 0.031$), while the saddle height mainly influenced the mean EMG of MG ($F(4,205) = 5.685$, $p < 0.0005$, $\eta^2 = 0.1$) and the its maximum EMG ($F(4,205) = 9.819$, $p < 0.0005$, $\eta^2 = 0.161$).

4.1.1 EMG envelope

Figure 4.1 displays the normalized EMG envelopes of RF, TA, BF, and MG. The sequence of subgraphs was organized based on saddle height, and within each one the influence of workload adjustments on the EMG envelope was evaluated. The horizontal axis represents the crank angle from 0° to 360° and the vertical axis represents the degree of muscle activation relative to MVC. The EMG envelopes of RF and BF increased as the workload increased from 25% to 50% and 75% of FTP, especially at the peaks when the crank angle was around 90°. Only the EMG envelope of MG showed a significant increase gradually with saddle height raised from 95% to 105% of GTH, and most significant at the peaks (the crank angle was about 180°). RF and BF are mainly activated in the propulsion period (crank angle from 0° to 180°). TA was mainly activated in the first and fourth cycling phases (crank angle from 0° to 90° and from 270° to 360°), while MG was mainly activated in the second and third cycling phases (crank angle from 90° to 180°). The activation levels of BF and MG were generally higher than those of TA and RF.

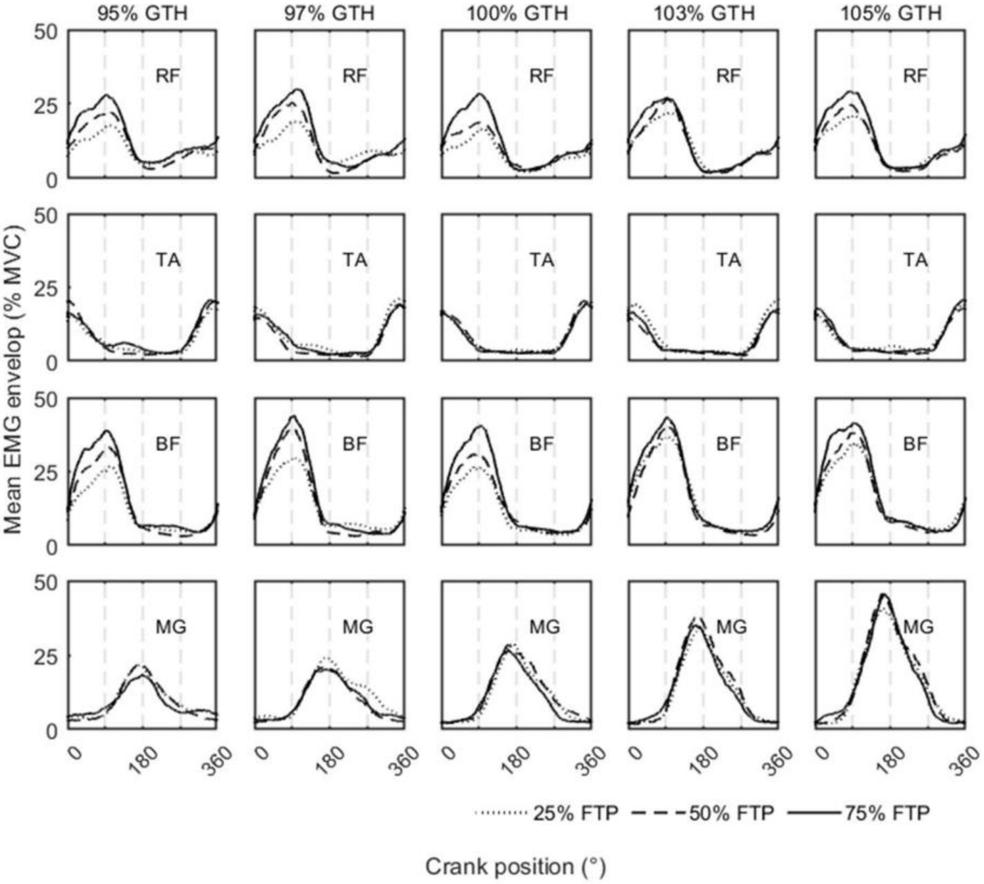

Figure 4.1 The normalized electromyography (EMG) signals of muscles under different saddle heights and workloads. RF: rectus femoris; TA: tibialis anterior; BF: biceps femoris; MG: medial gastrocnemius.

4.1.2 Mean and maximum of EMG

Table 4.1 summarizes the mean values of EMG of lower limb muscles during different riding conditions. The largest means of EMG for RF and BF occurred in the 75% FTP riding condition and 105% GTH condition which were 12.67 ± 10.55 %MVC and 17.04 ± 12.27 %MVC, respectively. That of TA was 8.14 ± 5.74 %MVC occurring in the riding condition of 95% GTH × 75% FTP. The maximum EMG readings for various lower-extremity muscles can be found in Table 4.2 which highlights their highest activity levels observed throughout the experiment. Similarly, the largest maximum EMG of RF and BF were 34.23 ± 27.41 %MVC and 43.82 ± 28.41 %MVC, respectively, when the workload was 75% FTP and saddle height was 105% GTH. The maximum EMG of TA also occurred in the condition of 95% GTH × 75% FTP which was 8.14 ± 5.74 %MVC. The trends of EMG changes with different riding conditions are compared in Figures 4.2 – 4.4.

Table 4.1 Means of processed electromyographic (EMG) of lower-limb muscles

Saddle height (%GTH)	Workload (%FTP)	Rectus femoris (%MVC)	Tibialis anterior (%MVC)	Biceps femoris (%MVC)	Medial gastrocnemius (%MVC)
95	25	9.19±7.60	6.96±4.01	10.73±7.58	10.58±5.76
	50	10.12±6.70	6.93±4.26	11.96±7.86	9.23±6.54
	75	13.38±9.66	8.14±5.74	14.64±9.15	10.50±7.33
97	25	8.83±7.17	7.83±5.62	11.60±9.94	12.54±8.60
	50	10.48±7.93	6.62±4.17	12.93±8.69	10.87±7.43
	75	12.40±11.51	7.65±5.50	14.60±10.03	10.95±8.27
100	25	7.13±5.52	6.79±5.03	10.29±8.81	11.00±6.87
	50	9.32±6.97	7.04±4.68	12.58±9.68	12.48±7.36
	75	11.66±6.86	6.79±4.35	14.59±10.90	10.73±6.86
103	25	9.72±9.75	7.22±4.45	14.16±12.37	12.75±6.33
	50	10.44±8.23	6.22±4.34	14.54±2.98	13.44±7.79
	75	11.74±8.11	6.73±5.34	16.41±12.20	15.00±10.07
105	25	10.15±9.91	7.31±4.15	14.77±13.03	16.53±7.46
	50	10.30±7.35	6.82±4.56	15.00±11.99	18.71±9.56
	75	12.67±10.55	7.21±4.38	17.04±12.27	16.15±7.51

Values are presented as Mean ± SD. GTH, greater trochanter height; FTP, functional threshold power; MVC, maximum voluntary contraction.

Table 4.2 Maximums of processed electromyographic (EMG) of lower-limb muscles

Saddle height (%GTH)	Workload (%FTP)	Rectus femoris (%MVC)	Tibialis anterior (%MVC)	Biceps femoris (%MVC)	Medial gastrocnemius (%MVC)
95	25	21.71±15.90	22.11±15.35	26.42±19.00	29.02±14.72
	50	24.50±12.18	21.96±15.85	31.25±20.69	23.93±16.06
	75	34.19±21.37	24.91±20.07	39.87±26.50	28.41±20.21
97	25	20.53±12.54	23.97±17.33	27.73±19.45	32.34±18.42
	50	27.24±18.82	21.78±14.77	35.53±24.12	29.40±19.01
	75	33.00±29.15	22.48±18.39	39.73±27.86	29.11±21.37
100	25	18.60±14.30	20.54±16.31	25.25±24.05	31.68±18.58
	50	22.79±15.86	22.04±16.48	32.69±25.06	33.64±17.83
	75	31.11±16.73	20.33±14.05	38.22±28.38	30.73±23.34
103	25	22.63±20.50	20.94±14.17	33.58±28.63	39.45±19.50
	50	27.52±19.43	17.01±13.64	39.21±30.17	40.95±21.00
	75	31.43±19.63	19.92±16.15	41.12±30.60	43.43±26.16
105	25	22.80±18.46	20.74±13.42	34.43±29.63	45.63±17.20
	50	29.62±19.48	19.21±13.52	37.49±28.41	54.31±26.25
	75	34.23±27.41	21.75±15.94	43.82±28.41	52.35±21.56

Values are presented as Mean ± SD. GTH, greater trochanter height; FTP, functional threshold power; MVC, maximum voluntary contraction.

Effects of workload

Figure 4.2 compares the effect of workload on the mean values of the normalized EMG envelopes under different saddle heights. There were no significant differences in the mean EMG of TA (Figure 4.1.2 (b)) and only two significant differences in the mean EMG of MG (Figure 4.1.2 (d)). The average RF's EMG readings demonstrated a marked increase with each incremental step of 25% in applied workload as saddle heights were set to 97% and 100% GTH, while at saddle heights of 95% and 103% GTH, it showed a notable rise only when the workload reached 75% FTP. Figure 4.2 (c) presents a larger number of statistical differences. The average EMG value of BF demonstrated a steady increase in response to higher workloads across all tested saddle heights, especially in the 100% GTH case that improved from 10.29 ± 8.81 %MVC to 14.59 ± 10.90 %MVC.

The maximum values of EMG envelopes influenced by workload are displayed in Figure 4.3. The maximum values of EMG of RF and BF were more affected by the workload than those of TA and MG. For example, at the saddle height of 100% GTH, the maximum EMG of RF was increased from 18.60 ± 14.30 %MVC to 31.11 ± 16.73 %MVC. At saddle heights of 95% and 100% GTH, the BF muscle exhibited a marked increase in maximum EMG activity as the workload increased with each incremental step of 25% FTP. However, in the cases of 103% and 105% GTH, the maximum BF EMG increased significantly only when the workload improved by 50% of FTP. On the other hand, there was no uniform trend of the maximum values of EMG of TA and MG under different saddle heights.

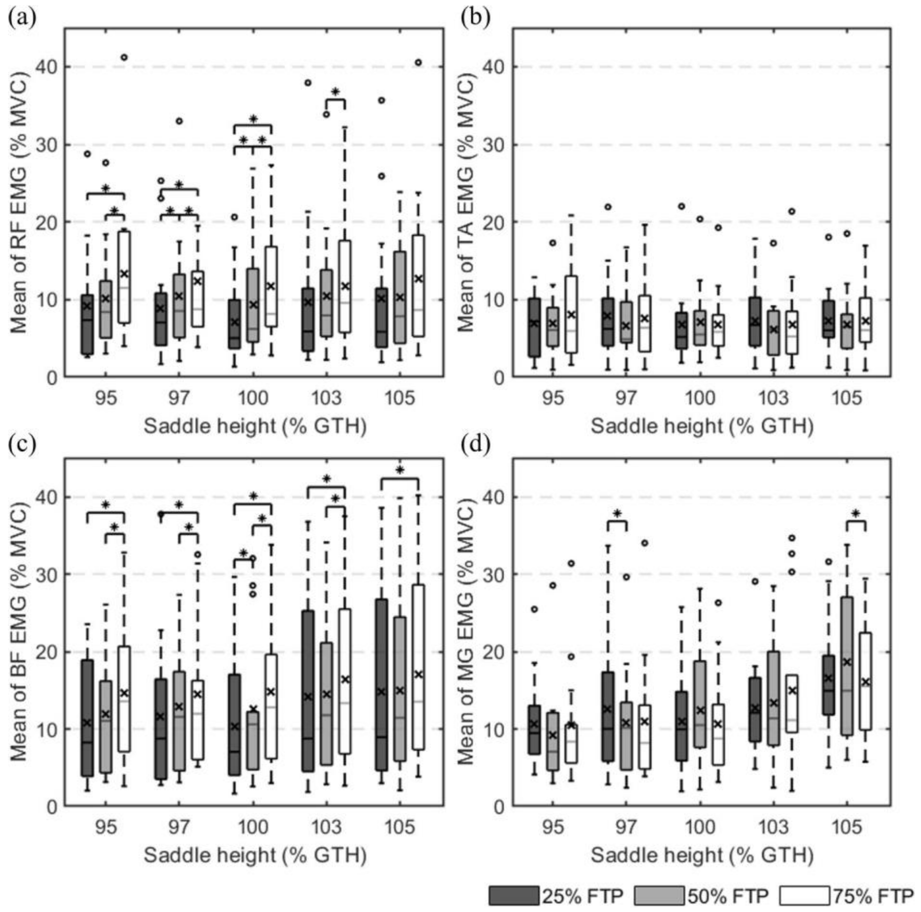

Figure 4.2 Comparison of the mean normalized electromyographic (EMG). RF: rectus femoris; TA: tibial anterior; BF: biceps femoris; MG: medial gastrocnemius; GTH: greater trochanter height; FTP: functional threshold power. ○ represents an outlier. * indicates a statistical difference ($p < 0.05$). × denotes the mean of the box values.

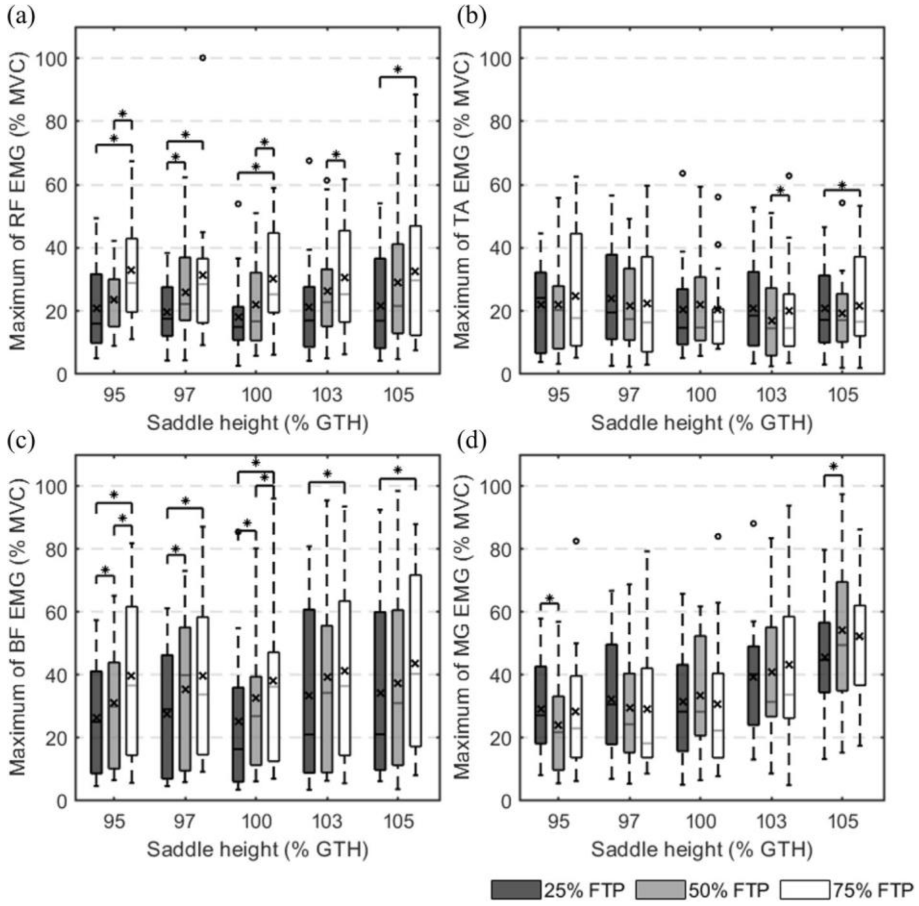

Figure 4.3 Comparison of the maximum normalized electromyographic (EMG). RF: rectus femoris; TA: tibial anterior; BF: biceps femoris; MG: medial gastrocnemius; GTH: greater trochanter height; FTP: functional threshold power. ○ represents an outlier. * indicates a statistical difference ($p < 0.05$). × denotes the mean of the box values.

Effects of saddle height

Because the EMG of RF and TA was almost unaffected by saddle height, Figure 4.4 shows the maximum and mean EMG of only BF and MG at various saddle heights. At a workload set at

25% FTP, adjustments in saddle height from 95% to 105% of GTH resulted in an increase in BF EMG activity, which serves as a measure of muscle contraction strength. The EMG readings escalated from 10.73 ± 7.58 %MVC up to 14.77 ± 13.03 %MVC during this adjustment, with the lowest value observed at 100% GTH, approximately 10.29 ± 8.81 %MVC. The maximum EMG of BF was significantly different only when comparing the cases of 100% GTH and 105% GTH. At a workload equivalent to 50% FTP, the analysis revealed no statistically significant variations in either the mean or maximum EMG readings for the BF muscle. At the workload of 75% FTP, the mean EMG of BF was increased by 2.44 %MVC only when the saddle height raised from 97% to 105% of GTH as shown in Figure 4.4 (a).

When workloads were set at 50% and 75% of FTP, adjustments in saddle elevation at intervals of 5% GTH caused the MG muscle’s EMG signals to experience growth in both peak and average activity levels, with variations observed across different increments. For instance, when the workload was set to 50% FTP, the peak EMG readings for the MG muscle starting at 23.93 ±16.06 %MVC at 95% GTH rose progressively to 29.40 ±19.01 %MVC at 97% and reached a maximum of 54.31 ±26.25 %MVC at the highest saddle position of 105% GTH. Under consistent workload conditions, adjusting the saddle elevation across a range extending from 95% up to 105% of the individual's GTH caused a substantial rise in average EMG readings for the MG muscle by over 100%. On the other hand, when the workload was 25% FTP, the mean and maximum EMG of MG increased with the saddle height raised from 100% to 105% of GTH, while the change of saddle height from 95% to 100% was an exception. Because the mean and maximum EMG of MG in the 97% GTH case were larger than the corresponding values in the 95% and 100% GTH cases.

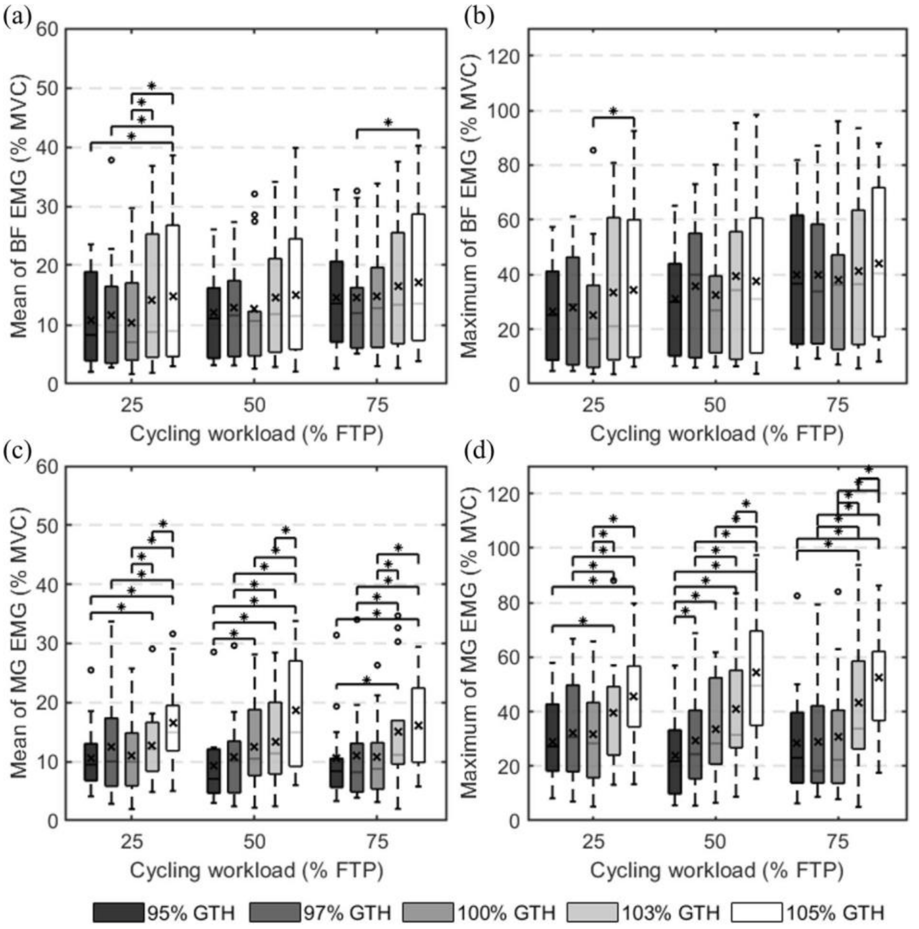

Figure 4.4 Comparison of mean and maximum values of the normalized electromyographic (EMG) of the biceps femoris (BF) and medial gastrocnemius (MG). BF: biceps femoris; MG: medial gastrocnemius; GTH: greater trochanter height; FTP: functional threshold power. ○ represents an outlier. * indicates a statistical difference ($P < 0.05$). × denotes the mean of the box values.

4.1.3 Duration of muscle activation

According to the predefined threshold of muscle activation, onset/offset timing and duration of muscle activation of RF, TA, BF, and MG muscles were obtained as shown in Figure 4.5. The horizontal axis represents the crank angle, and the vertical axis is the classification of riding conditions. The main activation phase of each muscle corresponded to EMG envelopes. Table 4.3 shows the percentage of muscle activation time during the propulsive phase, recovery period, and a complete crank cycle. Table 4.4 provides a summary of the statistical differences in these percentages for various cycling workloads at each saddle height level. Most of the comparison results were not statistically different. When the workload increased, the RF muscle experienced a diminished overall activation period. This reduction in activation duration became statistically significant when saddle height was raised from 100% to 105% of GTH. The duration percentage of MG in the propulsive period rose as the cycling workload increased, with the exception of the saddle height of 97% GTH. Specifically, the saddle height of 105% GTH was where the change was most noticeable. In this instance, when the workload climbed from 25% to 50% and to 75% of FTP, the percentage of activation duration increased from 45.38 ± 11.19% to 48.10 ± 7.16% and finally to 55.93 ± 12.89 (p = 0.009). At the saddle heights of 95%, 100%, and 105% of GTH, the activation duration during the recovery phase reduced as the workload increased. The percentage of total duration did not exhibit a consistent pattern across conditions.

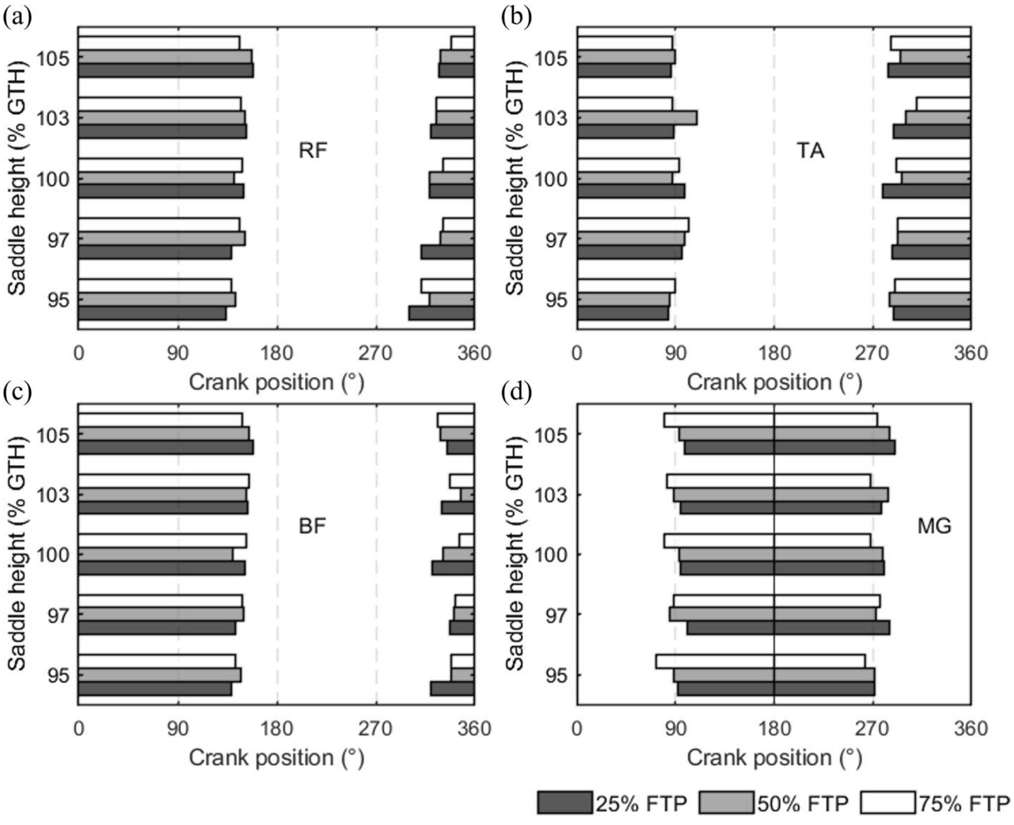

Figure 4.5 Onset timing, offset timing, and muscle activation duration.

Table 4.3 Percentage of muscle activation during propulsive/recovery phases and one cycle

Saddle height (%GTH)	Workload (%FTP)	Rectus femoris			Tibialis anterior			Biceps femoris			Medial gastrocnemius		
		Propulsive (%)	Recovery (%)	A cycle (%)	Propulsive (%)	Recovery (%)	A cycle (%)	Propulsive (%)	Recovery (%)	A cycle (%)	Propulsive (%)	Recovery (%)	A cycle (%)
95	25	74.15±15.32	33.38±26.62	53.77±10.64	46.18±18.42	39.60±14.32	42.89±11.80	77.15±18.02	22.44±22.57	49.79±8.19	49.13±9.62	50.88±8.19	50.01±4.30
	50	78.96±8.78	23.08±23.26	51.02±9.26	46.95±17.48	41.76±20.73	44.35±12.84	82.05±8.25	12.15±14.18	47.10±8.23	51.10±16.83	50.78±19.20	50.94±6.86
	75	77.14±16.75	26.82±23.74	51.98±8.03	49.55±18.41	38.77±12.51	44.16±12.38	79.38±19.25	12.14±19.84	45.76±1.10	59.46±17.82	46.38±12.21	52.92±8.61
97	25	76.91±16.72	26.73±25.38	51.82±10.70	52.98±18.30	39.96±19.40	46.47±12.52	79.20±12.92	12.62±16.73	45.91±7.18	43.87±11.73	58.34±17.68	51.10±7.80
	50	83.74±6.94	17.17±19.86	50.46±10.28	54.63±25.79	37.56±24.43	46.09±11.77	82.97±7.92	10.63±18.30	46.80±11.70	52.67±13.11	51.28±16.56	51.98±7.70
	75	81.00±6.10	16.06±17.58	48.53±9.27	56.53±22.08	37.62±23.18	47.07±12.75	82.31±9.91	9.63±12.30	45.97±5.90	50.54±4.80	53.28±13.41	51.91±5.50
100	25	83.15±10.41	23.21±22.92	53.18±8.98	54.61±20.81	44.97±23.33	49.79±11.85	83.71±8.72	21.87±19.85	52.79±9.57	47.38±13.47	55.95±10.65	51.66±3.70
	50	78.12±9.76	22.85±22.19	50.49±9.01	48.42±12.57	35.08±21.86	41.75±8.80	77.66±12.94	16.03±18.64	46.84±5.90	48.15±16.03	55.00±20.15	51.57±5.47
	75	82.68±7.81	16.04±19.44	49.36±9.14	51.68±20.77	37.90±20.09	44.79±14.18	84.65±7.58	7.90±12.46	46.27±6.33	55.39±10.89	48.98±8.87	52.19±4.14
103	25	84.84±11.77	22.44±22.03	53.64±9.04	49.46±12.25	39.85±15.18	44.65±9.58	85.19±10.64	16.78±20.49	50.99±8.58	47.61±9.79	54.38±13.58	51.00±4.67
	50	83.83±5.52	19.24±18.13	51.54±9.33	60.75±22.02	33.52±13.78	47.13±13.66	84.66±6.56	7.20±9.08	45.93±5.89	51.08±10.64	57.56±8.88	54.31±4.51
	75	81.63±13.62	19.43±21.86	50.53±9.01	48.68±20.31	27.96±8.71	38.22±9.49	86.02±14.50	12.93±21.79	49.47±8.14	54.62±15.64	49.12±12.43	51.87±5.13
105	25	87.70±8.09	18.49±23.72	53.09±10.34	47.76±13.56	42.26±14.95	45.01±9.05	87.27±7.53	14.07±18.63	50.97±9.68	45.38±11.19	61.03±15.14	53.21±5.65
	50	87.00±8.24	17.26±19.61	52.13±8.11	49.57±19.65	36.05±8.89	42.81±9.19	85.92±9.27	17.36±19.37	51.64±11.06	48.10±7.16	58.45±5.06	53.28±3.60
	75	81.04±10.83	11.97±15.48	46.50±5.81	48.39±5.75	41.23±19.12	44.81±9.84	82.76±12.37	18.81±27.21	50.78±13.79	55.93±12.89	52.30±9.71	54.12±4.80

Table 4.4 Statistical difference in the percentage of muscle activation across three workloads

Saddle height (%GTH)	Workload (%FTP)	Rectus femoris	Tibialis anterior	Biceps femoris	Medial gastrocnemius
95	25 vs. 50	*NS*	*NS*	*NS*	*NS*
	25 vs. 75	*NS*	*NS*	*	*a*
	50 vs. 75	*NS*	*NS*	*NS*	*NS*
97	25 vs. 50	*NS*	*NS*	*NS*	*NS*
	25 vs. 75	*NS*	*NS*	*NS*	*NS*
	50 vs. 75	*NS*	*NS*	*NS*	*NS*
100	25 vs. 50	*NS*	*	*NS*	*NS*
	25 vs. 75	*b* *	*NS*	*NS*	*a b*
	50 vs. 75	*NS*	*NS*	*NS*	*NS*
103	25 vs. 50	*NS*	*NS*	*	*NS*
	25 vs. 75	*	*b* *	*NS*	*NS*
	50 vs. 75	*NS*	*NS*	*NS*	*b*
105	25 vs. 50	*NS*	*NS*	*NS*	*NS*
	25 vs. 75	*	*NS*	*NS*	*a*
	50 vs. 75	*	*NS*	*NS*	*a*

*Statistical difference when $p < 0.05$. a indicates a statistical difference in the propulsive phases, b indicates a statistical difference in the recovery phase, and * indicates a statistical difference in a complete crank cycle. NS indicates nonsignificant.*

4.2 Results of Musculoskeletal Dynamic Simulation

4.2.1 Validation of the musculoskeletal model

The validity of the multibody MSK model was verified by comparing the calculated and experimentally measured muscle activations of RF, TA, BF, and GAS.

The Pearson correlation coefficient demonstrated a strong correlation between the calculated and measured muscle activations of TA ($r = 0.952$, $p < 0.001$) and BF ($r = 0.953$, $p < 0.001$). A moderate correlation was found in RF ($r = 0.501$, $p < 0.001$) and GAS ($r = 0.474$, $p < 0.001$).

Table 4.5 summarizes the comparison of peak value, peak timing (represented as the crank angle), cycling phase of peak, and duration of muscle activation (expressed as the proportion of a pedaling cycle) between the calculated and measured muscle activations. The difference in the time of peak and duration of muscle activation between the calculation and measurement of four muscles was less than 7% except that, the calculated peak timing of RF was 17.53° in the first cycling phase, which was quite different from its measured counterpart (94.20° in the second phase). The calculated activation peaks of all muscles were generally less than those of EMG, for instance, the calculated peak of RF was 16.74 %MVC while that of EMG was 23.86 %MVC.

Table 4.5 Peak value, peak timing, cycling phase of maximum muscle activation, the proportion of muscle activation duration in one cycle, and correlation coefficient between EMG data and the calculated muscle activations

		Peak value (% MVC)	Peak timing (°)	Cycling phase	Muscle activation (%)	Correlation coefficient
RF	EMG	23.86	94.20	2	23.58	0.501
	Model	16.74	17.53	1	25.08	
TA	EMG	19.57	354.47	4	22.20	0.953
	Model	13.42	344.60	4	22.31	
BF	EMG	36.33	93.73	2	25.26	0.952
	Model	20.37	89.10	1	25.32	
GAS	EMG	29.99	168.47	2	21.53	0.474
	Model	13.48	157.40	2	18.76	

RF: rectus femoris; TA: tibialis anterior; BF: biceps femoris; GAS: gastrocnemius; MVC: maximum voluntary contraction; EMG: electromyography.

4.2.2 Muscle forces

Figure 4.6 illustrates the muscle force envelopes of the eight major muscles of the right leg in cycling. The three blue lines with different line types, all at 75% FTP workload, were used to contrast the effect of saddle height on the overall trend of muscle forces. The muscle forces of RF, VL, VM, and GAS increased as the saddle height raised from 95% to 100% and 105% of GTH, especially at their peaks, while the SOL muscle force decreased. Muscle forces of BF and TA were affected by saddle height almost exclusively at the peaks, while that of GluMax was unchanged. The blue (75% FTP), yellow (50% FTP), and red (25% FTP) lines are used to compare the effect of workload with the same saddle height of 100% GTH. The muscle forces of RF, BF, TA, and GM increased when the workload improved from 25% to 50% and 75% of FTP, while the muscle forces of SOL and GAS (mainly the second peak) declined gradually. VL and VM varied slightly only at the minimums, which were the largest under the 75% FTP.

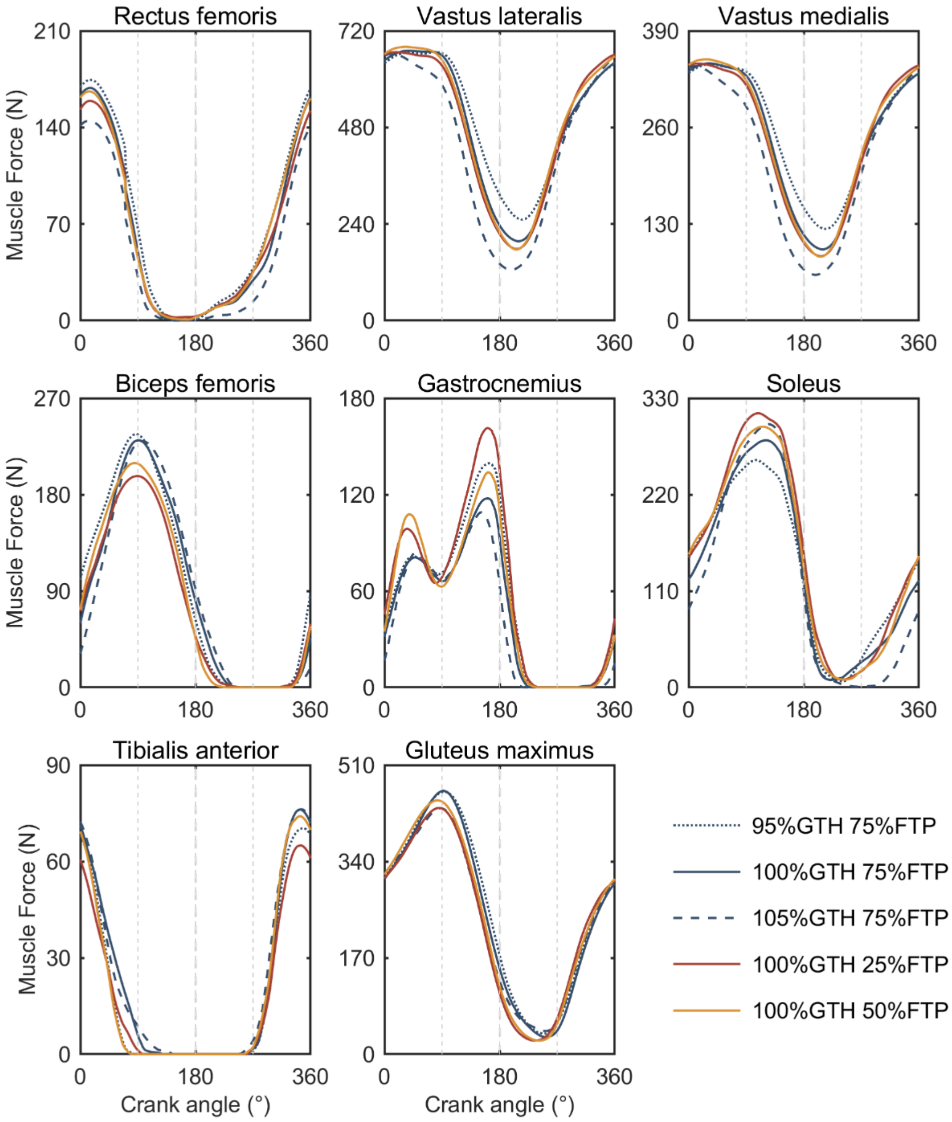

Figure 4.6 Muscle force envelopes of rectus femoris, vastus lateralis, vastus medialis, biceps femoris, gastrocnemius, soleus, tibialis anterior, and gluteus maximus under five riding conditions. FTP: functional threshold power.

The mean muscle forces under different cycling workloads are displayed in Figure 4.7. When the workload increased from 25% to 75% of FTP, the mean muscle forces of VL ($\beta = 0.018$, $p = 0.010$), VM ($\beta = 0.016$, $p = 0.017$), BF ($\beta = 0.119$, $p < 0.001$), TA ($\beta = 0.208$, $p = 0.010$), and GluMax ($\beta = 0.042$, $p < 0.001$) increased significantly, while those of GAS ($\beta = -0.268$, $p < 0.001$) and SOL ($\beta = -0.107$, $p = 0.001$) decreased by 11.0 N and 13.67 N, respectively. Among them, BF has the largest increment reaching 11.73%.

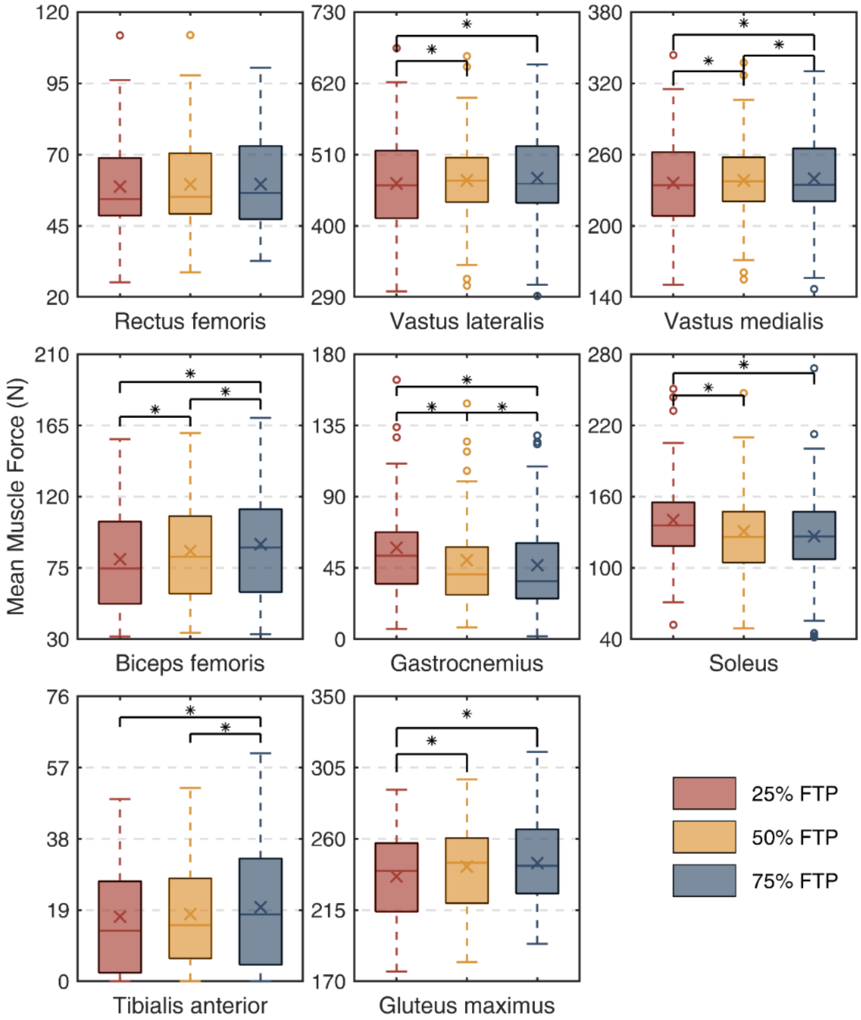

Figure 4.7 Mean muscle forces under the cycling workloads of 25%, 50%, and 75% of functional threshold power (FTP).

Figure 4.8 shows the maximum muscle force with different workloads. GEE analysis indicated that workload and saddle height had an interaction effect on the maximum muscle force of GluMax ($p = 0.004$), so their muscle forces were classified first to explore the effect of workload at a specific saddle height. The maximum RF muscle force was increased significantly only when the increment of workload reached 50% FTP ($\beta = 0.048$, $p = 0.006$). The pattern of maximum BF muscle force aligned with its average value, both demonstrating an upward trend as the workload became greater ($p \leq 0.038$). The maximum muscle forces of GAS ($\beta = -0.267$, $p < 0.001$) and SOL ($\beta = -0.087$, $p < 0.001$) reduced when the workload increased from 25% to 75% of FTP. For the GluMax muscle force, its maximum increased with the workload only with the saddle height of 100% GTH ($p < 0.001$).

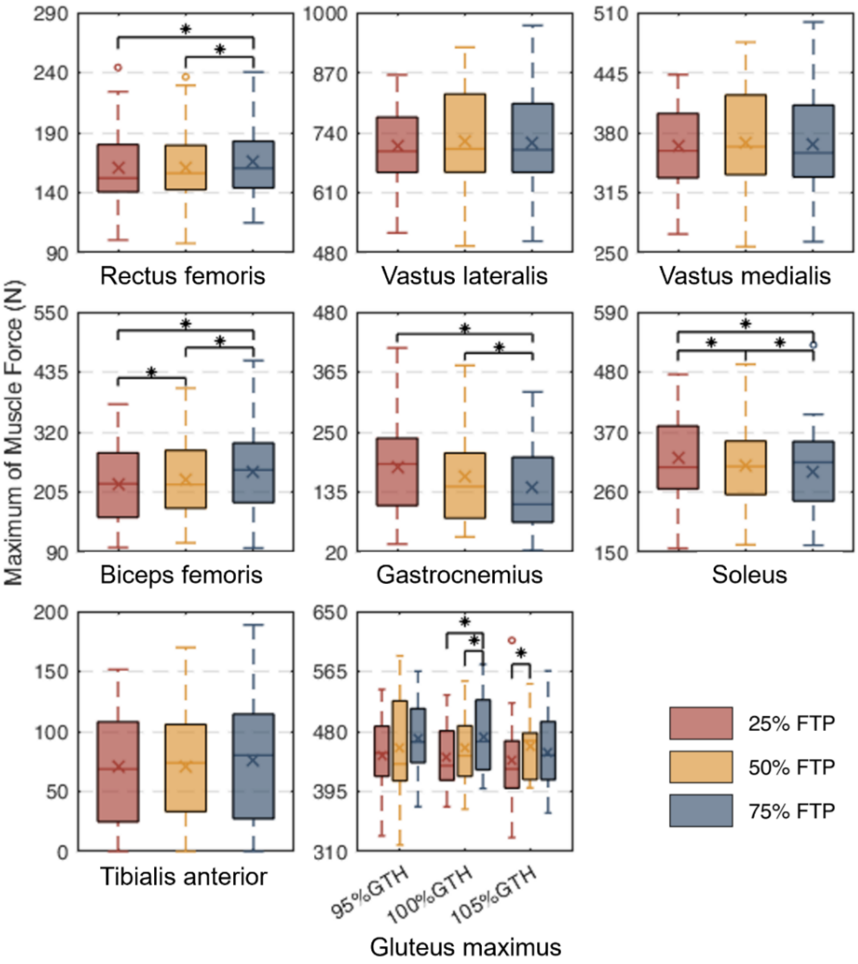

Figure 4.8 Maximum muscle forces under the cycling workloads of 25%, 50%, and 75% of functional threshold power (FTP).

Figure 4.9 shows the effect of saddle height on the means of lower-limb muscle forces. The muscle forces of RF, VL, VM, and GluMax showed a significant reduction with each 5% of GTH increase in saddle height. When the saddle height increased from 95% to 105% of GTH, the muscle forces of RF (β =-0.096, p < 0.001), VL (β =-0.032, p = 0.007), VM (β =-0.036, p = 0.003), GAS (β =-0.214, p = 0.026), and GluMax (β =-0.050, p < 0.001) decreased, while that of TA increased (β = 0.208, p = 0.010) by 32.96%.

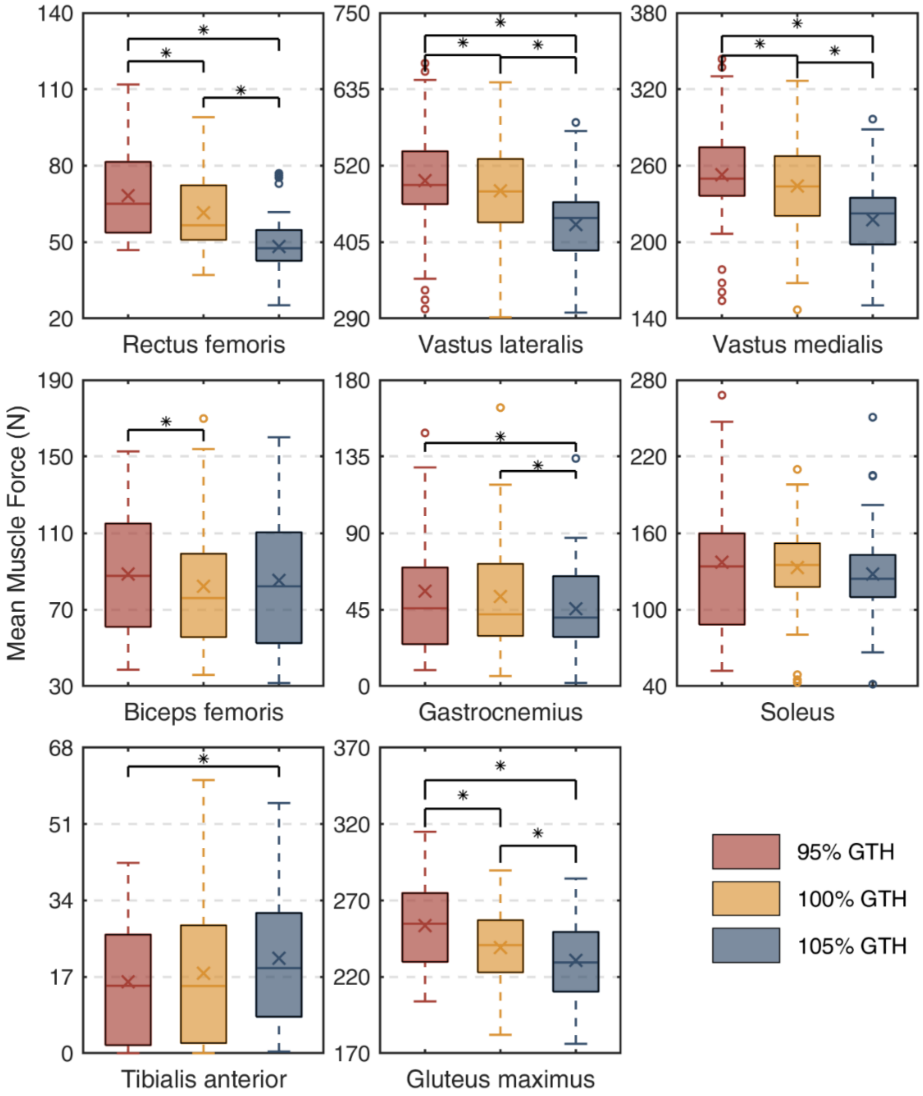

Figure 4.9 Mean muscle forces under the saddle height of 95%, 100%, and 105% of greater trochanter height (GTH).

Figure 4.10 displays the maximum of muscle forces influenced by saddle heights. The maximum of RF muscle force was declined as the saddle height raised by 10% of GTH (β = -0.158, $p < 0.001$). The maximum of VL and VM muscle forces, in contrast to their mean change, increased with the saddle height, but without statistical differences. The maximum SOL muscle force increased when the saddle height increased from 95% to 100% of GTH (β = 0.085, p = 0.003) and further to 105% of GTH (β = 0.136, $p < 0.001$). Because of the interaction effect of workload and saddle height on the maximum GluMax muscle force, it was analyzed under a specific workload. At the workload of 75% FTP, the maximum GluMax muscle force decreased when the saddle height increased from 100% to 105% of GTH.

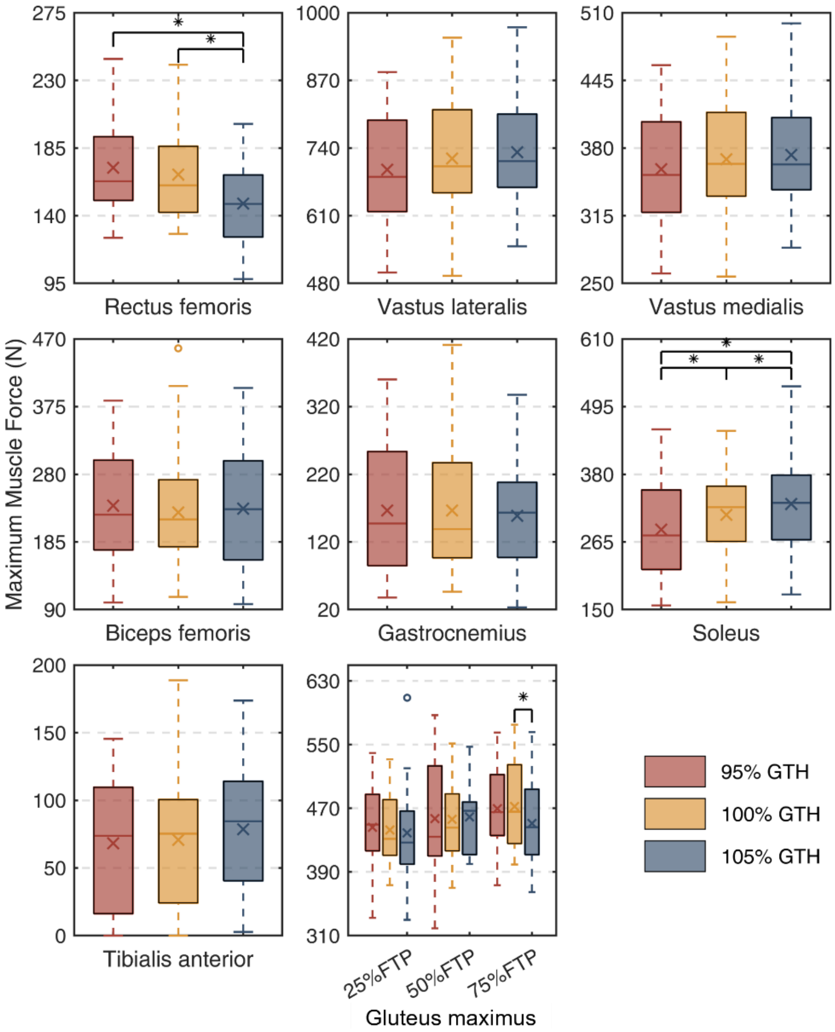

Figure 4.10 Maximum muscle forces under the saddle height of 95%, 100%, and 105% of greater trochanter height (GTH).

The GEE model suggested that cadence was a significant confounder for most measures of muscle forces. A higher cadence tended to result in greater muscle force. BMI was significantly associated with the forces of RF, BF, TA, and GluMax. Gender affected the muscle force of only BF. The detailed GEE analysis results of the effects of workload and saddle height on the muscle forces are seen in Appendix Table 1 and Table 2.

4.2.3 Joint contact forces

The influence of workload on the mean of joint contact forces is demonstrated in Figure 4.11. Only the mean of the hip forces showed significant changes in three directions. When the workload was improved to 75% FTP, the mean of M-L ($\beta = 0.043$, $p = 0.004$) and A-P ($\beta = 0.054$, $p = 0.024$) hip joint forces decreased, while its mean force in the P-D direction increased ($\beta = 0.052$, $p < 0.001$). The mean of resultant hip joint force also increased ($\beta = 0.051$, $p < 0.001$), since the force in the P-D direction was larger than that in the other two directions. GEE analysis suggested that there was an interaction effect of the workload and saddle height on the mean of M-L knee force, so it was compared in specific saddle height. At the saddle height of 95% GTH, the mean of M-L knee joint force showed an increasing trend with workload. The mean of P-D knee joint force declined as the workload increased to 75% FTP ($\beta = 0.065$, $p = 0.002$), and the mean of resultant knee joint force also increased ($\beta = 0.021$, $p = 0.026$). The absolute value of the mean ankle forces in P-D and A-P directions decreased with the increase of workload, resulting in the magnitude of the mean of the resultant ankle forces also reduced ($p \leq 0.010$). Figure 4.12 displays how the workload influenced the maximum joint forces. The maximum of hip joint forces in three directions increased with the increase of workload, leading to the maximum of the resultant hip joint force also increased ($p < 0.001$). There was no significant change in the maximum of the knee joint component force and only a slight increase in its resultant force ($\beta = 0.009$, $p = 0.546$). The maximum of ankle joint forces in the

P-D and A-P directions reduced as the workload increased from 25% to 75% of FTP, which in turn caused the resultant ankle joint force to decrease ($\beta = -0.082$, $p < 0.001$).

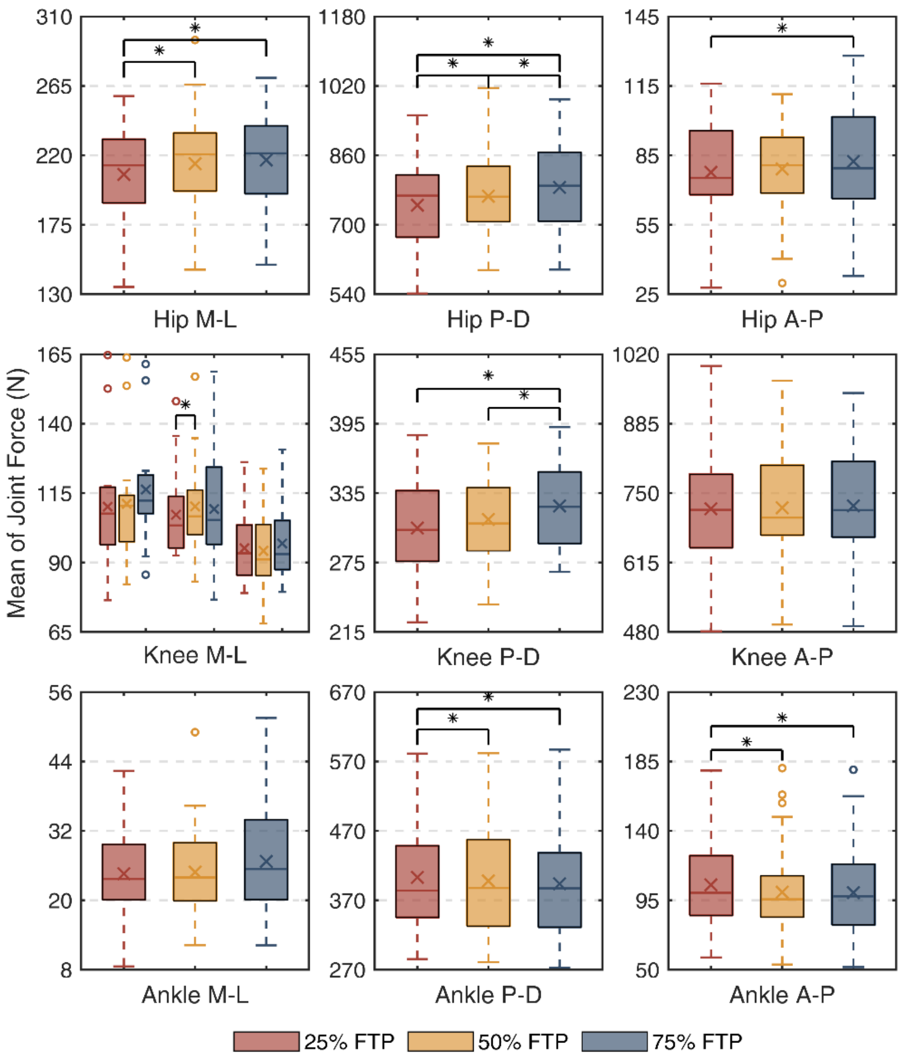

Figure 4.11 Mean joint forces of hip, knee, and ankle along the medial-lateral (M-L), proximal-distal (P-D), and anterior-posterior (A-P) directions with the cycling workloads of 25%, 50%, and 75% of functional threshold power (FTP).

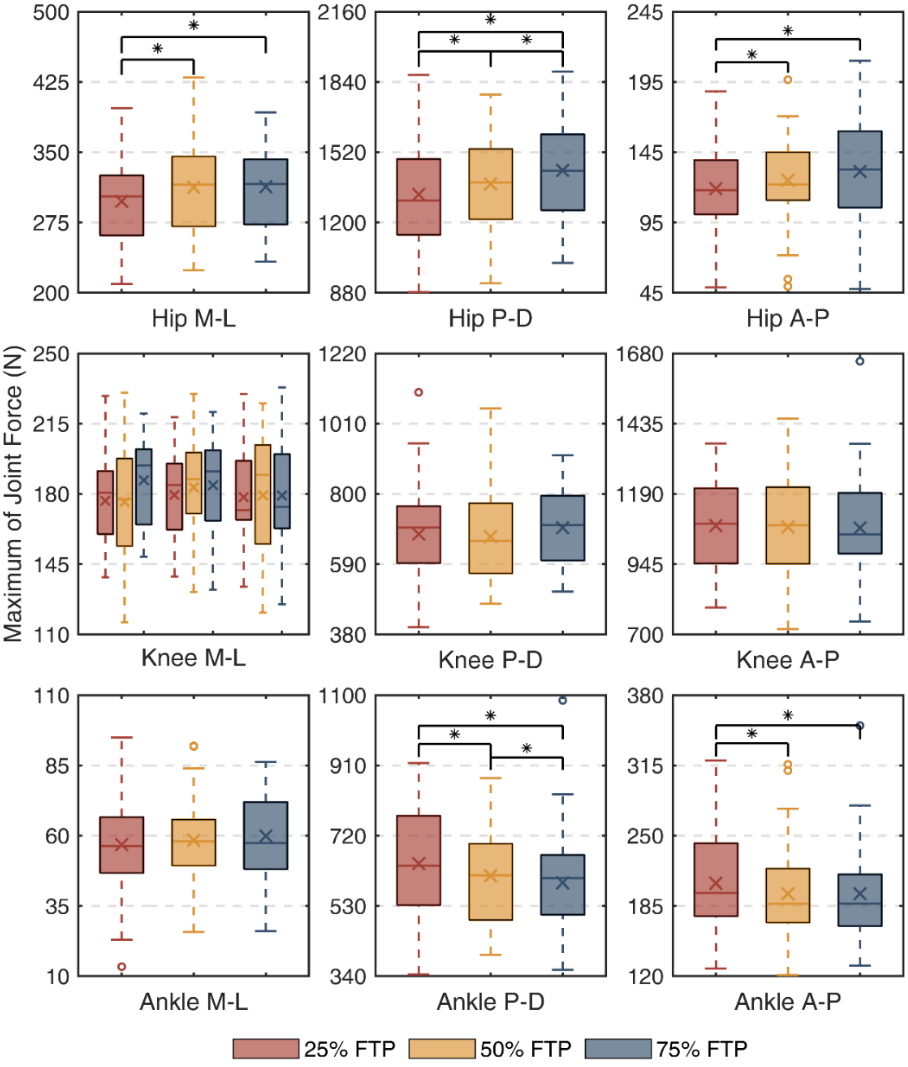

Figure 4.12 Maximum joint forces of hip, knee, and ankle along the medial and lateral (M-L), proximal-distal (P-D), and anterior-posterior (A-P) directions with the cycling workloads of 25%, 50%, and 75% of functional threshold power (FTP).

Figure 4.13 shows the mean of hip, knee, and ankle joint forces with various saddle heights. The magnitude of the mean of hip joint forces in the M-L ($p \leq 0.014$) and A-P ($p < 0.001$) directions decreased with every 5% increase in the saddle height. However, there was no significant change in the maximum of resultant hip joint force. The mean of M-L knee joint force was divided into three groups based on the workload because the two independent variables had an interaction effect on it. The mean of M-L knee joint force decreased with the increase of saddle height under any workload, especially when the saddle height reached 105% of GTH. At the same time, the absolute value of the mean of knee joint force increased in the P-D direction and decreased in the A-P direction. The mean of resultant knee joint force reduced ($\beta = -0.073$, $p < 0.001$) when the saddle height was raised to 105% GTH. The mean of ankle joint force in the M-L direction rose ($\beta = -0.211$, $p = 0.001$) while the force in the A-P direction dropped ($\beta = -0.227$, $p < 0.001$) as comparing the 105% GTH and 95% GTH cases. As shown in Figure 4.14, the maximum hip joint force in the A-P direction became smaller as the saddle height increased from 95% to 100% ($\beta = -0.064$, $p = 0.020$) and further to 105% ($\beta = -0.125$, $p < 0.001$) of GTH. The A-P knee joint force decreased only when the saddle height improved by 10% of GTH ($\beta = -0.070$, $p = 0.008$). Due to the interaction, the M-L knee joint forces were compared in three groups of three workload levels. When the workload was 75% of FTP, an increase of 10% GTH in saddle height resulted in a decrease of 13.13N in the maximum of M-L knee joint force. The maximum of the resultant knee joint force was only slightly reduced ($\beta = -0.009$, $p = 0.546$). The maximum ankle joint forces in the M-L ($\beta = -0.126$, $p = 0.045$) and A-P ($\beta = -0.089$, $p = 0.001$) directions were lower at the saddle height of 105% GTH compared to 95% GTH. The detailed GEE analysis results of the influence of workload and saddle height on the joint forces are seen in Appendix Table 3 and Table 4.

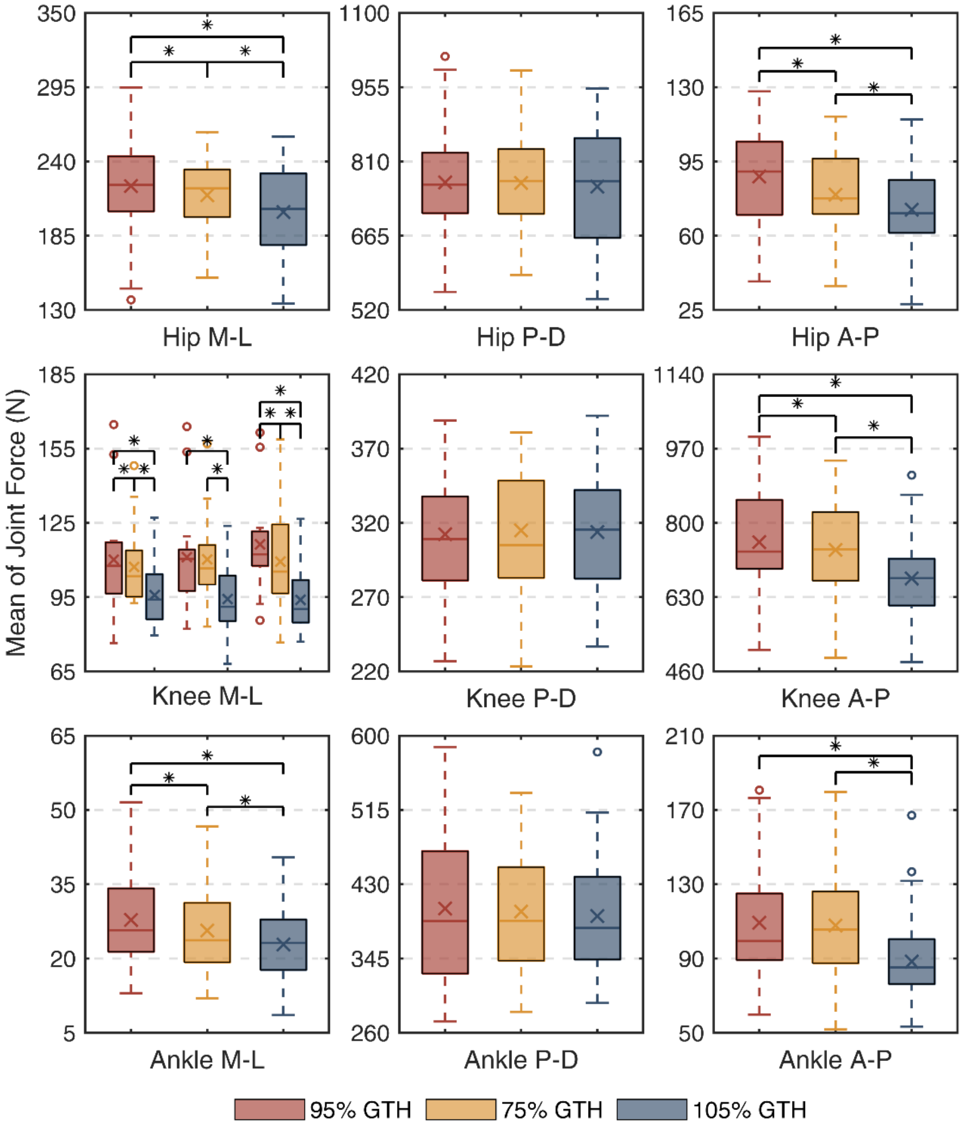

Figure 4.13 Mean of hip, knee, and ankle joint forces along the medial and lateral (M-L), proximal-distal (P-D), and anterior-posterior (A-P) directions with the saddle height of 95%, 100%, and 105% of greater trochanter height (GTH).

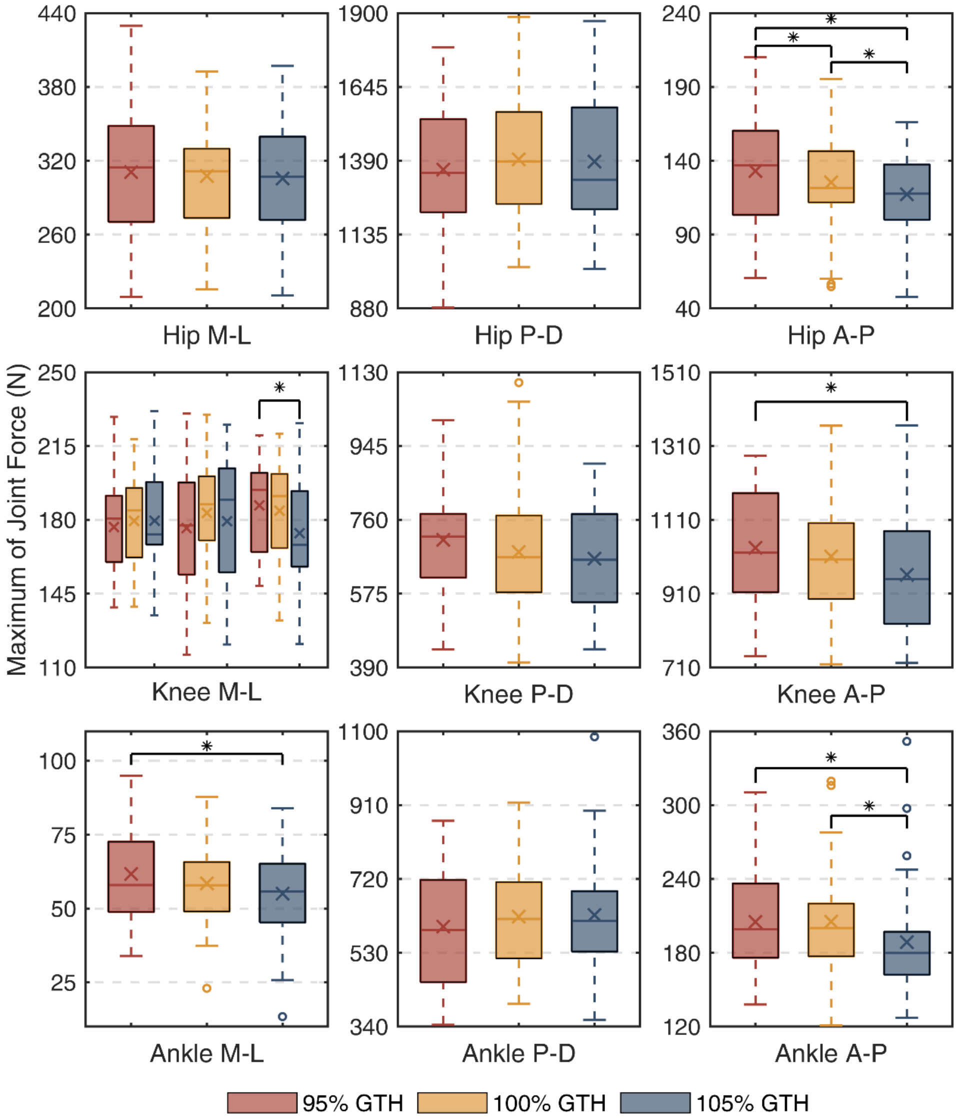

Figure 4.14 Maximum of hip, knee, and ankle joint forces along the medial and lateral (M-L), proximal-distal (P-D), and anterior-posterior (A-P) directions with the saddle height of 95%, 100%, and 105% of greater trochanter height (GTH).

4.3 Cycling Asymmetry

4.3.1 Pedal reaction forces

The asymmetry index of the PRF was assessed by the area integral of the force – crank angle curve. Figure 4.15 is an example of the pedal force curve with the saddle height of 100% GTH and the workload of 75% FTP. The red shaded part is the area integral interval of the left PRF, and the blue shaded part is that of the right side. Although the left and right PRFs of the Y-axis acted in opposite directions, the symmetry index did not consider the force direction.

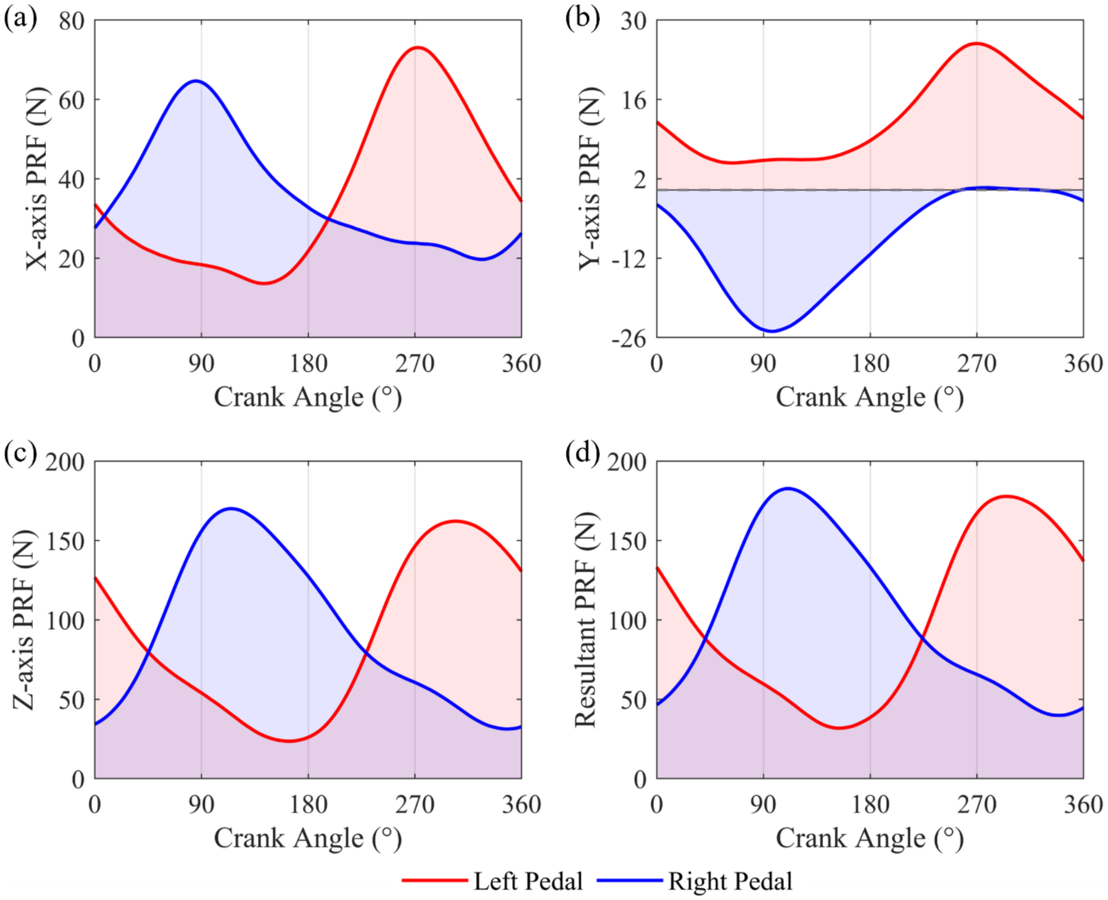

Figure 4.15 The left and right pedal reaction forces with the saddle height of 100% GTH and the workload of 75% FTP. (a) X-axis pedal reaction force (PRF); (b) Y-axis PRF; (c) Z-axis PRF; (d) resultant PRF. GTH: greater trochanter height; FTP: functional threshold power.

Figure 4.16 compares the ASIs under 15 riding conditions (5 saddle heights × 3 workload levels). The detailed ASIs are summarized in Table 4.6. The ASI of the Y-axis PRF was significantly larger than that of the X-axis and Z-axis PRFs. At the saddle height of 95%, 97%, and 105% of GTH, the ASI of X-axis PRF decreased with each 25% increase in workload. Regardless of the workload, the lowest ASI occurred under the 103% GTH case. The effect of workload on the ASI of the Y-axis PRF was consistent across all saddle height conditions, that is, as the workload raised, the ASI decreased. For example, its ASI declined from 64.15% to 27.84% when the workload increased from 25% to 75% of FTP at the saddle height of 95% GTH. When the workloads were 50% and 75% of FTP, the 103% GTH case had the smallest ASI of Y-axis PRF, which were 25.41% and 20.60%, respectively. But when the workload was 25% FTP, the smallest ASI of Y-axis PRF occurred in the case of 100% GTH. The ASI of the Z-axis PRF was lowest at the workload of 25% FTP, when the saddle heights were 95%, 103%, and 105% of GTH. However, when the workload was constant, the influence of saddle height on the Z-axis ASI had no uniform trend. As for the resultant PRF, when the workload increased, its ASI reduced at the saddle height of 95% and 97% of GTH but raised at 103% and 105% of GTH. When the workloads were fixed at 25%, 50%, and 75% of FTP, the smallest ASI of resultant PRF occurred at the saddle heights of 103%, 100%, and 97% of GTH, respectively. Considering all 15 riding conditions, the ASIs of both the Z-axis and resultant PRFs were minimized at 50% FTP and 100% GTH cases, about 3.68% and 1.01%.

Table 4.6 Asymmetry index of the left and right pedal reaction forces

Saddle height (%GTH)	Workload (%FTP)	X-axis PRF	Y-axis PRF	Z-axis PRF	Resultant PRF
95	25	12.76%	64.15%	8.10%	7.05%
	50	6.24%	50.46%	8.39%	5.80%
	75	2.63%	27.84%	8.36%	4.26%
97	25	14.80	61.84%	6.82%	5.69%
	50	7.90%	43.49%	11.09%	5.59%
	75	4.75%	31.79%	5.32%	3.74%
100	25	2.52%	56.70%	5.45%	3.05%
	50	6.22%	33.34%	3.68%	1.01%
	75	0.33%	29.14%	6.26%	4.23%
103	25	0.74%	59.07%	5.66%	2.83%
	50	0.41%	25.41%	6.57%	4.07%

	75	0.61%	20.60%	9.76%	5.73%
105	25	11.90%	57.61%	5.36%	4.16%
	50	11.56%	56.70%	7.18%	4.96%
	75	11.16%	32.76%	9.91%	7.64%

PRF: pedal reaction forces; GTH: greater trochanter height; FTP: functional threshold power.

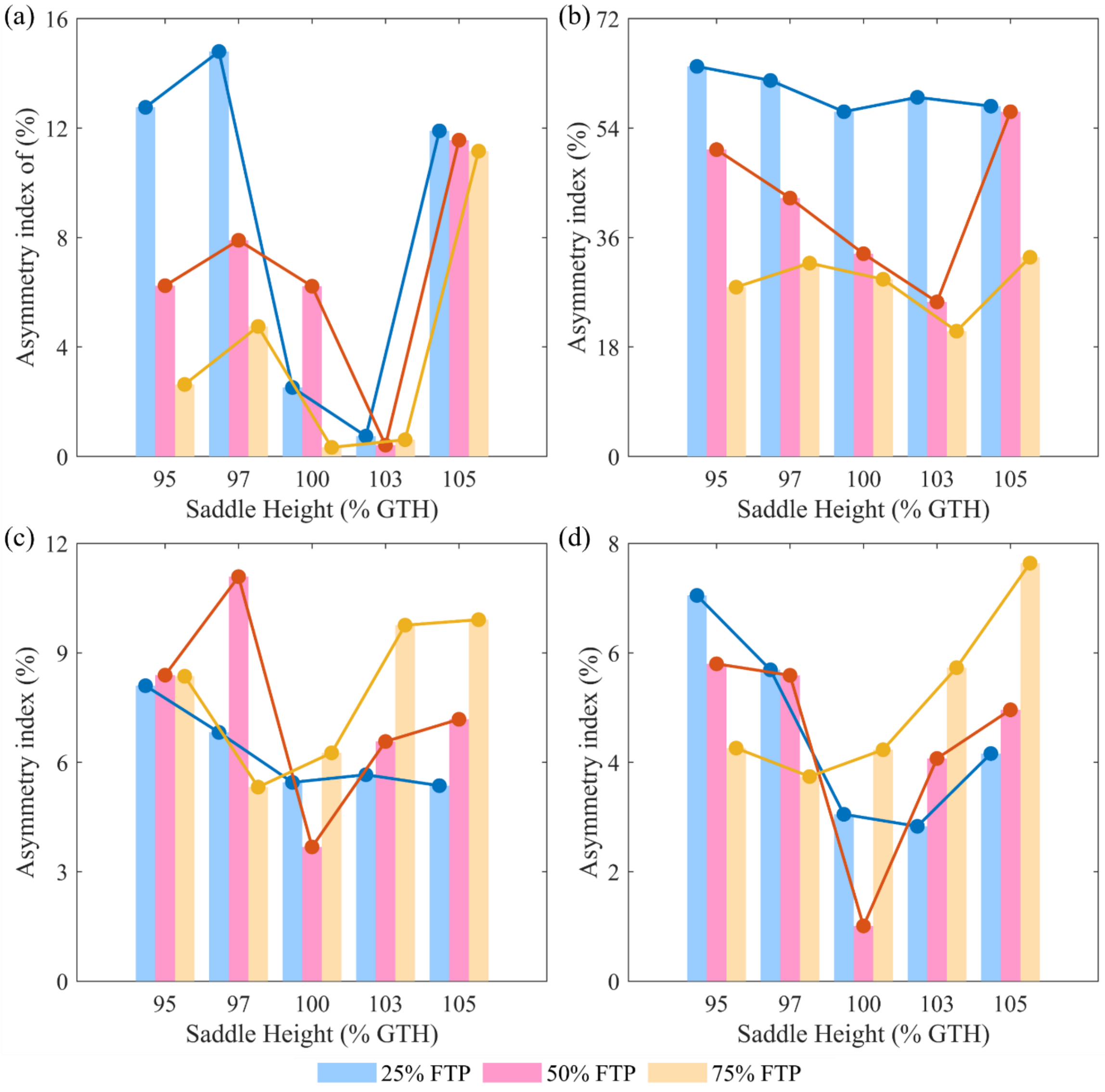

Figure 4.16 Asymmetry index of pedal reaction forces under five saddle heights (95%, 97%, 100%, 103%, and 105% of GTH) and three workloads (25%, 50%, and 75% of FTP). (a) X-axis pedal reaction force (PRF); (b) Y-axis PRF; (c) Z-axis PRF; (d) resultant PRF. GTH: greater trochanter height; FTP: functional threshold power.

4.3.2 Lower-limb joint angles

The effects of saddle height and workload on the ASIs of hip, knee, and ankle joint angles are demonstrated in Figure 4.17. Because the cycling motion mainly occurred in the sagittal plane of the human body, only the flexion-extension joint angles were compared. Table 4.7 lists the specific values of ASI of lower-limb joint angles. The ASIs of ankle joint angles were much larger than that of hip and knee joint angles which ranged from 26.88% to 42.58%. The effect of workload on the ASIs of three lower-limb joint angles was small and without a consistent changing trend. Both the ASIs of hip and ankle joint angles were minimum at the saddle height of 105% GTH, however they did not change consistently as the saddle height increased. The ASI of the hip joint angle was 2.58%, 2.15%, and 2.88% when the workload was 25%, 50%, and 75% of FTP, respectively, and the ASI of the ankle joint angle was 32.42%, 26.88%, and 34.56% at the corresponding workloads. The ASI of the knee joint angle basically increased with the saddle height, except for the case where the saddle height was 97% GTH and the workload was 75% FTP. The maximum ASI of knee joint angle was 1.25%, 1.24%, and 1.12% at the saddle height of 105% GTH, and its minimum value was 0.55%, 0.58%, and 0.69% at the saddle height of 95% GTH, when the workload was 25%, 50%, and 75% of FTP, respectively.

Table 4.7 Asymmetry index of hip, knee, and ankle flexion joint angles

Saddle height (%GTH)	Workload (%FTP)	Hip flexion	Knee flexion	Ankle plantar flexion
95	25	3.42%	0.55%	39.76%
	50	3.70%	0.58%	37.26%
	75	3.31%	0.69%	38.98%
97	25	2.88%	0.55%	34.13%
	50	2.86%	0.72%	32.87%
	75	2.52%	0.48%	33.96%

100	25	3.34%	0.82%	40.93%
	50	3.74%	0.77%	42.58%
	75	2.92%	0.79%	37.51%
103	25	3.08%	0.84%	34.79%
	50	2.98%	0.68%	37.47%
	75	3.08%	0.87%	35.91%
105	25	2.58%	1.25%	32.42%
	50	2.15%	1.24%	26.88%
	75	2.88%	1.12%	34.56%

GTH: greater trochanter height; FTP: functional threshold power.

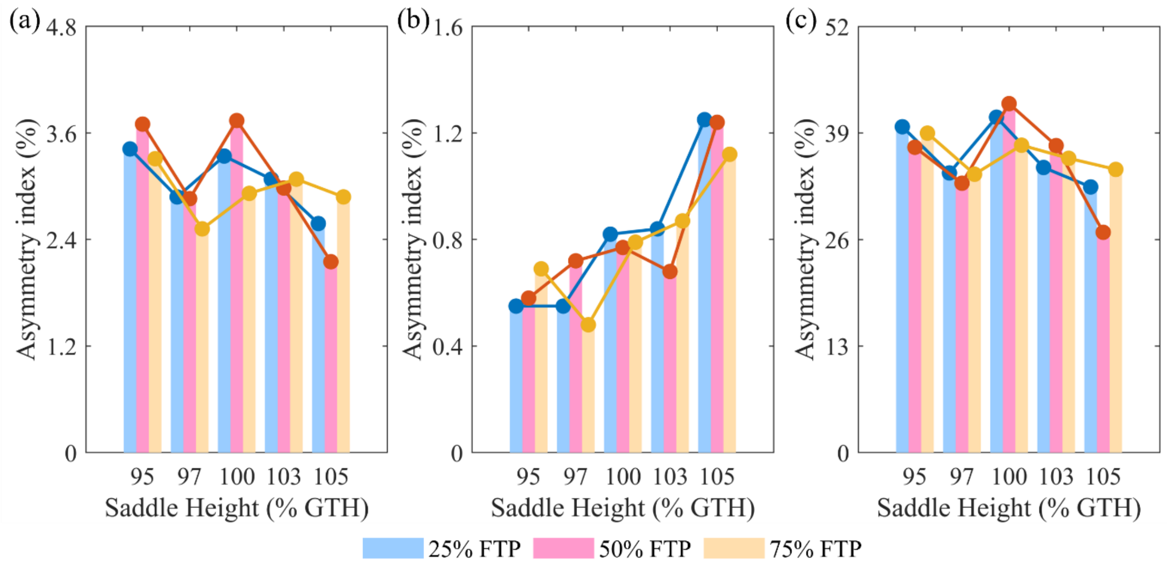

Figure 4.17 Asymmetry index of the joint angles under five saddle heights (95%, 97%, 100%, 103%, and 105% of GTH) and three workloads (25%, 50%, and 75% of FTP). (a) Hip flexion angles; (b) knee flexion angles; (c) ankle plantar flexion angles. GTH: greater trochanter height; FTP: functional threshold power.

4.3.3 Muscle activations

Figure 4.18 shows the ASIs of the integral area of muscle activation curves for the same muscles on the left and right sides under various riding conditions. The detailed ASIs are summarized in Table 4.8. Regardless of workload level, the ASI of BF activation was highest at the saddle height of 100% GTH (Figure 4.18 (a)). For workloads of 50% and 75% of FTP, the smallest ASIs of BF occurred at saddle heights of 95% GTH, which were 3.36% and 5.51%, respectively. When the cyclist maintained a power output corresponding to 25% of FTP, the most symmetric pedaling motion was achieved at a saddle height of 97% GTH, as evidenced by the minimal ASI of 0.60%. While for saddle heights of both 95% and 97% GTH, greater workloads resulted in higher ASI values, showing greater asymmetry in pedal strokes. For activation of the GAS muscle, the same regularity happened only in the 95% GTH case (Figure 4.18 (b)). When the saddle height was 100% and 103% of GTH, the ASI of GAS even declined with a greater workload. The ASI of GAS activation was minimum at 105% GTH as the workload was 25% and 75% of FTP, about 4.78% and 4.41% respectively. It was minimum at 97% GTH about 8.60%, when the workload was 50% FTP. The ASI of RF activation ranged from 0.70% to 14.32% (Figure 4.18 (c)). At saddle heights of 95% and 97% GTH, its ASI diminished as the workload increased. Conversely, the most symmetrical performance with the smallest ASI was observed at a saddle height of 100% GTH paired with a workload of 75% FTP and at 103% GTH with workloads ranging from 25% to 50% FTP. For the TA, its ASI was smallest at 95% GTH × 50% FTP about 0.76%, and largest at 100% GTH × 50% FTP about 20.49% (Figure 4.2.13 (d)). When the workload was 25% and 75% of FTP, the ASI of TA activation was minimum at 105% GTH about 0.81% and 2.50%, respectively.

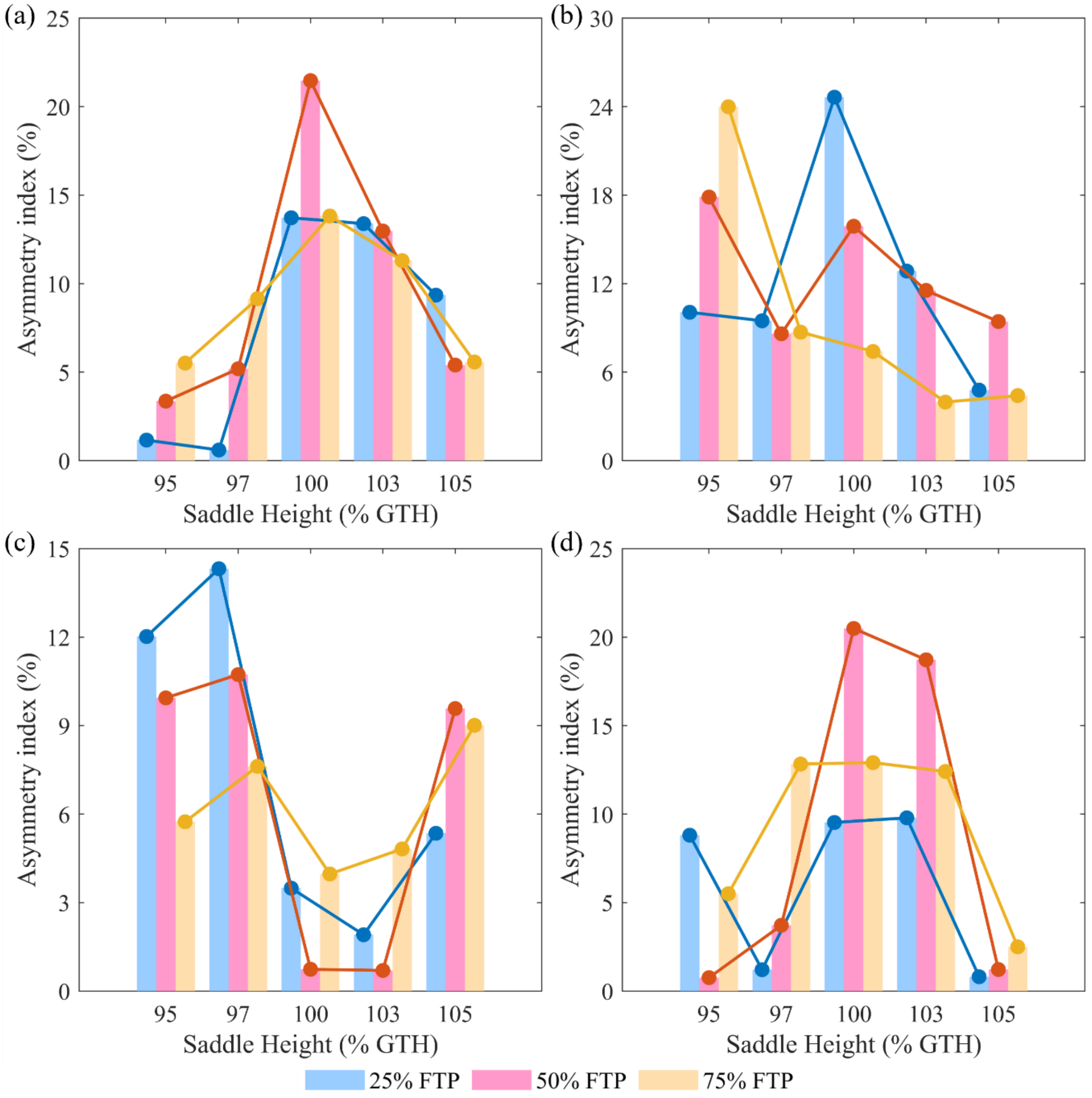

Figure 4.18 Asymmetry index of muscle activations under five saddle heights (95%, 97%, 100%, 103%, and 105% of GTH) and three workloads (25%, 50%, and 75% of FTP). (a) Biceps femoris; (b) gastrocnemius; (c) rectus femoris; (d) tibialis anterior. GTH: greater trochanter height; FTP: functional threshold power.

Table 4.8 Asymmetry index of muscle activations

Saddle height (%GTH)	Workload (%FTP)	Biceps femoris	Gastrocnemius	Rectus femoris	Tibialis anterior
95	25	1.16%	10.06%	12.02%	8.81%
	50	3.36%	17.87%	9.94%	0.76%

	75	5.51%	23.99%	5.74%	5.50%
97	25	0.60%	9.48%	14.32%	1.21%
	50	5.19%	8.60%	10.73%	3.72%
	75	9.15%	8.71%	7.62%	12.83%
100	25	13.72%	24.64%	3.49%	9.53%
	50	21.47%	15.89%	0.74%	20.49%
	75	13.82%	7.40%	3.97%	12.91%
103	25	13.39%	12.85%	1.91%	9.79%
	50	12.97%	11.54%	0.70%	18.72%
	75	11.30%	3.97%	4.82%	12.41%
105	25	9.35%	4.78%	5.35%	0.81%
	50	5.40%	9.43%	9.58%	1.22%
	75	5.57%	4.41%	9.01%	2.50%

GTH: greater trochanter height; FTP: functional threshold power.

4.4 Results of Finite Element Analysis

4.4.1 Stress and strain

The Mises stress nephograms in Figures 4.19 and 4.20 illustrate the stress distribution and stress concentration region of the femoral cartilage, tibial cartilage, and menisci during knee extension under three saddle heights (95%, 100%, and 105% of GTH). Figure 4.19 displayed the above calculated stress distribution when the crank angle was 90°. The stress was primarily localized at specific regions of the cartilages and menisci. For the saddle height of 95% GTH (Figure 4.19 (a) - (c)), stress concentration was higher and more pronounced, especially in regions near the contact interfaces between the cartilages and menisci. In comparison, the saddle heights of 100% GTH (Figure 4.19 (d) - (f)) and 105% GTH (Figure 4.19 (g) - (i)) exhibited a slightly more uniform stress distribution, with reduced peak stress. The overall color distribution suggested that the regions of high stress in Figure 4.19 (a) -(c) are also larger than those in Figure 4.19 (d) to (i).

Figure 4.20 is the results of stress distribution at a crank angle of 180°. The overall stress level was reduced compared to that at the crank angle of 90° in Figure 4.19. Similarly, the saddle height of 95% GTH (Figure 4.20 (a) - (c)) again displayed higher stress concentrations compared to the saddle heights of 100% and 105% of GTH (Figure 4.20 (d) - (i)), which showed a more evenly distributed stress profile. Notably, across both figures, the menisci had a relatively gradual stress gradient, while the femoral and tibial cartilages exhibited sharper localized stress peaks.

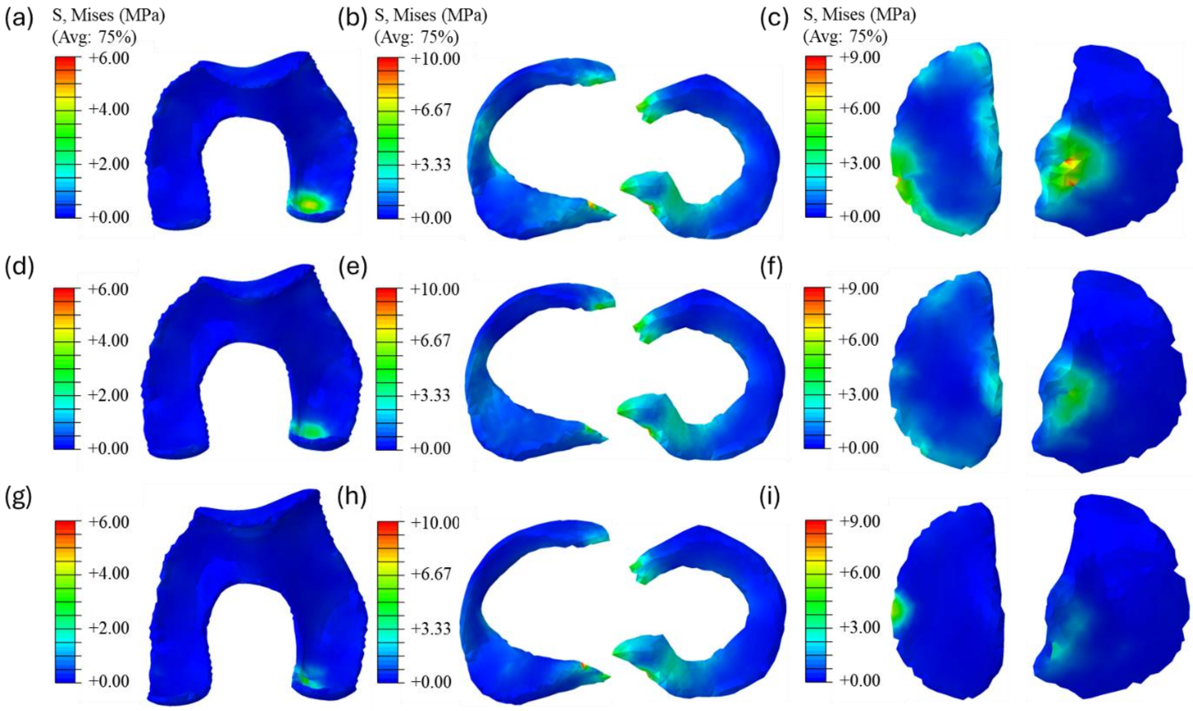

Figure 4.19 Mises stress nephogram of cartilage and menisci at a crank angle of 90°. With the saddle height of 95% GTH, the Mises stress of (a) femur cartilage, (b) menisci, and (c) tibia cartilage; with the saddle height of 100% GTH, the Mises stress of (d) femur cartilage, (e) menisci, and (f) tibia cartilage; with the saddle height of 105% GTH, the Mises stress of (g) femur cartilage, (h) menisci, and (i) tibia cartilage.

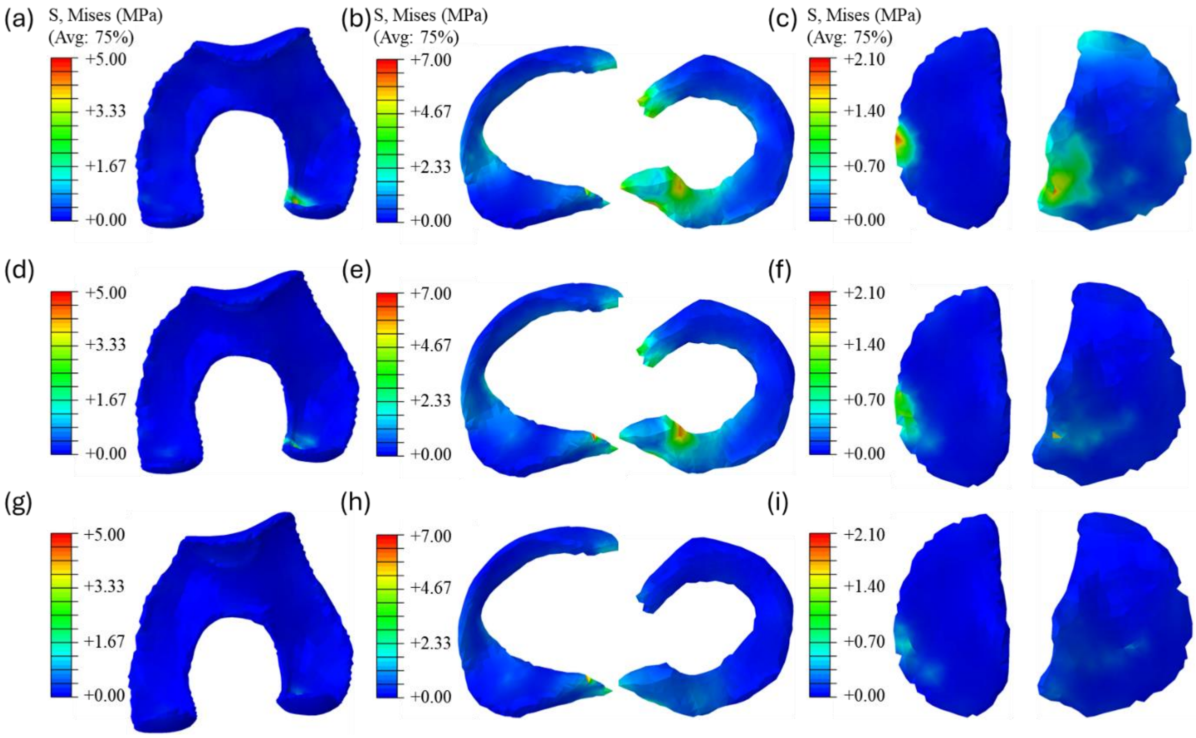

Figure 4.20 Mises stress nephogram of cartilage and menisci at a crank angle of 180°. With the saddle height of 95% GTH, the Mises stress of (a) femur cartilage, (b) menisci, and (c) tibia cartilage; with the saddle height of 100% GTH, the Mises stress of (d) femur cartilage, (e) menisci, and (f) tibia cartilage; with the saddle height of 105% GTH, the Mises stress of (g) femur cartilage, (h) menisci, and (i) tibia cartilage.

The FE results of knee joint during cycling under varying saddle heights (95%, 100%, and 105% GTH) are detailed in Tables 4.9, 4.10, and 4.11, including Mises stress, Max principal stress, Min principal stress, Max principal LE, SENER, and CPRESS.

For the femoral cartilage (Table 4.9), the maximum Mises stress showed a decreasing trend with increasing saddle height, dropping from 11.637 MPa at the saddle height of 95% GTH to 9.204 MPa at 100% GTH, and further to 5.30 MPa at 105% GTH. The corresponding mean value of stress also gradually decreased from 0.208 MPa at 95% GTH to 0.08 MPa at 105% GTH. Associated with the maximum value, the averaged stress range was reduced from 0.450

MPa to 0.206 MPa. The Max principal stress is the maximum tensile stress at a specific point of part where the normal stress is largest and the shear stress is zero. The maximum of Max principal stress of femoral cartilage was drastically reduced from 14.265 MPa at 95% GTH to 2.90 MPa at 105% GTH. Its mean value also declined by 44.4%. The Min principal stress is the maximum compressive stress which is generally negative. Similarly, the mean of Min principal stress of femoral cartilage gradually decreased with each 5% elevation in saddle height. However, its maximum of absolute Min principal stress at the saddle height of 100% GTH was the largest (-24.365 MPa) which was slightly larger than that at 95% GTH. Related to Max principal stress, Max principal LE reflects the tensile deformation under normal physiological loading. When the saddle was raised by 10% GTH, the maximum and mean values of Max principal LE decreased 0.261 MPa and 0.005 MPa, respectively.

Table 4.9 Biomechanical variables related to stress and strain of femoral cartilage

Variables	Conditions	Maximum	Mean	Averaged Range	Averaged SD
Mises stress (MPa)	95% GTH	11.637	0.208	0.450	0.102
	100% GTH	9.204	0.138	0.344	0.076
	105% GTH	5.30	0.08	0.206	0.049
Max principal stress (MPa)	95% GTH	14.265	0.045	0.705	0.139
	100% GTH	11.706	0.038	0.51	0.095
	105% GTH	2.90	0.025	0.246	0.053
Min principal stress (MPa)	95% GTH	-24.365	-0.188	0.773	0.165
	100% GTH	-20.711	-0.118	0.558	0.113
	105% GTH	-11.376	-0.065	0.291	0.069
Max principal LE	95% GTH	0.452	0.008	0.02	0.004
	100% GTH	0.341	0.005	0.015	0.003
	105% GTH	0.191	0.003	0.009	0.002

For the menisci (Table 4.10), the maximum of Mises stress and absolute Min principal stress increased with the increase of saddle height, but their mean values decreased. The maximum and mean values of Max principal stress consistently decreased by 24.69% and 33.94%, respectively, with the elevation of saddle height by 10% GTH.

Table 4.10 Biomechanical variables related to stress and strain of menisci

Variables	Conditions	Maximum	Mean	Averaged Range	Averaged SD
Mises stress (MPa)	95% GTH	8.582	1.637	1.934	0.397
	100% GTH	9.553	1.42	1.903	0.436
	105% GTH	10.523	1.050	1.467	0.380
Max principal stress (MPa)	95% GTH	15.416	0.878	1.521	0.297
	100% GTH	14.301	0.760	1.369	0.291
	105% GTH	9.141	0.580	0.915	0.234
Min principal stress (MPa)	95% GTH	-23.268	-0.927	1.399	0.279
	100% GTH	-26.657	-0.801	1.360	0.298
	105% GTH	-26.927	-0.570	0.956	0.243
Max principal LE	95% GTH	0.795	0.020	0.026	0.005
	100% GTH	0.546	0.017	0.024	0.005
	105% GTH	0.385	0.012	0.017	0.004

For the tibial cartilage (Table 4.11), the maximum Mises stress ranged from 3.822 MPa at the saddle height of 105% GTH to 12.030 MPa at 95% GTH. Its mean values ranged from 0.071 MPa at 105% GTH to 0.291 MPa at 95% GTH, reflecting a similar pattern of stress reduction with increased saddle height. Compared with the condition of 95% GTH, the maximum and mean values of the Max principal stress of tibial cartilage reduced only slightly at 100% GTH, and decreased sharply to the maximum of 2.080 MPa and mean of 0.010 MPa when the saddle height increased to 105% GTH. The decreasing trend of absolute Min principal stress of tibial cartilage was more uniform. Its absolute maximum and mean were 19.122 MPa and -0.308 MPa at 95% GTH, and 7.550 MPa and -0.069 MPa at 105% GTH. As for the strain of tibial cartilage, the Max principal LE declined progressively as the saddle increased.

These results suggested that increasing the saddle height reduced the magnitude of stress and strain within the cartilages and menisci.

Table 4.11 Biomechanical variables related to stress and strain of tibia cartilage

Variables	Conditions	Maximum	Mean	Averaged Range	Averaged SD
Mises stress (MPa)	95% GTH	12.030	0.291	0.638	0.157
	100% GTH	7.718	0.156	0.486	0.121
	105% GTH	3.822	0.071	0.207	0.050
Max principal stress (MPa)	95% GTH	8.587	0.019	0.887	0.180
	100% GTH	7.669	0.018	0.598	0.114
	105% GTH	2.080	0.010	0.227	0.048
Min principal stress (MPa)	95% GTH	-19.122	-0.308	1.085	0.253
	100% GTH	-11.160	-0.154	0.731	0.163
	105% GTH	-7.550	-0.069	0.301	0.070
Max principal LE	95% GTH	0.391	0.011	0.025	0.006
	100% GTH	0.260	0.006	0.020	0.005
	105% GTH	0.133	0.003	0.008	0.002

4.4.2 Contact pressure and area

Two types of contact surfaces were set between the menisci and femoral cartilage and between the menisci and tibial cartilage. Figure 4.21 (a)-(c) compare the mean CPRESS of cartilages and menisci under riding conditions of three saddle heights. Figure 4.21 (d)-(f) show the averaged range of CPRESS. Each of these figures exhibits a consistent pattern: as the saddle height increased from 95% GTH up to 100% and further to 105% GTH, there was a noticeable decrease in the ranges of CPRESS recorded. Among them, tibial cartilage had the largest reduction in the mean value, from 0.216 MPa to 0.041 MPa. The mean CPRESS of femoral cartilage and menisci decreased by 0.046 MPa and 0.061 MPa, respectively. Additionally, the maximum CPRESS of tibial cartilage peaked at 95% GTH about 13.378 MPa, and decreased to 5.813 MPa when the saddle height increased to 105% GTH. The maximum CPRESS of menisci decreased even more about 25.88 MPa, and that of femoral cartilage reduced by 14.609 MPa, as the saddle height increased by 10% GTH. The detailed results of CPRESS of cartilages and menisci are summarized in Table 4.12.

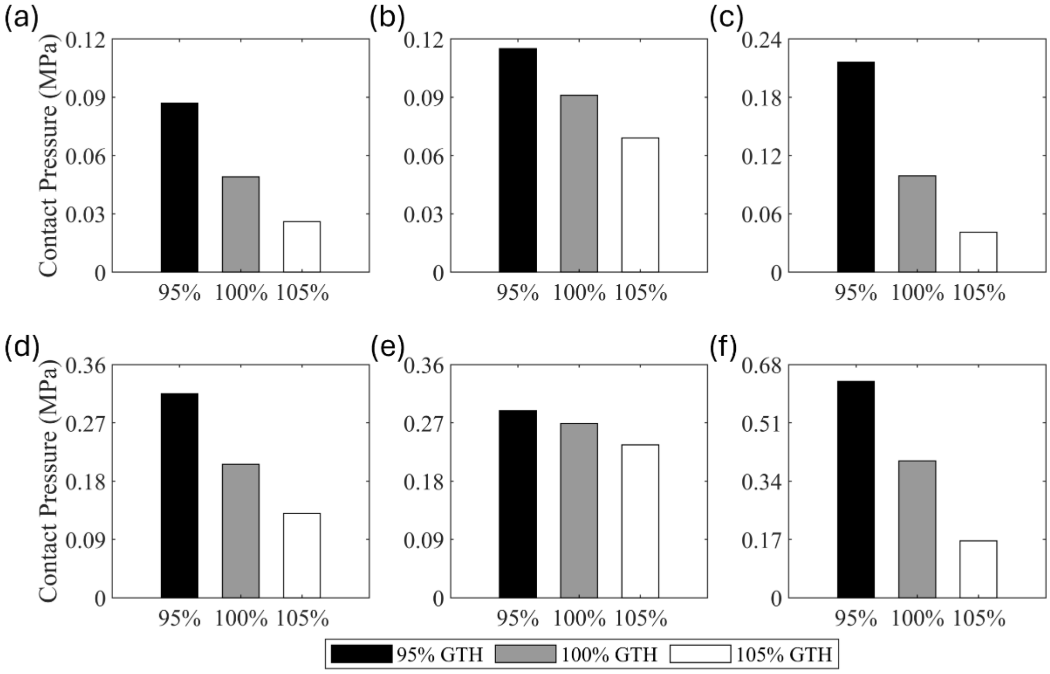

Figure 4.21 Mean and range of contact pressure of cartilages and menisci under three riding conditions. The mean contact pressure of (a) femoral cartilage, (b) menisci, and (c) tibia cartilage. Averaged range of contact pressure of (d) femoral cartilage, (e) menisci, and (f) tibia cartilage.

Table 4.12 The maximum, mean, average range, and average standard deviation (SD) of contact pressure (MPa) of cartilages and menisci.

Parts	Conditions	Maximum	Mean	Average Range	Average SD
Femoral cartilage	95% GTH	26.021	0.087	0.315	0.093
	100% GTH	17.566	0.049	0.206	0.062
	105% GTH	11.412	0.026	0.13	0.039
Menisci	95% GTH	36.047	0.115	0.289	0.067
	100% GTH	16.415	0.091	0.269	0.069
	105% GTH	10.167	0.069	0.236	0.063

Tibia cartilage	95% GTH	13.378	0.216	0.631	0.183
	100% GTH	8.863	0.099	0.399	0.111
	105% GTH	5.813	0.041	0.166	0.046

The contact area (CAREA) depends on the distribution of loads across the menisci and cartilages. The means and averaged ranges of CAREA were compared in Figure 4.22. The detailed results are summarized in Table 4.13. For the CAREA between femoral cartilage and menisci, either the mean or range did not show a uniform variation pattern with the increase in saddle height. Its mean value was maximum at the saddle height of 100% GTH about 137.023 mm^2, while the maximum average range occurred at 95% GTH. The mean of CAREA between tibial cartilage and menisci decreased from 168.214 mm^2 at the saddle height of 95% GTH to 165.666 mm^2 (100% GTH) and 162.034 mm^2 (105% GTH). The average range of CAREA between tibial cartilage and menisci was maximum at 95%GTH about 90.875 mm^2, and minimum at 100% GTH about 69.407 mm^2.

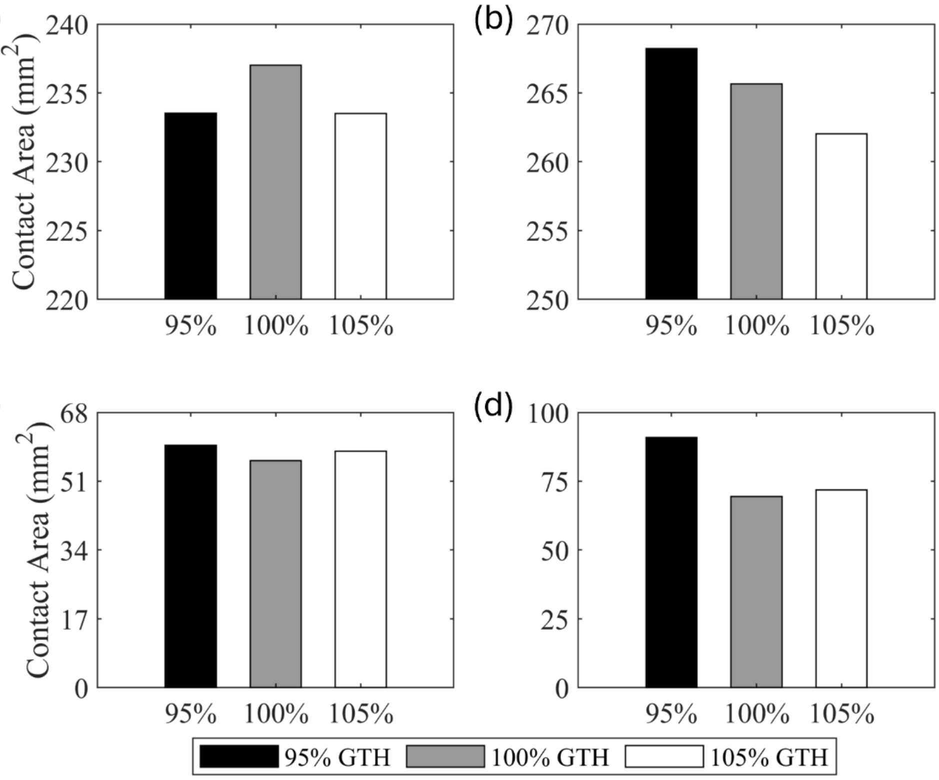

Figure 4.22 Mean and range of contact area of cartilages and menisci under three riding conditions. Mean of contact area (a) between femoral cartilage and menisci and (b) between tibia cartilage and menisci. The averaged range of contact area (c) between femoral cartilage and menisci and (d) between tibia cartilage and menisci.

Table 4.13 The maximum, mean, average range, and average standard deviation (SD) of contact area (mm^2) between cartilages and menisci

CAREA	Conditions	Maximum	Mean	Average Range	Average SD
Femur cartilage-	95% GTH	267.374	233.531	59.848	9.432
Menisci	100% GTH	264.497	237.023	56.087	10.884
	105% GTH	258.981	233.505	58.393	15.655
Tibia cartilage-	95% GTH	321.317	268.214	90.875	15.832
Menisci	100% GTH	304.435	265.666	69.407	12.283
	105% GTH	294.383	262.034	71.851	16.554

4.5 Machine Learning Results of Saddle Height Classification

4.5.1 Statistical results and classification accuracy of single feature

SVM model

By the forward sequential feature selection and five-fold cross validation, twenty features were selected for SVM model. Among them, nine features were related to hip joint angles ($\theta_{x,RMS}$, $\theta_{x,Range}$, $\theta_{y,RMS}$, $\theta_{y,Mean}$, $\theta_{y,Range}$, $\theta_{z,RMS}$, $\theta_{z,Mean}$, $\theta_{z,SD}$, and $\theta_{z,CV}$). Six features were identified from knee joint angles ($\theta_{x,Max}$, $\theta_{x,Min\ timing}$, $\theta_{x,RMS}$, $\theta_{y,Min}$, $\theta_{y,CV}$, and $\theta_{z,Max}$) and five features were extracted from ankle joint angles ($\theta_{x,Max}$, $\theta_{y,RMS}$, $\theta_{y,CV}$, $\theta_{z,Min}$, and $\theta_{z,CV}$). Figure 4.23 illustrates the statistical differences of selected features among three riding conditions for SVM model. Because most data did not satisfy normal distribution or homogeneity of variance, Kruskal-Wallis test was used. Among the selected features, RMS and CV types accounted for the largest proportion, totaling to nine. When the results of three groups were compared pairwise, all the features indicated significant differences ($p < 0.001$) in at least one pair. The $\theta_{x,Max}$ and $\theta_{x,RMS}$ of knee joint angle had a clear tendency to decrease with the saddle elevation, while $\theta_{x,Min\ timing}$ of knee joint angle increased significantly.

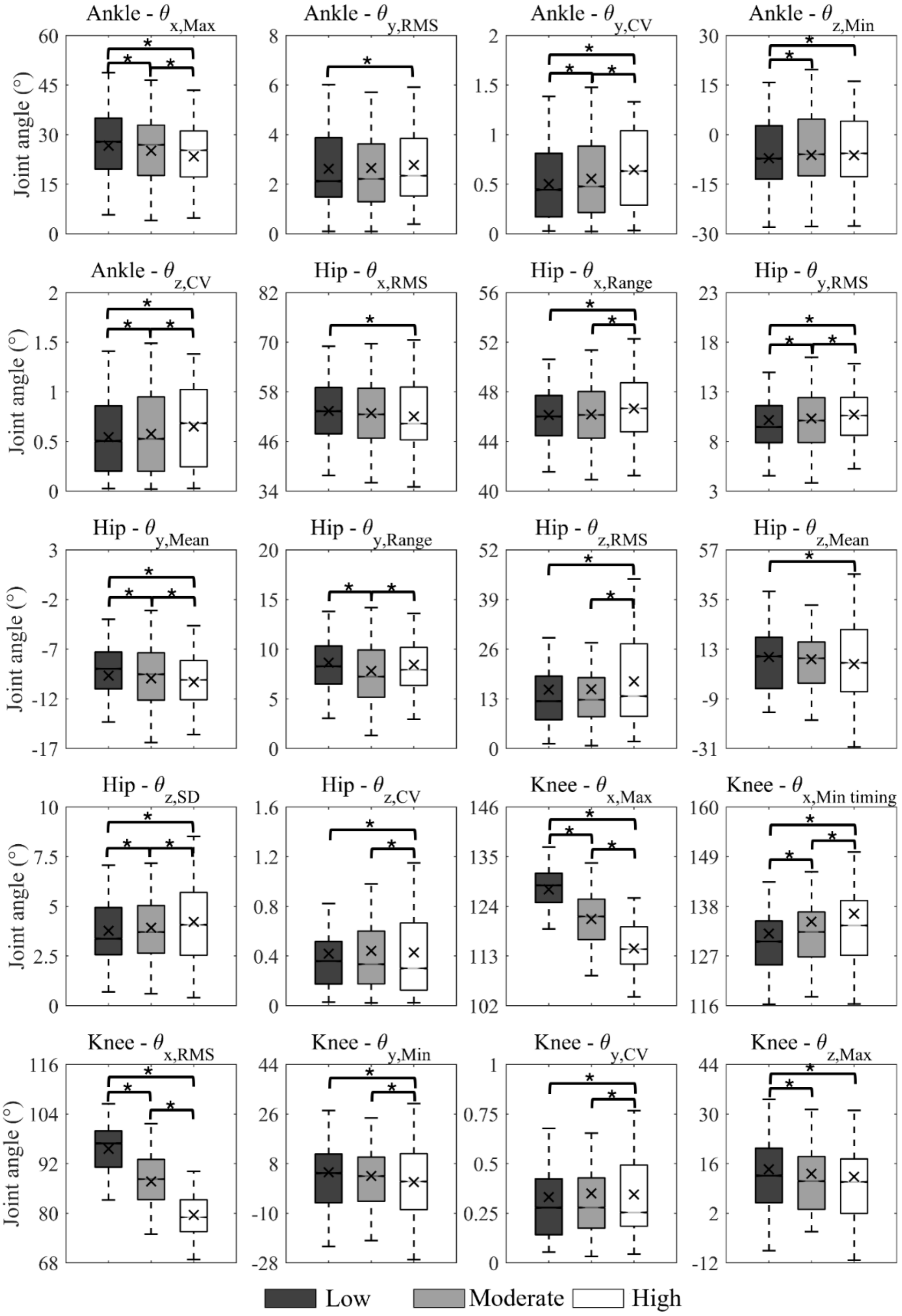

Figure 4.23 Statistical results of the selected features for support vector machine (SVM) model among three riding conditions. Low, moderate, and high refer to the saddle height levels.

Figure 4.24 illustrates the classification accuracies of saddle height by the SVM model based on the single feature described above. The highest classification accuracies based on $\theta_{x,RMS}$ and $\theta_{x,RMS}$ of knee joint were 80.26% and 79.58%, respectively. They were followed by that based on the $\theta_{z,Mean}$ feature of hip joint (71.21%) and the $\theta_{x,Min\ timing}$ feature of knee joints (70.41%). All of them had intuitive differences in Figure 4.23. The accuracy rate between 50% and 70% were $\theta_{y,Min}$, $\theta_{z,Max}$, $\theta_{y,CV}$ of knee joint, $\theta_{z,RMS}$, $\theta_{z,CV}$, $\theta_{x,RMS}$ of hip joint, and $\theta_{y,CV}$ of ankle joint. The classification accuracies of the remaining nine features were lower than 50%.

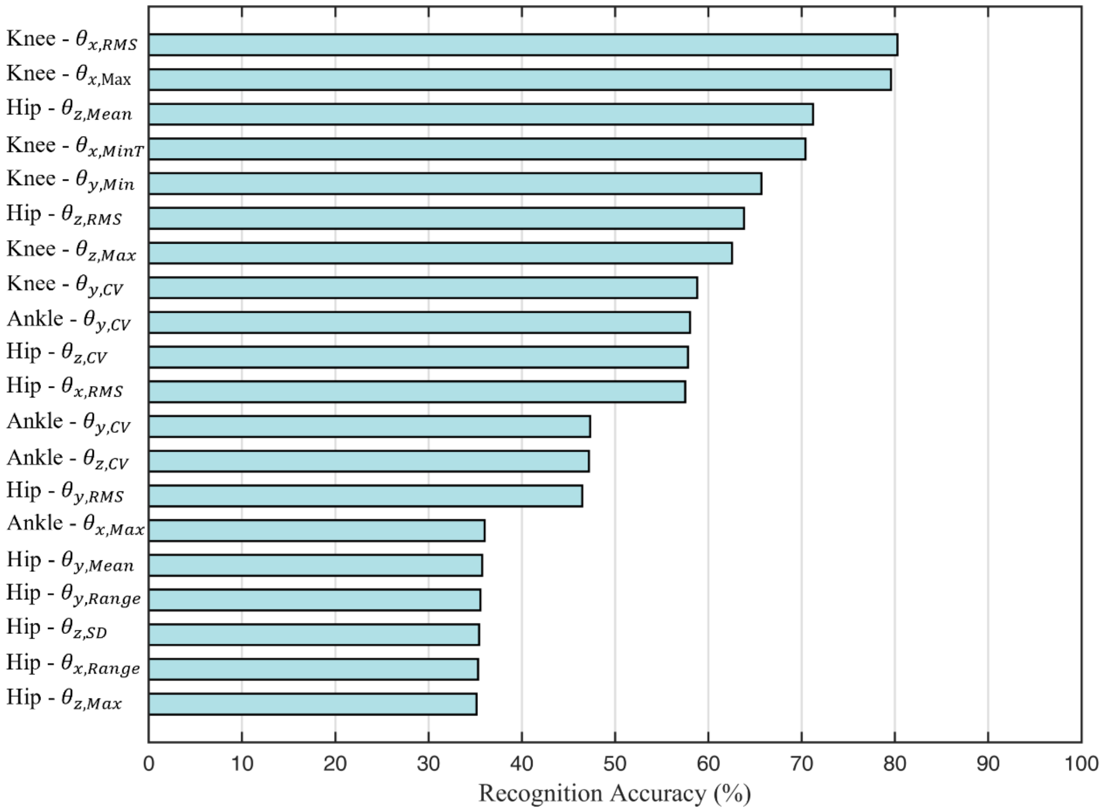

Figure 4.24 Classification accuracy of saddle height by support vector machine (SVM) model according to selected single feature.

KNN model

For the KNN model, 14 features were selected from 81 features including $\theta_{y,SD}$, $\theta_{z,RMS}$, $\theta_{z,SD}$ of ankle joint, $\theta_{x,SD}$, $\theta_{y,Mean}$, $\theta_{y,SD}$, $\theta_{z,RMS}$ of hip joint, and $\theta_{x,Max}$, $\theta_{x,Mean}$, $\theta_{x,Range}$, $\theta_{y,Mean}$, $\theta_{y,SD}$, $\theta_{z,Mean}$, $\theta_{z,SD}$ of knee joint. The statistical differences of these features under three riding conditions are presented in Figure 4.25. Similarly, each feature displayed at least one statistically significant change after adjusting the saddle height. Among them, the variations of $\theta_{x,Max}$, $\theta_{x,Mean}$, $\theta_{x,Range}$, and $\theta_{y,SD}$ of knee joint were the most remarkable.

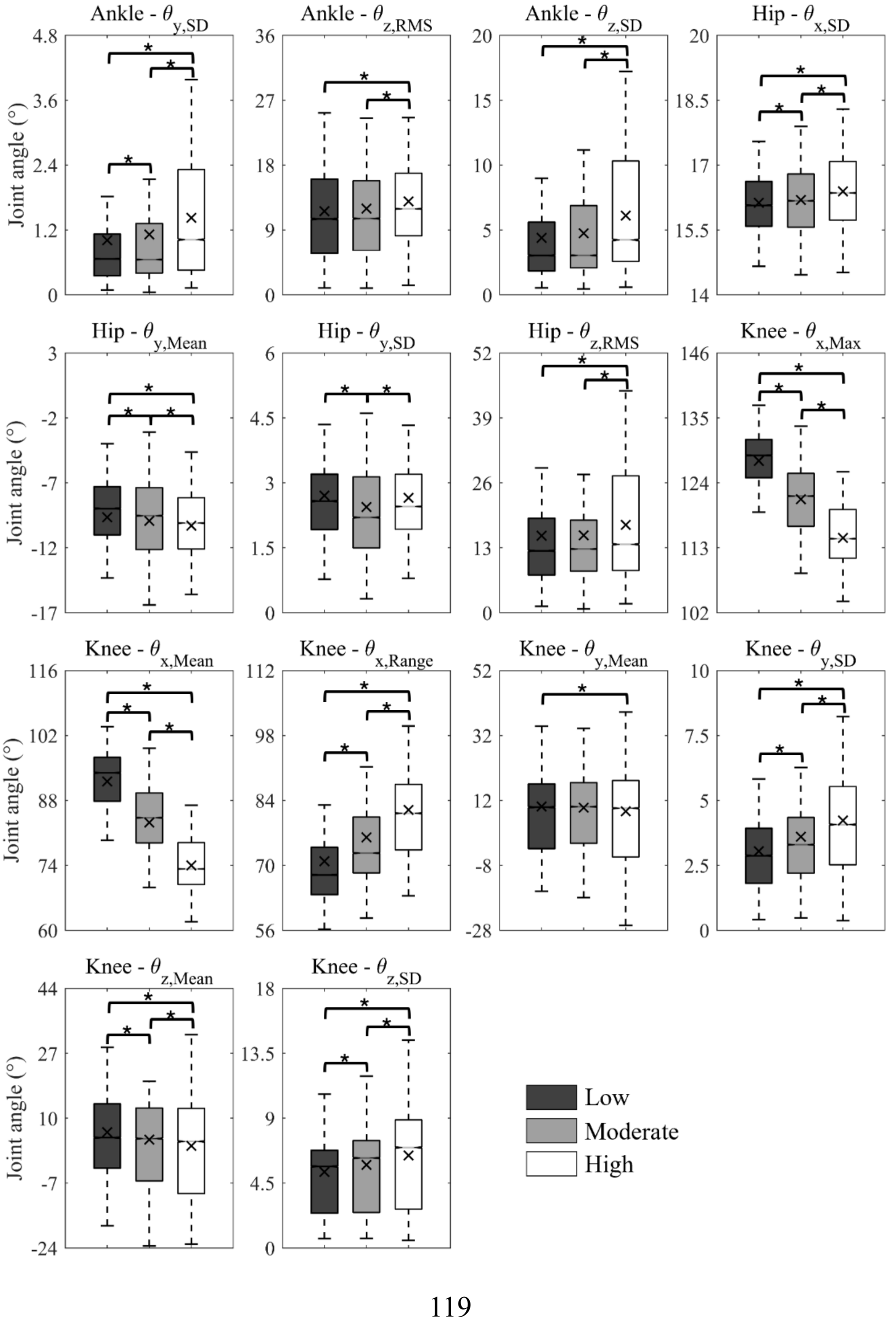

Figure 4.25 Statistical results of the selected features for the k-nearest neighbor (KNN) model among three riding conditions. Low, moderate, and high refer to the saddle height levels.

Figure 4.26 shows the classification accuracy rate of saddle height by the KNN model based on single selected feature. The highest accuracy was achieved by $\theta_{x,Mean}$ and $\theta_{x,Max}$ of knee joint angle, reaching 80.19% and 79.58%, respectively. The five features with the highest accuracy ranking and more than 65% were all extracted from knee joint angles. The three features ($\theta_{y,SD}$, $\theta_{y,Mean}$, and $\theta_{x,SD}$) with the lowest accuracy ranking were extracted from hip joint angles which were around 35%.

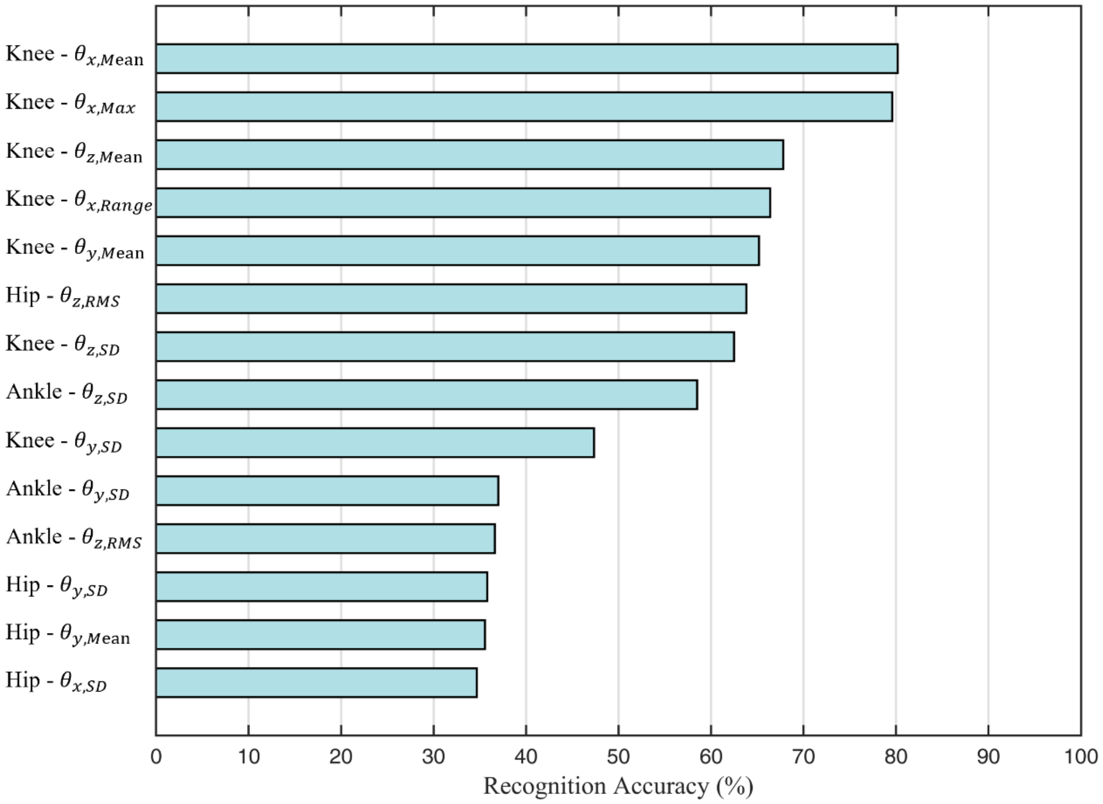

Figure 4.26 Classification accuracy of saddle height by k-nearest neighbor (KNN) model according to a selected single feature.

NB model

For the NB model, 14 features were selected. Eight of these features were repeated with the features selected in the SVM and KNN model, including $\theta_{x,Max}$, $\theta_{y,rms}$ of ankle joint angle, $\theta_{y,Mean}$, $\theta_{z,Min}$, $\theta_{z,Mean}$ of hip joint angle, and $\theta_{x,RMS}$, $\theta_{y,Min}$, $\theta_{y,Mean}$ of knee joint angle. Their statistical results are shown in Figure 4.23 and Figure 4.25. The statistical results of the remaining five features of the NB model are shown in Figure 4.27. There were notable variations in the $\theta_{y,RMS}$ and $\theta_{z,Max}$ of knee angle across the three riding groups ($p < 0.001$). $\theta_{y,Max}$ of ankle joint had statistically significant disparities when comparing the low saddle height with the moderate and high saddle heights, while its $\theta_{z,Max\ timing}$ feature was significantly different between the low and high saddle height, and between the moderate and high saddle height. The $\theta_{x,Max\ timing}$ of hip angle was analyzed and the results showed no significant differences across the conditions.

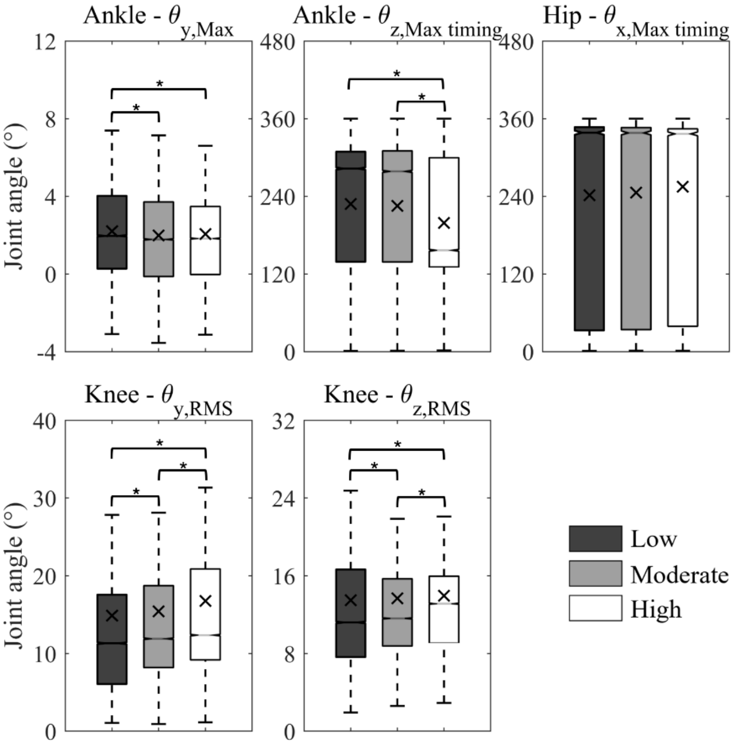

Figure 4.27 Statistical results of the selected features for the Naïve Bayes (NB) model among three riding conditions. Low, moderate, and high refer to the saddle height levels.

Figure 4.28 shows the classification accuracy predicted by the BN model based on a single selected feature. Like the prediction results of the SVM model, the $\theta_{x,RMS}$ of knee joint angle had the highest accuracy of 65.78%, followed by $\theta_{z,MaxT}$ of ankle angle, $\theta_{y,RMS}$ of knee angle, and $\theta_{y,Mean}$ of hip angle with accuracy rates between 48% and 50%. The classification accuracies based on the other nine features alone were only 30% to 40%.

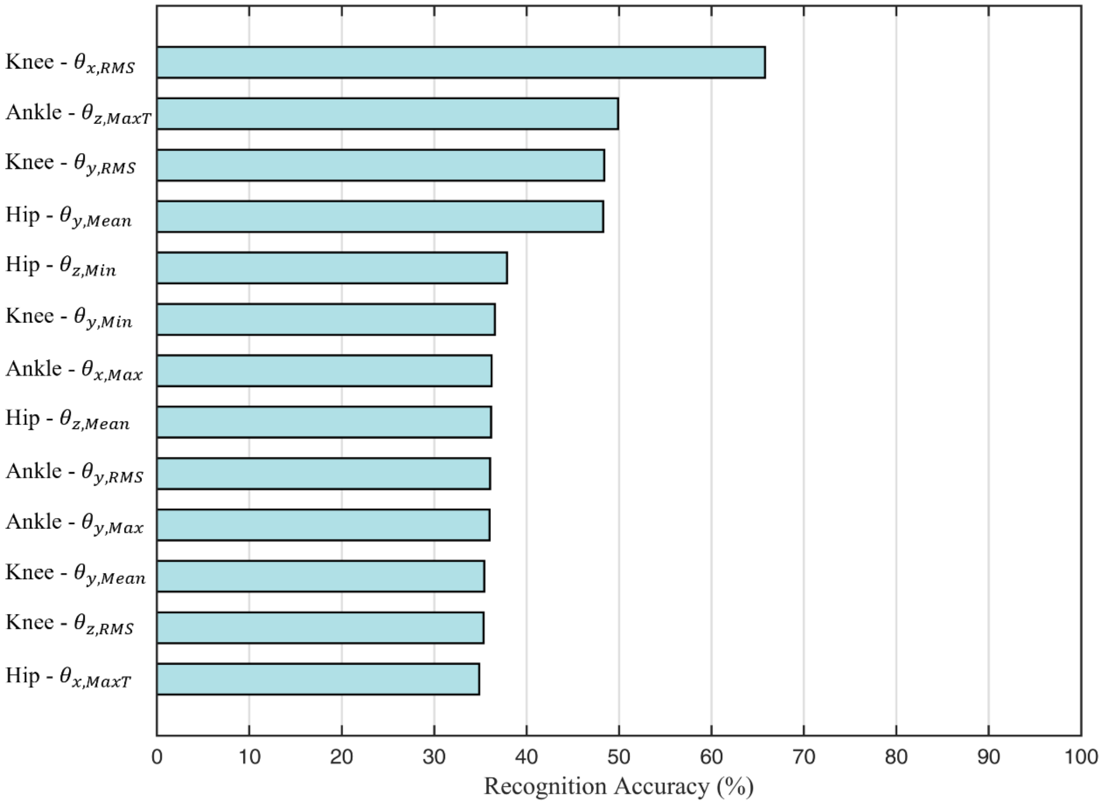

Figure 4.28 Classification accuracy of saddle height by Naïve Bayes (NB) model according to a selected single feature.

DT model

For DT model, nine features ($\theta_{y,Mean}$ of ankle angle, $\theta_{y,Mean}$, $\theta_{y,CV}$, $\theta_{z,RMS}$ of hip angle, and $\theta_{x,Mean}$, $\theta_{x,Range}$, $\theta_{y,Min}$, $\theta_{y,Mean}$, $\theta_{z,RMS}$ of knee angle) were selected. Only two features among the nine features did not appear in any of the chosen features in the above three ML models. Their statistical results are shown in Figure 4.29. Both $\theta_{y,Mean}$ of ankle joint and $\theta_{y,CV}$ of hip joint were statistically different across the three riding groups ($p < 0.001$).

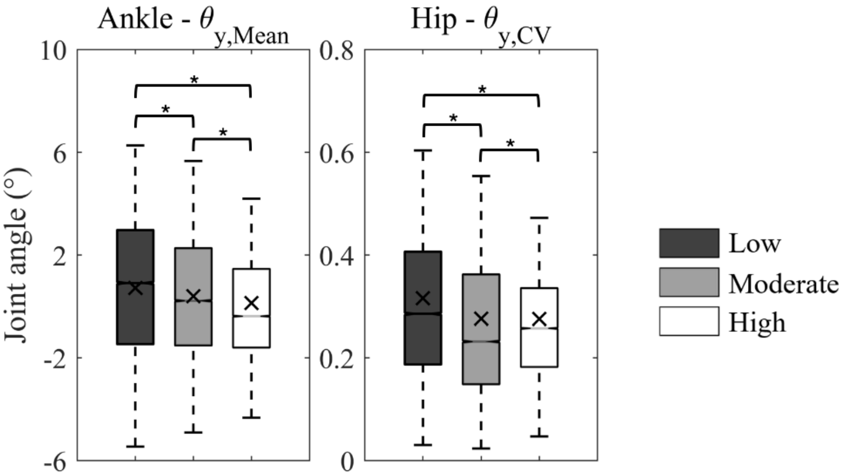

Figure 4.29 Statistical results of the selected features for the Decision Tree (DT) model among three riding conditions. Low, moderate, and high refer to the saddle height levels.

The classification accuracy of saddle height by the DT model based on a single feature from these nine features is presented in Figure 4.30. $\theta_{x,Mean}$ of knee joint angle was the feature with the highest accuracy rate, reaching 61.45%. The last two features with the lowest classification accuracy were $\theta_{y,CV}$ (36.55%) and $\theta_{y,Mean}$ (36.28%) of hip joint angle. The remaining other features had accuracy rates between 40% and 50%.

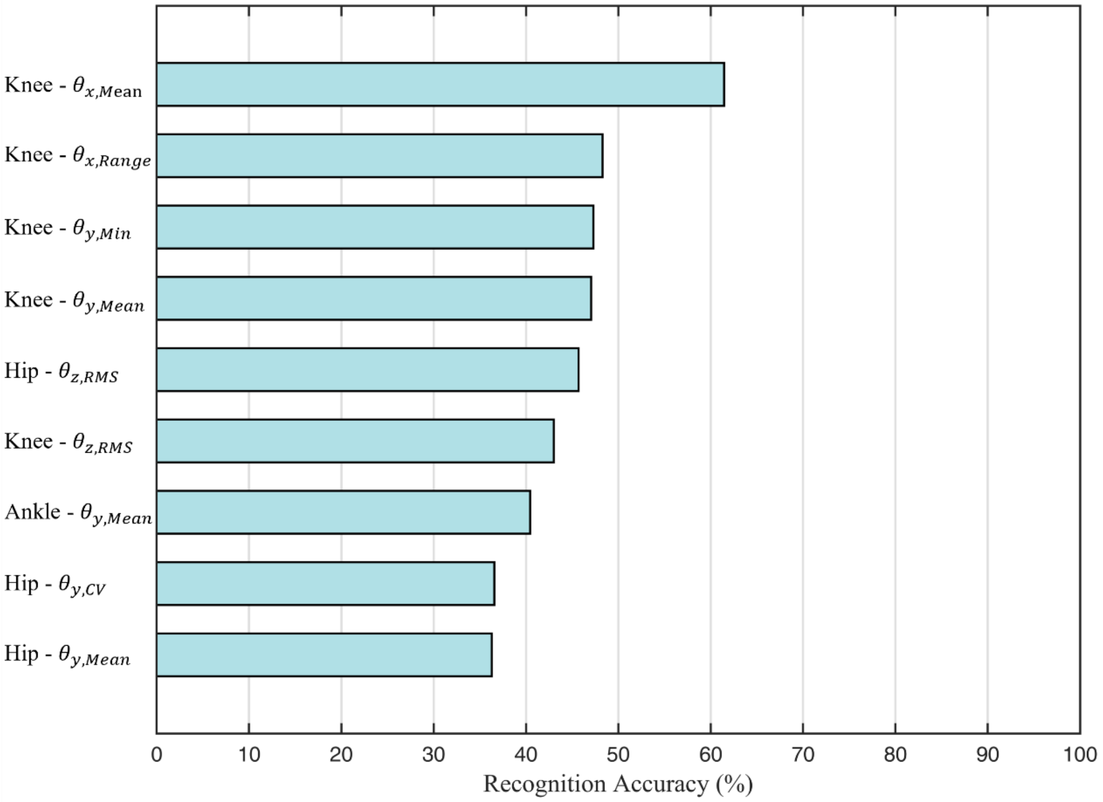

Figure 4.30 Classification accuracy of saddle height by the Decision Tree (DT) model according to a selected single feature.

4.5.2 Comparison of classification accuracy between models

Figure 4.31 compares the classification accuracy for each riding condition (low, medium, and high saddle heights) and the average accuracy of three conditions of four ML models. The NB model had the lowest classification accuracy in each riding condition, especially for the moderate saddle height with only a 59.91% accuracy rate. It had an average accuracy of 81.18%. The KNN model provided the highest average recognition accuracy of 99.79%. It also had the best classification accuracy in each riding condition, which was 99.96% for low height, 99.52% for medium height, and 99.89% for high saddle height, respectively. The DT model showed a slightly inferior classification accuracy than the KNN model but higher than that of the SVM model. The average accuracy across conditions of the DT model was 96.81%, with a high accuracy rate of 99.47% for the low saddle height case and a relatively low accuracy of 93.16%

for the moderate saddle height. The third highest average classification accuracy was the SVM model, which was 93.10%. Its accuracy rate for the moderate saddle height was lower than the other conditions, only 85.10%. Therefore, the KNN model performed best not only in the average accuracy but also in the accuracy of each riding condition.

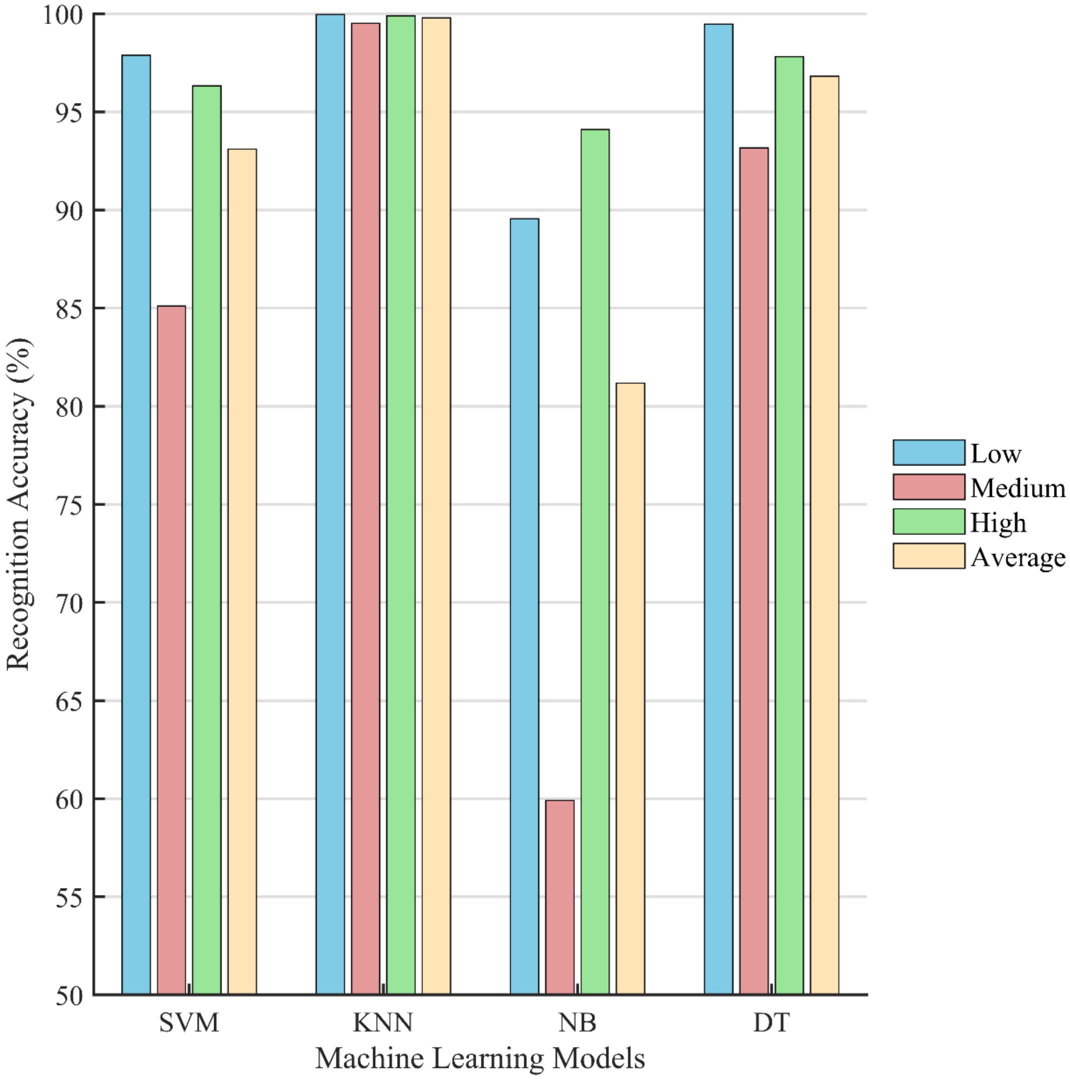

Figure 4.31 Comparison of classification accuracies of machine learning models. Low, medium, and high refer to the riding conditions of three saddle height levels. Average is the mean of the accuracies across the three conditions. SVM: support vector machine; KNN: k-nearest neighbors; NB: Naïve Bayes; DT: decision tree.

4.5.3 Correlation between features

Figure 4.32 displays the correlation between features in the optimal feature set for the KNN model. Most of the correlation coefficients were less than 0.5, which means that most features had small or moderate correlations with each other. There were still some strong correlations, such as the correlations between $\theta_{y,SD}$ and $\theta_{z,SD}$ of ankle joint (r = 0.86), $\theta_{y,SD}$ of ankle and $\theta_{z,RMS}$ of hip joint (r = 0.77), $\theta_{z,SD}$ of ankle and $\theta_{z,RMS}$ of hip joint (r = 0.80), as well as $\theta_{x,Max}$ and $\theta_{x,Mean}$ of knee joint (r = 0.77).

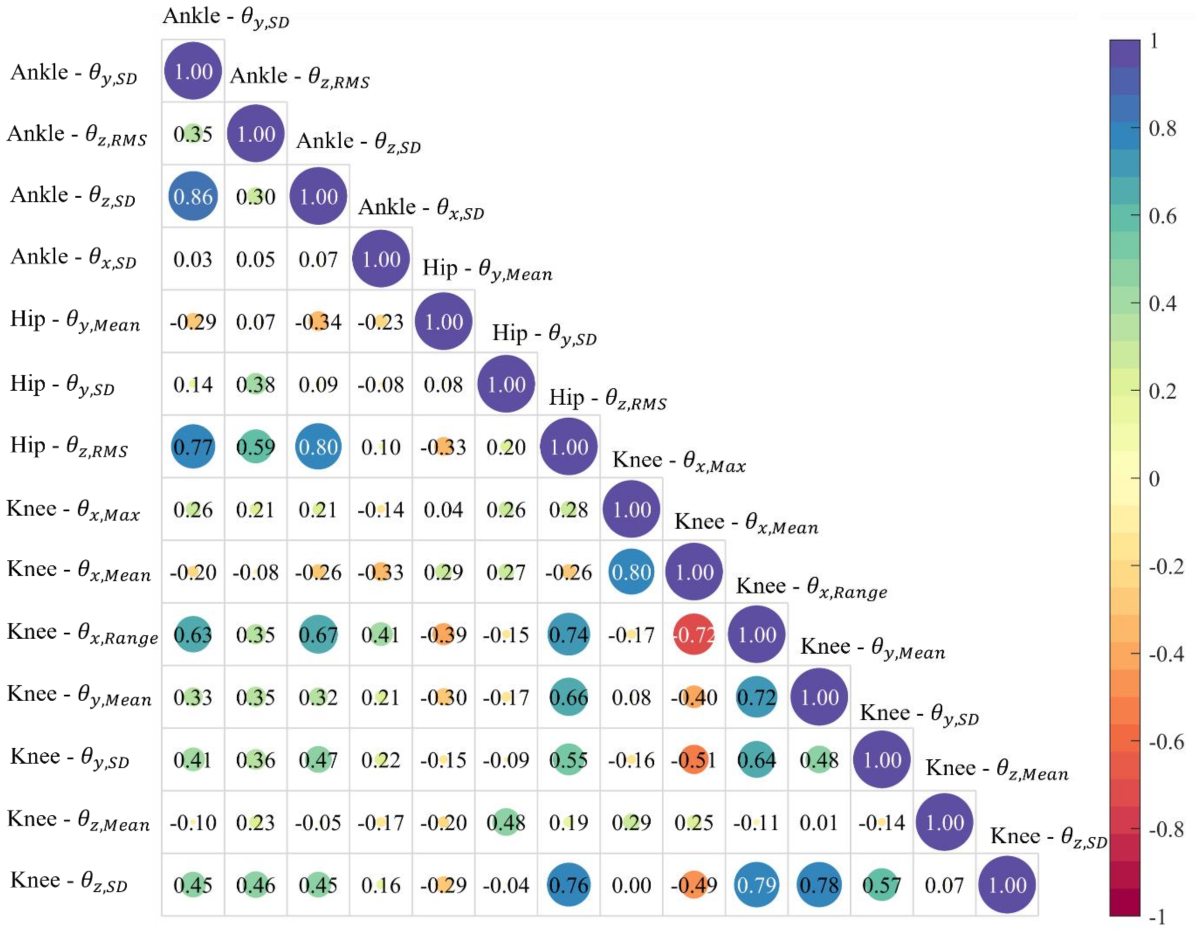

	Ankle - $\theta_{y,SD}$	Ankle - $\theta_{z,RMS}$	Ankle - $\theta_{z,SD}$	Ankle - $\theta_{x,SD}$	Hip - $\theta_{y,Mean}$	Hip - $\theta_{y,SD}$	Hip - $\theta_{z,RMS}$	Knee - $\theta_{x,Max}$	Knee - $\theta_{x,Mean}$	Knee - $\theta_{x,Range}$	Knee - $\theta_{y,Mean}$	Knee - $\theta_{y,SD}$	Knee - $\theta_{z,Mean}$	Knee - $\theta_{z,SD}$
Ankle - $\theta_{y,SD}$	1.00													
Ankle - $\theta_{z,RMS}$	0.35	1.00												
Ankle - $\theta_{z,SD}$	0.86	0.30	1.00											
Ankle - $\theta_{x,SD}$	0.03	0.05	0.07	1.00										
Hip - $\theta_{y,Mean}$	-0.29	0.07	-0.34	-0.23	1.00									
Hip - $\theta_{y,SD}$	0.14	0.38	0.09	-0.08	0.08	1.00								
Hip - $\theta_{z,RMS}$	0.77	0.59	0.80	0.10	-0.33	0.20	1.00							
Knee - $\theta_{x,Max}$	0.26	0.21	0.21	-0.14	0.04	0.26	0.28	1.00						
Knee - $\theta_{x,Mean}$	-0.20	-0.08	-0.26	-0.33	0.29	0.27	-0.26	0.80	1.00					
Knee - $\theta_{x,Range}$	0.63	0.35	0.67	0.41	-0.39	-0.15	0.74	-0.17	-0.72	1.00				
Knee - $\theta_{y,Mean}$	0.33	0.35	0.32	0.21	-0.30	-0.17	0.66	0.08	-0.40	0.72	1.00			
Knee - $\theta_{y,SD}$	0.41	0.36	0.47	0.22	-0.15	-0.09	0.55	-0.16	-0.51	0.64	0.48	1.00		
Knee - $\theta_{z,Mean}$	-0.10	0.23	-0.05	-0.17	-0.20	0.48	0.19	0.29	0.25	-0.11	0.01	-0.14	1.00	
Knee - $\theta_{z,SD}$	0.45	0.46	0.45	0.16	-0.29	-0.04	0.76	0.00	-0.49	0.79	0.78	0.57	0.07	1.00

Figure 4.32 The correlation coefficients between the selected optimal features for the k-nearest neighbor (KNN) model.

CHAPTER 5 DISCUSSION

This study provides a comprehensive analysis of the effects of cycling workload and saddle height on the biomechanics of the lower limbs of cyclists. While numerous studies have investigated these two critical cycling parameters, there is still debate regarding the optimal settings and the setting methods. Moreover, there still lacks a systematic and thorough exploration of the biomechanical aspects involved. The experimental measurement, modeling, simulation, and calculation approaches developed in this study are designed to be universally applicable to various cycling conditions. It provides a robust and scientific tool for cycling research. Its versatility makes it valuable not only for studying cycling parameters but also for optimizing equipment design, enhancing performance, and preventing injuries.

5.1 Muscle Activation

Among the analyzed muscles, only MG demonstrated a marked increase in EMG when saddle height was elevated, while both RF and BF muscles exhibited increased EMG as the cycling workload intensified. Although the EMG of TA and MG was also affected by workload, but it was not statistically different. The onset/offset timing and duration of muscle activations were not significantly changed, which suggests that the coordination pattern of muscle activation may not be affected by workload or saddle height.

5.1.1 Workload effects on muscle activations

Cycling workload plays a pivotal role in influencing the activation states of lower limb muscles, demonstrating a more significant effect compared to the adjustment of saddle height. In this study, an increasing trend in the EMG signals of the rectus femoris (RF) and biceps femoris (BF) was observed as the cycling workload increased. This aligns with prior research findings, where Sarre et al. (Sarre et al., 2003) reported that the normalized EMG signals of the RF, vastus medialis (VM), and vastus lateralis (VL) peaked at maximum workload, independent of cadence. Although their study employed different normalization methods and different workloads at 60%, 80%, and 100% of maximal aerobic power, leading to higher EMG amplitudes than observed in our research, the consistent trend in RF activation highlights the robustness of this pattern across various conditions.

Outdoor cycling experiments further validate these findings by demonstrating that increasing workloads corresponded to elevated muscle activities, particularly in the RF and VL, which are primarily responsible for generating higher power outputs (Blake & Wakeling, 2012). Although outdoor studies face challenges in data collection due to environmental factors, their results extend the applicability of our findings to real-world cycling scenarios. Additionally, research on incremental cycling showed substantial increases in the activations of VL and BF muscles with higher exercise intensity, irrespective of leg preference (Carpes et al., 2011). However, studies specifically addressing the workload-dependent activation of BF remain scarce. This study contributes valuable data on BF activation, shedding light on the crucial role of BF in cycling biomechanics and its response to varying workloads.

During this study, participants maintained a consistent cadence between 85 and 95 rpm as workloads increased, which required greater power output to overcome additional resistance and sustain a steady pedaling speed. The effect of cadence was ruled out. As a result, the overall mechanical requirement increased, especially in the power period, leading to adjustments in muscle activation through the recruitment of extra motor units. Approximately 39% of the total positive mechanical work during cycling was produced by the knee extensors, with the RF being a key contributor to knee extension and thigh flexion (Ericson, 1986). As expected, the EMG signals of the RF notably rose in response to greater workloads. Similarly, the hip extensor muscles, responsible for 27% of total positive mechanical work, also demonstrated enhanced activations. The BF, which connects the femoral trochanter to the tibia and fibula and supports both hip extension and knee flexion, exhibited a positive and proportional response to increased workloads.

As cycling workloads intensified, there was a shift in muscle recruitment patterns, transitioning from slow-twitch fibers to more fast-twitch fibers (Priego et al., 2014; Tesch, 1983). At lower workloads, slow-twitch fibers dominate, providing sustained contraction with lower force output. However, at higher workloads, the greater power output necessitates the recruitment of fast-twitch fibers, which are characterized by higher firing rates and greater force generation. This shift contributes to the observed increases in EMG signal amplitudes. Moreover, muscle contraction patterns evolve with workload changes, transitioning from predominantly concentric to increasingly eccentric contractions. During the recovery phase, the RF undergoes eccentric contraction while the BF contracts concentrically. During the propulsive phase, the rectus femoris actively contracts by shortening its fibers to generate force. Meanwhile, the biceps femoris undergoes an eccentric contraction, allowing it to lengthen and assist in controlling joint motion during this phase (Nisell, 1989). Since eccentric contractions produce more force than concentric ones, the prominence of eccentric activity under higher workloads explains the increased EMG amplitudes (Duncan, 1989).

Interestingly, not all muscles exhibited workload-dependent increases in activation. The medial gastrocnemius (MG) and tibialis anterior (TA) showed minimal changes in EMG signals despite rising workloads. These findings align with previous studies suggesting that the roles of these muscles are more associated with stabilization than power generation (Bini et al., 2008; Priego et al., 2014). For instance, a study involving competitive cyclists demonstrated slightly increased MG activation under higher workloads, and the increase was less pronounced compared to the BF (Bini et al., 2008). Another study on semi-reclined cycling revealed minimal MG changes but significant increases in RF and BF activity, corroborating the findings of this study despite differences in initial workload levels and cycling postures (Kamyar Momeni, 2014).

The primary activation of TA occurs during the recovery phase, where it stabilizes the ankle joint and maintains foot positioning on the pedal (Mornieux et al., 2010). This role differs in semi-reclined cycling, where altered onset timing and duration of TA activation enhance its co-activation with the RF. In upright cycling, however, the TA primarily is a stabilizer of the ankle joint. This stabilizing function, combined with its smaller muscle size and limited motor unit recruitment capacity, likely accounts for the absence of significant EMG changes with increasing workloads (Hug & Dorel, 2009; Mornieux et al., 2010). Similarly, the MG contributes to ankle stabilization and assists in knee flexion during the recovery period. Its consistent activation levels across workloads reflect its function as an endurance muscle, with high fatigue resistance and oxidative capacity (Maisarah Sulaiman, 2021).

Additionally, the interplay between the TA and MG further explains their relatively unchanged activation patterns. They co-activate during the recovery period to stabilize ankle joint and maintain knee flexion (Chapman et al., 2006). Unlike the quadriceps (e.g., RF) and hamstring (e.g., BF) muscles which are the power generators (Foure et al., 2011; Neptune, 1999), TA and MG have more specialized roles in stabilization and joint control. Their smaller size and reduced capacity for motor unit recruitment also limit their contribution to increased power output (Handsfield et al., 2014; Ito, 2003; Kanehisa, 1995).

In summary, the observed increases in EMG signals of the RF and BF with rising cycling workloads can be attributed to enhanced motor unit recruitment, elevated firing rates, and a shift in muscle activation patterns. These changes are further influenced by the transition from concentric contractions to eccentric contractions under a higher workload. Conversely, the consistent activation levels of the TA and MG highlight their roles in stabilization and endurance rather than power generation. These findings offer valuable insights into workload-induced adaptations in lower-limb muscle activations and provide a foundation for optimizing cycling performance, preventing injuries, and improving training strategies.

The time between the onset and offset timing is the activation duration when the EMG signal exceeds a predefined baseline (Neptune, 1997). Our findings revealed minimal statistically significant variations in the timing of muscle activation onset/offset and its duration. However, prior research by Brian et al. observed that RF and BF muscles activated earlier as the workload increased (Baum & Li, 2003). Despite the lack of significant differences in our findings, Figure 4.1 reveals similar trends in the timing of RF and BF activation. A critical difference in our and previous riding experiments is that cadence was held constant in our research, whereas it was an experimental variable in theirs (Baum & Li, 2003). Cadence has been demonstrated to significantly influence activation timing and duration of lower-limb muscles (Bieuzen et al., 2007; Brian D. Moore, 2002), and its interaction with workload may amplify alterations in muscle activation patterns. Studies exploring cadence as a variable provide additional context. For example, Neptune and Herzog reported negligible negative crank torque at a cadence of 90 rpm, while higher cadences exceeding 105 rpm introduced notable negative torque, leading to changes in muscle activation duration (Neptune, 1999). This suggests that maintaining a moderate cadence, such as 90 rpm, might help stabilize activation timing by minimizing torque-related disturbances. Consistently, a study examining both athlete and non-athlete cyclists under a controlled cadence of 90 rpm found no significant differences in the onset and offset timing of muscle activations across various cycling tests (Jobson et al., 2013). In incremental riding tests, earlier onset timing of RF activation in the final stages of effort has been observed, whereas no significant differences were noted between the middle and initial stages (da Silva et al., 2018). This earlier activation timing was attributed to fatigue, as prolonged cycling with increasing workload can induce neuromuscular changes. The evidence is that two participants in their study had to withdraw due to fatigue, reinforcing the possibility that muscle exhaustion caused the alterations of onset activity timing. Our findings, focusing on medium-intensity cycling without inducing fatigue, align with the absence of significant timing shifts for BF and RF, as participants remained in a non-fatigue state during testing. In summary, the minimal changes in activation timing and duration observed in our study likely reflect the stabilizing effects of maintaining a moderate cadence and avoiding fatigue-inducing workloads.

5.1.2 Saddle height effects on muscle activations

The significant impact of saddle height on the EMG signals of the medial gastrocnemius (MG) aligns closely with prior research findings. Specifically, the integrated EMG values of the MG increased substantially when the saddle was set at 105% of the preferred height compared to both the self-selected height and a lower setting of 90% (Sanderson & Amoroso, 2009). Using anthropometric parameters such as GTH provides a more systematic and unbiased method for determining optimal saddle height compared to self-selection. A comparative study on saddle heights of 90% and 100% of GTH demonstrated that the EMG integral value and maximum at the lower saddle height were only 65% and 62%, respectively, of those observed at the higher setting (CAWSEY, 2008). The findings of this study reinforce those results and can be attributed to changes in joint kinematics. An increased saddle height alters knee and ankle joint angles, reducing knee joint flexion while increasing its extension (R. R. Bini et al., 2014). Simultaneously, the ankle shows increased dorsiflexion at higher saddle settings (Tim Evens, 2019). This heightened dorsiflexion demand requires greater torque, which may explain the elevated MG activation. The role of MG in stabilizing the ankle during riding becomes increasingly significant at higher saddle heights, leading to greater EMG signal amplitudes (Wang et al., 2020). Additionally, the lengthening velocity of MG muscle increases during the propulsive phase and decreases during the recovery phase at elevated saddle heights (Sanderson & Amoroso, 2009). This reflects its engagement in eccentric contraction during the propulsive phase and concentric contraction during the recovery phase (Fonda & Sarabon, 2010). Based on the force-velocity relationship of muscles (Farris & Sawicki, 2012), these changes allow the MG to produce more tension across both phases, further supporting the observed rise in its activation.

The absence of significant effects of saddle height on the EMG signals of the RF, BF, and TA observed in this study contrasts with findings from previous research (Connick & Li, 2013; Moura et al., 2017). Earlier research observed that raising the saddle height led to a reduction in the eccentric contraction period of MG, whereas that of BF lengthened (Connick & Li, 2013). This aligns with our results when improving saddle height from 95% to 100% of GTH with a constant workload, although the degree of change was minimal and statistically insignificant. A possible explanation for this discrepancy could be the lower workload level in our study compared to the 200 W workload used in theirs (Connick & Li, 2013). Conversely, our findings are consistent with another study that reported a significant increase in the activation of the VL at higher saddle heights, while the EMG signals for BF, RF, and GAS showed no significant differences (Moura et al., 2017). This outcome may be attributed to the unique roles of these muscles: the VL, a monoarticular muscle, is a primary power producer with less variability in activation patterns, whereas the RF and BF, as biarticular muscles, exhibit more complex behaviors influenced by different phases of the cycling motion (Hug et al., 2004; Ryan, 1992). Consequently, the combined effects of saddle height adjustments on muscle activation intensity, recruitment of motor units, and coordination patterns result in relatively minor EMG signal variations. The inconsistency in findings across studies can be attributed to variations in applied cycling workloads and methodologies for calculating saddle heights. For instance, one study reported increased activation levels of RF and BF at a saddle height of 95% of the optimal level compared to those at the optimal height (Jorge, 1986), while another found no relationship between saddle height and quadriceps (RF and VM) activations (Ericson, 1986; Moura et al., 2017). Contrarily, some studies indicated reduced activations of RF and BF at lower saddle heights (Moura et al., 2017). These discrepancies likely stem from differences in experimental protocols, including the use of different reference heights for saddle adjustment. Aligned with ours, a prior study revealed heightened MG activation and almost unaffected TA signals at increased saddle height (Verma et al., 2016). These similar results are partly attributed to the comparable reference height for the saddle. RF presented an interesting change in our study, whichever the workload level was, its activation was lowest at 100% GTH saddle height. BF showed a similar activation pattern at 25% and 75% FTP workloads, except at the workload of 50% FTP. Besides, the TA also exhibited the least muscle activation at 100% GTH with the 25% FTP workload. These findings suggest that a saddle height of 100% GTH may provide a unique advantage, as it reduces muscle activation while maintaining the same cycling workload, likely contributing to less muscle fatigue and increased comfort during cycling (Moura et al., 2017). This result is consistent with previous studies that highlight the importance of optimizing saddle height for comfort and performance. A saddle of 109% inseam height was suggested (Hamley & Thomas, 1967). This height generally corresponds to 99% – 102% of GTH, a metric considered to offer a more consistent relationship with the rider's biomechanics compared to inseam length. However, some recent research challenges the validity of these recommendations, pointing to substantial variability in knee angle with saddle heights within this range and no clear advantage in cycling economy (Peveler, 2011, 2007). This variability could be due to differences in the kinematic patterns of the lower limbs, which move around the greater trochanter rather than following a fixed axis based solely on inseam length. As such, GTH provides a potentially more reliable reference point for determining saddle height. Further research suggests that the relationship between saddle height and joint angles is not straightforward. In particular, the knee angle, often used as a key indicator of optimal saddle height, is influenced by a variety of factors, including riding technique, bike configuration, and crank length (Mileva & Turner, 2003). Joint angles may also differ significantly between static and dynamic cycling conditions, with a reported variation of 5° to 10° (Encarnación-Martínez, 2021; Millour, 2019). This dynamic variability highlights the complexity of achieving an ideal saddle height based on joint angle alone. As a result, while anthropometric measurements, such as GTH, continue to serve as the foundation for bike fitting, additional factors like muscle activation, cycling technique, and personal comfort during long-duration rides should be incorporated into saddle height optimization. Moreover, numerous studies have suggested the need for more precise models that account for both linear and angular kinematics to predict optimal saddle height more accurately. Leg length remains a critical variable in these mathematical models, although the validity and generality of many proposed formulas need to be further tested, as they are often based on limited sample sizes and may not fully account for individual differences in biomechanics (Encarnación-Martínez, 2021; Ferrer-Roca, 2012; Gatti et al., 2022). While only 17% of previous studies on saddle height have investigated muscle activation directly (Bini & Priego-Quesada, 2022), the growing interest in this area indicates the importance of considering muscle efficiency and fatigue in the assessment of saddle height.

Cycling economy was relatively unaffected by variations in saddle height between 96% and 100% of GTH, even though muscle activation patterns and cycling techniques had been affected (Diefenthaeler et al., 2008; Sanderson & Amoroso, 2009). Preferred saddle height frequently leads to the lowest peak power and muscular activation. The activation would increase more when increasing the saddle height than reducing it (Moura et al., 2017). This contrast may stem from individual variations in saddle height preferences, as self-selected height is not always equal to 100% GTH. However, both our study and others highlight that higher saddle heights are associated with greater muscle fatigue. This notion was supported by subjective reports from 20 cycling club members, who found the highest saddle heights to be the least comfortable, causing increased fatigue and pain in the thighs and knees (Priego Quesada et al., 2017). Saddle height adjustments of 97% GTH have been suggested to minimize average hip and knee moments. However, studies supporting this claim have typically involved small sample sizes and specific subjects, such as just three trained male cyclists, which may limit the generalizability of the conclusion. GTH has been referenced in other research as well. For instance, one study identified the optimal saddle height range as between 96% and 100% of GTH based on minimizing VO_2 (Price & Donne, 1997). Another study found the saddle height of 100% GTH minimized VO_2 while also promoting better cycling biomechanics, including lower-limb joint angles and muscle coordination (Nordeen-Snyder, 1977). While these studies involved different populations (competitive cyclists and female cyclists), their findings are still in agreement with our results, reinforcing the notion that 100% GTH provides a balanced and effective saddle height. We also found that only the EMG signals of the MG muscle were significantly impacted by saddle heights, while the signals from the RF, BF, and TA muscles showed no substantial differences across varying saddle heights. Interestingly, the maximum and mean EMG values for RF, BF, and TA were lowest at the saddle height of 100% GTH with a specific workload, suggesting that this saddle height may be the most optimal among those tested heights. These results support other studies proposing that the saddle height of 100% GTH offers a favorable compromise between minimizing fatigue and optimizing performance (Moura et al., 2017; Neptune, 1997). Research on saddle height is still ongoing, with numerous studies focusing on its impact on muscle activation and cycling efficiency. However, the variations in the types of individual bodies, cycling styles, and competition levels mean that further research is necessary to refine these recommendations.

Although some studies suggest that saddle height may influence the onset/offset timing of muscle activation (GREGOR et al., 1991), the evidence remains inconclusive. One study observed significant differences in the offset timing of RF, BF, and TA activations rather than the onset timing when the saddle height was adjusted to extremes — either allowing full leg extension or increasing knee flexion (Dedieu, 2020). These discrepancies might stem from individual variations in the preferred saddle height and leg length of participants, leading to inconsistent baseline settings and adjustment degrees. Standardizing saddle height measurement methods could improve the reliability and comparability of such findings across studies. In support of our results, another study found no significant changes in the onset timing or activation duration of BF, MG, and VL when the saddle height was adjusted between 96% and 100% of GTH (Connick & Li, 2013). However, they did report a delayed eccentric contraction offset timing of BF at higher saddle heights, possibly reflecting neural adaptations aimed at maintaining cycling efficiency at a constant cadence. This delayed offset might serve to optimize the transition between eccentric contractions and concentric contractions during the pedal stroke. However, the study did not differentiate between the contributions of the contractile and series-elastic elements, leaving a gap in understanding the precise biomechanical adjustments. The duration of muscle activation in cycling is another important aspect to consider, as it reflects the functional demands placed on muscles during different phases of the pedal stroke. Research has shown that higher saddle heights can reduce activation duration for certain muscles, such as BF, by altering joint kinematics and reducing the time spent in positions requiring high-force output (Connick & Li, 2013). Conversely, lower saddle heights may increase activation duration due to greater knee flexion, which demands prolonged engagement of stabilizing muscles (Dedieu, 2020). These variations highlight the complex interplay between saddle height, joint mechanics, and muscle coordination. Additionally, inconsistencies in defining muscle activation thresholds significantly hinder comparisons between studies. Variations in the criteria used to determine onset and offset timing can also lead to divergent conclusions, emphasizing the need for a unified approach. Employing consistent activation thresholds and standardized methods for saddle height adjustment would enhance the robustness and comparability of research outcomes.

Future investigations should also consider the interaction between the duration of muscle activations and other factors such as workload, cadence, and fatigue. Prolonged activation durations under high workloads or at extreme saddle heights may contribute to the earlier onset of fatigue and increased risk of overuse injuries. By exploring these dynamics and refining methodologies, researchers can develop evidence-based guidelines for optimal saddle height adjustment to improve cycling performance and minimize injury risks.

5.2 Cycling Asymmetry

Although cycling is a symmetrical sport, people tend to use the dominant side during voluntary exercise. The relationship between cycling symmetry and performance is complex. It is still difficult to conclude that the better the cycling performance, the higher the symmetry, despite a great deal of prior research. Asymmetry in cycling is common, and the difference in power output between the right and left legs can reach 20% (Carpes, 2007). The authors note that asymmetries in cycling might be a sign of reduced cycling performance, increased injury risk, and muscle fatigue.

5.2.1 Workload effects on cycling asymmetry

The results of this study reveal that workload has a nuanced impact on cycling asymmetry, with varying effects under different saddle height conditions. Specifically, when the saddle height was set at 95% and 97% of GTH, the ASI of the resultant PRF decreased as the workload increased. In contrast, at 103% and 105% of GTH, ASI of the resultant PRF increased with higher workloads. While ASI of the Y-axis PRF consistently decreased with increasing workloads across all saddle heights, no such uniform trend was observed for the Z-axis PRF, resultant PRF, or other biomechanical variables like joint angles and muscle activations. This highlights the unique sensitivity of medial-lateral force balance to workload changes, in contrast to the more variable responses of other biomechanical metrics.

The changes in the ASI of Y-axis PRF align with previous findings, such as the study by Carpes et al. (2007), which reported that increased exercise intensity reduced pedaling asymmetry in a 40-km riding test (Carpes, 2007). In their study, the intensity was defined by $\%O_{2peak}$ measured by a VO_{2peak} cycling test. However, the workload range in their study was higher than that used in our experiment, as they started at 100 W and increased power with an increment of 25 W. Furthermore, their methodology of ASI calculation, which was based on the peak crank torque, focused on isolated moments during the pedal stroke rather than evaluating symmetry over the entire pedaling cycle. This difference in ASI calculation may partially explain the discrepancies between the studies. The ASI of joint angles and muscle activations in this study did not show a uniform changing pattern with different workloads. This is aligned with a previous finding that no significant effects of speed or resistance on cycling symmetry (Daly & Cavanagh, 1976). Similarly, García-López et al. observed no association between workload and symmetry in kinetic variables like torque and impulse contributions when the pedaling power output improved from 200W to 300W (García-López, 2015). However, a recent study put forward that the cycling intensity was related to the asymmetry (Aleksieva et al., 2020). They observed a significant decrease in asymmetry as the intensity increased from 55% to 85% of heart rate reserve (HRR), whereas no significant difference was found between 35% and 55% HRR. This suggests that workload changes could affect cycling symmetry only when the baseline workload is sufficiently high to elicit neuromuscular and biomechanical adaptations. One study supports this that significant asymmetries weren't present at the beginning of the task but appeared during the last phase of an incremental exam (Trecroci et al., 2018). In both incremental and constant workload cycling trials, fatigue may have an impact on the asymmetry. Although a lower workload was used in this study to avoid muscle fatigue of participants, it may also lead to insignificant variations in the outcomes.

The lack of a uniform influence of workload on the most calculated symmetry indices, including the joint angles and muscle activations, suggests that workload alone is not a definitive factor in determining cycling symmetry. Instead, the interplay between workload and other variables, such as saddle height, body biomechanics, and neuromuscular control, likely shapes the observed patterns. The consistent response of Y-axis PRF may be attributed to its specific role in maintaining lateral stability during cycling, which becomes more critical as the workload increases and greater force output is required.

The evaluation index of cycling symmetry and calculation method of ASI are different in previous studies as well as in this study, which greatly affects the results. For example, when comparing the mean power output among different cycling intensity conditions, the absolute symmetry (expressed as the difference between the power of left and right limbs) changed very little, but the relative symmetry declined as the intensity increased (Murray, 2023). Therefore, it is necessary to explore more kinetic and kinematic metrics and unify the calculation formula in future research.

5.2.2 Saddle height effects on cycling asymmetry

The influence of saddle height on cycling asymmetry, in terms of PRFs, joint angles, and muscle activations, seems to be greater than workload. The findings reveal that no single saddle height consistently minimizes asymmetry across all metrics, indicating that the optimal saddle height for symmetry is task-dependent and influenced by workload and individual biomechanics.

The minimum ASIs of the PRF components and resultant PRF mostly occurred at the saddle height of 100% and 103% of GTH, and it was larger at the highest (105% GTH) and lowest (95% GTH) saddle height conditions. This indicates that extreme saddle heights disrupt the overall balance of force application, likely due to excessive lower-limb joint extension/flexion and altered joint mechanics. On the other hand, 100% GTH appears to provide the best overall alignment for balanced force generation, as the minimum ASI of resultant PRF occurred in this condition.

On the other hand, the 100% GTH did not seem to have such a special status in ASI of lower-limb joint angles. The ASI of knee joint angles generally increased with the increased saddle height. The knee joint serves as the primary driver of pedaling force which contributes more than 50% of total mechanical work. Greater saddle height results in an expanded ROM in the knee angle (R. R. Bini et al., 2014). The expanded ROM can exacerbate pre-existing asymmetries in knee mechanics, such as differences in limb length, muscle strength, and neuromuscular control between the legs. Unlike the knee joint, the ASI of hip and ankle joint angles did not exhibit a uniform trend with changes in saddle height, although both of them had a minimum ASI at 105% GTH. As the saddle height increases, the mean of hip joint angle increases but its ROM slightly decreases (R. R. Bini et al., 2014). A hip with a larger flexion angle could reduce the range of side-to-side swings and provide better pelvic alignment. At the saddle height of 105% GTH, the increased leg extension promotes more uniform dorsiflexion and plantarflexion of the left and right ankles. This may result from the improved alignment of the tibia and foot, allowing ankles to follow a more symmetrical motion path. Additionally, the changing trends of ASIs of ankle and hip joints are very similar. This may be because they all have larger average joint angles at higher saddle height which means more flexion, but the mean of knee joint angle reduces (R. R. Bini et al., 2014). Both hip and ankle joints are responsible for stability and force transmission during cycling. Therefore, the similar changes in ASI can be explained by the similar motor function and comparable changes in kinematics. Our results suggest that the knee joint is sensitive to saddle height, with higher positions exacerbating asymmetry. However, a previous study showed that the asymmetry is a constant individual pattern despite variations in cycling workload or saddle height (Diefenthaeler et al., 2016). It is worth noting that the variation amount in saddle height in their study is only 2.5% of the distance from the pubic symphysis to the ground. Bini et al. pointed out that muscle length, joint angles, and moments were impacted by a 5% change in saddle height (Rodrigo Bini, 2011). Therefore, a 2.5% change may not be enough to affect the asymmetry between lower limbs. Besides, they used peak torque during the propulsive phase to calculate the ASI which was different from ours but could be a complement to the kinetic asymmetry.

The ASI of muscle activations, as illustrated in Figure 4.18, provides insight into how saddle height and workload influence the symmetry of muscle recruitment during cycling. The changes in ASI of the BF, MG, RF, and TA muscles were totally different with saddle height, which correlated with their respective physiological positions, shapes, and motor functions. The maximum muscle activation of BF which facilitates hip extension and knee flexion was minimum at 100% GTH saddle height (Figure 4.4). This could imply that the reduction in the maximum BF activation was not uniform for both legs at moderate saddle height, thus increasing the asymmetry. RF is also located in the thigh but on the anterior side. As a bi-articular muscle spanning the hip and knee joints, RF facilitates hip flexion and knee extension enhancing movement coordination between these two joints. However, the ASI of RF showed an opposite trend, that is, its minimum was at the saddle height of 100% or 103% of GTH, and its maximum was at 97% or 105% of GTH. The moderate saddle height may place RF in an optimal position for force generation, resulting in smaller ASI. A previous study showed that the continuous relative phase between the knee and hip at low saddle height was smaller than that at the usual height level, but neither was significantly different from that at high saddle height (Dedieu, 2020). This could explain why the difference in ASI of RF and BF between low and medium saddle height was greatest, and moderate ASI occurred at high saddle height (105% GTH). Although the activation level of MG was most obviously affected by saddle height, its ASI did not show a clear changing pattern, except that the ASI was generally minimal at 105% GTH. The MG muscle plays a crucial role in facilitating plantarflexion movements and is essential for maintaining steadiness within the ankle joint during cycling. The ankle increased means of flexion angle and ROM at high saddle heights, and its activation level also increased. However, the increase of the two variables possibly is not consistent, which would lead to irregular changes in ASI. TA, as a dorsiflexor, acts during the first and fourth pedaling phases (crank angle: 0°- 90° and 270° - 360°). When the saddle height was 100% - 103% of GTH, TA might compensate for uneven forces in the lower limbs, leading to a higher ASI of activation. The reduction in ASI at 105% GTH supports the idea that optimized alignment reduces compensatory mechanisms and promotes symmetry (Rodrigo Bini, 2011).

In summary, the effect of workload on the ASI of PRFs, lower-limb joint angles, and muscle activations does not have a uniform rule and may be synergistically influenced by other factors.

Part of the interested variables are affected by saddle height. 100% GTH may be an optimal choice for generating symmetrical PRF and RF muscle activation but does not apply to RF and TA muscles. The symmetry of the knee joint angle declined with the increased saddle height. Therefore, the effects of saddle height on their symmetry are clearly different between the different kinetic and kinematic parameters which require further investigation.

5.3 Muscle Forces and Joint Contact Forces

In the second sub-study, we developed a multibody MSK model for cycling and examined how changes in saddle height and workload, along with their interactions, influenced the muscle forces and joint loadings of the lower limbs during cycling. The findings provided partial support for our hypotheses. As the workload increased, the most lower-limb muscle forces, along with the maximum forces at the hip and knee joints, showed corresponding increases. In contrast, the engagement of calf muscles and the ankle joint contact forces declined. On the other hand, when saddle height increased, there was a general reduction in muscle forces across the lower limbs, except for the TA. Means of all joint contact forces decreased, and a significant reduction was observed in the maximum forces at the hip and ankle joints, particularly in the A-P direction. Notably, the interaction between workload and saddle height significantly influenced the M-L force of knee joint and the force generated by GluMax muscle. These findings emphasize the complex interplay between biomechanical factors, workload, and saddle height in shaping joint and muscle forces during cycling.

5.3.1 Validity of the musculoskeletal multibody model

A comprehensive MSK multibody model was developed to simulate cycling dynamics effectively. The model incorporated the pedal forces and torques measured by six-axis force sensors, enhancing both computational efficiency and accuracy. Validation of the model against

EMG measurements for selected muscles (BF, GAS, RF, and TA) showed moderate to strong agreement, supporting its reliability. However, residual discrepancies likely stemmed from factors such as the reduced sensitivity of the activation-force relationship under conditions of significant joint angulation and artifacts like inter-muscle crosstalk during EMG acquisition. Notably, the lowest correlation coefficient observed for GAS may be attributed to differences in target muscle between measurement versus calculation. The model estimated activation of GAS across both its medial and lateral heads, while the EMG sensor was attached solely to the medial head. Despite this limitation, the model surpasses earlier cycling simulations by incorporating a broader range of lower-limb muscles, detailed ligaments, and real pedal forces and torques (Thelen et al., 2003; Zongxing et al., 2021).

Furthermore, by employing advanced scaling techniques and parameter tuning, the model is adaptable to diverse cyclist anthropometries and cycling conditions, making it versatile for various applications. Such adaptability is crucial for refining cycling biomechanics, optimizing performance, and reducing the risk of MSK injuries, particularly in studies focused on varying saddle heights, workloads, and pedal dynamics.

5.3.2 Workload effects on the muscle forces

Consistent with prior research (Baum & Li, 2003; Holliday et al., 2023; Priego et al., 2014), increased workload led to higher muscle forces across major lower-limb muscles, reflecting the growing demand for power production during cycling. Hip and knee extensors, the primary contributors during the propulsive phase, exhibited notable force increases with a greater workload. However, the increments were unevenly distributed among synergistic muscles. For example, VL and VM demonstrated substantial growth in their mean forces, whereas RF showed a marked increase only in its maximum muscle force. This distinction aligns with the biomechanical roles of these muscles. VL and VM, being mono-articular, focus on direct power generation, while RF, as a bi-articular muscle, primarily transmits forces across joints. VL and VM had a significant moderate correlation in transverse relaxation times that correlate with the metabolic state of the skeletal muscle (Akima et al., 2004), and their EMG signals are well matched (Akima et al., 2023). Therefore, the muscle force patterns of VL and VM were highly consistent in the results. Nonetheless, the average muscle force of VL was roughly 250N greater than that of VM, because of the advantages of VL in the mass, pennation angle, and physiological cross-sectional area (Ward et al., 2009). The results demonstrate that a higher workload increased the mean muscle forces of VL and VL but had no effect on their maximum, which is consistent with a previous study (da Silva et al., 2018). This suggests that rather than increasing muscle activation at a certain moment, VL and VM tend to improve it uniformly in a pedaling cycle. RF also belongs to the quadriceps muscle group as VL and VM, so it also increased the muscle force with the increase of workload. However, it has an entirely distinct activation pattern, because of the different physiological structures and motor functions described above. The increase in BF muscle force with increasing workload was reflected in both mean and maximum values, which is confirmed by previous research (Priego et al., 2014). With the elevated workload, BF could have experienced greater activation of the fast-twitch muscle fibers, which are better suited for generating high-force contractions (Chalmers, 2008).

The SOL and GAS displayed reduced force production as workload increased, while opposed results were reported in a previous study (M. O. Ericson, Nisell, R., Arborelius, U. P. & Ekholm, J. , 1985). They found that the mean of SOL's EMG increased when they improved workload from 0 W to 120 W and 240 W. Another study using sandbags to set the cycling workload even showed that muscle activation of SOL was unaffected (Baum & Li, 2003). These inconsistencies likely arise from methodological differences, including variations in bike setups, such as cleat positioning, and how workload intensities are defined. Our study employed FTP as the workload metric, emphasizing sustained force output, whereas earlier studies often relied on incremental cycling tests, which prioritize peak power. Such distinctions in workload characterization likely influenced the observed disparities. On the other hand, SOL consists predominately of slow-twitch fibers and limited fast-twitch fibers (Edgerton et al., 1975). Cyclists naturally recruit muscles with a higher proportion of fast-twitch fibers, such as the quadriceps and gluteal muscles (Crouzier et al., 2018), to meet the growing demand for power generation. This shift in recruitment pattern could explain the observed decrease in SOL engagement alongside the increased activation of muscles like the RF and BF under higher workloads. There was a redistribution of force-sharing among synergistic muscles (Herzog, 2000). The mean and maximum values of GAS muscle force diminished as the workload increased. This is generally consistent with the experimental results, but contrary to a previous study (Priego et al., 2014). Although the target muscle in their study was medial GAS, the increase in its muscle force was the least among the measured muscles. In another study (Kamyar Momeni, 2014), when the workload increased from 0 W to 100 W, the EMG of medial GAS little changed, and its peak value even decreased slightly. This supports our results to some extent. Besides, the EMG of TA in their study increased slightly as the workload increased from 0 W to 50 W and displayed a notable increase when the workload continuously improved to 100 W, which agrees with our results of TA muscle forces.

5.3.3 Saddle height effects on the muscle forces

Saddle height mainly affected the mean rather than the maximum values of muscle forces. One of the most prominent observations was the reduction in the means of VL, VM, and RF muscle forces with the increased saddle height. These muscles, functioning as synergistic knee extensors, play a critical role during the propulsive phase (Raasch, 1997). According to the muscle length-tension relationship, knee extensors operate most efficiently when the knee joint flexes at an angle of 60° – 70° (Ichinose et al., 1997). An elevated saddle height can shift the working range of these muscles closer to this optimal length, thereby lowering their activation levels.

Increased saddle height also induces biomechanical changes in the kinematic chain. It reduces knee flexion and increases the moment arms of the knee extensors relative to the knee joint. This adjustment decreases the force demand on the knee extensors to generate the same joint torque during the propulsion phase. This principle can similarly explain the reduced mean forces observed in other muscles, such as the GluMax, BF, and GAS, which are also actively engaged in the propulsion phase. These findings were supported by previous studies (Jorge, 1986; Moura et al., 2017). SOL was the only muscle that demonstrated a notable increase in maximum muscular force but no change in mean as saddle height increased. The main reason for the increase is the longer operating range and faster lengthening velocity which demanded a relatively higher excitation (Sanderson & Amoroso, 2009). This is confirmed by a study about EMG measurement (Sanderson et al., 2006).

Previous myoelectric studies mostly focused on medial GAS that showed only one peak (Baum & Li, 2003; Clancy et al., 2023). The EMG pattern of the lateral GAS might be the reason for the two peaks of the curve of GAS muscle force in this study (Cannon et al., 2007; CAWSEY, 2008). It has been proved that the lower saddle height would decrease the ROM of the knee joint angle and increase the flexion angle (R. R. Bini et al., 2014). The EMG of GAS, especially the lateral head, increased with greater knee flexion (Arampatzis et al., 2006) which means the greater mean value of GAS muscle force.

The observed increase in the mean muscle force of the TA with higher saddle heights (from 95% to 105% of GTH) but without a significant change in its maximum force can be explained by changes in muscle engagement patterns and cycling kinematics. As the saddle height increased, the ankle joint presented greater plantarflexion and a larger ROM which may require more muscle forces. The redistribution of calf muscle forces may lead to a more continuous engagement of TA throughout the recovery phase to compensate for reduced contributions from other muscles, such as SOL and GAS. Research has shown that changes in saddle height can alter muscle activation patterns and joint mechanics. Higher saddle heights are often associated with increased dorsiflexion moments and longer periods of TA engagement during the upstroke, explaining the rise in the mean muscle forces. However, peak forces tend to remain stable because the role of TA is not primarily to handle maximum load but to facilitate smooth pedal transitions and ankle stabilization.

The muscle forces of GluMax decreased with the increase of saddle height which coincides with the observation that the iEMG of GluMax declined within the range of crank angle from 105° to 360° as the saddle height decreased 5% of GTH (Jorge, 1986). Although the peak value of GluMax's iEMG decreased, the peak muscle force of GluMax was little change in our study. The divergence may be caused by that their peak value was the integrated EMG with a specific range, whereas that in our study was a single value of a specific time point. A kinematic study of cycling (Rodrigo R. Bini, 2010) suggested that an elevated saddle height led to reduced ROM of hip joint angle. This consequently lessens the power requirement for the primary hip extensor - GluMax (M. O. Ericson, Nisell, R., Arborelius, U. P. & Ekholm, J. , 1985).

5.3.4 Workload effects on the joint contact forces

Our study revealed an increase in resultant forces at the hip and knee joints with higher workloads, while the forces at the ankle joint decreased which was primarily due to the decreased component force in the P-D and A-P directions. These findings align with earlier research documenting that power output and joint loadings at the hip and knee increased under greater workloads (Bini & Hume, 2013; Kutzner et al., 2012; Mats O. Ericson, 1986). The hip and knee joints, supported by large and powerful muscle groups like the GluMax (hip extensors) and quadriceps (knee extensors), are the primary contributors to generating riding power. Studies have attributed such increments to the heightened activity of these around muscles, which generate the necessary propulsive forces during cycling (Damm et al., 2017). While the ankle contributes to the pedal stroke, its role becomes secondary at higher workloads. It primarily stabilizes the foot and adjusts for variations in pedal forces, leading to reduced joint contact forces compared to the hip and knee. However, our findings differed from the research reporting that adding 120 W to the workload increased the ankle compressive force (M. O. Ericson, Ekholm, J., Svensson, O., & Nisell, R., 1985). The study assumed that the ankle compressive force was the sum of the component pedal force along the long axis of the tibia and the Achilles tendon force. This assumption compromised the strength of the outcomes due to the imprecise estimations of the moment arm and oversimplified computations without considering muscle forces. The SOL and GAS, which play a key role in stabilizing the ankle and assisting with plantarflexion, showed reduced activation at higher workloads. This reduction contributed to the decreased loading on the ankle joint. The fact that the contributions of knee and hip joints were shown to significantly rise under conditions of increased physical demands, while those of the ankle joint remained unchanged or even decreased, provides more evidence in favor of this view (Bini & Diefenthaeler, 2010).

5.3.5 Saddle height effects on the joint contact forces

Adjusting saddle height significantly impacts joint contact forces in cycling, particularly along the A-P direction. Research suggests that increasing saddle height generally reduces joint angulation in the lower limbs, thereby decreasing forces in the shear planes (Rodrigo Bini, 2011). An in-vivo study using hip implants reported a 7% – 15% reduction in hip contact forces with every 9 cm increase in saddle height (Damm et al., 2017). We also observed a decrease of about 11.7% in hip joint forces aligning closely with the previous study which is attributed to the similar adjustment interval in saddle height which was 8.76 cm in our study. As saddle height increases, the lower limb adopts a more extended position, aligning joint force vectors more closely with the pedal force direction. This alignment could shift more load into the P-D direction. Therefore, the mean of P-D knee joint force increased, but the increasing trend did not exhibit at the forces of hip and ankle joints. Increased saddle height optimizes the mechanical leverage of the lower limbs by increasing the effective moment arms of key muscles, especially those spanning the hip and knee joints. This reduces the overall force demanded for propulsion, which can be reflected by the reduced muscle forces of VL and RF. However, it does not eliminate the need for stability and control, such as TA and GAS who play a crucial role in pedal control throughout the pedaling cycle. Therefore, the changes of joint contact forces in the P-D direction are the combined result of shifted muscle recruitment, changed kinematics, and mechanical efficiency. Finally, when saddle height increased, the resultant joint forces of the three joints declined, suggesting that a higher saddle height helps lower the risk of overuse injuries in lower-limb joints during cycling.

A higher saddle height offers potential benefits for cyclists by reducing joint contact forces and muscle forces, particularly at high flexion angles in the hip, knee, and ankle joints. In contrast, lower saddle height settings can induce excessive flexion, leading to higher forces and increased risk of musculoskeletal strain (Gatti et al., 2021). However, excessively raising the saddle height introduces other injury risks such as perineal numbness and Achilles tendinopathy (Silberman, 2013). This underscores the need for a balanced approach.

Our findings further emphasize that workload affects loadings on the lower-limb joints, highlighting the importance of tailoring saddle height to individual needs. The ideal saddle height likely balances injury prevention with performance optimization, requiring a nuanced approach based on the cyclist’s physical attributes, training intensity, and riding conditions.

These insights, combined with MSK modeling, can aid in developing personalized strategies for enhancing cycling efficiency while minimizing the risk of overuse injuries.

5.4 Biomechanics of Knee Cartilage and Meniscus

The FE model was built based on the MRI data of a male subject, so there might be individual variations in the calculated outcomes. However, at present, there are limited studies on the stress distribution of the knee joint during riding and even fewer FE models for cycling that can dynamically simulate the flexion and extension movement of the knee joint. This study can compensate for the lack of knowledge in this regard and provide more detailed biomechanical results of knee joints for cycling research.

The von Mises stress provides the overall stress level experienced by cartilages and menisci during cycling. The Max and Min principal stresses represent the largest tensile stress and compressive stress, respectively. As the saddle height increased, the stress of femoral and tibial cartilages decreased. The mean stress of the menisci also decreased, except for several increases in maximum stress which might be caused by the local stress concentration. The regions of stress concentration were consistent across different saddle heights and cycling phases, appearing in the medial side of the femoral cartilage, the end of the menisci, and the medial and marginal parts of the tibial cartilage. These correspond to the areas of knee pain that are prone to wear during periodic exercise (Silberman, 2013). Cyclists with overused knee pain showed a greater medial projection of the knees which could be the result of the long-term improper stress of cartilages and altered muscle activations (Bini & Flores Bini, 2018). Previous studies indicate that lower saddle height is linked to increased knee joint loads and greater compressive stress on the patellofemoral joint, which could lead to joint pain such as patellar pain syndrome (Callaghan, 2005; Wanich et al., 2007). This is supported by our results from FE analysis that both stress and contact pressure on cartilage and meniscus were less at a higher saddle height. Knee flexion from upright to 90° was simulated in another FE study (Zhang, 2009). They came to the same conclusions, and the stress of menisci and cartilages they reported were comparable to ours, even though the adopted knee flexion angle was less than that in cycling. The maximum principal logarithmic strain is the largest tensile strain reflecting the elongation of cartilages and menisci. Excessive tensile strain can indicate areas prone to damage or overloading. This parameter also declined with the increase of saddle height, because lower stress translates to reduced deformation in the tissues.

From a kinematic point, higher saddle heights lead to a lower flexion angle of the knee joint (R. R. Bini et al., 2014). This less extreme knee position reduces shear and compressive loads. According to the results of a cadaveric experiment (Hofer et al., 2011), the posterior translation of knee flexion was limited by the PCL. But the limiting effect almost disappears at a higher flexion angle (more than 90°), and the knee may depend on impingement between the posterior cartilages and menisci which would cause the high stress and strain of these soft tissues.

The pressure between the femur and tibia is influenced by the quadriceps and hamstring muscles as well as the contact area between the bone cartilages. The greater muscle forces of the quadriceps and increased contact area are related to lower saddle heights (Salsich et al., 2003). However, our results suggest that only the contact area between the tibial cartilage and the menisci increased as the saddle height decreased. The discrepancy could be due to the different range of knee joint angles that were examined. Many studies have reported a wide range of contact areas between knee cartilages and menisci from 140 to 1350 mm^2 (Wang et al., 2014). Our results are in this range but on the low side. The differences of these area data stem from the quality of MRI data, modeling variations, and the angle range of knee joint flexion. The conclusions of this study cannot be directly verified because no study has yet to describe the contact area between cartilage and meniscus during cycling. Additionally, the contact force of the knee joint and stress of cartilages were reduced at a higher saddle height. Therefore, it is reasonable that the contact area, as a conversion bridge between the joint contact force and tissue stress, was maximum at 100% GTH between the femoral cartilage and menisci. The reduced joint contact force combined with the increased contact area contributes to the reduction in its stress. Studies have demonstrated that patellofemoral pressure tends to reach a plateau at saddle heights close to 100 ± 4% of GTH which matches the results of our study (Rodrigo Rico Bini & Patria A Hume, 2014). On the other hand, the variation range of the contact area was minimal at the saddle height of 100% GTH, which indicates the stability of knee motion at this moderate height. However, the condition of 105% GTH had the smallest range of variation for contact pressure and stress, which might be because the high saddle height significantly lowered their maximum values.

In summary, this study developed a FE model to investigate the biomechanics of the knee joint during cycling, focusing on the stress distribution, strain, contact pressure, and contact area. The findings align with prior research that lower saddle height and greater flexion angle lead to increased stress and pressure on the knee joint. While individual variations in outcomes may exist, the results provide valuable insights into knee joint behavior with different saddle heights, compensating for the limited research on dynamic FE models of knee movements during cycling.

5.5 Machine Learning Model for Saddle Height Classification

Saddle height optimization is crucial for preventing injuries, maximizing cycling performance, and ensuring comfort (Peveler, 2008). Traditional methods for setting the saddle height could be subjective and prone to inaccuracies such as goniometry or the LeMond formula. The joint angle of lower limbs is one of the kinematic metrics that is significantly affected by saddle height during cycling (R. R. Bini et al., 2014). Some studies defined a recommended range of saddle height based on the flexion angle of the knee joint (Peveler, 2011; Rodrigo Bini, 2011). However, the static joint angle cannot reflect the individual differences in the movement. ML models can provide data-driven and personalized feedback, which offers more objective and precise recommendations. A series of features related to joint angles of the hip, knee, and ankle were calculated, and some of them were selected into training and testing sets. The final ML model, after training, refining, and comparing with other algorithms, can accurately recognize whether the saddle height is too high, too low, or appropriate.

Most parameters of the lower-limb joint angles differed significantly among the three levels of saddle heights, including the joint motions in sagittal, frontal, and transverse planes. Previous studies (Bini, 2021; R. R. Bini et al., 2014; Hummer et al., 2021; Tim Evens, 2019) showed that when the saddle height decreased, the dorsiflexion and ROM of the ankle, the flexion and abduction of the knee, and the flexion of the hip would increase, while the abduction-adduction ROM of the hip would reduce. These changes would be reflected by the range, maximum, minimum, and means of joint angles. Additionally, the RMS, Max timing, Min timing, CV, and SD of joint angles were calculated. The statistical results indicated that the X-axis knee joint angle, which was the abduction-adduction angle, had the most significant difference among the three groups. When the saddle height increased, the maximum, mean, and RMS declined significantly, which supports the earlier findings that the abduction knee joint angle increased by 4.5° at the low saddle height (Wang et al., 2020). The mean and RMS values of the X-axis knee joint angle also were the most accurate predictors to classify the saddle height in four ML models. This implies that the potential effects of saddle height on the joint kinematics on the frontal plane of the knee are even greater than the widely studied effects on the sagittal plane.

The loads on the frontal plane of the knee joint are closely related to cycling-overuse injuries. For instance, excessive internal knee abduction moments can lead to medial knee pain and even aggravate knee osteoarthritis (Thorsen et al., 2020). The increased adduction moment could change patellar tracking and lead to patellofemoral pain syndrome (Van Zyl, 2001). Even relatively low joint force and moment over thousands of abduction-adduction motions in cycling may cause damage (Nigg, 1985). Therefore, it is crucial to investigate the effects of saddle height on the kinematics and the loads in the frontal plane of the knee.

The classification accuracy of selected features based on knee joints was higher than that of hip and ankle joints, regardless of the ML models. This is consistent with previous findings that the kinematics of knee joints were most affected by the varied saddle height. The analysis of earlier research (Rodrigo R. Bini, 2010) reported a higher F value of the mean angle of the knee joint than that of the ankle and hip joints, meaning a stronger relationship. A change of 15% in saddle height affected the ROM of knee joint mostly among the lower limb joints (Rugg & Gregor, 1987). This may be because the knee joint has the largest ROM and contributes more than half of the total mechanical work in cycling (R. R. Bini et al., 2014). However, features of hip and ankle joints must be included to increase accuracy, as the classification accuracy based on only the features of knee joints was about 80%.

The KNN model outperformed the other three ML models in terms of saddle height classification. A common characteristic of the four models is that they presented a lower accuracy rate in the recognition of moderate saddle height compared to high and low saddle heights, especially the NB model with an accuracy of only 59.91%. This is because joint angles alter more significantly at more extreme saddle height conditions, enabling the model to capture features that are more significantly different. Compared to the high and low saddle height levels, which contained only one condition (105% GTH for high level and 95% GTH for low level), the moderate height level included conditions from 97% to 103% of GTH, leading to a greater range of variation in joint angles. This increases the difficulty of model identification. The individual riding habits and characteristics of participants were reduced by data normalization. This operation improved the recognition accuracy. Although the dataset contains features of only lower-limb joint angles, the low correlation coefficients suggest that the feature selection process successfully identified a set of complementary and non-redundant features. Some studies demonstrated that knee extension moment, oxygen uptake, and cycling efficiency were substantially impacted by variations in saddle height (Ferrer-Roca, 2012; Hummer et al., 2021). However, some conclusions remain controversial. Other non-controversial metrics affected by saddle height, especially about the kinetics, could perhaps be included in the model later.

We are unable to compare the accuracy rate with other studies since we could not find a ML model that identified the saddle heights during dynamic cycling. But the KNN model in this study reached a classification accuracy of 99.79% which already shows its superiority and adaptability. Additionally, there are ML models for recognizing cadence (Hollaus et al., 2022) and pedaling profile (Xu et al., 2015) with accuracy rates of over 95%, with conveniently acquiring data by inertial measurement unit (IMU). The joint angles adopted in this study can also be measured conveniently by IMU with low errors per pedaling cycle (Obradović & Stančin, 2023). Therefore, IMU can be used to measure joint angles in future studies which facilitates the measurement process. Integrated with other ML models can achieve the purpose of the real-time comprehensive assessment of the cyclist's riding state.

5.6 Practical Implication and Recommendations

This study established a complete set of methods and tools for studying cycling biomechanics comprehensively by adopting saddle heights and workload levels as the independent variables. Muscle activations, muscle forces, joint contact forces, and riding symmetry of lower limbs have been thoroughly studied. The findings have significant practical implications for cycling performance, injury prevention, and optimization of bike fitting techniques.

Saddle height is one of the most crucial factors influencing cycling comfort, performance, and injury risk. A well-adjusted saddle height helps maintain optimal biomechanics by reducing muscle fatigue, preventing joint strain, and ensuring efficient energy transfer. The study of muscle activation, muscle forces, and joint loads revealed that 100% of GTH is likely the optimal saddle height for most cyclists. Cycling symmetry is also important for improving efficiency and reducing the risk of overuse injuries. We found that the symmetry of PRFs was best maintained at the saddle heights between 100% and 103% of GTH, while higher saddle height led to an increase in the asymmetry of knee joint angle. On the other hand, the FE analysis showed that the stress and strain on the menisci and cartilages of the knee joint decreased as the saddle height increased, which could reduce the likelihood of degenerative joint conditions such as osteoarthritis and meniscus wear. But too high saddle height may lead to decreased riding efficiency, discomfort, reduced stability, and more asymmetry. Therefore, cyclists should make adjustments based on the saddle height of 100% GTH which provides a balanced position that minimizes stress on the knee joint, optimizes pedaling efficiency, and ensures symmetric distribution of PRF. According to our results, small adjustments to saddle height within 3% are recommended given individual differences in comfort and riding characteristics.

The study demonstrated that higher workloads resulted in increased activation of RF and BF muscles, as well as higher joint forces in the hip, knee, and ankle. Therefore, managing cycling workload is a critical factor in preventing muscle fatigue and joint overload, both of which can lead to acute or chronic injuries. Cyclists should monitor their training intensity and adjust their workload according to their individual fitness level and biomechanical feedback. Coaches should design training regimens to gradually increase the workload while ensuring the cyclists have built muscle strength without overwhelming their MSK system. Clinicians working with injured cyclists should consider lower-intensity cycling sessions (e.g., 25% FTP) to promote rehabilitation while maintaining aerobic fitness.

The developed KNN model has a high classification accuracy for the saddle height. By using the features of lower-limb joint angles as inputs, the model accounts for individual dynamic differences in riding, offering a more personalized and objective alternative to generic saddle height formulas. Bike fitters could consider integrating it into the fitting process to automate bike fitting and provide recommendations.

5.7 Limitations

Although this study provides valuable insights into the relationship between saddle height, workload level and cycling biomechanics such as muscle activation and joint loads, several limitations must be acknowledged.

First, the standardized bicycle structure may not meet the personalized needs of the subjects for other settings, such as the height and distance of the handlebar. This could lead to an uncomfortable riding state for the subjects and negatively affect the experimental data. Second, only young subjects with amateur riding experience were recruited. Research showed that cyclists with different riding levels and experiences had obvious physiological differences (Sallet, 2006) and used distinct muscle recruitment strategies (Chapman et al., 2008). Cyclists at different ages also have distinct degrees of physical fitness. Therefore, the conclusions might not apply to riders of competitional levels or without experience. Age-related differences in flexibility, strength, and joint mobility may further limit the applicability of the findings across diverse populations. Thirdly, because of the limited number of EMG sensors, EMG signals were measured for only four muscles of each leg, which limited the in-depth study of muscle coordination patterns and failed to verify the correctness of other muscle forces calculated from the MSK model. Fourthly, we employed a lower workload compared to previous studies (Bini & Hume, 2013; Fang et al., 2015; Rodrigo R. Bini, 2010) to lessen the fatigue impact, which might contribute to the lack of significant differences in the results.

The developed MSK multibody model contains detailed lower limb muscles and only simplified upper body, since cycling is primarily a periodic motion of lower limbs. But research indicates that upper body position has influence on muscle forces, aerodynamics, and mechanical contributions of lower-limb joints (Bini et al., 2019). Therefore, it is necessary to establish a model with detailed upper body for cycling. On the other hand, given the large computation cost of FE analysis, the bones in the established knee joint model were simplified as rigid bodies, and main ligaments and muscles were simplified to connectors without considering their morphology. The material properties of individual components such as PFL and OPL were empirically fitted using engineering formulas, because no relevant experimental data were found. These might weaken the calculation accuracy. Studies indicated that knee flexion was accompanied by internal rotation (Wilson, 2000), but no internal rotation load was applied in this study. Although the rotation angle during cycling is small (Thorsen et al., 2020), this may compromise the simulation accuracy to some extent.

In the development of ML model for saddle height classification, only the joint angles of right leg were used. The inclusion of data from both legs and the additional kinetic parameters would enable a more comprehensive analysis. Besides, the joint angles were measured and calculated by the motion capture system which is more complex than IMU measurement.

CHAPTER 6 CONCLUSION AND FUTURE WORK

6.1 Significance of Study

Saddle height and workload level are important factors in cycling sports, which are closely related to cycling performance and injury risks. Although they have been investigated in previous studies, the conclusions remain controversial. This study carried out a systematic and in-depth analysis of their influence through experimental measurement, dynamics simulation, and FE analysis.

The findings highlight the importance of selecting an appropriate saddle height, not only for improving muscle activation and pedaling symmetry but also for minimizing joint stresses and the likelihood of overuse injuries. Besides, the workload significantly affected the muscle forces of the main power muscles during cycling and the joint contact forces of the hip, knee, and ankle. This suggests that pursuing a large workload mindlessly for building muscle is improper which could cause overuse injuries of lower limb joints. For injured cyclists and patients, the individual FTP should be used as a reference standard to set a relatively lower workload. In the last part, we developed a ML model for identifying the appropriateness of saddle height using the features calculated from joint angles. This provides an accurate and efficient tool for personalized and data-driven solutions in cycling biomechanics.

The developed MSK model contains more lower-limb muscles than previous models. It can be applied to each cyclist by length–mass–fat scaling, and various riding conditions by changing input parameters such as PRFs and trajectories of markers. These improve the generality of the MSK model and provide a powerful tool for future research on muscle forces, joint forces, and their coordination patterns in cycling. The established FE model may be the first model that dynamically simulates the motion of the knee joint during cycling driven by muscle forces and pedal forces, even though this model was based on the MRI of a specific subject. The FE results offer more detailed biomechanical information, namely the influence of saddle height on the cartilages and menisci of knee joints, which is crucial for the examination and prevention of cycling-related meniscus wear and cartilage degradation.

This research holds significant value for cyclists, coaches, and rehabilitation clinicians by providing critical insights into the complex interplay between saddle height, cycling workload, and the biomechanics of lower limb muscles and joints. Cyclists can benefit from the recommendations on selecting an appropriate saddle height (100%-103% of GTH) to enhance pedaling symmetry, reduce joint stress, and balance muscle activation, as well as improve both comfort and riding efficiency. Coaches can leverage the findings to design targeted training programs that optimize biomechanics, monitor symmetry, and incorporate ML models for precise adjustments. For rehabilitation clinicians, the study offers practical guidance on managing joint loads, mitigating injury risks, and tailoring recovery plans that prioritize joint and muscle health. These contributions advance cycling biomechanics, fostering safer, more efficient, and personalized cycling practices.

6.2 Conclusions

This research provides a comprehensive analysis of how saddle height and workload level influence the biomechanics of lower limbs in cycling, offering key insights into optimizing performance and reducing injury risks for cyclists. Several important conclusions can be drawn:

Firstly, the GAS was most influenced by changes in saddle height, while the RF and BF were more sensitive to the variations in workload. A saddle height of around 100% of GTH balances muscle activation and is recommended for cyclists. Secondly, lower saddle heights and higher workloads increase the forces on the hip, knee, and ankle joints. Conversely, higher saddle heights within the physiological range could alleviate knee joint stress to prevent overuse injuries. Thirdly, optimal symmetry of PRFs was observed at the saddle heights of 100% and 103% of GTH, and increasing saddle height resulted in greater asymmetry in the knee joint flexion. Fourthly, FE analysis revealed that stress and strain on the cartilages and menisci of the knee joint decreased with higher saddle heights. Despite this, excessively high saddle heights may lead to biomechanical inefficiencies and discomfort, emphasizing the need for a moderate setting that balances joint protection and riding performance. Lastly, a KNN ML model with high accuracy was successfully developed to identify the saddle height using joint angle features. This approach highlights the potential for leveraging data-driven tools in cycling biomechanics to provide personalized and objective recommendations.

6.3 Future Study

This study has investigated the biomechanics of lower-limb muscles and joints during cycling with various saddle heights and workloads. As the adopted workload in the experiment was relatively low, investigating larger workloads and other cycling conditions such as varied terrains and sprinting could offer a more holistic understanding of the influence of workload. This study primarily involved a homogeneous group of participants. Future research should include a broader demographic, incorporating diverse age groups, genders, and cycling ability. Besides, longitudinal studies are needed to evaluate the long-term effects of saddle height adjustments and workload variations on the lower-limb biomechanics.

The current MSK multibody model only contains detailed lower limb muscles. An accurate full-body MSK model of cyclist should be developed to explore the effect of riding conditions on the activation levels and coordination patterns of whole-body muscles. In the FE model of the knee joint, the bones were simplified as rigid bodies to explore the stress and strain of soft tissues. The future FE model should employ material properties such as elastic modulus and Poisson's ratio for bones and even include hip and ankle joints. This would enable the computation of stress-strain distributions of hip, ankle, and bones under various riding conditions.

The KNN model demonstrated the potential of ML in saddle height identification. Future studies should incorporate additional features such as muscle activations, power output, and anthropometric parameters to predict and classify the different riding conditions and cycling performance. Additionally, IMU can be used to collect data easily under other riding conditions and even outdoor cycling to improve the universality of the model.

APPENDICES

Appendix table 1. A generalized estimating equation model to compare the effects of saddle height and workload level on the mean muscle forces adjusted for gender, BMI, and cadence

Muscle	Parameter	Mean muscle force		
		Effect (β)	*95% Wald CI*	*p-value*
RF	Gender	0.122	-0.10 to 0.344	0.282
	BMI	0.025	-0.035 to 0.086	0.406
	Cadence	0.004	-0.003 to 0.011	0.234
	Height = 105%GTH	-0.355	-0.423 to -0.288	$< 0.001^*$
	Height = 100%GTH	-0.096	-0.141 to -0.052	$< 0.001^*$
	Height = 95%GTH	Reference		
	Workload = 75%FTP	0.024	-0.005 to 0.053	0.106
	Workload = 50%FTP	0.019	-0.015 to 0.053	0.273
	Workload = 25%FTP	Reference		
VL	Gender	0.059	-0.064 to 0.181	0.347
	BMI	0	-0.045 to 0.045	0.994
	Cadence	0.001	-0.003 to 0.004	0.641
	Height = 105%GTH	-0.144	-0.183 to -0.104	$< 0.001^*$
	Height = 100%GTH	-0.032	-0.056 to -0.009	0.007^*
	Height = 95%GTH	Reference		
	Workload = 75%FTP	0.018	0.004 to 0.031	0.010^*
	Workload = 50%FTP	0.014	0.002 to 0.026	0.022^*
	Workload = 25%FTP	Reference		
VM	Gender	0.067	-0.057 to 0.191	0.289
	BMI	0	-0.045 to 0.045	0.995
	Cadence	0.001	-0.003 to 0.005	0.582
	Height = 105%GTH	-0.152	-0.190 to -0.113	$< 0.001^*$
	Height = 100%GTH	-0.036	-0.060 to -0.013	0.003^*
	Height = 95%GTH	Reference		
	Workload = 75%FTP	0.016	0.003 to 0.029	0.017^*
	Workload = 50%FTP	0.013	0.002 to 0.025	0.026^*
	Workload = 25%FTP	Reference		
BF	Gender	-0.287	-0.499 to -0.074	0.008^*
	BMI	0.112	0.051 to 0.173	$< 0.001^*$
	Cadence	0.012	0.004 to 0.021	0.004^*
	Height = 105%GTH	-0.062	-0.162 to 0.039	0.228
	Height = 100%GTH	-0.081	-0.144 to -0.017	0.013^*
	Height = 95%GTH	Reference		
	Workload = 75%FTP	0.119	0.054 to 0.184	$< 0.001^*$
	Workload = 50%FTP	0.053	0.016 to 0.091	0.005^*
	Workload = 25%FTP	Reference		

GAS	Gender	0.238	-0.379 to 0.855	0.449
	BMI	-0.127	-0.261 to 0.008	0.065
	Cadence	0.020	0.004 to 0.036	0.014^{*}
	Height = 105%GTH	-0.214	-0.403 to -0.026	0.026^{*}
	Height = 100%GTH	-0.066	-0.149 to 0.018	0.126
	Height = 95%GTH	Reference		
	Workload = 75%FTP	-0.268	-0.389 to -0.148	$< 0.001^{*}$
	Workload = 50%FTP	-0.142	-0.210 to -0.074	$< 0.001^{*}$
	Workload = 25%FTP	Reference		
SOL	Gender	0.014	-0.357 to 0.385	0.942
	BMI	-0.049	-0.130 to 0.033	0.244
	Cadence	0.002	-0.006 to 0.011	0.614
	Height = 105%GTH	-0.065	-0.147 to 0.016	0.115
	Height = 100%GTH	-0.047	-0.026 to 0.121	0.210
	Height = 95%GTH	Reference		
	Workload = 75%FTP	-0.107	-0.171 to -0.043	0.001^{*}
	Workload = 50%FTP	-0.060	-0.087 to -0.034	$< 0.001^{*}$
	Workload = 25%FTP	Reference		
TA	Gender	-0.585	-1.261 to 0.091	0.090
	BMI	0.214	0.066 to 0.362	0.004^{*}
	Cadence	0.030	-0.002 to 0.062	0.068
	Height = 105%GTH	0.294	0.058 to 0.531	0.015^{*}
	Height = 100%GTH	0.113	-0.082 to 0.308	0.257
	Height = 95%GTH	Reference		
	Workload = 75%FTP	0.208	0.049 to 0.366	0.010^{*}
	Workload = 50%FTP	0.052	-0.042 to 0.146	0.275
	Workload = 25%FTP	Reference		
GluMax	Height × Workload	-	-	0.596
	Gender	0.039	-0.023 to 0.101	0.215
	BMI	0.043	0.023 to 0.063	$< 0.001^{*}$
	Cadence	0.004	0.002 to 0.005	$< 0.001^{*}$
	Height = 105%GTH	-0.096	-0.117 to -0.075	$< 0.001^{*}$
	Height = 100%GTH	-0.050	-0.068 to -0.031	$< 0.001^{*}$
	Height = 95%GTH	Reference		
	Workload = 75%FTP	0.042	0.020 to 0.064	$< 0.001^{*}$
	Workload = 50%FTP	0.025	0.014 to 0.035	$< 0.001^{*}$
	Workload = 25%FTP	Reference		

RF: rectus femoris; VL: vastus lateralis; VM: vastus medialis; BF: biceps femoris; GAS: gastrocnemius; SOL: soleus; TA: tibialis anterior; GluMax: gluteus maximus; BMI: body mass index; GTH: greater trochanter height; FTP: functional threshold power. $^{*}p < 0.05$*, compared with reference riding condition (null model).*

Appendix table 2. A generalized estimating equation model to compare the effects of saddle height and workload level on the maximum muscle forces adjusted for gender, BMI, and cadence.

Muscle	**Parameter**	**Maximum muscle force**		
		Effect (β)	*95% Wald CI*	*p-value*
RF	Gender	0.004	-0.136 to 0.144	0.952
	BMI	0.041	0.006 to 0.076	0.021*
	Cadence	0.007	0 to 0.013	0.045*
	Height = 105%GTH	-0.158	-0.2 to -0.117	< 0.001*
	Height = 100%GTH	-0.019	-0.059 to 0.02	0.337
	Height = 95%GTH	Reference	-	-
	Workload = 75%FTP	0.048	0.014 to 0.081	0.006*
	Workload = 50%FTP	0.005	-0.031 to 0.041	0.791
	Workload = 25%FTP	Reference	-	-
VL	Gender	-0.056	-0.169 to 0.057	0.328
	BMI	0.001	-0.028 to 0.031	0.937
	Cadence	0.001	-0.007 to 0.008	0.817
	Height = 105%GTH	0.046	-0.003 to 0.095	0.067
	Height = 100%GTH	0.024	-0.011 to 0.059	0.184
	Height = 95%GTH	Reference		
	Workload = 75%FTP	0.007	-0.020 to 0.033	0.625
	Workload = 50%FTP	0.014	-0.009 to 0.037	0.228
	Workload = 25%FTP	Reference		
VM	Gender	-0.057	-0.167 to 0.053	0.312
	BMI	0.003	-0.026 to 0.033	0.817
	Cadence	0.001	-0.006 to 0.009	0.790
	Height = 105%GTH	0.038	-0.011 to 0.086	0.128
	Height = 100%GTH	0.020	-0.015 to 0.055	0.271
	Height = 95%GTH	Reference		
	Workload = 75%FTP	0.002	-0.023 to 0.028	0.855
	Workload = 50%FTP	0.013	-0.011 to 0.036	0.292
	Workload = 25%FTP	Reference		
BF	Gender	-0.230	-0.426 to -0.035	0.021*
	BMI	0.088	0.028 to 0.148	0.004*
	Cadence	0.010	0.003 to 0.016	0.003*
	Height = 105%GTH	-0.040	-0.128 to 0.048	0.376
	Height = 100%GTH	-0.049	-0.124 to 0.026	0.197
	Height = 95%GTH	Reference		
	Workload = 75%FTP	0.113	0.042 to 0.183	0.002*
	Workload = 50%FTP	0.040	0.002 to 0.078	0.038*
	Workload = 25%FTP	Reference		
GAS	Gender	0.159	-0.306 to 0.625	0.502
	BMI	-0.064	-0.201 to 0.073	0.358
	Cadence	0.022	0.009 to 0.035	0.001*
	Height = 105%GTH	-0.071	-0.239 to 0.097	0.409
	Height = 100%GTH	-0.011	-0.114 to 0.092	0.835
	Height = 95%GTH	Reference		
	Workload = 75%FTP	-0.267	-0.371 to -0.163	< 0.001*
	Workload = 50%FTP	-0.094	-0.201 to 0.012	0.083
	Workload = 25%FTP	Reference		

SOL	Gender		-0.066	-0.247 to 0.115	0.475
	BMI		< 0.001	-0.060 to 0.060	1
	Cadence		0.011	0.006 to 0.016	< 0.001*
	Height = 105%GTH		0.136	0.062 to 0.210	< 0.001*
	Height = 100%GTH		0.085	0.029 to 0.142	0.003*
	Height = 95%GTH		Reference		
	Workload = 75%FTP		-0.087	-0.129 to -0.048	< 0.001*
	Workload = 50%FTP		-0.044	-0.073 to -0.014	0.003*
	Workload = 25%FTP		Reference		
TA	Gender		-0.442	-1.016 to 0.131	0.131
	BMI		0.185	0.054 to 0.316	0.006*
	Cadence		0.020	-0.006 to 0.047	0.131
	Height = 105%GTH		0.151	-0.062 to 0.365	0.164
	Height = 100%GTH		0.039	-0.113 to 0.191	0.616
	Height = 95%GTH		Reference		
	Workload = 75%FTP		0.112	-0.023 to 0.247	0.104
	Workload = 50%FTP		0.019	-0.065 to 0.104	0.659
	Workload = 25%FTP		Reference		
GluMax	Height × Workload		-	-	0.004*
	Gender		0.170	-0.127 to 0.468	0.261
	BMI		0.027	-0.046 to 0.101	0.462
	Cadence		0	-0.003 to 0.004	0.809
	Height = 105%GTH	Workload = 75%FTP	0.035	-0.009 to 0.078	0.116
		Workload = 50%FTP	0.052	0.010 to 0.095	0.017*
		Workload = 25%FTP	Reference		
	Height = 100%GTH	Workload = 75%FTP	0.058	0.032 to 0.084	< 0.001*
		Workload = 50%FTP	0.026	-0.001 to 0.052	0.055
		Workload = 25%FTP	Reference		
	Height = 95%GTH	Workload = 75%FTP	0.035	-0.004 to 0.075	0.078
		Workload = 50%FTP	0.028	-0.002 to 0.057	0.063
		Workload = 25%FTP	Reference		
	Workload = 75%FTP	Height = 105%GTH	-0.034	-0.076 to 0.009	0.049*
		Height = 100%GTH	0.006	-0.045 to 0.058	0.813
		Height = 95%GTH	Reference		
	Workload = 50%FTP	Height = 105%GTH	0.013	-0.039 to 0.065	0.620
		Height = 100%GTH	0.010	-0.049 to 0.070	0.739
		Height = 95%GTH	Reference		
	Workload = 25%FTP	Height = 105%GTH	-0.023	-0.093 to 0.047	0.519
		Height = 100%GTH	-0.005	-0.047 to 0.037	0.804
		Height = 95%GTH	Reference		

RF: rectus femoris; VL: vastus lateralis; VM: vastus medialis; BF: biceps femoris; GAS: gastrocnemius; SOL: soleus; TA: tibialis anterior; GluMax: gluteus maximus; BMI: body mass index; GTH: greater trochanter height; FTP: functional threshold power. $^{*}p < 0.05$*, compared with reference riding condition (null model).*

Appendix table 3. A generalized estimating equation model to compare the effects of saddle height and workload level on the mean of absolute joint contact forces adjusted for gender, BMI, and cadence

Joint force	**Parameter**		**Mean joint force**		
			Effect (β)	*95% Wald CI*	*p-value*
Hip M-L	Gender		0.017	3.389 to 5.105	0.799
	BMI		0.017	0.011 to 0.077	0.010*
	Cadence		0.002	-0.001 to 0.005	0.220
	Height = 105%GTH		-0.089	-0.127 to -0.052	< 0.001*
	Height = 100%GTH		-0.033	-0.059 to -0.007	0.014*
	Height = 95%GTH		Reference		
	Workload = 75%FTP		0.043	0.014 to 0.072	0.004*
	Workload = 50%FTP		0.033	0.017 to 0.050	< 0.001*
	Workload = 25%FTP		Reference		
Hip P-D	Gender		-0.070	-0.158 to 0.019	0.123
	BMI		0.042	0.017 to 0.067	0.001*
	Cadence		0.003	0 to 0.006	0.031*
	Height = 105%GTH		-0.013	-0.043 to 0.016	0.374
	Height = 100%GTH		-0.008	-0.031 to 0.015	0.489
	Height = 95%GTH		Reference		
	Workload = 75%FTP		0.052	0.032 to 0.071	< 0.001*
	Workload = 50%FTP		0.028	0.017 to 0.039	< 0.001*
	Workload = 25%FTP		Reference		
Hip A-P	Gender		-0.058	-0.231 to 0.115	0.513
	BMI		0.108	0.069 to 0.147	< 0.001*
	Cadence		0.001	-0.007 to 0.010	0.796
	Height = 105%GTH		-0.193	-0.248 to -0.138	< 0.001*
	Height = 100%GTH		-0.107	-0.142 to -0.072	< 0.001*
	Height = 95%GTH		Reference		
	Workload = 75%FTP		0.054	0.007 to 0.100	0.024*
	Workload = 50%FTP		0.022	-0.002 to 0.046	0.072
	Workload = 25%FTP		Reference		
Hip resultant	Gender		-0.065	-0.154 to 0.025	0.155
	BMI		0.043	0.017 to 0.068	0.001*
	Cadence		0.003	0 to 0.005	0.037*
	Height = 105%GTH		-0.022	-0.051 to 0.007	0.139
	Height = 100%GTH		-0.011	-0.033 to 0.010	0.305
	Height = 95%GTH		Reference		
	Workload = 75%FTP		0.051	0.031 to 0.071	< 0.001*
	Workload = 50%FTP		0.029	0.018 to 0.039	< 0.001*
	Workload = 25%FTP		Reference		
Knee M-L	Height × Workload		-	-	< 0.001*
	Gender		-0.045	-0.148 to 0.058	0.391
	BMI		0.020	-0.019 to 0.059	0.325
	Cadence		0.001	-0.002 to 0.005	0.511
	Height = 105%GTH	Workload = 75%FTP	0.007	-0.0126 to 0.013	0.501
		Workload = 50%FTP	0.006	-0.026 to 0.037	0.721
		Workload = 25%FTP	Reference		
	Height = 100%GTH	Workload = 75%FTP	0.012	-0.018 to 0.042	0.438

		Workload = 50%FTP	0.024	0.003 to 0.045	0.024*
		Workload = 25%FTP	Reference		
	Height = 95%GTH	Workload = 75%FTP	0.036	-0.001 to 0.073	0.053
		Workload = 50%FTP	0.014	-0.008 to 0.034	0.234
		Workload = 25%FTP	Reference		
	Workload= 75%FTP	Height = 105%GTH	-0.269	-0.317 to -0.220	< 0.001*
		Height = 100%GTH	-0.084	-0.128 to -0.040	< 0.001*
		Height = 95%GTH	Reference		
	Workload= 50%FTP	Height = 105%GTH	-0.216	-0.274 to -0.158	< 0.001*
		Height = 100%GTH	-0.036	-0.076 to 0.004	0.080
		Height = 95%GTH	Reference		
	Workload= 25%FTP	Height = 105%GTH	-0.215	-0.274 to -0.155	< 0.001*
		Height = 100%GTH	-0.054	-0.097 to -0.010	0.016*
		Height = 95%GTH	Reference		
Knee P-D	Gender		-0.029	-0.104 to 0.047	0.454
	BMI		0.034	0.016 to 0.052	< 0.001*
	Cadence		0.006	0.004 to 0.008	< 0.001*
	Height = 105%GTH		0.001	-0.037 to 0.034	0.937
	Height = 100%GTH		0.008	-0.016 to 0.033	0.508
	Height = 95%GTH		Reference		
	Workload = 75%FTP		0.065	0.024 to 0.107	0.002*
	Workload = 50%FTP		0.027	-0.001 to 0.056	0.063
	Workload = 25%FTP		Reference		
Knee A-P	Gender		0.012	-0.112 to 0.136	0.853
	BMI		-0.001	-0.044 to 0.043	0.975
	Cadence		0.001	-0.003 to 0.005	0.501
	Height = 105%GTH		-0.118	-0.155 to -0.082	< 0.001*
	Height = 100%GTH		-0.026	-0.047 to -0.005	0.015*
	Height = 95%GTH		Reference		
	Workload = 75%FTP		0.008	-0.008 to 0.024	0.322
	Workload = 50%FTP		0.007	-0.006 to 0.020	0.306
	Workload = 25%FTP		Reference		
Knee resultant	Gender		-0.007	-0.121 to 0.108	0.908
	BMI		0.011	-0.021 to 0.044	0.503
	Cadence		0.002	-0.001 to 0.005	0.228
	Height = 105%GTH		-0.073	-0.101 to -0.044	< 0.001*
	Height = 100%GTH		-0.014	-0.037 to 0.010	0.261
	Height = 95%GTH		Reference		
	Workload = 75%FTP		0.021	0.003 to 0.039	0.026*
	Workload = 50%FTP		0.010	-0.003 to 0.022	0.124
	Workload = 25%FTP		Reference		
Ankle M-L	Gender		0.042	-0.226 to 0.311	0.757
	BMI		0.038	-0.060 to 0.136	0.447
	Cadence		0.007	0.003 to 0.011	0.002*
	Height = 105%GTH		-0.211	-0.339 to -0.083	0.001*
	Height = 100%GTH		-0.088	-0.161 to -0.015	0.018*
	Height = 95%GTH		Reference		
	Workload = 75%FTP		0.077	-0.010 to 0.164	0.083
	Workload = 50%FTP		0.008	-0.058 to 0.075	0.803
	Workload = 25%FTP		Reference		

Ankle P-D	Gender	-0.059	-0.292 to 0.174	0.620
	BMI	-0.004	-0.051 to 0.042	0.859
	Cadence	0.003	-0.002 to 0.008	0.184
	Height = 105%GTH	-0.024	-0.074 to 0.026	0.355
	Height = 100%GTH	-0.019	-0.021 to 0.069	0.351
	Height = 95%GTH	Reference		
	Workload = 75%FTP	-0.041	-0.072 to -0.011	0.009*
	Workload = 50%FTP	-0.032	-0.046 to -0.017	< 0.001*
	Workload = 25%FTP	Reference		
Ankle A-P	Gender	0.072	-0.231 to 0.375	0.643
	BMI	-0.036	-0.097 to 0.026	0.258
	Cadence	0.001	-0.007 to 0.009	0.821
	Height = 105%GTH	-0.227	-0.290 to -0.165	< 0.001*
	Height = 100%GTH	-0.041	-0.083 to 0.001	0.057
	Height = 95%GTH	Reference		
	Workload = 75%FTP	-0.038	-0.070 to -0.006	0.019*
	Workload = 50%FTP	-0.033	-0.052 to -0.015	< 0.001*
	Workload = 25%FTP	Reference		
Ankle resultant	Gender	-0.051	-0.284 to 0.182	0.668
	BMI	-0.005	-0.051 to 0.041	0.830
	Cadence	0.003	-0.002 to 0.008	0.219
	Height = 105%GTH	-0.036	-0.085 to 0.013	0.148
	Height = 100%GTH	-0.014	-0.023 to 0.051	0.466
	Height = 95%GTH	Reference		
	Workload = 75%FTP	-0.039	-0.068 to -0.009	0.010*
	Workload = 50%FTP	-0.031	-0.045 to -0.017	< 0.001*
	Workload = 25%FTP	Reference		

RF: rectus femoris; VL: vastus lateralis; VM: vastus medialis; BF: biceps femoris; GAS: gastrocnemius; SOL: soleus; TA: tibialis anterior; GluMax: gluteus maximus; BMI: body mass index; GTH: greater trochanter height; FTP: functional threshold power. $^{*}p < 0.05$*, compared with reference riding condition (null model).*

Appendix table 4. A generalized estimating equation model to compare the effects of saddle height and workload level on the maximum of absolute joint contact forces adjusted for gender, BMI, and cadence

Joint force	**Parameter**		**Maximum joint force**		
			Effect (β)	*95% Wald CI*	*p-value*
Hip M-L	Gender		0.059	-0.078 to 0.196	0.40
	BMI		0.046	0.004 to 0.088	0.031*
	Cadence		0.001	-0.002 to 0.004	0.540
	Height = 105%GTH		-0.015	-0.059 to 0.030	0.519
	Height = 100%GTH		-0.012	-0.060 to 0.037	0.640
	Height = 95%GTH		Reference		
	Workload = 75%FTP		0.048	0.018 to 0.078	0.002*
	Workload = 50%FTP		0.050	0.027 to 0.073	< 0.001*
	Workload = 25%FTP		Reference		
Hip P-D	Gender		-0.096	-0.221 to 0.029	0.132
	BMI		0.040	-0.001 to 0.081	0.054
	Cadence		0.001	-0.002 to 0.005	0.395
	Height = 105%GTH		0.018	-0.026 to 0.061	0.424
	Height = 100%GTH		0.015	-0.031 to 0.061	0.528
	Height = 95%GTH		Reference		
	Workload = 75%FTP		0.074	0.046 to 0.101	< 0.001*
	Workload = 50%FTP		0.036	0.026 to 0.046	< 0.001*
	Workload = 25%FTP		Reference		
Hip A-P	Gender		-0.140	-0.368 to 0.088	0.228
	BMI		0.084	0.030 to 0.137	0.002*
	Cadence		0.002	-0.003 to 0.007	0.403
	Height = 105%GTH		-0.125	-0.172 to -0.078	< 0.001*
	Height = 100%GTH		-0.064	-0.118 to -0.010	0.020*
	Height = 95%GTH		Reference		
	Workload = 75%FTP		0.087	0.045 to 0.129	< 0.001*
	Workload = 50%FTP		0.050	0.025 to 0.074	< 0.001*
	Workload = 25%FTP		Reference		
Hip resultant	Gender		-0.088	-0.214 to 0.037	0.169
	BMI		0.041	0 to 0.082	0.051
	Cadence		0.001	-0.002 to 0.004	0.408
	Height = 105%GTH		-0.015	-0.028 to 0.058	0.501
	Height = 100%GTH		-0.013	-0.033 to 0.059	0.579
	Height = 95%GTH		Reference		
	Workload = 75%FTP		0.074	0.047 to 0.101	< 0.001*
	Workload = 50%FTP		0.036	0.027 to 0.046	< 0.001*
	Workload = 25%FTP		Reference		
Knee M-L	Height × Workload		-	-	0.030*
	Gender		-0.126	-0.237 to -0.015	0.027*
	BMI		0.020	-0.005 to 0.045	0.110
	Cadence		0.001	-0.005 to 0.007	0.733
	Height = 105%GTH	Workload = 75%FTP	0.016	-0.054 to 0.022	0.414
		Workload = 50%FTP	0.012	-0.043 to 0.067	0.676
		Workload = 25%FTP	Reference		
	Height = 100%GTH	Workload = 75%FTP	0.018	-0.020 to 0.056	0.355

		Workload = 50%FTP	0.015	-0.018 to 0.049	0.371
		Workload = 25%FTP	Reference		
	Height = 95%GTH	Workload = 75%FTP	0.028	-0.024 to 0.080	0.289
		Workload = 50%FTP	0.002	-0.042 to 0.046	0.924
		Workload = 25%FTP	Reference		
	Workload= 75%FTP	Height = 105%GTH	-0.074	-0.149 to 0.001	0.050*
		Height = 100%GTH	-0.019	-0.071 to 0.032	0.459
		Height = 95%GTH	Reference		
	Workload= 50%FTP	Height = 105%GTH	0.020	-0.038 to 0.078	0.503
		Height = 100%GTH	0.025	-0.028 to 0.079	0.352
		Height = 95%GTH	Reference		
	Workload= 25%FTP	Height = 105%GTH	0.006	-0.065 to 0.077	0.875
		Height = 100%GTH	0.002	-0.044 to 0.047	0.936
		Height = 95%GTH	Reference		
Knee P-D	Gender		0.095	-0.063 to 0.252	0.237
	BMI		0.048	0.025 to 0.072	< 0.001*
	Cadence		0.009	0.005 to 0.014	< 0.001*
	Height = 105%GTH		-0.074	-0.178 to 0.031	0.168
	Height = 100%GTH		-0.038	-0.103 to 0.027	0.247
	Height = 95%GTH		Reference		
	Workload = 75%FTP		0.042	-0.031 to 0.115	0.259
	Workload = 50%FTP		-0.006	-0.045 to 0.033	0.765
	Workload = 25%FTP		Reference		
Knee A-P	Gender		-0.093	-0.20 to 0.014	0.088
	BMI		0.004	-0.026 to 0.034	0.807
	Cadence		0.002	-0.006 to 0.011	0.574
	Height = 105%GTH		-0.070	0.018 to 0.121	0.008*
	Height = 100%GTH		-0.038	-0.004 to 0.080	0.077
	Height = 95%GTH		Reference		
	Workload = 75%FTP		-0.008	-0.034 to 0.018	0.529
	Workload = 50%FTP		-0.003	-0.023 to 0.017	0.771
	Workload = 25%FTP		Reference		
Knee resultant	Gender		-0.066	-0.183 to 0.051	0.272
	BMI		0.010	-0.020 to 0.040	0.520
	Cadence		0.004	-0.003 to 0.011	0.284
	Height = 105%GTH		-0.020	-0.018 to 0.058	0.304
	Height = 100%GTH		-0.019	-0.012 to 0.049	0.231
	Height = 95%GTH		Reference		
	Workload = 75%FTP		0.009	-0.038 to 0.020	0.546
	Workload = 50%FTP		0.001	-0.018 to 0.016	0.915
	Workload = 25%FTP		Reference		
Ankle M-L	Gender		0.033	-0.134 to 0.201	0.696
	BMI		0.048	0 to 0.097	0.049*
	Cadence		0.011	0.006 to 0.016	< 0.001*
	Height = 105%GTH		-0.126	-0.248 to -0.003	0.045*
	Height = 100%GTH		-0.043	-0.133 to 0.046	0.341
	Height = 95%GTH		Reference		
	Workload = 75%FTP		0.066	-0.010 to 0.142	0.086
	Workload = 50%FTP		0.032	-0.034 to 0.097	0.340
	Workload = 25%FTP		Reference		

Ankle P-D	Gender	-0.016	-0.221 to 0.188	0.875
	BMI	0	-0.056 to 0.055	0.994
	Cadence	0.009	0.002 to 0.015	0.008*
	Height = 105%GTH	0.045	-0.022 to 0.112	0.192
	Height = 100%GTH	0.044	-0.001 to 0.088	0.055
	Height = 95%GTH	Reference		
	Workload = 75%FTP	-0.080	-0.120 to -0.040	< 0.001*
	Workload = 50%FTP	-0.048	-0.072 to -0.023	< 0.001*
	Workload = 25%FTP	Reference		
Ankle A-P	Gender	-0.001	-0.224 to 0.222	0.994
	BMI	-0.009	-0.052 to 0.034	0.684
	Cadence	0.009	0 to 0.017	0.042*
	Height = 105%GTH	-0.089	-0.142 to -0.036	0.001*
	Height = 100%GTH	0	-0.045 to 0.046	0.987
	Height = 95%GTH	Reference		
	Workload = 75%FTP	-0.047	-0.092 to -0.003	0.037*
	Workload = 50%FTP	-0.042	-0.075 to -0.009	0.014*
	Workload = 25%FTP	Reference		
Ankle resultant	Gender	-0.010	-0.216 to 0.195	0.921
	BMI	0.001	-0.054 to 0.055	0.980
	Cadence	0.009	0.003 to 0.016	0.005*
	Height = 105%GTH	0.032	-0.033 to 0.097	0.333
	Height = 100%GTH	0.035	-0.007 to 0.078	0.103
	Height = 95%GTH	Reference		
	Workload = 75%FTP	-0.082	-0.122 to -0.042	< 0.001*
	Workload = 50%FTP	-0.048	-0.073 to -0.024	< 0.001*
	Workload = 25%FTP	Reference		

RF: rectus femoris; VL: vastus lateralis; VM: vastus medialis; BF: biceps femoris; GAS: gastrocnemius; SOL: soleus; TA: tibialis anterior; GluMax: gluteus maximus; BMI: body mass index; GTH: greater trochanter height; FTP: functional threshold power. $^{*}p < 0.05$*, compared with reference riding condition (null model).*

REFERENCES

Abdullah, M. N., Mustapha, F., Muda, M. K. H., Arrifin, M. K. A., Rafie, A. S. M., & Shamsudin, M. A. (2015). Simulating bio-composite cycling helmet performance through FEA and CFD approaches. *Malaysian Journal of Movement, Health & Exercise*, *4*(1), 77-91.

Adouni, M., Aydelik, H., Faisal, T. R., & Hajji, R. (2024). The effect of body weight on the knee joint biomechanics based on subject-specific finite element-musculoskeletal approach. *Scientific Reports*, *14*(1). https://doi.org/10.1038/s41598-024-63745-x

Ahmadi, R., Rasoulian, S., Veisari, S. F., Parsaei, A., Heidary, H., Herzog, W., & Komeili, A. (2024). A Machine Learning Approach for Predicting Pedaling Force Profile in Cycling. *Sensors (Basel)*, *24*(19). https://doi.org/10.3390/s24196440

Akima, H., Maeda, K., & Shima, N. (2023). Neuromuscular activation of the quadriceps femoris, including the vastus intermedius, during isokinetic knee extensions. *Sci Rep*, *13*(1), 7674. https://doi.org/10.1038/s41598-023-34532-x

Akima, H., Takahashi, H., Kuno, S. Y., & Katsuta, S. (2004). Coactivation pattern in human quadriceps during isokinetic knee-extension by muscle functional MRI. *Eur J Appl Physiol*, *91*(1), 7-14. https://doi.org/10.1007/s00421-003-0942-z

Aleksieva, D., Ivanov, I., & Stefanov, L. G. (2020). Bilateral asymmetry of pedaling force at different levels of exercise intensity in cycle ergometer. *Pedagogy of Physical Culture and Sports*, *24*(5), 264-270. https://doi.org/10.15561/26649837.2020.0507

Althunyan, A. K., Darwish, M. A., & Abdel Wahab, M. M. (2017). Knee problems and its associated factors among active cyclists in Eastern Province, Saudi Arabia. *J Family Community Med*, *24*(1), 23-29. https://doi.org/10.4103/2230-8229.197178

Althunyan, A. K., Darwish, M. A., & Wahab, M. M. A. (2017). Knee problems and its associated factors among active cyclists in Eastern Province, Saudi Arabia. *Journal of Family & Community Medicine*, *24*(1), 23.

Amoroso, A., David J. Sanderson, and E. M. Henning. (1993). Kinematic and kinetic changes in cycling resulting from fatigue. *Proceedings of the 17th meeting of the American society of biomechanics*, *17*, 157-158.

Amoroso, A., Sanderson, D. J., & Henning, E. (1993). Kinematic and kinetic changes in cycling resulting from fatigue. Proceedings of the 17th meeting of the American society of biomechanics,

Arampatzis, A., Karamanidis, K., Stafilidis, S., Morey-Klapsing, G., DeMonte, G., & Bruggemann, G. P. (2006). Effect of different ankle- and knee-joint positions on gastrocnemius medialis fascicle length and EMG activity during isometric plantar flexion. *J Biomech*, *39*(10), 1891-1902. https://doi.org/10.1016/j.jbiomech.2005.05.010

Asplund, C., & St Pierre, P. (2004). Knee pain and bicycling: fitting concepts for clinicians. *The Physician and sportsmedicine*, *32*(4), 23-30.

Baino, F. (2011). Evaluation of the relationship between the body positioning and the postural comfort of non-professional cyclists: a new approach. *The Journal of sports medicine and physical fitness*, *51*(1), 59-65.

Bansal, M., Goyal, A., & Choudhary, A. (2022). A comparative analysis of K-Nearest Neighbor, Genetic, Support Vector Machine, Decision Tree, and Long Short Term Memory algorithms in machine learning. *Decision Analytics Journal*, *3*. https://doi.org/10.1016/j.dajour.2022.100071

Barbarossa, L. (2020). The Post Pandemic City: Challenges and Opportunities for a Non-Motorized Urban Environment. An Overview of Italian Cases. *Sustainability*, *12*(17). https://doi.org/10.3390/su12177172

Barratt, P. R., Martin, J. C., Elmer, S. J., & Korff, T. (2016). Effects of Pedal Speed and Crank Length on Pedaling Mechanics during Submaximal Cycling. *Med Sci Sports Exerc*, *48*(4), 705-713. https://doi.org/10.1249/MSS.0000000000000817

Barrios, C., Sala, D., Terrados, N., & Valentí, J. R. . (1997). Traumatic and overuse injuries in elite professional cyclists. *Sports Exercise and Injury*, *3*(4), 176-179.

Baum, B. S., & Li, L. (2003). Lower extremity muscle activities during cycling are influenced by load and frequency. *J Electromyogr Kinesiol*, *13*(2), 181-190. https://doi.org/10.1016/s1050-6411(02)00110-4

Bieuzen, F., Lepers, R., Vercruyssen, F., Hausswirth, C., & Brisswalter, J. (2007). Muscle activation during cycling at different cadences: effect of maximal strength capacity. *J Electromyogr Kinesiol*, *17*(6), 731-738. https://doi.org/10.1016/j.jelekin.2006.07.007

Bini, R. (2021). Influence of saddle height in 3D knee loads commuter cyclists: A statistical parametric mapping analysis. *Journal of sports sciences*, *39*(3), 275-288. https://doi.org/10.1080/02640414.2020.1816289

Bini, R., & Priego-Quesada, J. (2022). Methods to determine saddle height in cycling and implications of changes in saddle height in performance and injury risk: A systematic review. *J Sports Sci*, *40*(4), 386-400. https://doi.org/10.1080/02640414.2021.1994727

Bini, R. R., & Hume, P. A. (2015). Relationship between pedal force asymmetry and performance in cycling time trial. *J Sports Med Phys Fitness*, *55*, 892-898.

Bini, R. R., & Carpes, F. P. (2014). *Biomechanics of cycling*. Springer.

Bini, R. R., Carpes, F. P., Diefenthaeler, F., Mota, C. B., Guimaraes, A. C., & Grupo de Estudo e Pesquisa em, C. (2008). Physiological and electromyographic responses during 40-km cycling time trial: relationship to muscle coordination and performance. *J Sci Med Sport*, *11*(4), 363-370. https://doi.org/10.1016/j.jsams.2007.03.006

Bini, R. R., Daly, L., & Kingsley, M. (2019). Muscle force adaptation to changes in upper body position during seated sprint cycling. *J Sports Sci*, *37*(19), 2270-2278. https://doi.org/10.1080/02640414.2019.1627983

Bini, R. R., & Diefenthaeler, F. (2010). Kinetics and kinematics analysis of incremental cycling to exhaustion. *Sports Biomech*, *9*(4), 223-235. https://doi.org/10.1080/14763141.2010.540672

Bini, R. R., Diefenthaeler, F., & Mota, C. B. (2010). Fatigue effects on the coordinative pattern during cycling: kinetics and kinematics evaluation. *J Electromyogr Kinesiol*, *20*(1), 102-107. https://doi.org/10.1016/j.jelekin.2008.10.003

Bini, R. R., & Flores Bini, A. (2018). Potential factors associated with knee pain in cyclists: a systematic review. *Open Access J Sports Med*, *9*, 99-106. https://doi.org/10.2147/OAJSM.S136653

Bini, R. R., & Hume, P. (2016). A Comparison of Static and Dynamic Measures of Lower Limb Joint Angles in Cycling: Application to Bicycle Fitting. *Human Movement*, *17*(1). https://doi.org/10.1515/humo-2016-0005

Bini, R. R., & Hume, P. A. (2013). Effects of workload and pedalling cadence on knee forces in competitive cyclists. *Sports Biomech*, *12*(2), 93-107. https://doi.org/10.1080/14763141.2012.731428

Bini, R. R., & Hume, P. A. (2014). Assessment of bilateral asymmetry in cycling using a commercial instrumented crank system and instrumented pedals. *International journal of sports physiology and performance*, *9*(5), 876-881.

Bini, R. R., & Hume, P. A. (2014). Effects of saddle height on knee forces of recreational cyclists with and without knee pain. *International SportMed Journal*, *15*(2), 188-199.

Bini, R. R., Hume, P. A., & Croft, J. (2014). Cyclists and triathletes have different body positions on the bicycle. *European journal of sport science*, *14*(sup1), S109-S115.

Bini, R. R., Hume, P. A., & Kilding, A. E. (2014). Saddle height effects on pedal forces, joint mechanical work and kinematics of cyclists and triathletes. *Eur J Sport Sci*, *14*(1), 44-52. https://doi.org/10.1080/17461391.2012.725105

Bini, R. R., Hume, P. A., Lanferdini, F. J., & Vaz, M. A. l. (2013). Effects of moving forward or backward on the saddle on knee joint forces during cycling. *Physical Therapy in Sport*, *14*(1), 23-27.

Bini, R. R., Jacques, T. C., Sperb, C. H., Lanferdini, F. J., & Vaz, M. A. . (2016). Pedal force asymmetries and performance during a 20-km cycling time trial. *Kinesiology*, *48*(2), 193-199.

Bini, R. R., Rossato, M., Diefenthaeler, F., Carpes, F. P., dos Reis, D. C., & Moro, A. R. P. (2010). Pedaling cadence effects on joint mechanical work during cycling. *Isokinetics and Exercise Science*, *18*(1), 7-13. https://doi.org/10.3233/ies-2010-0361

Bini, R. R., Senger, D., Lanferdini, F., & Lopes, A. L. (2012). Joint kinematics assessment during cycling incremental test to exhaustion. *Isokinetics and Exercise Science*, *20*(2), 99-105.

Bini, R. R., Tamborindeguy, A. C., & Mota, C. B. (2010). Effects of saddle height, pedaling cadence, and workload on joint kinetics and kinematics during cycling. *J Sport Rehabil*, *19*(3), 301-314. https://doi.org/10.1123/jsr.19.3.301

Blake, O. M., & Wakeling, J. M. (2012). Muscle coordination during an outdoor cycling time trial. *Med Sci Sports Exerc*, *44*(5), 939-948. https://doi.org/10.1249/MSS.0b013e3182404eb4

Bratianu, C., Rinderu, P., & Gruionu, L. (2004). A 3D Finite Element Model of a Knee for Joint Contact Stress Analysis during Sport Activities. *Key Engineering Materials*, *261-263*, 513-518. https://doi.org/10.4028/www.scientific.net/KEM.261-263.513

Bressel, E., & Cronin, J. (2005). Bicycle seat interface pressure: reliability, validity, and influence of hand position and workload. *J Biomech*, *38*(6), 1325-1331. https://doi.org/10.1016/j.jbiomech.2004.06.006

Brian D. Moore, J. D., Bruce M. Gansneder, Sandra J. Shultz. (2002). The differential effects of fatigue on reflex response timing and amplitude in males and females. *Journal of electromyography and kinesiology*, *12*(5), 351-360. https://doi.org/https://doi.org/10.1016/S1050-6411(02)00032-9

Budi, D. R., Widyaningsih, R., Nur, L., Agustan, B., Dwi, D. R. S., Qohhar, W., & Asnaldi, A. (2021). Cycling during covid-19 pandemic: Sports or lifestyle? *International Journal of Human Movement and Sports Sciences*, *9*(4), 765-771. https://doi.org/10.13189/saj.2021.090422

Byrne, D. P., Mulhall, K. J., & Baker, J. F. (2010). Anatomy & biomechanics of the hip. *The open sports medicine Journal*, *4*(1).

Cahyono, S. I., Anwar, M., Diharjo, K., Triyono, T., Hapid, A., & Kaleg, S. (2017). *Finite element analysis of electric bicycle frame geometries*

Callaghan, M. J. (2005). Lower body problems and injury in cycling. *Journal of Bodywork and Movement Therapies*, *9*(3), 226-236.

Cannon, D. T., Kolkhorst, F. W., & Cipriani, D. J. (2007). Effect of pedaling technique on muscle activity and cycling efficiency. *Eur J Appl Physiol*, *99*(6), 659-664. https://doi.org/10.1007/s00421-006-0391-6

Carpes, F., Rossato, M., Faria, I., & Mota, C. B. . (2007). During a simulated 40-km cycling time-trial. *J. Sports Med. Phys. Fit*, *47*, 51-57.

Carpes, F. P., Dagnese, F., Kleinpaul, J. F., Martins Ede, A., & Mota, C. B. (2009). Effects of workload on seat pressure while cycling with two different saddles. *J Sex Med*, *6*(10), 2728-2735. https://doi.org/10.1111/j.1743-6109.2009.01394.x

Carpes, F. P., Diefenthaeler, F., Bini, R. R., Stefanyshyn, D. J., Faria, I. E., & Mota, C. B. (2011). Influence of leg preference on bilateral muscle activation during cycling. *J Sports Sci*, *29*(2), 151-159. https://doi.org/10.1080/02640414.2010.526625

Carpes, F. P., Mota, C. B., & Faria, I. E. (2010). On the bilateral asymmetry during running and cycling–A review considering leg preference. *Physical therapy in sport*, *11*(4), 136-142.

CAWSEY, R. P. (2008). *Does a decrease in seat height modify the effect of cadence on activation of the triceps surae during cycling?* University of British Columbia].

Chalmers, G. R. (2008). Can fast-twitch muscle fibres be selectively recruited during lengthening contractions? Review and applications to sport movements. *Sports Biomech*, *7*(1), 137-157. https://doi.org/10.1080/14763140701683023

Chapman, A., Vicenzino, B., Blanch, P., & Hodges, P. (2009). Do differences in muscle recruitment between novice and elite cyclists reflect different movement patterns or less skilled muscle recruitment? *Journal of Science and Medicine in Sport*, *12*(1), 31-34.

Chapman, A. R., Vicenzino, B., Blanch, P., & Hodges, P. W. (2008). Patterns of leg muscle recruitment vary between novice and highly trained cyclists. *J Electromyogr Kinesiol*, *18*(3), 359-371. https://doi.org/10.1016/j.jelekin.2005.12.007

Chapman, A. R., Vicenzino, B., Blanch, P., Knox, J. J., & Hodges, P. W. (2006). Leg muscle recruitment in highly trained cyclists. *J Sports Sci*, *24*(2), 115-124. https://doi.org/10.1080/02640410500131159

Chen, W.-P., Ju, C.-W., & Tang, F.-T. (2003). Effects of total contact insoles on the plantar stress redistribution: a finite element analysis. *Clinical Biomechanics*, *18*(6), S17-S24.

Clancy, C. E., Gatti, A. A., Ong, C. F., Maly, M. R., & Delp, S. L. (2023). Muscle-driven simulations and experimental data of cycling. *Sci Rep*, *13*(1), 21534. https://doi.org/10.1038/s41598-023-47945-5

Clarsen, B., Krosshaug, T., & Bahr, R. (2010). Overuse injuries in professional road cyclists. *Am J Sports Med*, *38*(12), 2494-2501. https://doi.org/10.1177/0363546510376816

Clohisy, J. C., Knaus, E. R., Hunt, D. M., Lesher, J. M., Harris-Hayes, M., & Prather, H. (2009). Clinical presentation of patients with symptomatic anterior hip impingement. *Clin Orthop Relat Res*, *467*(3), 638-644. https://doi.org/10.1007/s11999-008-0680-y

Connick, M. J., & Li, F. X. (2013). The impact of altered task mechanics on timing and duration of eccentric bi-articular muscle contractions during cycling. *J Electromyogr Kinesiol*, *23*(1), 223-229. https://doi.org/10.1016/j.jelekin.2012.08.012

Costes, A., Turpin, N. A., Villeger, D., Moretto, P., & Watier, B. (2016). Influence of position and power output on upper limb kinetics in cycling. *Journal of Applied Biomechanics*, *32*(2), 140-149.

Crouzier, M., Lacourpaille, L., Nordez, A., Tucker, K., & Hug, F. (2018). Neuromechanical coupling within the human triceps surae and its consequence on individual force-sharing strategies. *J Exp Biol*, *221*(Pt 21). https://doi.org/10.1242/jeb.187260

Čuk, T., Leben-Seljak, P., & Štefančič, M. . (2001). *Lateral asymmetry of human long bones*. Adam Mickiewicz University.

da Silva, J. C. L., Ekblom, M. M., Tarassova, O., Andersson, E., Ronquist, G., Grundstrom, H., & Arndt, A. (2018). Effect of increasing workload on knee extensor and flexor muscular activity during cycling as measured with intramuscular electromyography. *PloS one*, *13*(8), e0201014. https://doi.org/10.1371/journal.pone.0201014

Daly, D. J., & Cavanagh, P. R. (1976). Asymmetry in bicycle ergometer pedalling. *Medicine and science in sports*, *8*(3), 204-208.

Damm, P., Dymke, J., Bender, A., Duda, G., & Bergmann, G. (2017). In vivo hip joint loads and pedal forces during ergometer cycling. *J Biomech*, *60*, 197-202. https://doi.org/10.1016/j.jbiomech.2017.06.047

De Pieri, E., Lund, M. E., Gopalakrishnan, A., Rasmussen, K. P., Lunn, D. E., & Ferguson, S. J. (2018). Refining muscle geometry and wrapping in the TLEM 2 model for improved hip contact force prediction. *PloS one*, *13*(9), e0204109. https://doi.org/10.1371/journal.pone.0204109

de Sousa, A. C. C., Ramos, F. M., Dorado, M. C. N., da Fonseca, L. O., & Bó, A. P. L. . (2016). A comparative study on control strategies for FES cycling using a detailed musculoskeletal model. *IFAC-PapersOnLine*, *49*(32), 204-209.

de Vey Mestdagh, K. (1998). Personal perspective: in search of an optimum cycling posture. *Applied ergonomics*, *29*(5), 325-334.

Deakon, R. T. (2012). Chronic musculoskeletal conditions associated with the cycling segment of the triathlon; prevention and treatment with an emphasis on proper bicycle fitting. *Sports medicine and arthroscopy review*, *20*(4), 200-205.

Dedieu, P., Pelaez, M., Poirier, É., & Zanone, P. G. . (2020). Effects of saddle height on muscular pattern and interlimb coordination in cycling. *Citius Altius Fortius–Journal of Physical Education and Sport*, *20*(1), 222-228.

Dettori, N. J., and Daniel C. Norvell. (2006). Non-traumatic bicycle injuries: a review of the literature. *Sports Medicine*, *36*(1), 7-18.

Diefenthaeler, F., Berneira, J. D. O., Moro, V. L., & Carpes, F. P. (2016). Influence of saddle height and exercise intensity on pedalling asymmetries in cyclists. *Brazilian Journal of Kinanthropometry and Human Performance*, *18*(4). https://doi.org/10.5007/1980-0037.2016v18n4p411

Diefenthaeler, F., Bini, R. R., Carpes, F. P., & Vaz, M. A. (2007). Analysis of pedaling technique during a maximal cycling exercise. ISBS-Conference Proceedings Archive,

Diefenthaeler, F., Bini, R. R., Karolczak, A., & Carpes, F. (2008). Muscle activation during pedaling in different saddle position. *Brazilian Journal of Kineanthropometry & Human Performance*, *10*(2), 161-169. https://doi.org/10.5007/1980-0037.2008v10n2p161

Dingwell, J. B., Joubert, J. E., Diefenthaeler, F., & Trinity, J. D. (2008). Changes in muscle activity and kinematics of highly trained cyclists during fatigue. *IEEE Trans Biomed Eng*, *55*(11), 2666-2674. https://doi.org/10.1109/TBME.2008.2001130

Duncan, P. W., Chandler, J. M., Cavanaugh, D. K., Johnson, K. R., & Buehler, A. G. . (1989). Mode and speed specificity of eccentric and concentric exercise training. *journal of orthopaedic & sports physical therapy*, *11*(2), 70-75. https://doi.org/10.2519/jospt.1989.11.2.70

Edeline, O., Polin, D., Tourny-Chollet, C., & Weber, J. (2004). Effect of workload on bilateral pedaling kinematics in non-trained cyclists. *Journal of Human Movement Studies*, *46*(6), 493-518.

Edgerton, V. R., Smith, J. L., & Simpson, D. R. (1975). Muscle fibre type populations of human leg muscles. *Histochem J*, *7*(3), 259-266. https://doi.org/10.1007/BF01003594

Encarnación-Martínez, A. F.-R., Ventura; García-López, Juan. (2021). Influence of Sex on Current Methods of Adjusting Saddle Height in Indoor Cycling. *The Journal of Strength & Conditioning Research*, *35*(2), 519-526. https://doi.org/10.1519/JSC.0000000000002689

Erdemir, A., Guess, T. M., Halloran, J., Tadepalli, S. C., & Morrison, T. M. (2012). Considerations for reporting finite element analysis studies in biomechanics. *J Biomech*, *45*(4), 625-633. https://doi.org/10.1016/j.jbiomech.2011.11.038

Ericson, M. (1986). On the biomechanics of cycling. A study of joint and muscle load during exercise on the bicycle ergometer. *Scandinavian journal of rehabilitation medicine. Supplement*, *16*, 1-43.

Ericson M O, N. R., Németh G. (1988). Joint motions of the lower limb during ergometer cycling. *journal of orthopaedic & sports physical therapy*, *9*(8), 273-278. https://doi.org/10.2519/jospt.1988.9.8.273

Ericson, M. O., Ekholm, J., Svensson, O., & Nisell, R. (1985). The Forces of Ankle Joint Structures During Ergometer Cycling. *Foot & ankle*, *6*(3), 135-142.

Ericson, M. O., Nisell, R., Arborelius, U. P. & Ekholm, J. . (1985). Muscular activity during ergometer cycling. *Scandinavian journal of rehabilitation medicine*, *17*(2), 53-61.

Ericson, M. O., Ralph Nisell, and Gunnar Németh. . (1988). Joint Motions of the Lower Limb during Ergometer Cycling. *journal of orthopaedic & sports physical therapy*, *9*(8), 273-278.

Fang, Y., Fitzhugh, E. C., Crouter, S. E., Gardner, J. K., & Zhang, S. (2015). Effects of workloads and cadences on frontal plane knee biomechanics in cycling. *Med Sci Sports Exerc*, *48*(2), 260-266. https://doi.org/10.1249/MSS.0000000000000759

Fang, Y., Fitzhugh, E. C., Crouter, S. E., Gardner, J. K., & Zhang, S. (2016). Effects of Workloads and Cadences on Frontal Plane Knee Biomechanics in Cycling. *Med Sci Sports Exerc*, *48*(2), 260-266. https://doi.org/10.1249/MSS.0000000000000759

Farahani, S. D., Bertucci, W., Andersen, M. S., De Zee, M., & Rasmussen, J. (2015). Prediction of crank torque and pedal angle profiles during pedaling movements by biomechanical optimization. *Structural and Multidisciplinary Optimization*, *51*(1), 251-266.

Farina, D., Stegeman, D. F., and Merletti, R. (2016). Biophysics of the generation of EMG signals. *Surface electromyography: Physiology, engineering, and applications*, 1-24.

Farrell, J. W., & Neira, V. E. (2023). Contralateral Asymmetry in Cycling Power Is Reproducible and Independent of Exercise Intensity at Submaximal Power Outputs. *Symmetry*, *15*(6). https://doi.org/10.3390/sym15061142

Farris, D. J., & Sawicki, G. S. (2012). Human medial gastrocnemius force-velocity behavior shifts with locomotion speed and gait. *Proc Natl Acad Sci U S A*, *109*(3), 977-982. https://doi.org/10.1073/pnas.1107972109

Ferrer-Roca, V., Rivero-Palomo, V., Ogueta-Alday, A., Rodríguez-Marroyo, J. A., & García-López, J. (2016). Acute effects of small changes in crank length on gross efficiency and pedalling technique during submaximal cycling. *Journal of sports sciences*, *35*(14), 1328-1335. https://doi.org/10.1080/02640414.2016.1215490

Ferrer-Roca, V. B., Raúl; Roig, Andreu; Galilea, Piero; Valero, Oliver; García-López, Juan. (2014). Acute effects of small changes in bicycle saddle height on gross efficiency and lower limb kinematics. *Journal of Strength and Conditioning Research 28(3):p 784-791, March 2014. | DOI:* , *28*(3), 784-791. https://doi.org/10.1519/JSC.0b013e3182a1f1a9

Ferrer-Roca, V. R., Andreu; Galilea, Piero; García-López, Juan. (2012). Influence of Saddle Height on Lower Limb Kinematics in Well-Trained Cyclists. *Journal of Strength and Conditioning Research*, *26*(11), 3025-3029. https://doi.org/10.1519/JSC.0b013e318245c09d

Fonda, B., & Sarabon, N. (2010). *Biomechanics of Cycling* (Vol. 19). https://doi.org/10.2478/v10237-011-0012-0

Foss, O., & Hallen, J. (2004). The most economical cadence increases with increasing workload. *Eur J Appl Physiol*, *92*(4-5), 443-451. https://doi.org/10.1007/s00421-004-1175-5

Foure, A., Nordez, A., McNair, P., & Cornu, C. (2011). Effects of plyometric training on both active and passive parts of the plantarflexors series elastic component stiffness of muscle-tendon complex. *Eur J Appl Physiol*, *111*(3), 539-548. https://doi.org/10.1007/s00421-010-1667-4

García-López, J., Díez-Leal, S., Larrazabal, J., & Ogueta-Alday, A. (2015). No bilateral asymmetry during pedallilng in healthy cyclists of difference performance levels. *In ISBS-Conference Proceedings Archive*.

Gatti, A. A., Keir, P. J., Noseworthy, M. D., Beauchamp, M. K., & Maly, M. R. (2021). Hip and ankle kinematics are the most important predictors of knee joint loading during bicycling. *J Sci Med Sport*, *24*(1), 98-104. https://doi.org/10.1016/j.jsams.2020.07.001

Gatti, A. A., Keir, P. J., Noseworthy, M. D., Beauchamp, M. K., & Maly, M. R. (2022). Equations to Prescribe Bicycle Saddle Height based on Desired Joint Kinematics and Bicycle Geometry. *Eur J Sport Sci*, *22*(3), 344-353. https://doi.org/10.1080/17461391.2021.1902570

Gautam, K., Hefzy, M. S., Mustapha, A. A., & Kyle, B. (2024). Comparison of OpenSim and AnyBody modeling system™ predictions in biomechanical modeling of upper extremities. *International Journal of Research in Orthopaedics*, *10*(4), 717-724. https://doi.org/10.18203/issn.2455-4510.IntJResOrthop20241695

Gavin, T. P., Van Meter, J. B., Brophy, P. M., Dubis, G. S., Potts, K. N., & Hickner, R. C. (2012). Comparison of a field-based test to estimate functional threshold power and power output at lactate threshold. *The Journal of Strength & Conditioning Research*, *26*(2), 416-421.

Gilman, M. B., & Wells, C. L. (1993). The use of heart rates to monitor exercise intensity in relation to metabolic variables. *International journal of sports medicine*, *14*(6), 339-344.

Graham, P. L., Zoeller, R. F., Jacobs, P. L., & Whitehurst, M. A. (2018). Effect of cadence on time trial performance in recreational female cyclists. *The Journal of Strength & Conditioning Research*, *32*(6), 1739-1744.

Green, S., Sakuls, P., & Levitt, S. (2021). Cycling for health: Improving health and mitigating the climate crisis. , 67(10), . (2021). Cycling for health: Improving health and mitigating the climate crisis. *Canadian family physician*, *67*(10), 739-742. https://doi.org/10.46747/cfp.6710739

Gregor, R. J., & Wheeler, J. B. (1994). Biomechanical factors associated with shoe pedal interfaces Implications for injury. *Sports Medicine*, *17*, 117-131.

GREGOR, R. J., BROKER, J. P., & RYAN, M. M. (1991). The biomechanics of cycling. *Exercise and sport sciences reviews*, *19*(1), 127-170.

Halloran, J. P., Ackermann, M., Erdemir, A., & van den Bogert, A. J. (2010). Concurrent musculoskeletal dynamics and finite element analysis predicts altered gait patterns to reduce foot tissue loading. *J Biomech*, *43*(14), 2810-2815. https://doi.org/10.1016/j.jbiomech.2010.05.036

Halonen, K. S., Mononen, M. E., Jurvelin, J. S., Toyras, J., Salo, J., & Korhonen, R. K. (2014). Deformation of articular cartilage during static loading of a knee joint--experimental and finite element analysis. *J Biomech*, *47*(10), 2467-2474. https://doi.org/10.1016/j.jbiomech.2014.04.013

Hamley, E., & Thomas, V. (1967). Physiological and postural factors in the calibration of the bicycle ergometer. *The Journal of physiology*, *191*(2), 55P-56P.

Handsfield, G. G., Meyer, C. H., Hart, J. M., Abel, M. F., & Blemker, S. S. (2014). Relationships of 35 lower limb muscles to height and body mass quantified using MRI. *J Biomech*, *47*(3), 631-638. https://doi.org/10.1016/j.jbiomech.2013.12.002

Hedge, E. T., Amelard, R., & Hughson, R. L. (2023). Prediction of oxygen uptake kinetics during heavy-intensity cycling exercise by machine learning analysis. *J Appl Physiol (1985)*, *134*(6), 1530-1536. https://doi.org/10.1152/japplphysiol.00148.2023

Hermens, H. J., Freriks, B., Merletti, R., Stegeman, D., Blok, J., Rau, G. n., Disselhorst-Klug, C., & HÃ¤gg, G. r. (1999). European recommendations for surface electromyography. *Roessingh research and development*, *8*(2), 13-54.

Herzog, W. (2000). Muscle properties and coordination during voluntary movement. *J Sports Sci*, *18*(3), 141-152. https://doi.org/10.1080/026404100365045

Hilmkil, A., Ivarsson, O., Johansson, M., Kuylenstierna, D., & van Erp, T. (2018). Towards machine learning on data from professional cyclists. *arXiv preprint arXiv:1808.00198*.

Hofer, J. K., Gejo, R., McGarry, M. H., & Lee, T. Q. (2011). Effects on tibiofemoral biomechanics from kneeling. *Clin Biomech (Bristol)*, *26*(6), 605-611. https://doi.org/10.1016/j.clinbiomech.2011.01.016

Hollaus, B., Volmer, J. C., & Fleischmann, T. (2022). Cadence Detection in Road Cycling Using Saddle Tube Motion and Machine Learning. *Sensors (Basel)*, *22*(16). https://doi.org/10.3390/s22166140

Holliday, W., Theo, R., Fisher, J., & Swart, J. (2023). Cycling: joint kinematics and muscle activity during differing intensities. *Sports Biomech*, *22*(5), 660-674. https://doi.org/10.1080/14763141.2019.1640279

Horton, J. F., Stergiou, P., Fung, T. S., & Katz, L. (2017). Comparison of Polar M600 optical heart rate and ECG heart rate during exercise. *Med Sci Sports Exerc*, *49*(12), 2600-2607.

Hug, F., Bendahan, D., Le Fur, Y., Cozzone, P. J., & Grelot, L. (2004). Heterogeneity of muscle recruitment pattern during pedaling in professional road cyclists: a magnetic resonance imaging and electromyography study. *Eur J Appl Physiol*, *92*(3), 334-342. https://doi.org/10.1007/s00421-004-1096-3

Hug, F., & Dorel, S. (2009). Electromyographic analysis of pedaling: a review. *J Electromyogr Kinesiol*, *19*(2), 182-198. https://doi.org/10.1016/j.jelekin.2007.10.010

Hummer, E., Thorsen, T., & Zhang, S. (2021). Does saddle height influence knee frontal-plane biomechanics during stationary cycling? *Knee*, *29*, 233-240. https://doi.org/10.1016/j.knee.2021.01.026

Ichinose, Y., Kawakami, Y., Ito, M., & Fukunaga, T. (1997). Estimation of active force-length characteristics of human vastus lateralis muscle. *Cells Tissues Organs*, *159*(2-3), 78-83.

Ito, J., Moriyama, H., Inokuchi, S., & Goto, N. (2003). (2003). Human lower limb muscles: an evaluation of weight and fiber size. *Okajimas folia anatomica Japonica*, *80*(2.3), 47-56. https://doi.org/10.2535/ofaj.80.47

Jobson, S. A., Hopker, J., Arkesteijn, M., & Passfield, L. (2013). Inter- and intra-session reliability of muscle activity patterns during cycling. *J Electromyogr Kinesiol*, *23*(1), 230-237. https://doi.org/10.1016/j.jelekin.2012.08.013

Johnston, T. E. (2007). Biomechanical Considerations for Cycling Interventions in Rehabilitation. *Physical Therapy & Rehabilitaion Journal*, *87*(9), 1243-1252.

Jorge, M., and M. L. Hull. . (1986). Analysis of EMG measurements during bicycle pedalling. *Journal of biomechanics*, *19*(9), 683-694. https://doi.org/10.1016/0021-9290(86)90192-2

Kamyar Momeni, P. D. F. M. E. (2014). Lower-extremity joint kinematics and muscle activations during semi-reclined cycling at different workloads in healthy individuals. https://doi.org/10.1186/1743-0003-11-146

Kanehisa, H., Yata, H., Ikegawa, S., & Fukunaga, T. (1995). A cross-sectional study of the size and strength of the lower leg muscles during growth. *European journal of applied physiology and occupational physiology*, *72*, 150-156. https://doi.org/10.1007/bf00964130

Kataoka, Y., & Gray, P. (2019). Real-Time Power Performance Prediction in Tour de France. In *Machine Learning and Data Mining for Sports Analytics* (pp. 121-130). https://doi.org/10.1007/978-3-030-17274-9_10

Kholkine, L., De Schepper, T., Verdonck, T., & Latré, S. . (2020, September 14-18). A machine learning approach for road cycling race performance prediction. Machine Learning and Data Mining for Sports Analytics: 7th International Workshop, Ghent, Belgium.

Kiapour, A. M., Kaul, V., Kiapour, A., Quatman, C. E., Wordeman, S. C., Hewett, T. E., Demetropoulos, C. K., & Goel, V. K. (2014). The Effect of Ligament Modeling Technique on Knee Joint Kinematics: A Finite Element Study. *Appl Math (Irvine)*, *4*(5A), 91-97. https://doi.org/10.4236/am.2013.45A011

Kolehmainen, I., Harms-Ringdahl, K., & Lanshammart, H. (1989). Cervical spine positions and load moments during bicycling with different handlebar positions. *Clinical biomechanics*, *4*(2), 105-110.

Kotler, D. H., Babu, A. N., & Robidoux, G. (2016). Prevention, Evaluation, and Rehabilitation of Cycling-Related Injury. *Current Sports Medicine Reports*, *15*(9), 199-206. https://doi.org/10.1249/JSR.0000000000000262

Kutzner, I., Heinlein, B., Graichen, F., Rohlmann, A., Halder, A. M., Beier, A., & Bergmann, G. (2012). Loading of the knee joint during ergometer cycling: telemetric in vivo data. *journal of orthopaedic & sports physical therapy*, *42*(12), 1032-1038.

Lanferdini, F. J., Jacques, T. C., Bini, R. R., & Vaz, M. A. (2014). Cyclists and triathletes do not differ in muscle volume, muscle recruitment or pedal force effectiveness. *Isokinetics and Exercise Science*, *22*(4), 279-286. https://doi.org/10.3233/ies-140549

Lemaitre, G., & Lemaitre, C. (2018). Estimate Power without Measuring it: a Machine Learning Application. *Journal of Science and Cycling*, *7*(2), 48-49.

LeMond, G. (1988). Greg LeMond. *PDM*, *1985*(1987).

Lepasalu, L., Ereline, J., Reinvee, M., & Pääsuke, M. (2024). Seat Pressure Asymmetries after Cycling at Constant Intensity. *Symmetry*, *16*(3). https://doi.org/10.3390/sym16030270

Li, N., Hu, W., Ma, Y., & Xiang, H. (2024). Machine learning prediction of pulmonary oxygen uptake from muscle oxygen in cycling. *J Sports Sci*, *42*(14), 1299-1307. https://doi.org/10.1080/02640414.2024.2388996

Liu, T., & Jensen, J. L. (2012). Age-related differences in bilateral asymmetry in cycling performance. *Res Q Exerc Sport*, *83*(1), 114-119. https://doi.org/10.1080/02701367.2012.10599832

Macaluso, A., Young, A., Gibb, K. S., Rowe, D. A., & De Vito, G. (2003). Cycling as a novel approach to resistance training increases muscle strength, power, and selected functional abilities in healthy older women. *Journal of applied physiology*, *95*(6), 2544-2553. https://doi.org/10.1152/japplphysiol.00416.2003

MacInnis, M. J., Thomas, A. C. Q., & Phillips, S. M. (2018). The Reliability of 4-min and 20-min Time Trials and Their Relationships to Functional Threshold Power in Trained Cyclists. *Int J Sports Physiol Perform*, 1-27. https://doi.org/10.1123/ijspp.2018-0100

Maisarah Sulaiman, A. A., Noor Aimie Salleh, and Azli Yahya. (2021). Lower Limb Muscles Activation of Endurance and Power Athletes. *11th Asian-Pacific Conference on Medical and Biological Engineering*, 111-117. https://doi.org/https://doi.org/10.1007/978-3-030-66169-4_15

Mats O. Ericson, M., and Ralph Nisell, MD, PhDView all authors and affiliations. (1986). Tibiofemoral joint forces during ergometer cycling. *The American journal of sports medicine*, *14*(4), 285-290. https://doi.org/10.1177/036354658601400407

Matsuura, R., Arimitsu, T., Yunoki, T., & Yano, T. (2011). Effects of resistive load on performance and surface EMG activity during repeated cycling sprints on a non-isokinetic cycle ergometer. *Br J Sports Med*, *45*(10), 820-824. https://doi.org/10.1136/bjsm.2009.068007

Menard, M., Domalain, M., Decatoire, A., & Lacouture, P. (2020). Influence of saddle setback on knee joint forces in cycling. *Sports Biomech*, *19*(2), 245-257. https://doi.org/10.1080/14763141.2018.1466906

Michelle Lee, L. h., Evan Thomas, Wanda van Niekerk, Kim Jackson, Vidya Acharya, Laura Ritchie, Scott Buxton, Naomi O'Reilly and WikiSysop. (2016). *Cycling Biomechanics*. Retrieved 20 April 2023 from https://www.physio-pedia.com/Cycling_Biomechanics

Mileva, K., & Turner, D. (2003). Neuromuscular and biomechanical coupling in human cycling: adaptations to changes in crank length. *Exp Brain Res*, *152*(3), 393-403. https://doi.org/10.1007/s00221-003-1561-y

Millour, G., & Bertucci, W. (2017). Comparison of Genzling method vs Hamley method allowing a postural adjustment in cycling: preliminary study. *Computer methods in BiomeChaniCs and BiomediCal engineering*, *20*(sup1), S135-S136.

Millour, G., Duc, S., Puel, F., & Bertucci, W. (2019). Comparison of static and dynamic methods based on knee kinematics to determine optimal saddle height in cycling. *Acta of Bioengineering and Biomechanics*, *21*(4), 93-99.

Millour, G., Duc, S., Puel, F., & Bertucci, W. (2019). Comparison of static and dynamic methods based on knee kinematics to determine optimal saddle height in cycling., 21(4), 93-99. (2019). Comparison of static and dynamic methods based on knee kinematics to determine optimal saddle height in cycling. *Acta of Bioengineering and Biomechanics*, *21*(4), 93-99.

Mo, F., Li, J., Dan, M., Liu, T., & Behr, M. (2019). Implementation of controlling strategy in a biomechanical lower limb model with active muscles for coupling multibody dynamics and finite element analysis. *Journal of biomechanics*, *91*, 51-60.

Moissenet, F., Chèze, L., & Dumas, R. (2017). Individual muscle contributions to ground reaction and to joint contact, ligament and bone forces during normal gait. *Multibody System Dynamics*, *40*(2), 193-211. https://doi.org/10.1007/s11044-017-9564-9

Mornieux, G., Gollhofer, A., & Stapelfeldt, B. (2010). Muscle coordination while pulling up during cycling. *Int J Sports Med*, *31*(12), 843-846. https://doi.org/10.1055/s-0030-1263140

Mornieux, G., Guenette, J. A., Sheel, A. W., & Sanderson, D. J. (2007). Influence of cadence, power output and hypoxia on the joint moment distribution during cycling. *Eur J Appl Physiol*, *102*(1), 11-18. https://doi.org/10.1007/s00421-007-0555-z

Moura, B. M. d., Moro, V. L., Rossato, M., Lucas, R. D. d., & Diefenthaeler, F. (2017). Effects of Saddle Height on Performance and Muscular Activity during the Wingate Test. *Journal of Physical Education*, *28*(1). https://doi.org/10.4025/jphyseduc.v28i1.2838

Mukaka, M. M. (2012). A guide to appropriate use of correlation coefficient in medical research. *Malawi medical journal*, *24*(3), 69-71.

Murray, K. A. (2023). *An investigation of asymmetries in cycling: methods and performance implications* [Research thesis, University of Essex].

Muyor, J. M. (2015). The influence of handlebar-hands position on spinal posture in professional cyclists. *J Back Musculoskelet Rehabil*, *28*(1), 167-172. https://doi.org/10.3233/BMR-140506

Neptune, R. R., & Herzog, W. (1999). The association between negative muscle work and pedaling rate. *Journal of biomechanics*, *32*(10), 1021-1026. https://doi.org/10.1016/S0021-9290(99)00100-1

Neptune, R. R., Kautz, S. A., & Hull, M. L. (1997). The effect of pedaling rate on coordination in cycling. *Journal of biomechanics*, *30*(10), 1051-1058.

Nigg, B. M. (1985). Biomechanics, load analysis and sports injuries. *Sports Medicine*, *2*(5), 367-379. https://doi.org/10.2165/00007256-198502050-00005

Nisell, R., Ericson, M. O., Nemeth, G., & Ekholm, J. (1989). Tibiofemoral joint forces during isokinetic knee extension. *The American journal of sports medicine*, *17*(1), 49-54.

Nordeen-Snyder, K. S. (1977). The effect of bicycle seat height variation upon oxygen consumption and lower limb kinematics. *Medicine and science in sports*, *9*(2), 113-117.

Obradović, S., & Stančin, S. (2023). Inertial Measurement Units' Reliability for Measuring Knee Joint Angle during Road Cycling. *Electronics*, *12*(3). https://doi.org/10.3390/electronics12030751

Ofoghi, B., Zeleznikow, J., MacMahon, C., & Dwyer, D. (2013). Supporting athlete selection and strategic planning in track cycling omnium: A statistical and machine learning approach. *Information Sciences*, *233*, 200-213. https://doi.org/10.1016/j.ins.2012.12.050

Oja, P., Titze, S., Bauman, A., de Geus, B., Krenn, P., Reger-Nash, B., & Kohlberger, T. (2011). Health benefits of cycling: a systematic review. *Scand J Med Sci Sports*, *21*(4), 496-509. https://doi.org/10.1111/j.1600-0838.2011.01299.x

Oloyede, A., Flachsmann, R., & Broom, N. D. (1992). The dramatic influence of loading velocity on the compressive response of articular cartilage. *Connect Tissue Res*, *27*(4), 211-224. https://doi.org/10.3109/03008209209006997

Park, S., Roh, J., Hyeong, J., & Kim, S. (2022). Effect of crank length on biomechanical parameters and muscle activity during standing cycling. *J Sports Sci*, *40*(2), 185-194. https://doi.org/10.1080/02640414.2021.1982516

Parsaei, A., Ahmadi, R., Aboodarda, S. J., & Komeili, A. (2024, May 28-30, 2024). Predict Knee Kinematics During Stationary Cycling via Machine Learning Regression Models. CMBES Proceedings, Toronto.

Paton, C. D. (2009). Effects of shoe cleat position on physiology and performance of competitive cyclists. *Int J Sports Physiol Perform*, *4*(4), 517-523. https://doi.org/10.1123/ijspp.4.4.517

Peveler, W., Bishop, P., Smith, J., Richardson, M., & Whitehorn, E. (2005). COMPARING METHODS FOR SETTING SADDLE HEIGHT IN TRAINED CYCLISTS. *Journal of Exercise Physiology Online*, *8*(1).

Peveler, W. W. (2008). Effects of Saddle Height on Economy in Cycling. *The Journal of Strength & Conditioning Research*, *22*(4), 1355-1359.

Peveler, W. W., & Green, J. M. (2011). Effects of saddle height on economy and anaerobic power in well-trained cyclists. , 25(3), 629-633. (2011). Effects of saddle height on economy and anaerobic power in well-trained cyclists. *The Journal of Strength & Conditioning Research*, *25*(3), 629-633.

Peveler, W. W., Pounders, J. D., & Bishop, P. A. (2007). Effects of saddle height on anaerobic power production in cycling. , 21(4), 1023-1027. (2007). Effects of saddle height on anaerobic power production in cycling. *The Journal of Strength & Conditioning Research*, *21*(4), 1023-1027.

Peveler, W. W. S., Brandy; Johnson, Samantha; Palmer, Thomas G. (2012). A kinematic comparison of alterations to knee and ankle angles from resting measures to active pedaling during a graded exercise protocol. *Journal of Strength and Conditioning Research*, *26*(11), 3004-3009. https://doi.org/10.1519/JSC.0b013e318243fdcb

Price, D., & Donne, B. (1997). Effect of variation in seat tube angle at different seat heights on submaximal cycling performance in man. *Journal of sports sciences*, *15*(4), 395-402.

Priego, J. I., Bini, R. R., Lanferdini, F. J., & Carpes, F. P. (2014). Effects of workload level on muscle recruitment in cycling. *Human Movement*, *15*(1), 45-50. https://doi.org/10.2478/humo-2014-0001

Priego Quesada, J. I., Kerr, Z. Y., Bertucci, W. M., & Carpes, F. P. (2019). A retrospective international study on factors associated with injury, discomfort and pain perception among cyclists. *PloS one*, *14*(1), e0211197. https://doi.org/10.1371/journal.pone.0211197

Priego Quesada, J. I., Perez-Soriano, P., Lucas-Cuevas, A. G., Salvador Palmer, R., & Cibrian Ortiz de Anda, R. M. (2017). Effect of bike-fit in the perception of comfort, fatigue and pain. *J Sports Sci*, *35*(14), 1459-1465. https://doi.org/10.1080/02640414.2016.1215496

Priego Quesada, J. I., Pérez-Soriano, P., Lucas-Cuevas, A. G., Salvador Palmer, R., & Cibrián Ortiz de Anda, R. M. (2016). Effect of bike-fit in the perception of comfort, fatigue and pain. *Journal of sports sciences*, *35*(14), 1459-1465. https://doi.org/10.1080/02640414.2016.1215496

Pucher, J., & Buehler, R. (2017). Cycling towards a more sustainable transport future. *Transport Reviews*, *37*(6), 689-694. https://doi.org/10.1080/01441647.2017.1340234

R.R. Neptune, S. A. K. (2000). Knee joint loading in forward versus backward pedaling implications for rehabilitation strategies. *Clinical biomechanics*, *15*, 528-535. https://doi.org/10.1016/S0268-0033(00)00005-X

Raasch, C. C., & Zajac, F. E. (1999). Locomotor strategy for pedaling muscle groups and biomechanical functions. *Journal of neurophysiology*, *82*(2), 515-525.

Raasch, C. C., Zajac, F. E., Ma, B., & Levine, W. S. . (1997). Muscle coordination of maximum-speed pedaling. *Journal of biomechanics*, *30*(6), 595-602.

Rachelle Bordlee, a. C. K. W. (2015). *Surface EMG: A how-to guide for practitioners*. LER Magazine. https://lermagazine.com/article/surface-emg-a-how-to-guide-for-practitioners

Rannama, I., Port, K., Bazanov, B., & Pedak, K. (2015). Sprint cycling performance and asymmetry. *Journal of Human Sport and Exercise*, *10*(Proc1). https://doi.org/10.14198/jhse.2015.10.Proc1.12

Regenwetter, L. (2022). *Data-driven bicycle design using performance-aware deep generative models* Massachusetts Institute of Technology].

Ricard, M. D., Hills-Meyer, P., Miller, M. G., & Michael, T. J. . (2006). The effects of bicycle frame geometry on muscle activation and power during a Wingate anaerobic test. *Journal of sports science & medicine*, *5*(1), 25-32.

Rodrigo Bini, P. A. H. J. L. C. (2011). Effects of Bicycle Saddle Height on Knee Injury Risk and Cycling Performance. *Sports Medicine*, *41*, 463-476. https://doi.org/10.2165/11588740-000000000-00000

Rodrigo R Bini, P. H., James Croft, Andrew Kilding (2013). Pedal force effectiveness in cycling A review of constraints and training effects. *J Sci Cycling*, *1*(2), 11-24.

Rodrigo R. Bini, A. C. T., and Carlos B. Mota. (2010). Effects of saddle height, pedaling cadence, and workload on joint kinetics and kinematics during cycling. *Journal of sport rehabilitation*, *19*, 301-314.

Rodrigo Rico Bini, F. D., Felipe P Carpes. (2014). Determining force and power in cycling: A review of methods and instruments for pedal force and crank torque measurements. *International SportMed Journal*.

Rossato, M., Bini, R. R., Carpes, F. P., Diefenthaeler, F., & Moro, A. R. (2008). Cadence and workload effects on pedaling technique of well-trained cyclists. *Int J Sports Med*, *29*(9), 746-752. https://doi.org/10.1055/s-2008-1038375

Rossi, A. P., Rubele, S., Calugi, S., Caliari, C., Pedelini, F., Soave, F., Chignola, E., Vittoria Bazzani, P., Mazzali, G., Dalle Grave, R., & Zamboni, M. (2019). Weight Cycling as a Risk Factor for Low Muscle Mass and Strength in a Population of Males and Females with Obesity. *Obesity (Silver Spring)*, *27*(7), 1068-1075. https://doi.org/10.1002/oby.22493

Rouffet, D. M., & Hautier, C. A. (2008). EMG normalization to study muscle activation in cycling. *J Electromyogr Kinesiol*, *18*(5), 866-878. https://doi.org/10.1016/j.jelekin.2007.03.008

Rugg, S., & Gregor, R. (1987). The effect of seat height on muscle lengths, velocities and moment arm lengths during cycling. *Journal of biomechanics*, *20*(9), 899.

Ryan, M. M., and Robert J. Gregor. (1992). EMG profiles of lower extremity muscles during cycling at constant workload and cadence. *Journal of electromyography and kinesiology*, *2*(2), 69-80. https://doi.org/10.1016/1050-6411(92)90018-E

Sabeti-Aschraf, M., Serek, M., Geisler, M., Schmidt, M. I., Pachtner, T., Ochsner, A., & Graf, A. . (2010). Overuse Injuries Correlated to the Mountain Bike`s Adjustment A Prospective Field Study. *The Open Sports Sciences Journal*, *3*.

Salacinski, A. J., Krohn, K., Lewis, S. F., Holland, M. L., Ireland, K., & Marchetti, G. (2012). The effects of group cycling on gait and pain-related disability in individuals with mild-to-moderate knee osteoarthritis: a randomized controlled trial. *J Orthop Sports Phys Ther*, *42*(12), 985-995. https://doi.org/10.2519/jospt.2012.3813

Sallet, P., Mathieu, R., Fenech, G., & Baverei, G. (2006). Physiological differences of elite and professional road cyclists related to competition level and rider specialization. *Journal of sports medicine and physical fitness*, *46*(3), 17.

Salsich, G. B., Ward, S. R., Terk, M. R., & Powers, C. M. (2003). In vivo assessment of patellofemoral joint contact area in individuals who are pain free. *Clin Orthop Relat Res*(417), 277-284. https://doi.org/10.1097/01.blo.0000093024.56370.79

Sanderson, D. J. (1991). The influence of cadence and power output on the biomechanics of force application during steady-rate cycling in competitive and recreational cyclists. *J Sports Sci*, *9*(2), 191-203. https://doi.org/10.1080/02640419108729880

Sanderson, D. J., & Amoroso, A. T. (2009). The influence of seat height on the mechanical function of the triceps surae muscles during steady-rate cycling. *J Electromyogr Kinesiol*, *19*(6), e465-471. https://doi.org/10.1016/j.jelekin.2008.09.011

Sanderson, D. J., & Black, A. (2003). The effect of prolonged cycling on pedal forces. *Journal of sports sciences*, *21*(3), 191-199.

Sanderson, D. J., Martin, P., Honeyman, G., & Keefer, J. (2006). Gastrocnemius and soleus muscle length, velocity, and EMG responses to changes in pedalling cadence. *Journal of electromyography and kinesiology*, *16*(6), 642-649.

Sarre, G., Lepers, R., Maffiuletti, N., Millet, G., & Martin, A. (2003). Influence of cycling cadence on neuromuscular activity of the knee extensors in humans. *Eur J Appl Physiol*, *88*(4-5), 476-479. https://doi.org/10.1007/s00421-002-0738-6

Sayers, M. G., Tweddle, A. L., Every, J., & Wiegand, A. (2012). Changes in drive phase lower limb kinematics during a 60 min cycling time trial. *Journal of Science and Medicine in Sport*, *15*(2), 169-174.

Schutte, L. M., Rodgers, M. M., Zajac, F. E., & Glaser, R. M. (1993). Improving the Efficacy of Electrical StimulationInduced Leg Cycle Ergometry An Analysis Based on a

Dynamic Musculoskeletal Model. *IEEE Transactions on Rehabilitation Engineering*, *1*(2), 109-125.

Silberman, M. R. (2013). Bicycling injuries. *Current Sports Medicine Reports*, *12*(5), 337-345.

Smak W, N. R. R., Hull M L. (1999). The influence of pedaling rate on bilateral asymmetry in cycling. *Journal of biomechanics*, *32*(9), 899-906. https://doi.org/10.1016/S0021-9290(99)00090-1

Smiley, A., & Finkelstein, J. (2024). Dynamic Prediction of Physical Exertion: Leveraging AI Models and Wearable Sensor Data During Cycling Exercise. *Diagnostics (Basel)*, *15*(1). https://doi.org/10.3390/diagnostics15010052

So, R. C., Ng, J. K.-F., & Ng, G. Y. (2005). Muscle recruitment pattern in cycling: a review. *Physical Therapy in Sport*, *6*(2), 89-96.

So, R. C. H., Ng, J. K. F., & Ng, G. Y. F. (2005). Muscle recruitment pattern in cycling: a review. *Physical therapy in sport*, *6*(2), 89-96. https://doi.org/10.1016/j.ptsp.2005.02.004

Spears, I. R., Cummins, N. K., Brenchley, Z., Donohue, C., Turnbull, C., Burton, S., & Macho, G. A. (2003). The effect of saddle design on stresses in the perineum during cycling. *Med Sci Sports Exerc*, *35*(9), 1620-1625. https://doi.org/10.1249/01.MSS.0000084559.35162.73

Stessens, L., Gielen, J., Meeusen, R., & Aerts, J.-M. (2024). Physical performance estimation in practice: A systematic review of advancements in performance prediction and modeling in cycling. *International Journal of Sports Science & Coaching*, *19*(5), 2222-2243. https://doi.org/10.1177/17479541241262385

Stockwell, R. A., & Corradini, A. (2023, 2023, November). *A Machine Learning Approach to Predict Cyclists' Functional Threshold Power* In International Conference on Intelligent Data Engineering and Automated Learning,

Stone, A. V., Howse, E. A., Mannava, S., & Stubbs, A. J. (2016). Cyclists Have Greater Chondromalacia Index Than Age-Matched Controls at the Time of Hip Arthroscopy. *Arthroscopy*, *32*(10), 2102-2109. https://doi.org/10.1016/j.arthro.2016.04.014

Strutzenberger, G., Wunsch, T., Kroell, J., Dastl, J., & Schwameder, H. (2014). Effect of chainring ovality on joint power during cycling at different workloads and cadences. *Sports Biomech*, *13*(2), 97-108. https://doi.org/10.1080/14763141.2014.908946

Suzuki, S., Watanabe, S., & Homma, S. (1982). EMG activity and kinematics of human cycling movements at different constant velocities. *Brain Research*, *240*(2), 245-258.

Tang, Y., Wang, D., Wang, Y., Yin, K., Zhang, C., Zou, L., & Liu, Y. (2020). Do Surface Slope and Posture Influence Lower Extremity Joint Kinetics during Cycling? *Int J Environ Res Public Health*, *17*(8). https://doi.org/10.3390/ijerph17082846

Tawhai, M., Bischoff, J., Einstein, D., Erdemir, A., Guess, T., & Reinbolt, J. (2009). Multiscale modeling in computational biomechanics. *IEEE Eng Med Biol Mag*, *28*(3), 41-49. https://doi.org/10.1109/MEMB.2009.932489

Tesch, P. A., and James E. Wright. . (1983). Recovery from short term intense exercise its relation to capillary supply and blood lactate concentration. *European journal of applied physiology and occupational physiology*, *52*, 98-103. https://doi.org/10.1007/bf00429033

Thelen, D. G., Anderson, F. C., & Delp, S. L. (2003). Generating dynamic simulations of movement using computed muscle control. *J Biomech*, *36*(3), 321-328. https://doi.org/10.1016/s0021-9290(02)00432-3

Thorsen, T., Strohacker, K., Weinhandl, J. T., & Zhang, S. (2020). Increased Q-Factor increases frontal-plane knee joint loading in stationary cycling. *J Sport Health Sci*, *9*(3), 258-264. https://doi.org/10.1016/j.jshs.2019.07.011

Tim Evens, J. D. (2019). The Effects of Saddle Alignment and Pedal Stroke Training on a Competitive Cyclist with Anterior Knee Pain: A Case Report. *The Internet Journal of Allied Health Sciences and Practice*, *17*(3). https://doi.org/10.46743/1540-580X/2019.1818

Toh, S. M. S., Ashkanfar, A., English, R., Rothwell, G., Langton, D. J., & Joyce, T. J. (2023). How does bicycling affect the longevity of Total Hip Arthroplasty? A finite element wear analysis. *J Mech Behav Biomed Mater*, *139*, 105673. https://doi.org/10.1016/j.jmbbm.2023.105673

Torres, A., Nougarou, F., & Domingue, F. (2024). Machine learning models to predict kinetic variables in cycling. *Journal of Science & Cycling*, *23*, 3.

Trad, Z., Barkaoui, A., & Chafra, M. (2017). A Three Dimensional Finite Element Analysis of Mechanical Stresses in the Human Knee Joint: Problem of Cartilage Destruction. *Journal of Biomimetics, Biomaterials and Biomedical Engineering*, *32*, 29-39. https://doi.org/10.4028/www.scientific.net/JBBBE.32.29

Trecroci, A., Formenti, D., Ludwig, N., Gargano, M., Bosio, A., Rampinini, E., & Alberti, G. (2018). Bilateral asymmetry of skin temperature is not related to bilateral asymmetry of crank torque during an incremental cycling exercise to exhaustion. *PeerJ*, *6*, e4438. https://doi.org/10.7717/peerj.4438

Underwood, L., & Jermy, M. (2013). Optimal handlebar position for track cyclists. *Sports Engineering*, *16*(2), 81-90. https://doi.org/10.1007/s12283-013-0111-5

Van der walt, A. (2014). Non-traumatic injury profile of amateur cyclists. *South African Journal of Sports Medicine*, *26*(4), 119-122. https://doi.org/10.7196/sajsm.555

van der Zwaard, S., de Ruiter, C. J., Jaspers, R. T., & de Koning, J. J. (2019). Anthropometric Clusters of Competitive Cyclists and Their Sprint and Endurance Performance. *Front Physiol*, *10*, 1276. https://doi.org/10.3389/fphys.2019.01276

Van Zyl, E., Schwellnus, M. P., & Noakes, T. D. (2001). A review of the etiology, biomechanics, diagnosis, and management of patellofemoral pain in cyclists. *International SportMed Journal*, *2*(1), 1-34.

Vehtari, A., Gelman, A., & Gabry, J. (2016). Practical Bayesian model evaluation using leave-one-out cross-validation and WAIC. *Statistics and Computing*, *27*(5), 1413-1432. https://doi.org/10.1007/s11222-016-9696-4

Verma, R., Hansen, E. A., de Zee, M., & Madeleine, P. (2016). Effect of seat positions on discomfort, muscle activation, pressure distribution and pedal force during cycling. *J Electromyogr Kinesiol*, *27*, 78-86. https://doi.org/10.1016/j.jelekin.2016.02.003

Wadsworth, D. J. S., & Weinrauch, P. (2019). THE ROLE of a BIKE FIT in CYCLISTS with HIP PAIN. A CLINICAL COMMENTARY. *Int J Sports Phys Ther*, *14*(3), 468-486. https://doi.org/10.26603/ijspt20190468

Wang, F., Wu, J., Hu, L., Yu, C., Wang, B., Huang, X., Miller, K., & Wittek, A. (2021). Evaluation of the head protection effectiveness of cyclist helmets using full-scale computational biomechanics modelling of cycling accidents. *Journal of Safety Research*. https://doi.org/10.1016/j.jsr.2021.11.005

Wang, Y., Fan, Y., & Zhang, M. (2014). Comparison of stress on knee cartilage during kneeling and standing using finite element models. *Med Eng Phys*, *36*(4), 439-447. https://doi.org/10.1016/j.medengphy.2014.01.004

Wang, Y., Liang, L., Wang, D., Tang, Y., Wu, X., Li, L., & Liu, Y. (2020). Cycling with Low Saddle Height is Related to Increased Knee Adduction Moments in Healthy Recreational Cyclists. *Eur J Sport Sci*, *20*(4), 461-467. https://doi.org/10.1080/17461391.2019.1635651

Wanich, T., Hodgkins, C., Columbier, J.-A., Muraski, E., & Kennedy, J. G. (2007). Cycling injuries of the lower extremity. *JAAOS-Journal of the American Academy of Orthopaedic Surgeons*, *15*(12), 748-756.

Ward, S. R., Eng, C. M., Smallwood, L. H., & Lieber, R. L. (2009). Are current measurements of lower extremity muscle architecture accurate? *Clin Orthop Relat Res*, *467*(4), 1074-1082. https://doi.org/10.1007/s11999-008-0594-8

Wilson, D. R., Feikes, J. D., Zavatsky, A. B., & O'connor, J. J. (2000). The components of passive knee movement are coupled to flexion angle. *Journal of biomechanics*, *33*(4), 465-473.

Wong, T.-T., & Yeh, P.-Y. (2020). Reliable Accuracy Estimates from k-Fold Cross Validation. *IEEE Transactions on Knowledge and Data Engineering*, *32*(8), 1586-1594. https://doi.org/10.1109/tkde.2019.2912815

Wu, Y., Ma, Z., Zhao, H., Li, Y., & Sun, Y. (2020). Achieve Personalized Exercise Intensity through an Intelligent System and Cycling Equipment: A Machine Learning Approach. *Applied Sciences*, *10*(21). https://doi.org/10.3390/app10217688

Xu, J. Y., Nan, X., Ebken, V., Wang, Y., Pottie, G. J., & Kaiser, W. J. (2015). Integrated inertial sensors and mobile computing for real-time cycling performance guidance via pedaling profile classification. *IEEE J Biomed Health Inform*, *19*(2), 440-445. https://doi.org/10.1109/JBHI.2014.2322871

Yazdkhasti, A. (2023). *Subject-specific Human Knee FEA Models for Transtibial Amputees Vs Control Tibial Cartilage Pressure in Gait, Cycling and Elliptical Training* the Faculty of California Polytechnic State University]. San Luis Obispo.

Yoon- Ho Shin, J.-S. C., Dong-Won Kang, Jeong-Woo Seo, Joo-Hack Lee, Ju-Young Kim, Dae-Hyeok Kim, Seung-Tae Yang, Gye-Rae Tack. (2015). A Study on Human Musculoskeletal Model for Cycle Fitting: Comparison with EMG. *International Journal of Medical, Health, Pharmaceutical and Biomedical Engineering*, *9*, 43-47.

Zajac, F. E., Neptune, R. R., & Kautz, S. A. (2002). Biomechanics and muscle coordination of human walking: Part I: Introduction to concepts, power transfer, dynamics and simulations. *Gait & posture*, *16*(3), 215-232.

Zhang, B., & Ma, B. (2023). Meniscus Injuries under High-Intensity Training in Cycling Athletes. *Revista Brasileira de Medicina do Esporte*, *29*. https://doi.org/10.1590/1517-8692202329012022_0306

Zhang, G., Hong, T. T., Li, L., & Zhang, M. (2024). Automatic Detection of Fatigued Gait Patterns in Older Adults: An Intelligent Portable Device Integrating Force and Inertial

Measurements with Machine Learning. *Ann Biomed Eng*. https://doi.org/10.1007/s10439-024-03603-z

Zhang, X. S., Guo, Y., & Chen, W. (2009). *3-D Finite Element Method Modeling and Contact Pressure Analysis of the Total Knee Joint in Flexion* In 2009 3rd International Conference on Bioinformatics and Biomedical Engineering,

Zignoli, A., Fornasiero, A., Ragni, M., Pellegrini, B., Schena, F., Biral, F., & Laursen, P. B. (2020). Estimating an individual's oxygen uptake during cycling exercise with a recurrent neural network trained from easy-to-obtain inputs: A pilot study. *PloS one*, *15*(3), e0229466. https://doi.org/10.1371/journal.pone.0229466

Zinoubi, B., Zbidi, S., Vandewalle, H., Chamari, K., & Driss, T. (2018). Relationships between rating of perceived exertion, heart rate and blood lactate during continuous and alternated-intensity cycling exercises. *Biol Sport*, *35*(1), 29-37. https://doi.org/10.5114/biolsport.2018.70749

Zongxing, L., Shengxian, Y., Xiangwen, W., Xiaohui, C., & Chao, J. (2021). The Effect of Crank Length Changes from Cycling Rehabilitation on Muscle Behaviors. *Appl Bionics Biomech*, *2021*, 8873426. https://doi.org/10.1155/2021/8873426